

Imperial College
London

Design and testing of additively manufactured lattice structures for musculoskeletal applications

Umar Hossain

July 2020

A thesis submitted to Imperial College London
for the degree of Doctor of Philosophy
and for the Diploma of Imperial College

Department of Mechanical Engineering
Imperial College London, SW7 2AZ

Declaration of originality

I hereby declare that all work contained in this thesis has been produced by me, unless otherwise referenced.

Copyright declaration

The copyright of this thesis rests with the author. Unless otherwise indicated, its contents are licensed under a Creative Commons Attribution-Non Commercial-No Derivatives 4.0 International Licence (CC BY-NC-ND).

Under this licence, you may copy and redistribute the material in any medium or format on the condition that; you credit the author, do not use it for commercial purposes and do not distribute modified versions of the work.

When reusing or sharing this work, ensure you make the licence terms clear to others by naming the licence and linking to the licence text.

Please seek permission from the copyright holder for uses of this work that are not included in this licence or permitted under UK Copyright Law.

Abstract

Additive manufacturing (AM) methods present a new frontier in engineering, allowing the fabrication of porous lattice structures with tailored mechanical properties. AM structures can be made using bio-inert metals, creating controlled stiffness biomaterials. As bone formation is strain dependent, these AM biomaterials can be used in implants to optimise the strain in surrounding trabecular bone for peak bone formation. However, the behaviour of AM lattices varies and is subject to manufacturing constraints. The aim of this PhD was to investigate the mechanical behaviour of AM lattices, and maximise the clinical benefits of AM for musculoskeletal applications. Lattice architecture was shown to affect the anisotropy of an AM lattice biomaterial, increasing the stiffness in directions not often tested in the literature. The mechanical and morphological properties of individual struts within powder bed fusion (PBF) lattices were also shown to vary depending on the orientation of the struts to the build direction. The ultimate tensile strength of titanium alloy (Ti6Al4V) struts more than doubled when built at a low angle versus perpendicular to the build platform, and other properties were substantially lower than for the bulk material. Geometric imperfections were found for struts built at low angles. As such, a low stiffness modified stochastic lattice was designed and tested which avoided the problems found with struts built at low angles. The resulting lattice had improved stiffness isotropy and could be used for musculoskeletal applications, tuned to match the mechanical properties in local trabecular bone and enhancing bone formation.

Acknowledgements

Firstly, I would like to thank my main supervisor, Dr Jonathan Jeffers. Thank you for providing an exciting project, offering excellent and kind guidance, and always having an open door. I have been able to thoroughly explore my interests in this burgeoning field, and your enthusiasm and knowledge has helped me along greatly.

Secondly, I would like to thank Dr Shaaz Ghouse, for his immense support and foundational work in the Biomechanics group, which made much of my research possible. Your patience and willingness to help, either with improving my methodologies or teaching me the additive manufacturing process, has been invaluable.

Dr. Richard Van Arkel, thank you also for giving so much time in inducting me on the Renishaw machine, through the thick and thin of powder sieving and failed builds. Your optimism was unflinching, even in the oppressive heat of the AM lab. And to all the members of the Biomechanics group at large, thank you for the camaraderie and academic firepower. I have learnt a lot from being around such intelligent and welcoming people, and hope to continue the friendship and collaboration into the future.

My viva examiners, Dr. Angela Kedgley and Dr. Alex Dickinson, made excellent comments on the final version of this thesis. Thank you for your scrutiny. It was enjoyable to see how the thesis narrative and conclusions were made much more consistent by following your advice.

Thank you to all who helped proof-read the work in this thesis: Meva Armaing, Gwen Page Roberts, Hugh Lawrence, Mischa Stevens, Kalim Ahmed, Khadija Hossain and Aarti Jhoke. I count you amongst my dearest friends and family, not forgetting others who helped encourage me during my PhD. Your collective superior intellect has made this work far more coherent.

I would like to gratefully acknowledge the financial support that I have received, from The Engineering and Physical Sciences Research Council and Renishaw PLC for undertaking the degree, and also to The National Institute for Health Research and The Wellcome Trust for further supporting my research.

Finally, I would like to thank my family, and the lovely Meva, for taking care of me during the writing process, and for all that you do.

Contents

1	Introduction	2
1.1	Clinical context	2
1.2	Aim of the thesis	3
1.3	Thesis structure	3
2	Literature review	6
2.1	Biocompatible materials	7
2.1.1	First generation materials in arthroplasty	7
2.1.2	Stress shielding	9
2.1.3	Fixation and aseptic loosening	12
2.1.4	Bioactive materials	13
2.1.5	Current manufacturing methods	14
2.1.6	Porous structure theory	17
2.2	Additive manufacturing	21
2.2.1	Powder bed fusion of metal	24
2.2.2	Porous lattices and musculoskeletal research	28
2.2.3	Anisotropy and control of porous lattices	32
2.2.4	Mechanical testing	34
2.2.5	Manufacturing limitations	37
2.3	Bone properties	40
2.3.1	Mechanical behaviour of bone	41
2.3.2	Bone architecture	43
2.3.3	Bone remodelling	45
2.4	Musculoskeletal applications for metal AM	48
2.4.1	Optimising mechanical behaviour	48
2.4.2	Aims and objectives of the thesis	49
3	Lattice architecture and anisotropy	52
3.1	Introduction	53

3.2	Materials and methods	54
3.2.1	3D models for architecture investigation	54
3.2.2	Star length distribution.....	56
3.2.3	Printed specimens for mechanical testing	58
3.2.4	Materials and manufacturing	58
3.2.5	Mechanical testing	59
3.3	Results.....	59
3.3.1	Star length distribution rose diagrams	59
3.3.2	Mechanical testing	61
3.4	Discussion.....	63
4	Tensile testing of struts.....	66
4.1	Introduction.....	67
4.2	Materials and methods	70
4.2.1	Specimen manufacture	70
4.2.2	Micro-CT scanning.....	71
4.2.3	Segmentation and analysis.....	73
4.2.4	Tensile testing	80
4.3	Results.....	84
4.3.1	Diameter measurements.....	84
4.3.2	Strut morphology.....	85
4.3.3	Tensile testing results	87
4.4	Discussion.....	90
5	Compression testing of structures	96
5.1	Introduction.....	97
5.2	Materials and methods	98
5.2.1	Specimen design and manufacture	98
5.2.2	Materials and manufacturing.....	102
5.2.3	Mechanical testing	102

5.3	Results	103
5.3.1	Mechanical testing.....	104
5.3.2	SEM imaging	109
5.4	Discussion	110
6	Discussion	114
6.1	Most important findings.....	114
6.2	Implications of the findings for implant design.....	115
6.3	Limitations.....	115
6.4	Comparison to existing work.....	116
6.5	Future work.....	117
6.6	Further applications of the work	118
6.7	Research impact.....	119
6.8	Conclusion	119
7	Bibliography.....	120
8	Appendices	160
A1	Tensile testing of struts.....	160
A1.1	Further strut morphology.....	160
A2	Compression testing of structures	161
A2.1	Pilot data	161
A2.2	Patent filing receipt.....	165
A3	Permission documents.....	167
A3.1	Permissions granted.....	167
A3.2	Permission communications.....	174

Figures

Figure 2.1: Diagram of the hip joint, natural and implanted, with a modern metal-on-plastic implant.....	7
Figure 2.2: Free-body diagram showing simplified forces acting on femur.....	10
Figure 2.3: Modelling and clinical evidence of stress shielding.	11
Figure 2.4: Clinical evidence of aseptic loosening.	13
Figure 2.5: Conventional manufacturing processes for current metallic prostheses.....	15
Figure 2.6: Micrographs of Zimmer Biomet Trabecular Metal™	16
Figure 2.7: Example compressive stress-strain curves for porous materials.....	17
Figure 2.8: Compression tests of additively manufactured porous structures.....	18
Figure 2.9: Idealised open-cell structures drawn using definitions from Gibson and Ashby. [140].....	19
Figure 2.10: Simple pin-jointed structures.....	20
Figure 2.11: Overview of different AM technologies, and the materials with which they are generally associated.	23
Figure 2.12: Schematic of the powder bed fusion process, which is an example of additive manufacturing.....	25
Figure 2.13: Renishaw AM250 with build chamber highlighted.....	26
Figure 2.14: Laser PBF manufacturing for musculoskeletal applications.....	27
Figure 2.15: Compilation of unit cells and lattice structures made using metal PBF, categorised by type.....	30
Figure 2.16: Compilation of reported elastic moduli versus lattice porosity for lattices in the literature designed for musculoskeletal applications.....	31
Figure 2.17: Compilation of functionally graded lattices and optimised femoral stems.	34
Figure 2.18: Example stress-strain curve for uniaxial compression test of porous cellular material.	36
Figure 2.19: Effects of printing with and without support material	38
Figure 2.20: Varying strut aspect ratio for EBM struts.....	39
Figure 2.21: SEM micrographs of cancellous or trabecular bone from the femoral head. ..	40
Figure 2.22: Idealised models of trabecular bone structures.	41
Figure 2.23: Visual representations of bone architecture quantification methods.....	44
Figure 2.24: Further illustration of the star length distribution method.	44
Figure 2.25: Comparison between stiffness tensor and resulting stiffness tensor using measurements from FE model.....	45

Figure 2.26: Diagram of bone formation as described by Elliot in BHN theory.....	46
Figure 2.27: Bone formation frequency as a function of tissue loading.	47
Figure 3.1: Process to calculate star length distribution measure from 3D model of structure.	57
Figure 3.2: Test directions for structures.....	58
Figure 3.3: Rose diagram and interpolated results in 10 directions for all three structures	60
Figure 3.4: Results for mechanical testing shown as a rose diagram and bar chart.	62
Figure 4.1: Tensile testing specimens on build platform.	70
Figure 4.2: 3D-printed radioluscent strut holder.	72
Figure 4.3: Example slice of reconstructed micro computed tomography (microCT) volume.	73
Figure 4.4: Flowchart of segmentation and analysis of micro-CT data, showing overview of full process	75
Figure 4.5: In depth flowchart of last three stages of analysis, for cross sections, roughness and minimum effective area	76
Figure 4.6: Operations on strut cross sections showing the results of the ellipse fit and minimum bounding rectangle algorithm	77
Figure 4.7: Removal of eccentricity from strut mesh before roughness analysis.	79
Figure 4.8: Process of calculating the core area, and the ideal elliptical prism representing the mean surface of the strut.....	79
Figure 4.9: Tensile testing rig using linear variable differential transformers (LVDTs).....	82
Figure 4.10: Example stress-strain curve for a stainless steel specimen.	83
Figure 4.11: Comparison of diameter measurement methods per designed diameters of tensile specimens.....	84
Figure 4.12: Changing elliptical ratio over build angle for strut cross-sections.....	85
Figure 4.13: Average S_a roughness values (over entire strut surface) versus build angle. ...	86
Figure 4.14: Elastic modulus (E) for SS316L struts.	87
Figure 4.15: Elastic modulus (E) for Ti6Al4V struts.	88
Figure 4.16: Ultimate tensile strength (σ_{UTS}) for SS316L struts.	89
Figure 4.17: Ultimate tensile strength (σ_{UTS}) for Ti6Al4V struts.	89
Figure 4.18: Yield stress (σ_y) for SS316L struts.....	90
Figure 4.19: DIC strain map for a SS316L tensile specimen.	93
Figure 5.1: Stochastic structure variations.....	99
Figure 5.2: Detailed process description for creating structure variant A, B and C.....	100

Figure 5.3: Test directions for uniaxial compression of structures.....	101
Figure 5.4: Stress strain curve for a specimen of variant C in the '0' direction.....	104
Figure 5.5: Photographs of variant A specimens in the '0' direction for both SS316L and Ti6Al4V undergoing compression.	105
Figure 5.6: Elastic modulus vs test directions.....	106
Figure 5.7: Yield stress vs test directions.....	107
Figure 5.8: Strength over stiffness ratio vs test directions.....	108
Figure 5.9: SEM images of the same location on a Ti6Al4V specimen '0' structure for each variant A, B and C.	109
Figure 8.1: Average eccentricity of the strut over build angle.....	160
Figure 8.2: Elastic modulus vs test directions 0, 3, 1 and 2, ordered by increasing vertical orientation.	162
Figure 8.3: Yield stress vs test directions 0, 3, 1 and 2, ordered by increasing vertical orientation.	163
Figure 8.4: Plateau stress vs test directions 0, 3, 1 and 2, ordered by increasing vertical orientation.	164

Tables

Table 2.1:	Typical elasticity of materials used in joint replacement.....	9
Table 2.2:	Summary of EBM and laser PBF comparisons.....	27
Table 2.3:	Selection of tested mechanical properties for trabecular bone.....	42
Table 2.4:	Maximum anisotropic ratio found for Young's modulus in trabecular bone....	42
Table 3.1:	Lattice structures and trabecular structure to compare.....	56
Table 3.2:	Manufactured specimen dimensions compared to intended dimensions	61
Table 4.1:	Comparison of mechanical properties found for micro-struts built using laser PBF in SS316L and Ti6Al4V	68
Table 4.2:	Comparison of methodologies for tensile tests of laser PBF micro-struts built in SS316L and Ti6Al4V	68
Table 4.3:	Comparison of strut cross-section using different scanning parameters, with final selection in red	72
Table 4.4:	Summary of diameter measurements for each strut	80
Table 5.1:	Comparison of each variant and the distribution of struts in each direction .	100
Table 5.2:	Manufactured specimen dimensions compared to intended dimensions	103

1 Introduction

1.1 Clinical context

Musculoskeletal (MSK) conditions include over 150 possible diagnoses, characterised mainly by pain and reduced physical function [1]. These diagnoses include back and neck pain, osteoarthritis, rheumatoid arthritis and fractures, all of which can cause significant disability, and are projected to be the greatest loss of productive life years in the older workforce [2]. Impact of disease can be quantified by the number of years lived with disability (YLDs) within the world population. In 2015, MSK diseases were ranked second after 'mental and substance use disorders', in terms of YLDs according to data from the World Health Organisation [3]. Osteoarthritis is a significant contributor to YLDs, and YLDs attributed to osteoarthritis increased by 75% from 1990 to 2013, highlighting it as a growing concern [4]. This rise could be attributed to an aging population and exposure to risk factors such as obesity and a sedentary lifestyle [5].

In 2018 over 200,000 hip and knee joint replacement surgeries occurred in the UK, using metal orthopaedic implants to restore joint function [6]. Osteoarthritis is the main reason for surgery, causing degeneration of the articular cartilage in the joint space, and in severe cases sclerosis or hardening of the subchondral bone [7]. This results in pain from the sliding together of roughened bony surfaces. Treatment by joint replacement, or arthroplasty, entails replacing the bearing surface of the joint and necessitates the removal of bone to seat implant components. Bone tissue engineering (BTE) is a burgeoning field, seeking to add clinical capabilities to the treatment of segmental and contained skeletal defects [8]. Bone grafts are the current standard, with over 500,000 bone grafts used annually in the US [9]. Autografts and allografts come from autologous (patient) and allogenic (donor) bone tissue respectively, whereas BTE aims to create so called biomaterials that imitate the structure and properties of bone [10]. However, further tests are needed to establish the clinical efficacy of biomaterials [11].

Therefore, arthroplasty and BTE represent the main fields requiring biomaterials and structures to replace bone and other tissue for musculoskeletal applications. Materials and manufacturing processes intended for biomedical use have evolved over the years; although, those pioneered in the 20th century initially came from industrial applications [12]. As the human body is a highly corrosive environment, materials that were as inert as possible and easily available were prioritised. Those same inert materials continue to be used in

arthroplasty today and substantially improve the quality of life for patients [13]. Further development has seen biomaterials take a 'biologically active' role in healing [14], and new manufacturing techniques such as additive manufacturing (AM) are poised to provide further clinical benefit [15]. Whilst AM methods have been used to augment the manufacturing of existing implant designs [16], as a set of manufacturing technologies, AM is capable of fabricating components with substantially new geometries. This includes micro-scale internal architectures that can be precisely controlled [17]. As such, a wide range of mechanical performance can be achieved using porous lattice structures made from the bio-inert metals used up until today in arthroplasty and BTE [15]. These mechanical properties could be used to provide new clinical benefits to implant design, by taking advantage of the strain-dependent mechanisms of bone formation [18]. However, the mechanical performance of these lattices has not yet been fully described. More research is needed to understand the implications of this new manufacturing technique and the choice of internal micro-architecture on the macro-scale behaviour of lattices, before being used in clinical applications.

1.2 Aim of the thesis

The aim of this thesis is to investigate the mechanical properties of AM lattice structures for musculoskeletal applications. There will be two main focuses:

1. The design of lattices, and the impact that the choice of internal architecture has on the macro-scale behaviour of the structure.
2. The fundamental mechanical and morphological properties of AM metal as fabricated, and the effect of these on lattice structure behaviour.

1.3 Thesis structure

A review of literature covering the topics that have been established in this introduction follows. Chapter 3 uses mechanical testing and other methods to make initial comparisons between lattice architectures. Parts of Chapter 3 have been published in Additive Manufacturing 32 (2020) [19] and were presented at the International Society for Technology in Arthroplasty (ISTA) 2018 Congress, in the 3D Printed Implants and PSI seminar. All material within the chapter is my own work. Chapter 4 explores more of the fundamental mechanical properties of AM metal, and has been submitted to Additive Manufacturing. Chapter 5 details the design and manufacture of a modified lattice structure for musculoskeletal applications. This chapter has been accepted for publication in Additive Manufacturing, and the work within Chapter 5 has resulted in a patent application (UK Patent Application No 2005050.6). The details for this patent application can be found in the

Appendix, A2.2. Lastly, the main findings are discussed, and the potential for future work is considered.

2 Literature review

2.1 Biocompatible materials

In engineering design, a successful material for a given application will meet the necessary mechanical requirements. A successful biomaterial used as part of a load bearing medical device or implant also requires various biological compatibility with its local environment, termed 'biocompatibility'. Foreign body reaction (especially due to wear debris), cytotoxicity (potential to cause death to cells), and allergenic effect must be considered as well as matching mechanical behaviour [12,20]. As a first generation of biomaterials, metallic materials became especially prevalent due to their high specific strength and manufacturability, allowing them to replace hard tissue [21].

2.1.1 First generation materials in arthroplasty

Metal alloys currently used in bone implants today for joint replacement include cobalt-chrome molybdenum alloy (CoCrMo), commercially pure titanium (CPTi) and titanium aluminium vanadium alloy (Ti6Al4V), all of which are suitably biologically inert as bulk materials. The first hip prosthesis pioneered by G.K. McKee and Sir John Charnley was made of stainless steel, first implanted in 1960, however this soon gave way to CoCrMo when it was shown to mitigate friction and prevented loosening of the components [22–24]. An example hip prosthesis with the various components are shown in Figure 2.1.

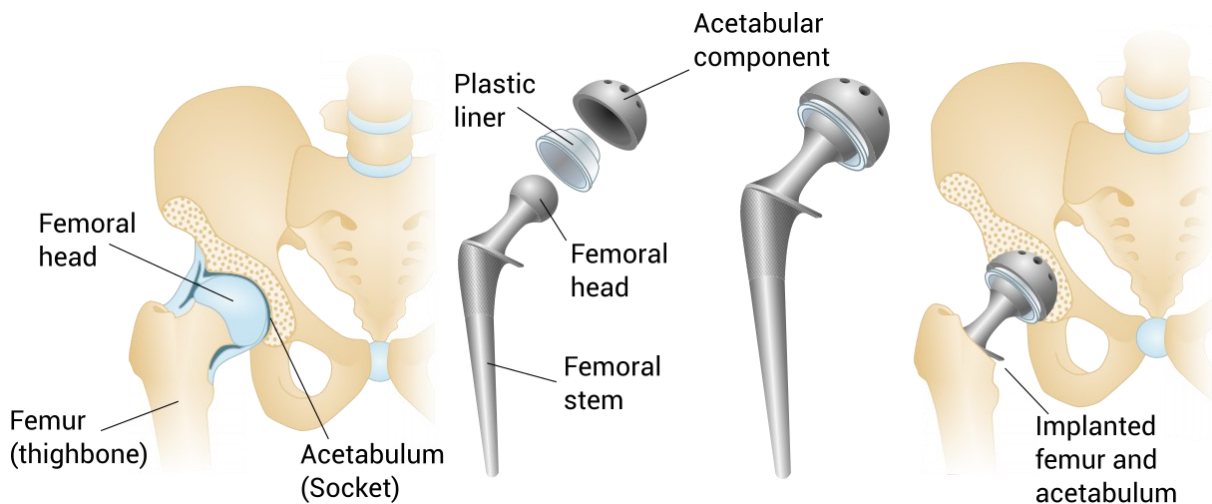


Figure 2.1: Diagram of the hip joint, natural and implanted, with a modern metal-on-plastic implant.

Femoral head and acetabulum are depicted, and the replacement of the biological interface with hip implant components.

These early designs were 'metal-on-metal', i.e. with a CoCrMo femoral and acetabular component. These had high loosening rates due to poor fits between the articulation surface, resulting in excessive wear, and concerns about binding up and 'self-welding' of the joint [23,24]. Therefore, ultra high molecular weight polyethylene (UHMWPE) was introduced as an

acetabular cup material to improve the tribology of the joint, and has since been used as a bearing material in other total joint replacement prostheses [25–27]. Charnley also introduced the use of polymethyl-methacrylate (PMMA), commonly known as bone cement, instead of fixation screws, increasing the short-term implantation success rate to over 90% [28,29]. Bone cement thus joins UHMWPE as a non-metallic biocompatible material that has become highly prevalent in orthopaedic solutions.

However, observation of wear particles from UHMWPE bearing surfaces prompted extensive research on the wear rates of metal-on-polyethylene pairings for different metallic alloys [30–32]. Other avenues for wear reduction were also explored, such as changing the implant geometry (diameter of the femoral head) and changing UHMWPE chemistry. An increased wear rate was linked to increased incidence of osteolysis, a resorption or loss of the bone around the implant as a consequence of cellular response to wear debris [33,34]. The wear rates of metal-on-metal prostheses were also examined and were subsequently shown to be low, due to improved manufacturing and design of the bearing surface [35–37]; although, osteolysis due to resulting metal ions was still an ongoing concern [38–40]. A recall of the DePuy ASR XL total hip replacement in 2010, a CoCrMo metal-on-metal prosthesis, brought issues with metal debris to the fore [41–43]. Failure of the implant was associated with adverse tissue reactions and high blood metal ion levels [44–46]. Further development of the bearing surface has also seen two ceramic materials, aluminum and zirconium oxide, being used in both the femoral and acetabular components of the hip prosthesis [47,48], which have shown low wear rates [30,48–50]. A further systematic review has shown ceramic bearings to have high survivorship [51]. Polyether ether ketone (PEEK) polymer has also been explored as an alternative bearing material [52,53], although it is used more regularly in other medical applications [54].

Regarding the mechanical behaviour and biomechanical compatibility of these materials, CoCrMo has a Young's modulus of approximately 230 GPa, over double that of Ti6Al4V, 110 GPa (see Table 2.1). The trabecular bone surrounding implants is much less stiff at 0.02–2 GPa, and the compact cortical bone is stiffer at 3–30 GPa [15,55]. CPTi and Ti based alloys, whilst more expensive, possess a superior mechanical match to the surrounding bone and a better corrosion resistance [20,28,55,56]. Of the two titanium offerings, titanium alloy Ti6Al4V exhibits higher strength than other grades of CPTi. Tantalum has a similar biocompatibility to Ti and has been used as an implant material [57,58], with a middling Young's modulus of 185 GPa. Therefore, whilst they may not be the ideal materials for a joint bearing surface, metallic alloys are still indispensable as structural biomaterials. Titanium alloys with

different alloying elements have also been developed, such as Ti–Nb–Zr–Ta (TNZT) alloys, which have a lower Young's modulus so as to better match the elastic modulus of bone [20,28,59]. Table 2.1 below compares the elastic modulus of many prevalent biomaterials to those of bone and articular cartilage.

Table 2.1: Typical elasticity of materials used in joint replacement.

Material	Elastic modulus (GPa)
Articular cartilage	0.001 – 0.17
Trabecular bone	0.02 – 2
Cortical bone	3 – 30
UHMW-PE	0.5
Bone cement (PMMA)	3
TNZT alloys	55 – 66
Commercially pure titanium (CPTi)	105
Ti6Al4V alloy	110
CoCrMo alloy	230
Tantalum	185
Stainless steel	205
Zirconium oxide	200
Aluminum oxide	380

Adapted from [15,28,55,58,60].

2.1.2 Stress shielding

The potential for bone loss due to wear debris (osteolysis) has been explored, but bone loss can also occur due to a poor mechanical match of the implant material to the surrounding bone (termed 'periprosthetic' bone), which is referred to as stress shielding.

The mechanical forces that act on an intact femur within the hip joint can be summarised as a combination of bodyweight forces and abductor muscle forces, which vary depending on the geometry of the hip and muscle strength [61]. Using a simplified free-body diagram, the reaction force at the hip joint bearing surface can be thought of as a resolution of these forces creating moments acting on the femur. These can be seen in Figure 2.2, where changing geometry (dimensions a and b) of the femur results in different loading in the femur itself. When considering the implantation of the femoral component of a hip implant, this loading regime changes substantially.

This altered loading regime changes the strain throughout the femur, shown in Figure 2.3a using an FEA model, where strain energy density (SED) has been plotted. Lower SED is found in the thicker bone around the femoral component, as stress is absorbed by the stiffer implant [62]. This causes an adaptive response of lower mass in the periprosthetic bone, due to a phenomenon known as 'Wolff's Law' where bone remodels in response to its mechanical environment [63]. A typical X-ray or radiograph of a patient two years postoperatively is seen

in Figure 2.3b, where lower density bone surrounds the femoral component and a thickening of bone occurs at the tip of the femoral stem as load is redistributed to the femur. Further detail on how bone mass is influenced by mechanical triggers is explored later in section 2.3.3.

The link between lower stiffness implants and the reduction of this stress shielding effect was first established in the 90s through canine model studies, and later with clinical follow-up and patient autopsies [64–68]. Material choice was shown to be an important factor, with less bone loss occurring with titanium hip prostheses compared to cobalt chrome [69–71]. Finite element analysis (FEA) models created of the hip and knee also showed mechanical mismatch could cause reduced bone mass [72,73], and 'hollow stem' femoral components for the hip have been explored in FEA to reduce stiffness [74]. These methods were compared to canine models and showed good agreement with bone loss measurements [75,76]. The clinical consequences of stress shielding potentially include greater risk of fracture due to poor bone quality [66,68]. Poorer quality trabecular bone around the implant may make revision surgery more difficult.

The effect of femoral stem geometry on bone formation and resorption has been explored, with various femoral stems designed specifically with the aim to minimise stress shielding. Adding a 'collar', sometimes specifically called a calcar collar, aimed to change how load is distributed to the outer cortex of the femur and the resulting strain distribution in the femur. FEA studies have shown changes in how a calcar collar would affect bone formation [77,78], and both cadaveric and meta-analyses have shown that collared stems have greater immediate stability than collarless stems [79,80].

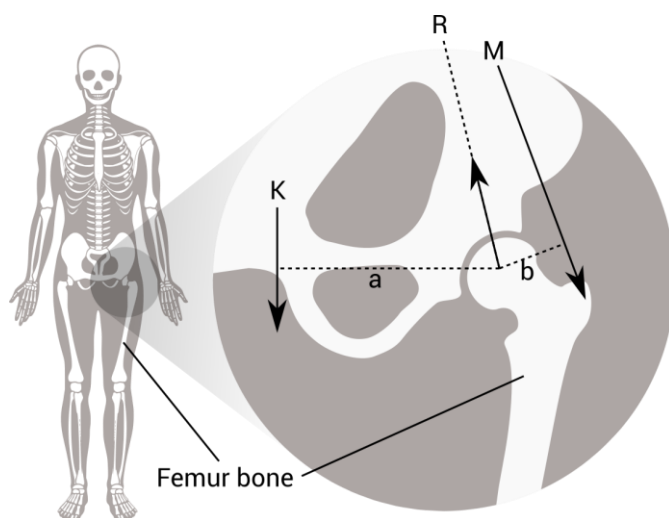
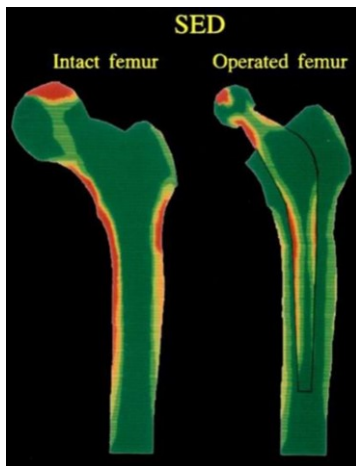
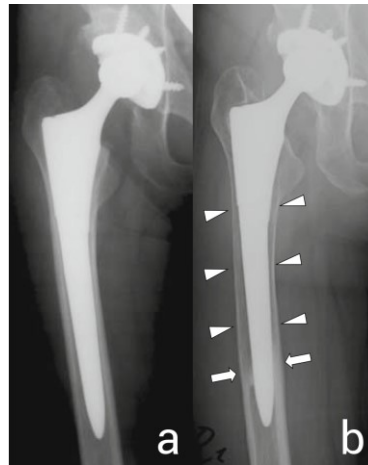


Figure 2.2:
Free-body diagram showing simplified forces acting on femur.

K is the force of bodyweight (halved when standing on two legs, and minus weight bearing legs) acting at a perpendicular distance **a** from femoral joint. **M** is the abductor muscle force, acting at distance **b**. **R** is the joint reaction force. Arrows are not to scale.



(a)



(b)

Figure 2.3:
Modelling and clinical evidence of stress shielding.

(a) Strain energy density (SED) in FE model of femur. Image reproduced with permission from the rights holder, Elsevier. [62]

(b) Radiographs from patient postoperatively (a) and 5 years after surgery (b). Shows stress shielding at arrows, and bone formation at arrowheads. Image reproduced with permission from the rights holder, Elsevier. [81]

Reducing the cross-sectional area of the stem reduces the moment of inertia, and therefore the stiffness of the implant. The Alloclassic® stem was flattened and tapered, reducing the overall stiffness and showed favourable results [82]. Other designs reduce the material at the tip of the implant by using a 'clothes-pin' design, or using flutes and hollows [83,84]. All prostheses mentioned here were made from Ti6Al4V, which has come to be a reliable metallic alloy biomaterial. However, polymer and carbon composite stems have been attempted. The Robert Mathys isoelastic total hip replacement, first designed in 1975, used a stainless steel core, encased in polyacetyl resin [85]. The term isoelastic referred to the concept of continuous elasticity of bone and implant, allowing them to deform as one unit. Similar implants were coated in Proplast, a composite of polytetrafluoroethylene reinforced with carbon fibre (PCFC), and others with porous polysulfone [86,87]. Initial animal studies with implanted polymer specimens in canine femurs showed some promise with bone ingrowth, demonstrating that a lower stiffness material does not 'stress shield' the surrounding bone [87].

The Mathys implant enjoyed some initial success [88], though follow-up studies tracking the performance after 15 years have shown unacceptably poor clinical outcomes, citing high debris production and poor fixation of the implant [89]. Proplast coated stems suffered from delamination and disintegration of the coating, causing loosening of the implant and high incidence of thigh pain. Osteolysis was also reported [90–92]. Similar issues existed for a porous polysulfone stem with titanium alloy core [87]. Overall, low-stiffness isoelastic stems were limited by poor fixation of the implant at the polymer-bone interface [93], with only soft tissue ingrowth [94,95], as well as mechanical failure due to inability to withstand cyclic load, resulting in fragmentation and sometimes early fracture [96]. The implants also presented a lack of suitable surface for the bone to grow into [86]. FEA models of low-stiffness femoral

stems indicated that whilst stress shielding may be reduced, shear stresses at the bone-implant interface may increase, which would exacerbate any poor fixation of the implant [72]. In choosing a material for a femoral stem, higher modulus materials could cause stress shielding, leading to poorer quality bone, and increased motion of the implant as bone quality and fixation suffer [97]. However, in the absence of perfect fixation, lower modulus materials would cause greater stresses at the interface, also leading to increased motion of the implant relative to the bone [98], as shown in FEA studies. Indeed, this effect was shown in a canine model, with a titanium alloy stem implanted in one femur and a composite stem implanted in the other that was 3-5 times less stiff than the canine femur. There was a negligible difference in overall femoral stress shielding, and a significant decrease of bone ingrowth into the composite stem, as well as a three times higher growth of a fibrous tissue around the implant, indicating poor connection with solid bone [99]. Therefore, especially in the case of hip arthroplasty, a compromise must be found in the stem stiffness between stress-shielding induced loosening and loosening due to poor bone ingrowth into low-stiffness materials.

However, the implications of high stresses at the bone-implant interface, exacerbated by polymer and composite low-stiffness implants, are particular to the loading requirements of the femoral component in hip arthroplasty, and depend on poor fixation of the implant. Therefore, these unsatisfactory clinical results with lower modulus polymers and composites encouraged a return to metallic alloys, and a greater focus on improving fixation of implants and bone growth at the bone-implant interface.

2.1.3 Fixation and aseptic loosening

This first generation of successful biomaterials from the 1960s and 1970s (mainly metallic alloys) were essentially inert and aimed to elicit as little biological response as possible [12]. Despite this, after implantation, an adverse biological response was still found to occur, consisting of the formation of a fibrous tissue around the implant, known as fibrosis or fibrotic reaction, leading to encapsulation of the biomaterial [100]. This can inhibit integration of the implant, known as osseointegration, where there is a direct structural connection between the load-bearing components and the surrounding bone. It can also be defined as the lack of relative motion at the implant/bone interface, termed micromotion [101,102].

The undesirable biological processes described so far, osteolysis, stress shielding and fibrosis can all contribute to poor osseointegration, ultimately leading to loosening of the implant [103]. This is termed aseptic loosening, which was the most common reason for surgery revision of hip and knee implants in the UK in 2018 [6]. This is diagnosed by

progressive 'radiolucent zones' in patient X-rays, shown in Figure 2.4. The mean width of these zones in one study of failed implants was 2.8 mm [104]. Therefore, a combination of a good mechanical match to bone and strong fixation are important to avoid aseptic loosening, as well as minimised wear debris from the bearing material pair. Mitigating the development of a fibrous layer at the implant/bone interface, improving fixation and reducing micromotion have all been driving forces in the development of bioactive materials, the second generation of biomaterials [12].

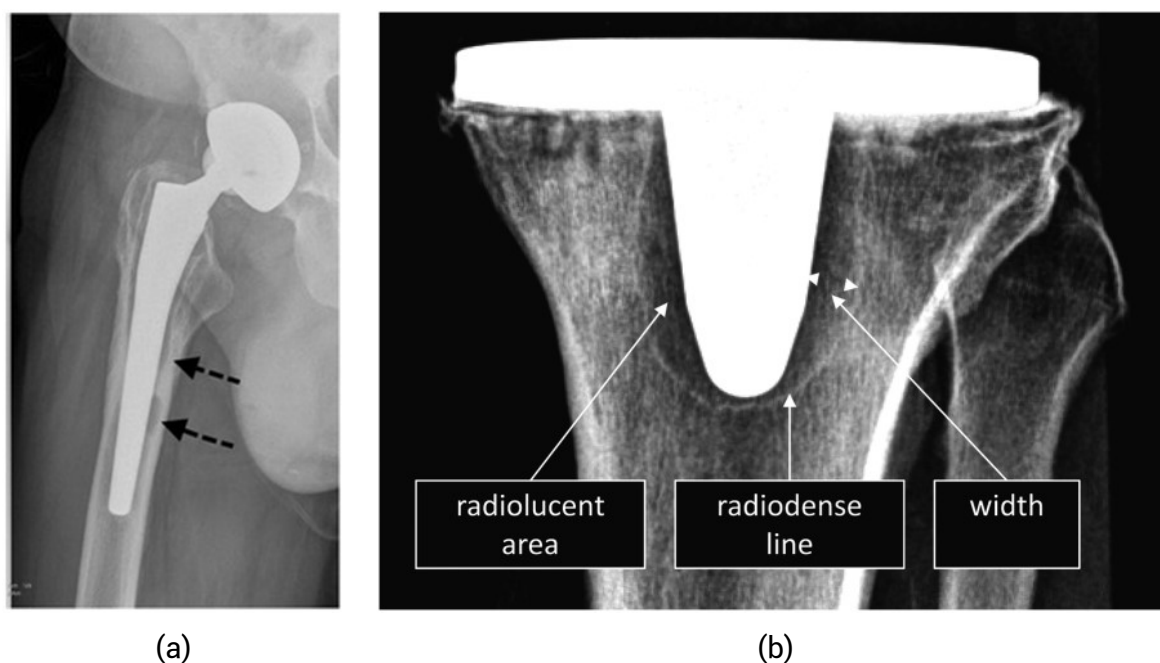


Figure 2.4: Clinical evidence of aseptic loosening.

(a) Arrows pointing to radiolucent areas near a femoral stem that indicate aseptic loosening. Image reproduced with permission from the rights holder, SAGE Publications. [101]

(b) Similar labelled x-ray with radiolucent areas for a tibial tray. Image reproduced with permission from rights holder, Taylor & Francis. [104]

2.1.4 Bioactive materials

The second generation of biomaterials include 'bioactive' components that elicit a tissue response, and mainly involve ceramic materials. Hydroxyapatite (HA) is a material made from calcium phosphate that can be sintered into ceramic form, and has been used since the 1980s in dentistry and orthopaedics [105–107]. HA was shown to promote a tissue response of osteoconduction, where bone grows along the material, forming a mechanically strong interface, thereby becoming osseointegrated [108]. It has since become routinely used as a coating on metallic prostheses, and has been shown to promote earlier and stronger fixation of an implant into the surrounding bone [109–112]. In addition, HA enhances bone ingrowth

into an implant across a 1mm gap [113], in both stable and unstable conditions [114]. HA coatings can also overcome an existing fibrous membrane, thereby limiting fibrosis [115], and potentially seal the bone/implant interface, preventing migration of wear particles [116]. Therefore, HA helps osseointegrate implants with an imperfect mechanical fit and overcome fibrosis and osteolysis, reducing the possibility of aseptic loosening [111].

Other bioactive ceramic materials like HA include other calcium phosphates, such as β -tricalcium phosphate (β -TCP) and bioactive glasses [10,12]. Newer third generation biomaterials related to bone tissue engineering (BTE) aim to fully imitate bone, creating living tissue constructs that mimic the bone tissue microenvironment, helping the body heal itself once implanted [10,14]. This requires the ability for the material to resorb into the body at the same rate as being replaced by tissue, and not just provide structural support in the body. There is some resorption or biodegradation of ceramic materials in the body, with β -TCP having a higher solubility than HA [106,111]. However, fully resorbable materials used in third generation BTE tend to be polymers. Synthetic polymers such as polyactide, polyglycolide and poly(ϵ -caprolactone) are used, as well as natural polymers such as chitosan and hyaluronic acid, which are modified with various bone morphogenetic proteins to encourage bioactivity [12]. Bone remodelling is explored further in section 2.3.3.

2.1.5 Current manufacturing methods

First generation biomaterials have been combined with second generation bioactive materials to create solutions for musculoskeletal disease with clinical impact. Overall, metallic alloys have shown the most promise for larger structural requirements, a semi-permanent solution, necessary until bone tissue engineering potentially provides biomaterials that resorb and are replaced by hard tissue. However, the elastic moduli of these materials are still orders of magnitude larger than trabecular bone, as shown in Table 2.1.

Current conventional methods for manufacturing metallic prostheses involve various forming processes, machining processes and finishing processes as shown in Figure 2.5. The bulk material is usually formed by forging, sintering, or casting. As these methods create solid objects, they constrain the stiffness of the component to be that of the bulk material. For machining, conventional methods include milling, turning and drilling, but newer methods include water-jet machining, ultrasonic machining and technologies which use ion or electron beams [117]. Metallic biomaterials such as Ti6Al4V and CoCr alloys can have particular machining characteristics, such as segmented chip formation, which need to be accounted for in machining operations. Prostheses also require high surface quality and tight tolerances, especially on bearing surfaces [118].

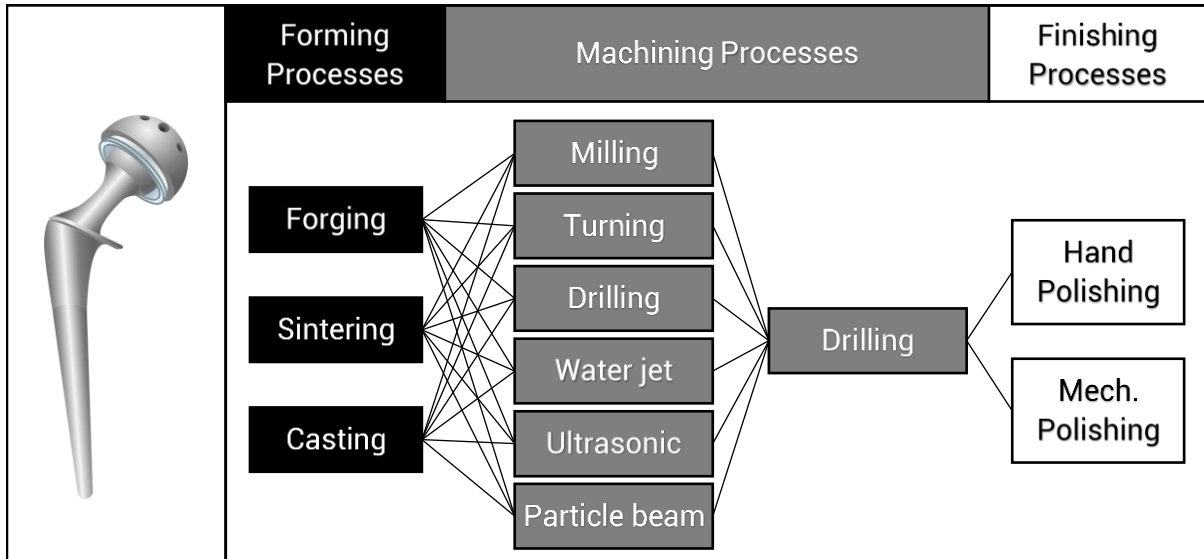


Figure 2.5: Conventional manufacturing processes for current metallic prostheses.

Adapted with added machining processes [118].

Whilst Ti and Ti alloys already exhibit a lower bulk elastic modulus, various techniques have been used to reduce the stiffness of the material without changing the alloying elements. Introducing porosity into the bulk material, and adding negative space, reduces the amount of solid material in the macro volume and therefore the overall stiffness of the whole component. Porous metals were first considered for use as implant materials in the 1970s, with some positive results; although, these mainly related to bone ingrowth into pores rather than preventing stress shielding [119–122]. Plasma spraying for titanium (or hydroxyapatite) coatings has since been employed regularly in implants [123,124], and are technically a way of adding porosity to the metal. When applied thickly they show a porosity of around 30% by volume [54]. However, they are usually only used as a thin (<150 μm thick [54]) coating, again intended to increase roughness and improve osseointegration. This would not necessarily cause a change in overall stiffness of the component.

Many industrial manufacturing methods exist that create true porous metals, referred to as 'solid foams' or cellular solids [125]. These can mainly be divided between closed-cell or open-cell foams. Closed-cell foams have individual voids or pores that are disconnected, whereas open-cell foams have voids that connect together, allowing other materials to traverse through the metal foam, which in the case of orthopaedics may include biological fluids or bone tissue [126]. Closed-cell foams are usually manufactured using bubbles in liquid metals, either by gas injection or foaming agents within molten metal which decompose to a gas, producing limited closed cell structures [125,127]. However, it is difficult to control the size and distribution of the resulting pores.

Open cell structures can be manufactured using multiple methods, including sintering or diffusion bonding of metal powders and fibres [128–130], investment casting of open-cell polymer foams [131], or casting around space holder materials [132]. The distribution of pores in these methods depends on the size and shape of the powders/fibres, or in the case of casting methods, the 'mould' used, which may be an uncontrolled polymer foam. Another method, chemical vapour deposition, allows gaseous metallic compounds to condense on a colder substrate, forming a solid foam. This has yielded a commercial orthopaedic product called Zimmer Biomet Trabecular Metal™, which is created using vaporised tantalum deposited on a carbon skeleton left from a pyrolysed polyurethane foam [126]. A scanning electron micrograph of this material is shown in Figure 2.6 below. This material has a relatively homogenous porosity of 75-85% and a low elastic modulus of 2.5-3.9 GPa, compared to a bulk modulus of 185 GPa [58,133]. The material showed good bone ingrowth performance [134], and acetabular cups and tibial components made out of Trabecular Metal™ have been used successfully in hip and knee arthroplasty [135,136].

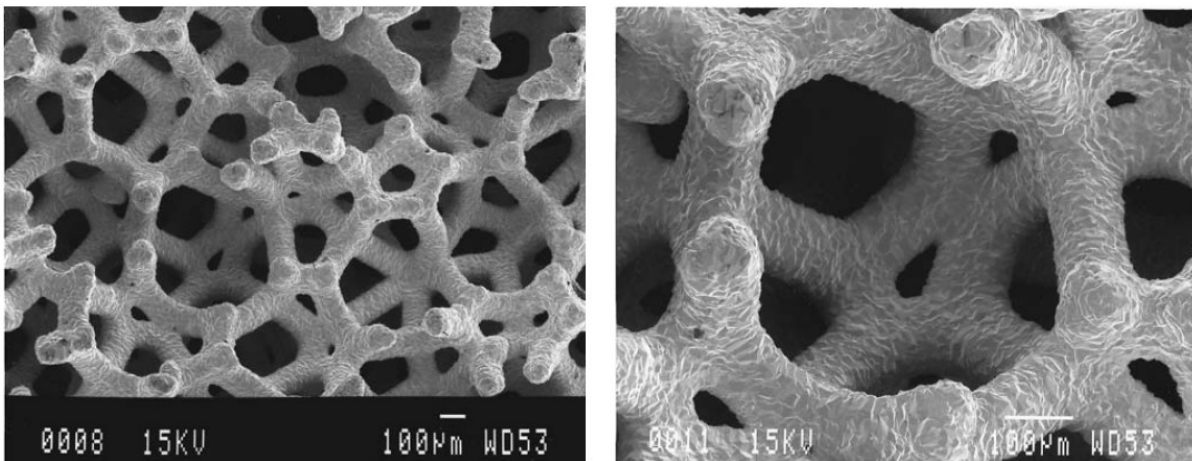


Figure 2.6: Micrographs of Zimmer Biomet Trabecular Metal™.

As seen with a scanning electron microscope, showing the porous structure achieved with vapour deposition. Closer zoom on right. Image reproduced with permission from the rights holder, the British Editorial Society of Bone & Joint Surgery. [134]

The mechanical performance of these cellular solids is directly dependent on the porosity of the material. A higher porosity was shown to decrease the elastic modulus of these industrial metal foams, whether closed-cell or open-cell [137–139]. An analytical approach to cellular solids, relating the architecture and amount of porosity to elastic and plastic behaviour was written by Gibson and Ashby [140], which provided a framework to analyse mechanical behaviour. As newer additive manufacturing (AM) methods for creating cellular solids have become available, greater dynamic control of the distribution of pores and architecture within

the component has become possible [125,126], leading to further exploration of porous materials for musculoskeletal applications.

2.1.6 Porous structure theory

The following summarises material from Chapter 5 of Cellular solids: Structure and properties by Gibson and Ashby (1997) and related papers, which focus on the analytical relationships between the geometry or morphology of the cells in a 3D cellular solid, and the resulting mechanical performance of the whole solid [140]. The most important characteristic of a cellular solid is its relative density, ρ^*/ρ_s , the fraction of solid material in a unit volume. The terms in the ratio refer to the density of the porous material in kgm^{-3} (ρ^*), and the density of the bulk material (ρ_s). This reflects the way that this value is calculated experimentally, by the dry weighing of a given volume of each material. The fraction of empty space in the material is the porosity, related to the relative density as the complement to 1, as follows: $(1 - \rho^*/\rho_s)$. Both are usually expressed as a percentage.

The behaviour of a cellular solid or foam under compression is shown in Figure 2.7, for foams where the bulk material has a ductile or plastic method of yielding, versus one with a brittle response. Three distinct regions are visible. The linear elastic regime is controlled by bending of cell beams or struts in an open-cell foam, and cell walls in closed-cell foams. The plateau of stress is due to continual plastic yielding, and the collapse of cells by buckling. In areas of high bending moment, plastic hinging occurs in ductile materials, and sudden brittle crushing in brittle materials, such as ceramics. Eventually, as cell members are compacted together, densification occurs, accompanied by a steep increase in stress as the specimen acts more like a solid material.

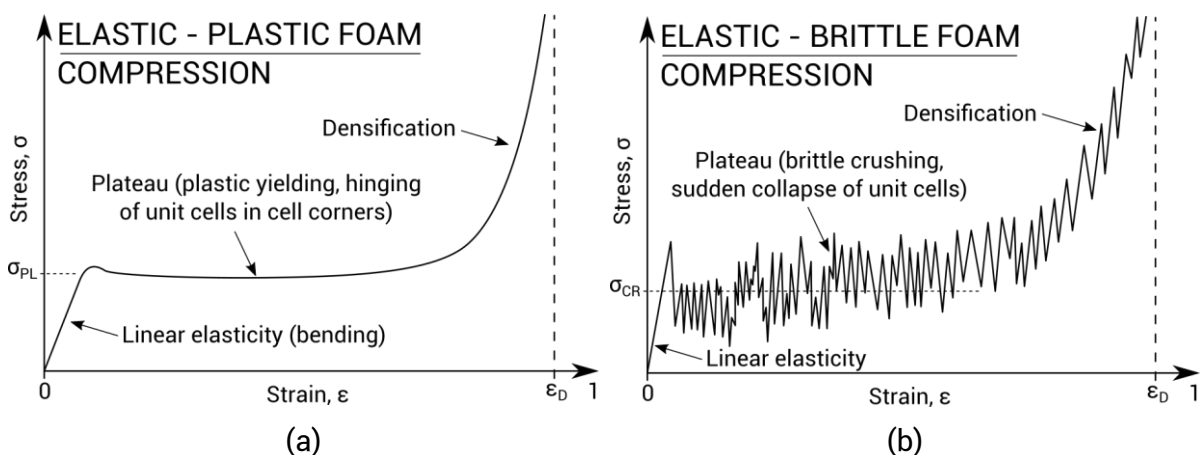


Figure 2.7: Example compressive stress-strain curves for porous materials.

(a) Elastic-plastic and (b) elastic brittle foams, showing linear elasticity, plastic collapse and densification. σ_{PL} and σ_{CR} are the plastic yielding and crushing strength respectively. ϵ_D is the strain at which densification occurs.

This three-stage behaviour is shown for compression specimens made using additive manufacturing (AM) methods in Figure 2.8. The stainless steel structure in Figure 2.8a displays 'elastic-plastic' behaviour, whereas the same structure in Figure 2.8b made from Ti6Al4V alloy fails in a brittle manner.

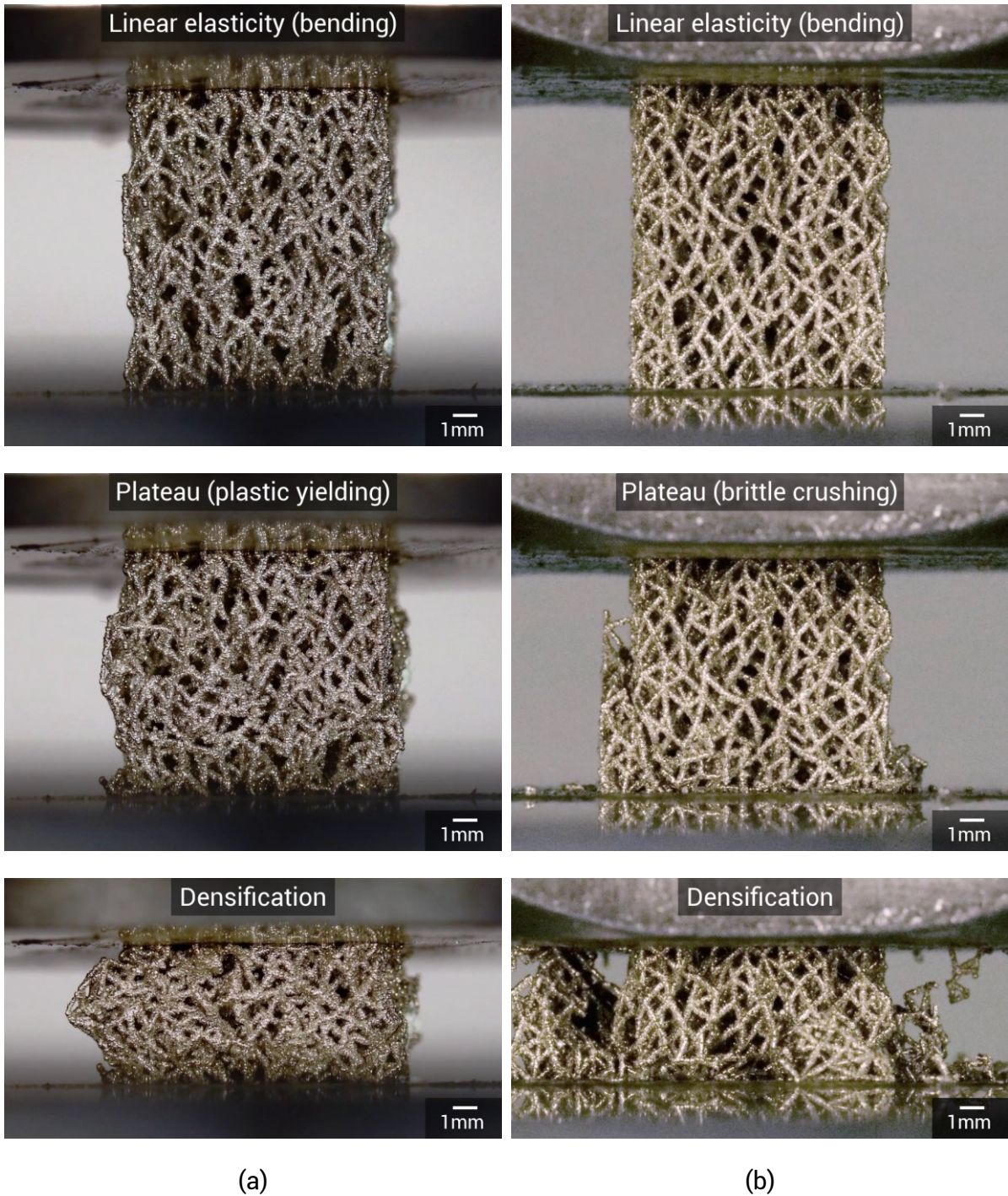


Figure 2.8: Compression tests of additively manufactured porous structures.

(a) Stainless steel and (b) Ti6Al4V structures showing the three stages of linear elasticity, plateau stress and densification during compression test.

Idealised open-cell structure

An idealised open-cell structure is shown below in Figure 2.9, whereby a cubic array of struts with length l and thickness t are joined in a staggered fashion, with struts meeting at midpoints. The Young's modulus for the cellular solid can be derived analytically, assuming that the struts deflect at the midpoint by load F using standard beam theory, and that the relative density is low enough ($\rho^*/\rho_s < 0.1$) that shear and axial forces are insignificant. A square cross section is used, whereas the cells in real foams may have different geometry. Assuming that deformation occurs by bending of cell struts, any constants that arise from more complex cell geometry can be accounted for later.

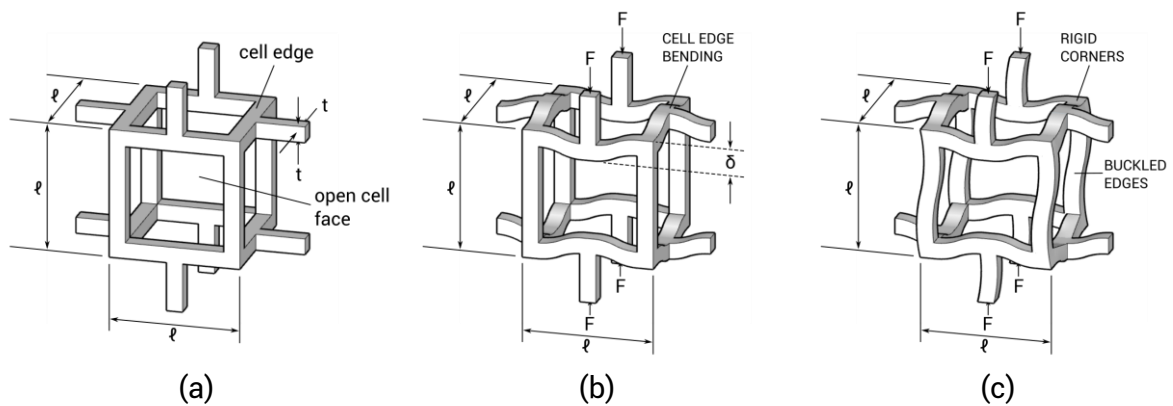


Figure 2.9: Idealised open-cell structures drawn using definitions from Gibson and Ashby. [140]

Cubic array of members of length l and thickness t , where:

- (a) is undeformed,
- (b) shows the bending of cell struts and
- (c) shows the eventual buckling at critical load.

Using beam theory and dimensional analysis, the relationship between Young's modulus and relative density of the foam is shown in Equation 2.1,

$$\frac{E^*}{E_s} = C \left(\frac{\rho^*}{\rho_s} \right)^2 \quad \text{Equation 2.1}$$

where C is a constant of proportionality that includes geometric constants that arise from the dimensions of the unit cell l and t . E^* is the resulting Young's modulus of the porous structure, and E_s is that of the bulk material. The Young's modulus is proportional to the square of the relative density for this structure. Assuming that the failure of the open-cell structure is caused by buckling of the cell struts as in Figure 2.9c, using Euler's formula, and that cell corners account for a significant part of the volume, the elastic collapse stress σ_{el}^* is shown to be:

$$\frac{\sigma_{el}^*}{E_s} = C \left(\frac{\rho^*}{\rho_s} \right)^2 \left(1 + \left(\frac{\rho^*}{\rho_s} \right)^{1/2} \right)^2 \quad \text{Equation 2.2}$$

This relationship to σ_{el}^* includes some higher exponents of the relative density for this idealised structure. However, these relationships only work for structures that have a similar connectivity to the ideal structure and for which the assumptions are valid as described. In practice, the properties of open-cell foams have been shown to scale with the relative density as follows: stiffness scales with $(\rho^*/\rho_s)^2$ and strength with $(\rho^*/\rho_s)^{1.5}$, where the deformation is governed with cell wall bending [141,142]. This includes some closed-cell foams, where cell walls provide low contribution to stiffness. Where other assumptions fail, such as the failure of unit cells by buckling, this may change the exponent of the relative density. The mechanical properties of cellular solids in general will follow the form of Equation 2.3 below [143], where connectivity and cell geometry will control constants C and n .

$$\frac{\text{foam property}}{\text{bulk material property}} = C \left(\frac{\rho^*}{\rho_s} \right)^n \quad \text{Equation 2.3}$$

Other structures

A distinction was made between 'bending-dominated' and 'stretch-dominated' structures. Where structures have a greater connectivity, struts are prevented from bending and act in uniaxial tension or compression. Figure 2.10a shows a pin-joint structure or 'mechanism', which according to Maxwell's criterion is statically indeterminate and would collapse on application of force F . Adding a strut, as in Figure 2.10b, creates a determinate structure where all forces are uniaxial, and no bending occurs.

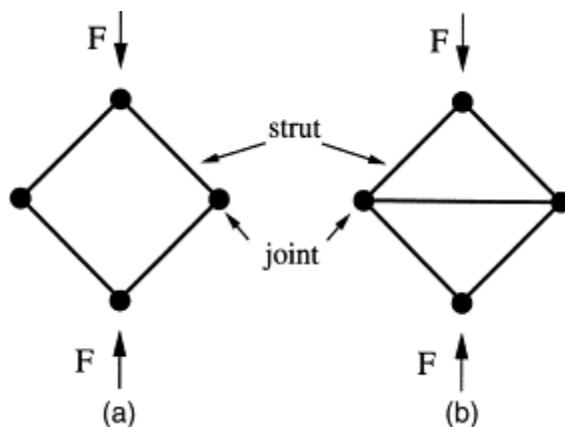


Figure 2.10:
Simple pin-jointed structures.

- (a) Shows a mechanism, and
- (b) shows a determinate structure.

Image reproduced with permission
from the rights holders, Elsevier.
[142]

For the case where all pin-joints became rigid, the previous analysis assuming bending of the open-cell beams in compression would apply to the mechanism in Figure 2.10a and no longer to the structure in Figure 2.10b. Where rigidity is increased in this way throughout a foam, making it stretch-dominated, the stiffness is increased by ten times and the strength

by three times for the same relative density [142]. In a complex foam made using traditional techniques, it may be difficult to establish the topology or ensure true rigidity. A full structural analysis can be carried out to determine whether a structure is statically and kinematically determinate [144], though decreasing the number of mechanisms throughout the structure overall would encourage stretch-dominated behaviour. Controlling this through casting methods or metal powder sintering would be highly impractical; however, by using AM methods to create porous lattices, specific control over the topology of structures is indeed possible.

2.2 Additive manufacturing

Additive manufacturing (AM) methods deliver a new range of engineering possibilities due to precise control of internal architecture and material deposition within a component. AM, otherwise known as 3D printing, is juxtaposed to traditional subtractive manufacturing such as CNC milling and machining, as material is deposited additively until the final component is created. This allows for a wider range of complex geometries at no added 'cost', i.e. solid parts take as long to manufacture as parts with internal architecture, something which subtractive tooling does not achieve. An overview of the different hardware methods that exist is shown in Figure 2.11, as well as the materials which they are associated with. These range from metals, through to ceramics and plastics, including the biomedical metallic alloys which have been discussed. AM methods use a 3D CAD model of a component as an input. For this model, a toolpath is created that allows deposition of the desired material where necessary to recreate the model geometry. For almost all AM methods, the 3D model is 'sliced' into cross sections, which are then built layer by layer until the component is completed.

Many AM systems exist for metal, which are mainly shown in the top half of Figure 2.11. The majority of traditional metal AM systems can be categorised into two groups: direct energy deposition systems and powder bed fusion systems [145]. Direct energy deposition (DED) involves the creation of parts by melting material feedstock as it is deposited, either using a wire feed or powder feed [146]. Wire feed systems such as wire and arc AM (WAAM) uses a welding arc to melt and deposit wire feedstock, used by RAMLAB (ramlab.com, Rotterdam, Netherlands) to manufacture on-demand maritime components [147–149]. Electron beams and gas metal arcs or plasma arcs are also used as a heat source [150]. Powder feed systems include direct metal deposition (DMD), commercialised by Optomec as laser engineered net shaping (LENS), use powder feedstock through a nozzle which is melted by laser as needed [151,152]. Variations of this technique include laser consolidation or deposition (LC/LD) [153] as well as construction laser additive directe (CLAD®) a French commercialisation of DED [154,155].

Powder bed fusion (PBF) systems also use a heat source to melt or sinter powder particles. However, rather than depositing the powder on demand, the powder is spread in thin successive layers, upon which the heat source melts the powder in the shape of the specific 'slice' needed. The melted material solidifies to the solid component under the current layer, and the process is repeated until the final component is completed and surrounded with unused powder. A schematic for the PBF process is shown in Figure 2.12.

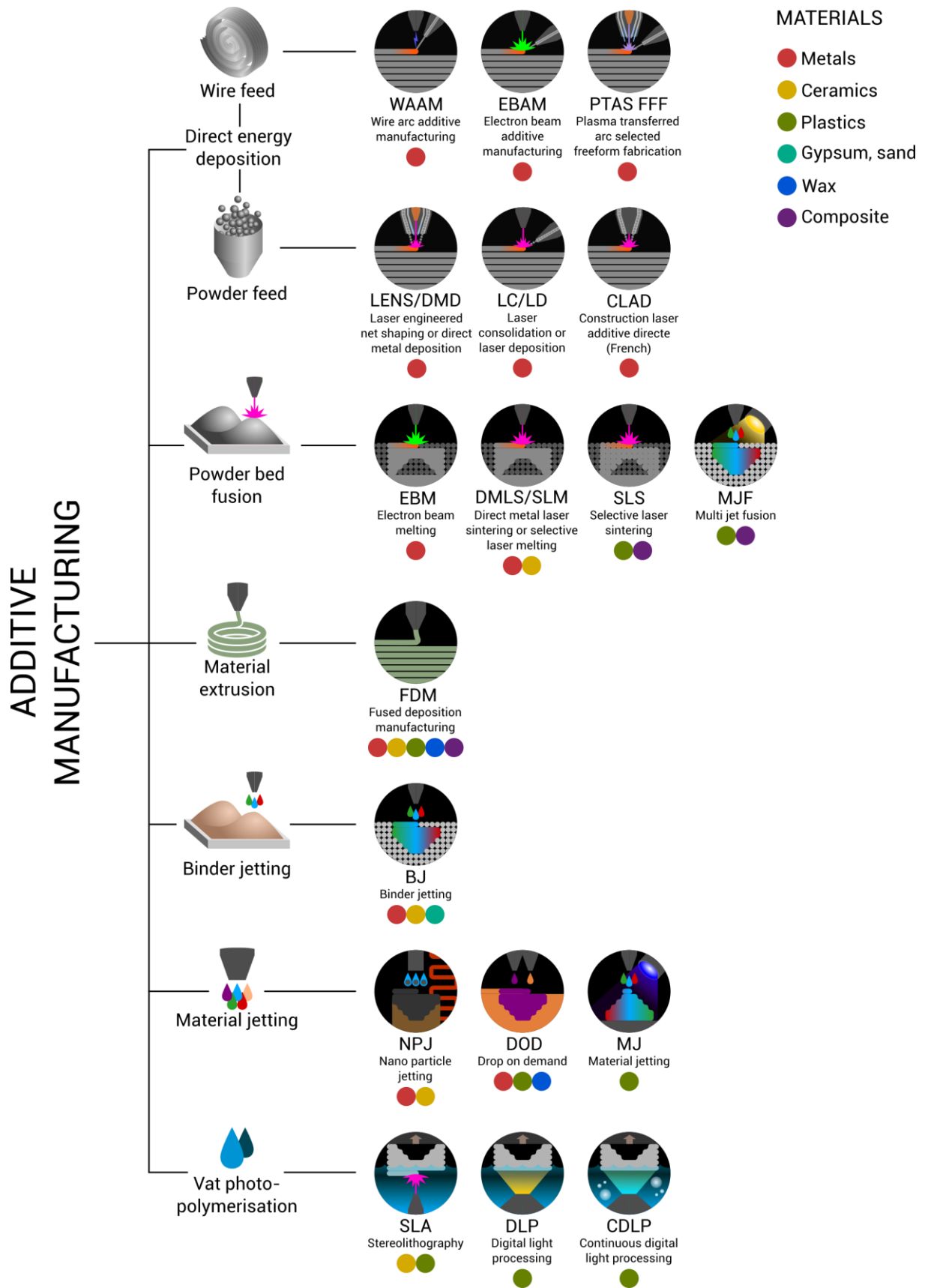


Figure 2.11: Overview of different AM technologies, and the materials with which they are generally associated.

PBF systems can be divided into those which melt metallic or ceramic powders, and those which sinter polymers. Systems that deal with metal can be further divided by heat source, either laser or electron beam. Many competing terminologies have been used to describe laser-based systems for direct melting of metal powders, partly due to the number of manufacturers in the area: Renishaw plc (UK), EOS, Realizer, SLM Solutions and Concept Laser (Germany) and 3D Systems (France/USA) [156]. Trademarked terms include LaserCUSING® of Concept Laser (now owned by GE Additive) as well as selective laser melting or SLM®, by SLM Solutions, a term which is often used in the literature. Direct metal laser sintering (DMLS) is another recurrent term. Electron beam melting (EBM) is the main terminology for the PBF method using an electron beam as a heat source, commercialised by Arcam AB (Sweden).

Other AM technologies which can be used to create metal components include fused deposition modelling (FDM), binder jetting (BJ) and material jetting methods, such as nano-particle jetting (NPJ) and drop on demand (DOD). FDM and BJ methods technically use metal powder composite filaments and slurries respectively to produce 'green' parts, which are then sintered to join together metal particles and pyrolyse any polymer or solvent based binders, during which the part may shrink [157,158]. NPJ uses nano particles of metal in the slurry to replace binder, improving the strength and reducing shrinkage of parts [157]. DOD methods, usually used with wax, have been shown to produce micrometre scale metal structures [159,160]. However, PBF methods have proven to be the most flexible approach to metal AM and resulted in the most end-use components [156].

2.2.1 Powder bed fusion of metal

A schematic of the PBF process is shown in Figure 2.12 below. In step 1, powder is deposited by the powder hopper and a wiper blade spreads it evenly over the build platform surface. In step 2, any excess powder falls down the chute to be recycled later and the wiper blade retracts. In step 3, the laser is directed by mirror galvanometers, and through lenses, to focus and melt the required cross section. Finally in step 4 the build platform is lowered by the thickness of one layer, so that the next layer of powder can be spread over the component, and the process repeats until the component is completed and surrounded by unused powder. Metal PBF systems vary according to their features; the number and power of lasers, powder handling, maximum build volume, and laser scanning strategy (the laser pattern used to melt the full cross section) [156]. Powder can be delivered from above or below, and rollers may be used to spread the powder [161].

Most metal PBF systems print components onto a substrate of the same metal, connecting the component to the substrate rigidly with metal support material, which is removed in post processing. This helps conduct heat away from the component whilst building, and prevents warping from residual stress, as well as providing support for metal that may be branching away from the component and 'overhanging'. Manufacturing limitations of AM are explored in section 2.2.5.

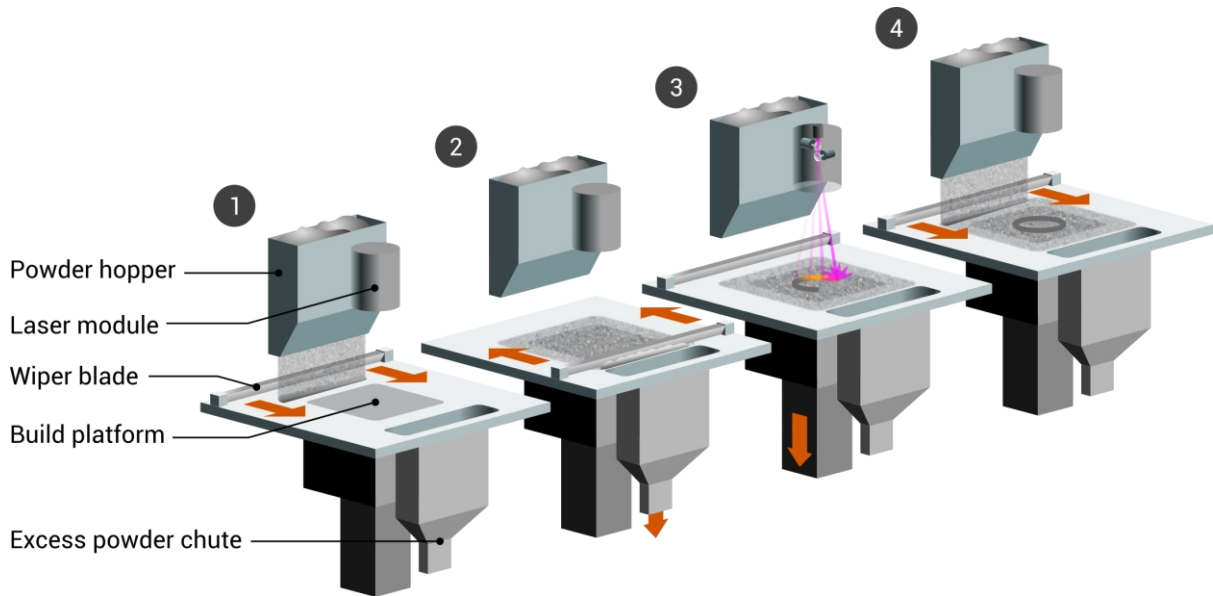


Figure 2.12: Schematic of the powder bed fusion process, which is an example of additive manufacturing. Deposition of a powder layer is shown, and the laser melting of the required cross section.

The work in this thesis uses a Renishaw AM250, a metal PBF system equipped with a Gaussian beam CW fibre laser, with a maximum power of 200 W, spot size of 70 μm and wavelength of 1.07 μm [162]. It has a build volume of 250mm W x 250mm D x 300mm H, allowing fabrication of parts that share the lengthscale of orthopaedic requirements. Powder is deposited using a gravity fed hopper. Before building parts, the build chamber is vacuumed to -960 mbar and the back-filled with 99.995% pure argon, so that oxidation and potential explosion of metal powders is minimised, especially in the case of Ti alloys. The resulting atmospheric oxygen content before building is $\sim 0.1\%$. Gas circulation is maintained through the chamber, from right to left, aiming to remove oxidised powder, sparks, and semi-fused ejected particles from the build platform as the component is built. Gas leaves the chamber and is fed through a high-capacity filter. A rubber wiper is used to compress the powder into layers between 25 and 50 μm thick, depending on the settings used when 'slicing' part geometry. Annotated photos of the Renishaw AM250 build chamber are seen in Figure 2.13 below.

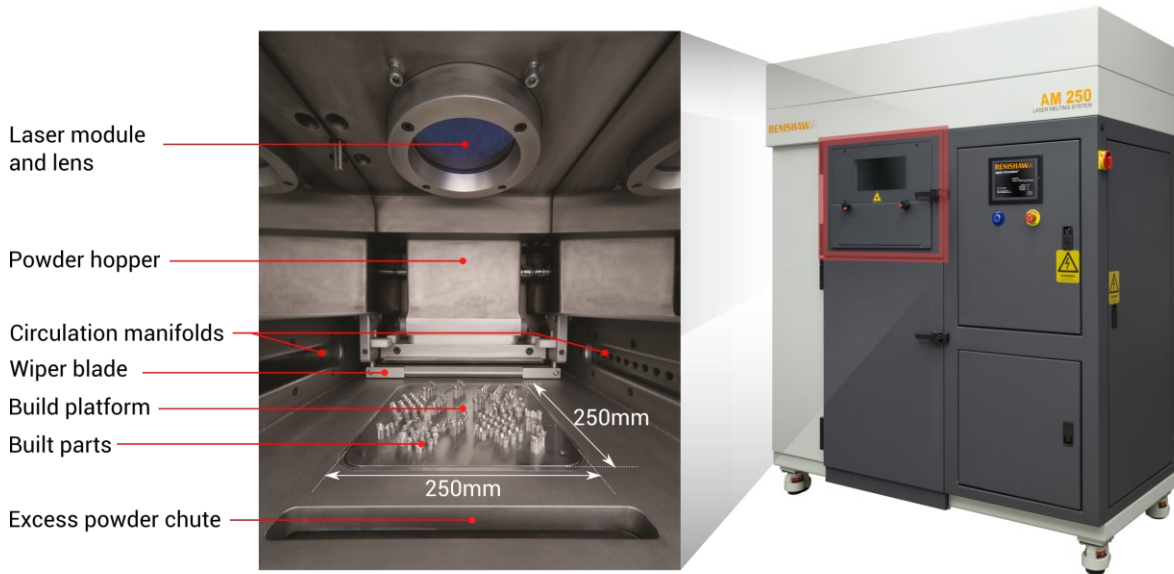


Figure 2.13: Renishaw AM250 with build chamber highlighted.

Powder handling components are annotated, and the visible built parts are dental components made using CoCr alloy. Images reproduced with permission from the rights holder, Renishaw plc. [163]

Laser-based PBF methods and their results can be compared to those of EBM. EBM uses an electron beam as a power source, so only conductive metal powders can be melted. Adjusting the wavelength of laser beams allows the use of ceramic and polymeric powders as well as metals. The surface roughness and minimum feature size is generally worse for EBM parts than SLM, due to a larger melt pool from the electron beam. Surface roughness R_a has been measured at $\sim 25\text{-}30\ \mu\text{m}$ for EBM parts and $\sim 15\ \mu\text{m}$ for SLM [164]. However EBM systems are typically faster because there are no moving parts to guide the beam and they have the ability to increase the beam diameter and subsequent melt pool from $\sim 200\ \mu\text{m}$ to 1 mm [15,165]. A summary of EBM and laser PBF comparisons is detailed in Table 2.2 below.

Table 2.2: Summary of EBM and laser PBF comparisons.

Characteristic	Electron beam melting	Laser PBF
Thermal source	Electron beam	Laser
Atmosphere	Vacuum	Inert gas
Scanning	Deflection coils	Galvanometers
Energy absorption	Conductivity-limited	Absorptivity-limited
Powder preheating	Use electron beam	Use infrared or resistive heaters
Scan speeds	Very fast, magnetically driven	Limited by galvanometer inertia
Energy costs	Moderate	High
Surface finish	Moderate to poor	Excellent to moderate
Feature resolution	Moderate	Excellent
Materials	Metals (conductors)	Polymers, metals and ceramics
Powder particle size	Medium	Fine

Adapted from [156].

Metal PBF has been used for solutions in orthopaedics, both in a clinical research setting and commercially. Due to the nature of reconstructive surgery, PBF has been useful for making customised one-off and patient specific implants. Laser PBF has been used to create custom Ti6Al4V craniomaxillofacial implants [166,167], (one of which is shown in Figure 2.14a) and Ti6Al4V hip implants [168]. Over 20 patient-specific AM implants (made mostly using EBM) have been successfully implanted at Stanmore Implants since Nov 2011, who specialise in orthopaedic oncology [169]. Regarding commercial applications, implants for mass manufacture include Stryker's Triathlon Titanium Knee system with porous tibial tray fixation surface, manufactured using a laser PBF system, seen in Figure 2.14b [16].

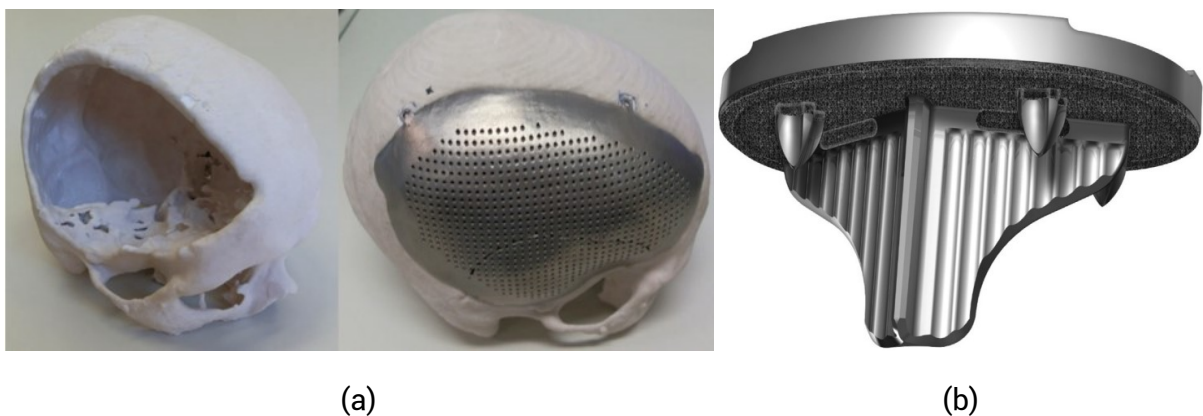


Figure 2.14: Laser PBF manufacturing for musculoskeletal applications

(a) Craniomaxillofacial implant. Image reproduced with permission from rights holder, Taylor & Francis. [170]
 (b) Tibial tray for Stryker's Triathlon Titanium Knee system, with 3D printed lower fixation surface. Image reproduced with permission from rights holder, Elsevier. [171]

As well as using AM methods to create patient specific implants with no internal porosity or architecture, AM is used in research to explore porous lattices with specific mechanical

properties, which tackle the previously discussed problems of stress shielding and osseointegration in traditional prostheses.

2.2.2 Porous lattices and musculoskeletal research

Since the advent of metal AM, porous lattices have been of interest as they allow control of a component's macro properties, by design of the micro-architecture. The arrangement of material in this micro-architecture may yield high specific stiffness structures for light-weighting applications, or high specific strength for impact energy absorption [172]. Various methods have been used to create lattice structures and topologies. A common starting point is the repeating of a cubic unit cell, similar to the idealised porous material analytical model by Gibson and Ashby discussed in section 2.1.6. This could include any tessellation of structures based on Platonic and Archimedean solids, or strut-based structures based on crystal packing, such as body-centred-cubic (BCC) or face-centred cubic (FCC) structures, which constitute much of the literature, including in structural mechanics [173].

A class of structures based on triply-periodic minimal surfaces (TPMS) have been used for metal PBF. Minimal surfaces, first described by Schwarz in 1865 [174], are surfaces of minimum area between any given boundaries, much like a soap film acting under tension, and this results in a mean curvature of zero. Triply-periodic minimal surfaces that repeat themselves in three dimensions, such as the Schwarz surface P and gyroid, were described by Schoen in 1970 and popularised in natural science [175]. They are generated using implicit field functions, the root of which can be solved to create a repeating iso-surface which divides 3D space evenly into two. When the implicit function is set to equal a different iso-value, the new surface which satisfies the equation will divide space such that a different 'volume fraction' is enclosed, providing a way to create repeating structures of different densities or porosities [176]. They have been of interest as candidates for biomaterials, due to research exploring the role of scaffold curvature for bone tissue regeneration [177], and how minimal surfaces may influence cell deposition [178]. High surface area to volume ratios may also enhance biological interactions [179].

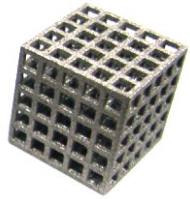
Porous lattices can also be created using topology optimisation (TO), a mathematical method linked to computational mechanics, which optimises material layout within a structure for a set of loading and boundary conditions. TO methods which maximise the stiffness of a structure use FEA to evaluate its performance, and then iterate to redistribute material to minimise strain energy. Material in the problem space can be represented by a voxel grid which is either 'on' or 'off', or with varying density (discrete vs continuous), depending on the method used [180]. Since its inception with the homogenisation approach

[181], methods such as the SIMP method, level-set method, and evolutionary structural optimisation (ESO) method have all attempted to improve convergence or nature of solutions [180]. They have also been extended to the optimisation of theoretical unit cells which create lattices with certain mechanical properties, such as elastic isotropy or orthotropy [182,183], maximised shear modulus [184] and also grading those properties throughout the lattice [185].

Pseudorandom or stochastic porous lattices have also been explored. These do not use a regular unit-cell approach, and instead, create lattices using distributions of points that are generated algorithmically, closer resembling open-cell metallic foams made with traditional techniques. Nodes for the structure are evenly distributed throughout a volume, either by adding pseudorandom noise or disturbance to the nodes of an existing regular lattice [186], or by using an algorithm such as the Poisson-disc method to distribute points [162], subject to parameters which control their density. In the former case, struts making up the regular lattice are redrawn in their shifted positions, or in the latter new points are joined based on proximity, creating a stochastic strut-based lattice. A subtractive method can also be used, whereby spheres of pseudorandom location and diameter are subtracted from a solid volume [187]. Related to these are unit cells which are based on direct reproductions of micro-CT scans of existing porous solids, such as metal foams and trabecular bone [188].

Certain unit cells may not be possible to make using metal PBF, due to manufacturing limitations, which are explored in section 2.2.5. In this case, they may be made by other means, such as lost wax casting [189]. Mechanical testing of the porous lattice is necessary to evaluate the impact of layer-wise PBF manufacturing on the mechanical performance, outside of FEA simulation. A compilation of unit cells which have been manufactured using metal PBF are shown below in Figure 2.15, categorised by type.

SPACE FILLING/STRUT BASED



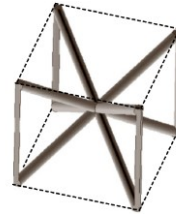
Cubic [166]



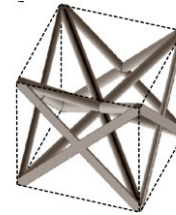
BCC [190]



BCCZ-I [191]



BCCZ-II [192]



f_2 BCC [192]



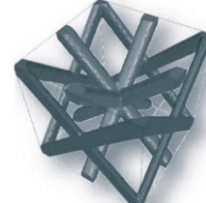
FCCZ [190]



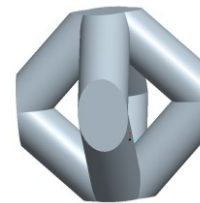
FBCCZ [190]



FBCCXYZ [190]



FCC-BCC mix [193]



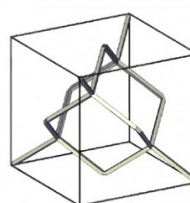
Octahedral [194]



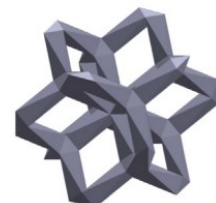
Dode thin [188]



Pillar octahedral [195]

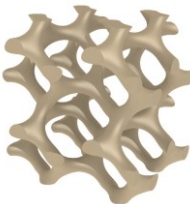


Diamond [196]



Dodecahedron [197]

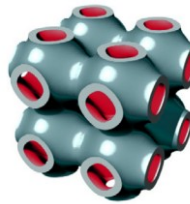
TRIPLY-PERIODIC MINIMAL SURFACES (TPMS)



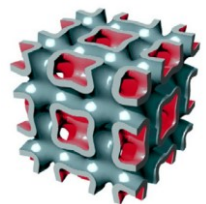
Gyroid I [172]



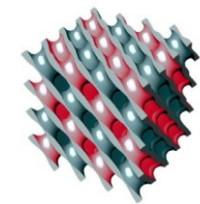
Gyroid II [198]



Primitive [198]



I-WP [198]

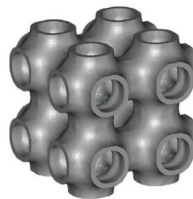


Diamond [198]

TOPOLOGY OPTIMISATION

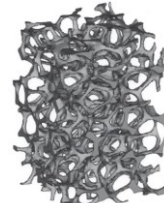


Optimised octet-truss [172]



Optimised primitive [182]

BASED ON IMAGING

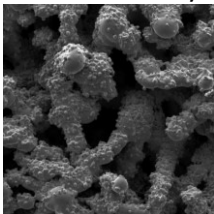


Metal foam micro-CT [188]



'Bone' unit cell [188]

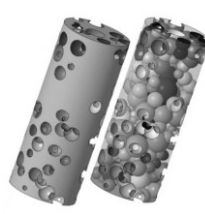
PSEUDORANDOM, STOCHASTIC



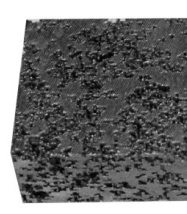
Pseudorandom [186]



Stochastic strut-based [162]



Random foam [187]



Stochastic cubic-based [199]

Figure 2.15: Compilation of unit cells and lattice structures made using metal PBF, categorised by type. All images reproduced with permission from the rights holders. See Appendix A3.1 for full details.

General investigations into the described porous lattice structures have been conducted outside of musculoskeletal applications [172,200,201], illustrating the link between porous structure theory and AM porous lattices. Extensive work has also covered the finite element analysis of porous lattices in order to further understand and model them [202–205]. In an orthopaedic context, specific literature exists on low stiffness porous lattices aimed at tackling stress shielding and bone remodelling, conducting uniaxial compression tests on specimens and plotting the variation in elastic modulus as a function of relative density or porosity, as in Equation 3 of section 2.1.6. Various unit cells have been investigated, with differing claims made about the suitability of the unit cell in a musculoskeletal context [206]. Ti6Al4V alloy is used extensively, due to its proven suitability as a biomaterial, though CPTi and CoCr also are included in the literature. A compilation of these results is shown in Figure 2.16 below, where different unit cells and materials are compared, showing the general decrease in stiffness for increasing porosity. This selection of data does not control for differing experimental methods; however, all studies were concerned with lattices for use in musculoskeletal applications.

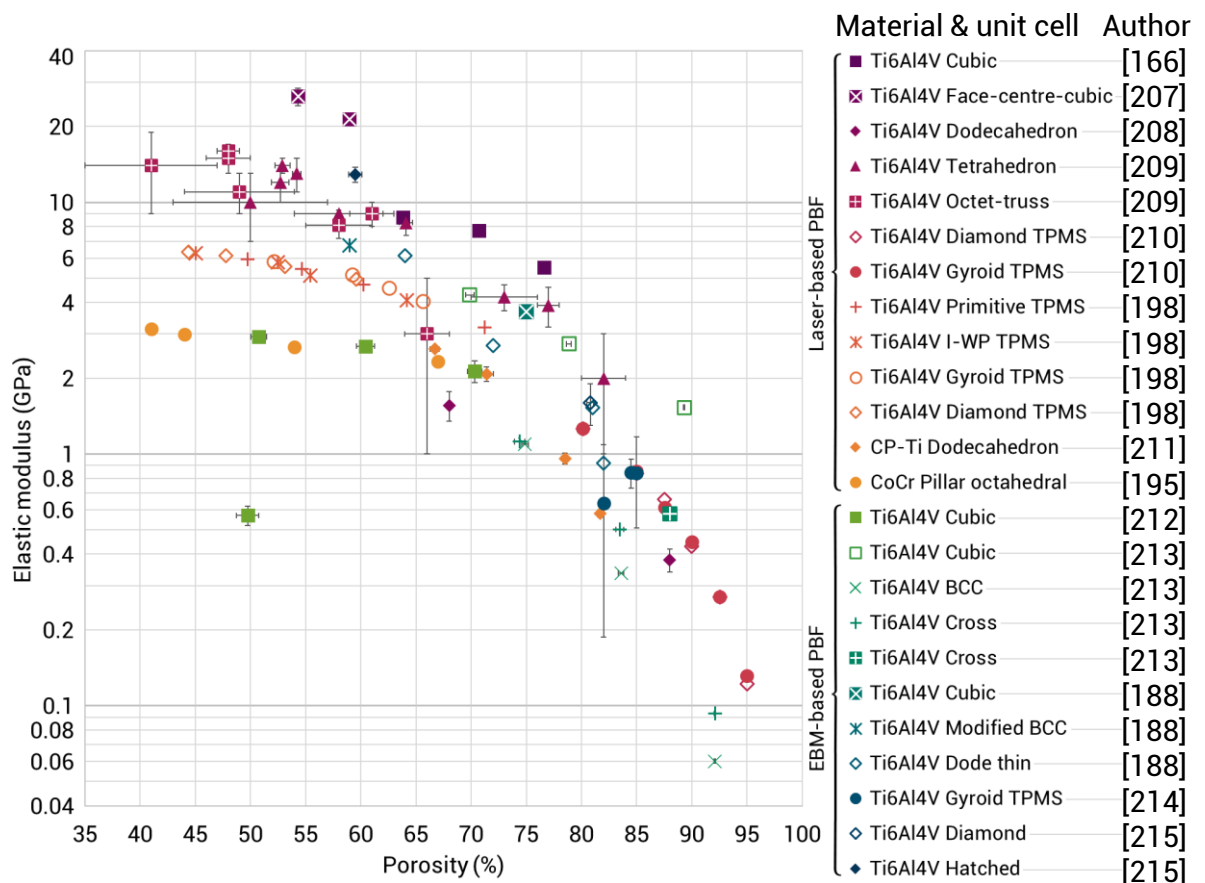


Figure 2.16: Compilation of reported elastic moduli versus lattice porosity for lattices in the literature designed for musculoskeletal applications

Purple to orange points indicate laser-based powder bed fusion (PBF) lattices, and green to blue indicate EBM based PBF. Where standard deviation was reported, error bars were added to show variation in each axis.

2.2.3 Anisotropy and control of porous lattices

As well as controlling the stiffness of the structure in one direction, the architecture of porous structures can be designed to add control over performance in other axes [216–219]. Lattices manufactured using laser PBF methods can subsequently have specified elastic moduli when loaded in different directions [172,182]. Bone also has a varying anisotropy of elastic modulus depending on the anatomical location, which is explored further in section 2.3.1. As such, when creating porous lattice structures that could be used as a structural biomaterial for musculoskeletal applications, the performance of the lattice in multiple orientations should be investigated.

Standard lattice structures, such as the cubic structure, which are manufactured using laser PBF have been shown using FEA to vary in elastic modulus by over 5 times depending on the orientation [166,172], and potentially more depending on the lattice dimensions used [220]. A similar FEA comparison between three unit cells, varying the orientation of the load applied showed a decrease in stiffness of roughly 2.5 times for all structures at a low loading angle [213]. Another structure resembling a stretched FCC structure was shown with mechanical testing to vary in elastic modulus by over 6 times when loading in a diagonal direction [207]. Other unit cells which have been investigated in this way include the gyroid, which was mechanically tested in two orthogonal directions, varying in elastic modulus by up to 1.7 times [214]. Loading of various unit cell designs axially and at 45° using FEA showed a greater increase in von Mises stress for strut-based structures compared to TPMS structures [206]. Therefore, unit cells have varying degrees of anisotropy, depending on their underlying structure, which contribute to their high or low stiffness depending on the test orientation. This may compromise the mechanical performance of components that use them. The anisotropies of unit cells are not fully described experimentally and are not accounted for in standard uniaxial compression tests in one direction.

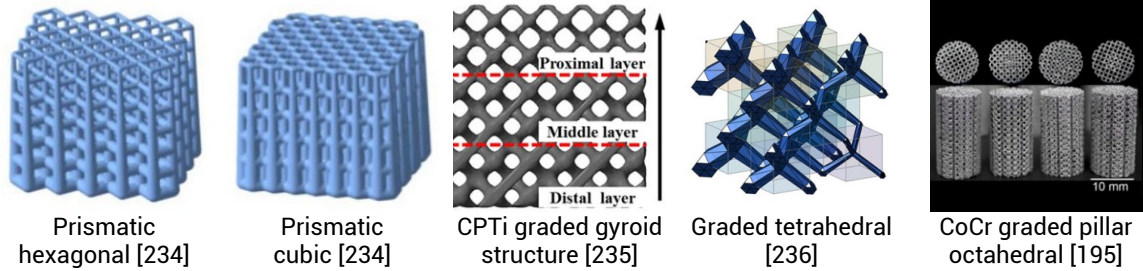
Further investigation into the control of porous lattice anisotropy has been addressed in literature aimed at structural mechanics. One study mixes plate lattice unit cells based on crystal packing planes, controlling the mechanical isotropy to a high degree [173]. However, the structures are closed-cell and manufactured using methods and materials not applicable to biomaterials. A similar approach uses FEA simulations of strut-based unit cells, and mixes them to achieve isotropic and controlled behaviour [216], but there is no mechanical testing to prove their behaviour when manufactured using laser PBF methods. Topology optimisation has been used to achieve isotropic mechanical behaviour, with one unit cell similar to a Schwarz–p primitive structure manufactured using EBM and tested in three

directions [182]. However, the structure has little open porosity and may not be suitable for bone ingrowth. Another topology-optimised octet truss unit cell study shows isotropy in FEA models, but is missing confirmatory mechanical testing in multiple directions [172]. Other approaches to varying the elastic isotropy include scaling a gyroid unit cell, controlling the stiffness in one direction [221].

Other areas of the literature where lattices are optimised for certain biomaterial behaviour tend to focus on femoral hip stems, and on functionally graded materials (FGMs), where the density of a lattice is varied, either linearly or radially for graded cylinders. These radially graded cylinders are sometimes tested as simplified femoral stems, investigating the stress transfer to surrounding material [195]. Much like earlier experimentation with polymers and composites in femoral stem design, the opportunity exists to lower the stiffness of a whole femoral stem using porous lattices. One example optimises the porosity required to minimise bone resorption and maximise fixation of implants at the bone-implant interface, varying the density of a tetrahedron unit cell to achieve certain mechanical properties [222–224]. Here, the effective elastic and plastic properties of the tetrahedral unit cell, that vary over relative density, are calculated using asymptotic homogenisation and the stiffness tensor [225]. It is not clear that these properties are confirmed using mechanical testing. A similar femoral stem with a stochastic lattice infill showed a poor match between observed strains and those in the initial FE model [199] and an improved stem from the same group with diamond lattice infill was still not able to model the lattice/solid metal transition accurately [226].

Many examples exist of FGMs manufactured using laser PBF that vary the density of a unit cell, changing the mechanical behaviour. However, multi-axial compression testing is usually still absent, as with regular porous lattices. Many more studies exist that vary the lattice density but only investigate using FEA [185,219,227–231]. Others do not use laser PBF but other AM techniques instead [217,232,233]. A compilation of various functionally graded lattices is shown in Figure 2.17 below, for which all specimens were manufactured using laser PBF and mechanically tested.

LINEARLY AND RADIALLY GRADED LATTICES



OPTIMISED FEMORAL STEMS

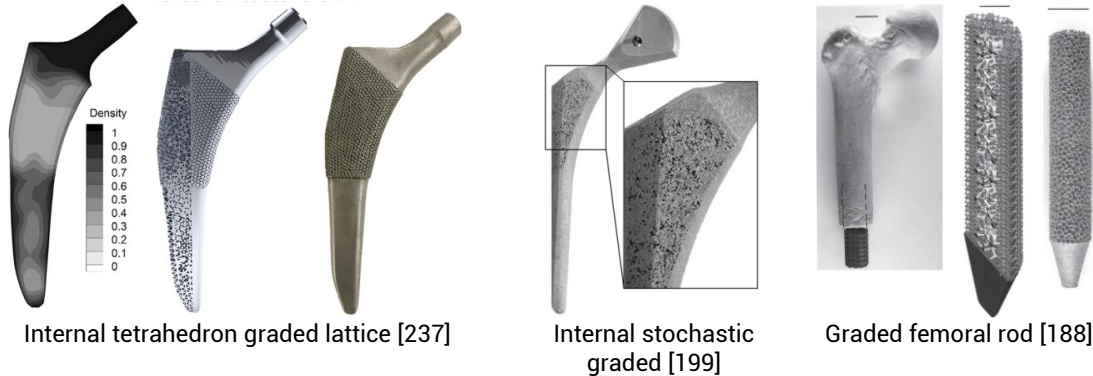


Figure 2.17: Compilation of functionally graded lattices and optimised femoral stems.

All images reproduced with permission from the rights holders. See Appendix A3.1 for full details.

2.2.4 Mechanical testing

Finding accurate mechanical characterisations of porous lattice structures requires extra consideration of specimen geometry, test procedure and measuring equipment, that capture the emergent behaviour of a material with a micro-architecture.

Quasi-static uniaxial compression tests

For quasi-static uniaxial compression testing, the specimen must be several times larger than the pore or cell size, so that a material continuum can be assumed, and ‘size effects’ are not introduced. This is because at the specimen walls, the structure can include ‘cut’ or partial cells, which are weaker than the fully connected structure in the centre of the specimen. Where these partial cells constitute a higher proportion of the total specimen, the measured stiffness will be less than is representative of the continuum structures.

Whether or not the specimen is constrained at the ends affects the stress state in the portions of the specimen that touch the compression platens, neither of which fully represent the loading that would occur as part of a larger continuum. These are termed ‘end effects’. Fully constraining the structure at the ends results in fewer degrees of freedom for the individual structure members to move, potentially resulting in a higher force required for deformation and a higher measured stiffness. Considering a frictionless environment, and the minimum amount of constraint at the specimen ends, less force would be required to

deform the specimen, and a lower stiffness may be measured than that which represents the continuum structure.

Where the specimen is small, friction at the platens interface can also cause bulging at the centre of the specimen, also known as 'barrelling'. This may interfere with assumptions about the cross-sectional area of the specimen for stress calculation. A higher true cross-sectional area than the nominal area may result in a measurement of stiffness that is higher than is accurate, overestimating the stiffness.

Ashby recommended a cylindrical or prismatic specimen with a smallest dimension which is at least seven times the pore or cell size to avoid size effects, and a height-to-thickness ratio of at least 1.5 to avoid end effects [141]. A British and ISO standard for compression testing of porous and cellular materials (ISO 13314:2011(E)) recommends cylindrical or rectangular specimens (cylindrical preferred), with all spatial dimensions at least 10 times the pore or cell size [238]. However, there is no recommendation regarding end constraint. Where mentioned, almost all compression tests referenced in Figure 2.16 used unconstrained specimens with some form of platens lubrication, with few exceptions. One study found little difference between specimens that did or did not use lubricant [198]. The standard also recommends that specimen ends should be machined flat where possible, so that no other stresses are introduced into the structure.

Due to the low stiffness of the specimens and small stresses involved, machine compliance is also an issue. This is where compliance and displacement of the test frame itself at low stresses contributes to the compliance of the specimens being investigated, resulting in lower stiffness values than the true value. Compliance correction is sometimes applied to remove effects of machine compliance, by assuming that the test fixture and the specimen act as two springs in series. By varying the length of a test specimen, the measured total compliance can be plotted against specimen length. The y-intercept of this graph is then the compliance of the fixture, which can be subtracted from further results. However, machine compliance is shown to be non-linear, and correction with this method to be unreliable [239]. ISO 13314:2011(E) [238] recommends an external measurement of strain, such as an extensometer, that captures the distance between platens, thereby removing machine compliance effects. Extensometers can also be fixed to the central section of specimens, to avoid end effects. However, this is often difficult because of the small dimensions involved.

A procedure for compression tests is also detailed in the standard [238]. An example stress-strain curve for the procedure is shown in Figure 2.18. Prior to the main test of the specimen, a preliminary compression test should be carried out with a sacrificial specimen of the same

type. The specimen should be compressed to at least 30% strain, and the plateau stress σ_{pl} should be calculated as the average stress from 20 to 30% strain ($\varepsilon = 20$ to $\varepsilon = 30$ on Figure 2.18). In the main test, a loading/unloading loop should be carried out wherein the specimen is compressed to 70% of the plateau stress (σ_{70}), and then unloaded until 20% of the plateau stress (σ_{20}), after which the specimen is reloaded until failure. This single cycle of loading results in some hysteresis due to the viscoelastic response or friction in the test. The elastic modulus is then calculated using a linear regression of the points in the loading loop, indicated on Figure 2.18. A 1% strain offset yield stress (σ_y) can be calculated from the intersection of the trace with an offset elastic gradient. The standard also recommends that tests are run at a constant strain rate between 10^{-3} s^{-1} and 10^{-2} s^{-1} .

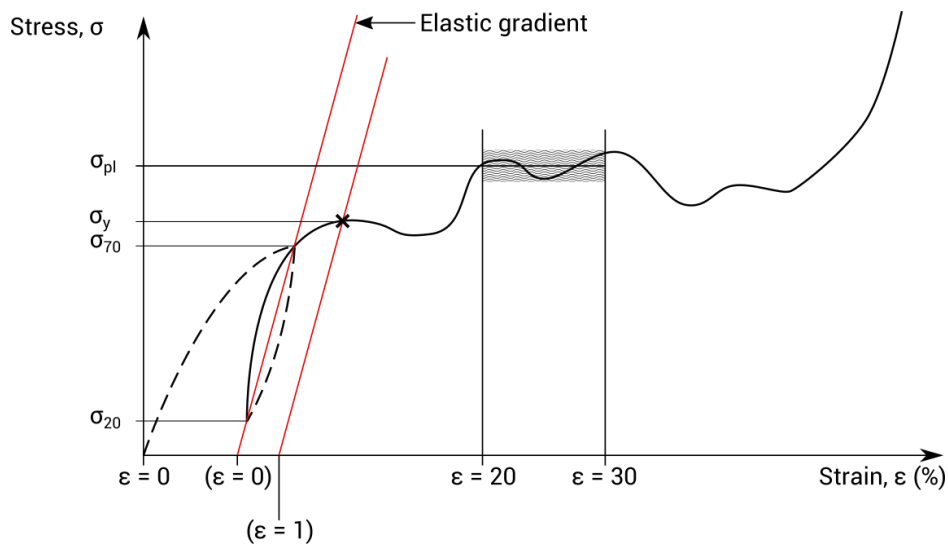


Figure 2.18: Example stress-strain curve for uniaxial compression test of porous cellular material.

σ_{pl} is the plateau stress, and σ_y is the 1% offset yield stress. Drawn using definitions in ISO 13314:2011(E) [238].

Individual strut tensile tests

Tensile tests of individual lattice struts built using laser PBF, sometimes termed 'micro-struts', have also been conducted, to investigate their mechanical properties and to analyse strut defects and surface quality. Various studies have shown the decrease in elastic modulus and strength for SS316L and Ti6Al4V micro-struts as compared to bulk AM solid components [201,203,204,240–242]. The elastic modulus of SS316L has been reported as between 37% and 74% of that for fully dense AM metal.

As with uniaxial compression testing, the tensile test procedure for micro-struts differs from conventional testing. For standard tests, dog-bone specimens are used. According to tensile testing standards, crosshead displacement can be adequate for strain measurement, as

machine compliance is less of a concern if the specimens have a relatively high stiffness compared to the compliance of the machine [243,244]. However single struts are much smaller and require specialised grips and strain measurement. Most studies build and test struts individually [201], sometimes using sandpaper for added friction when gripping [241], fix struts using adhesive [240], use custom fixtures [203,204], or add grip tabs at each end [191]. Groups of struts tested together, increasing the effective cross-sectional area of the specimen, have also been used [245]. Clip-gauge extensometers may remove machine compliance [201,240], though are especially unwieldy when used on single micro-struts compared to compression specimens, as struts may be 100 μ m to 300 μ m in diameter and will break easily. LVDTs measuring displacement between grips remove contact from the micro-strut, though its accuracy relies on the grip being adequate [204]. Optical methods are both non-contact and remove machine compliance [203], but care must be taken to track strut features without parallax and in good lighting.

Gauge length of the tensile specimen has been shown not to affect measurement of mechanical properties, assuming that end-effects are not present [204]. Accurate measurement of the diameter is important for accurate calculation of mechanical properties. The true diameter of micro-struts has been shown to differ from that measured externally [203,240,242]. SS316L strut diameters found by sectioning the strut was shown to be 86% of the value measured by Vernier caliper, due to variations in the strut surface [203]. The true diameter of SS316L struts has also been found by comparing the volume of a lattice to an analytical model [240]. Further investigation of strut surface quality and internal porosity has also been conducted, using advanced imaging techniques such as SEM and micro-CT [193,209,246–249], and the effect of those variations on overall lattice performance has been shown by incorporating them into FEA models [200,205,245,250–255]. Much of this variation is due to manufacturing limitations inherent in the laser PBF process.

2.2.5 Manufacturing limitations

Design for additive manufacturing (DfAM) is an area of engineering design practice which tries to best utilise the new AM capabilities to achieve desired performance [17]. However, this practice involves considering manufacturing limitations. Due to the layer-wise fabrication used in laser PBF, 'overhangs' in a component design will not have sufficient support during manufacture. Solid metal underneath a new weld pool will prevent distortion and provide a path for heat conduction away from the pool for quick solidification. This is described in the Renishaw best practice guide [256], and with the illustration in Figure 2.19 below. This layer-wise fabrication also results in slightly different mechanical properties

perpendicular and parallel to the build direction in solid metal built using laser PBF, with a 3.7% difference in the elastic modulus of AM SS316L and 2.4% difference for AM Ti6Al4V [257,258]. A 'stair-step' effect is also visible.

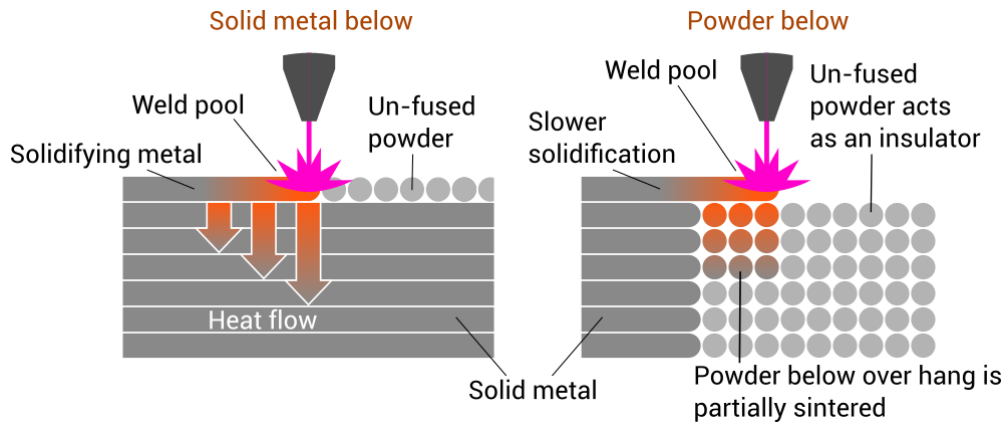


Figure 2.19: Effects of printing with and without support material

Left shows solid metal providing support and heat conduction to molten powder from below. Right shows molten powder supported only by further powder.

The layer-wise fabrication inherent to laser PBF has an impact on the stiffness of lattice structures overall, with build orientation affecting lattice stiffness [259]. This can be explained by the effect of orientation on individual micro-struts. Various studies show a difference in mechanical properties and morphology of single struts when built vertically, compared to a low angle to the build plate [191,200,263,205,209,245,248,249,260–262]. For the reasons shown in Figure 2.19, it is hard to build horizontal struts accurately using laser PBF, compromising the integrity of some potential unit cells. Using micro-CT or a microscope, the interaction between the 'stair-step' effect and the angle of struts to the build direction can be seen. The morphology of struts is greatly affected, with varying cross section [191,245,248], 'waviness' or eccentricity [200,209] and surface roughness [260], an example of which is shown in Figure 2.20. However, less data exists on the relationship between mechanical properties of these micro-struts and their build angle. Tensile tests of struts built at varying angles has been conducted in one study [201], but the direct relationship between build angle and elastic modulus or strength was not reported.

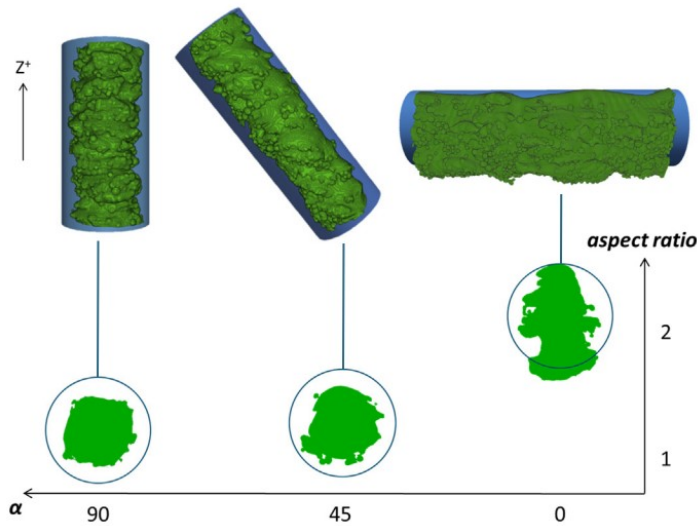


Figure 2.20:
Varying strut aspect
ratio for EBM struts.

Comparison of the
aspect ratio between
struts built at 90°, 45°
and 0° to the buildplate,
showing micro-CT
images of the strut
volume with semi-fused
particles attached.

Image reproduced with
permission from the
rights holders, Elsevier.
[249]

Rough surfaces introduce stress concentrations into lattices which may impede their performance. Modelling approaches which subdivide surfaces and remove stress concentrations help improve lattice fatigue life [264], as well as increase the strength and stiffness [265]. Post processing with heat treatment [259] and chemical etching [266] are other methods which can be used to alleviate problems with lattices made using laser PBF.

2.3 Bone properties

In designing and implementing AM structures that will benefit the patient's bone, the properties of bone must be examined. Bone is a complex material with internal architecture. This varies at different anatomical locations and at different length scales, due to functional remodelling attributed to Wolff's Law [267,268]. A distinction is made between the spongy interior of the bone, referred to as cancellous or trabecular bone with a 55-70% porosity (shown in the SEM micrographs of Figure 2.21), and the much denser outer cortical bone which has a higher strength [269].

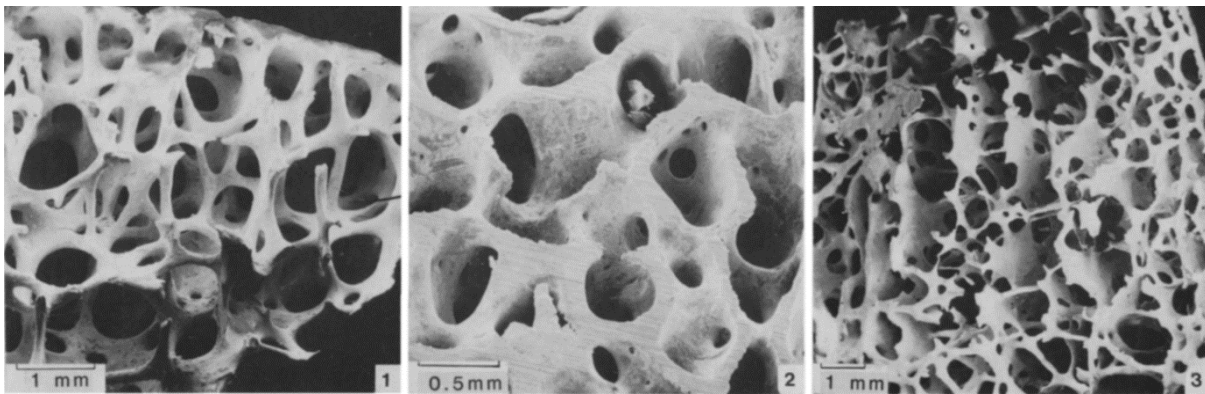


Figure 2.21: SEM micrographs of cancellous or trabecular bone from the femoral head.

(1) showing low density structure, (2) high density, plate-like structure and (3) columnar structure. Images reproduced with permission from the rights holders, Elsevier. [269]

As a porous material, bone acts much like an idealised foam. Gibson and Ashby derived equations based on idealised structures like those previously discussed, but now based on four distinct structure types, rod-like or plate-like with either a columnar or asymmetric structure, seen in Figure 2.21 and Figure 2.22.

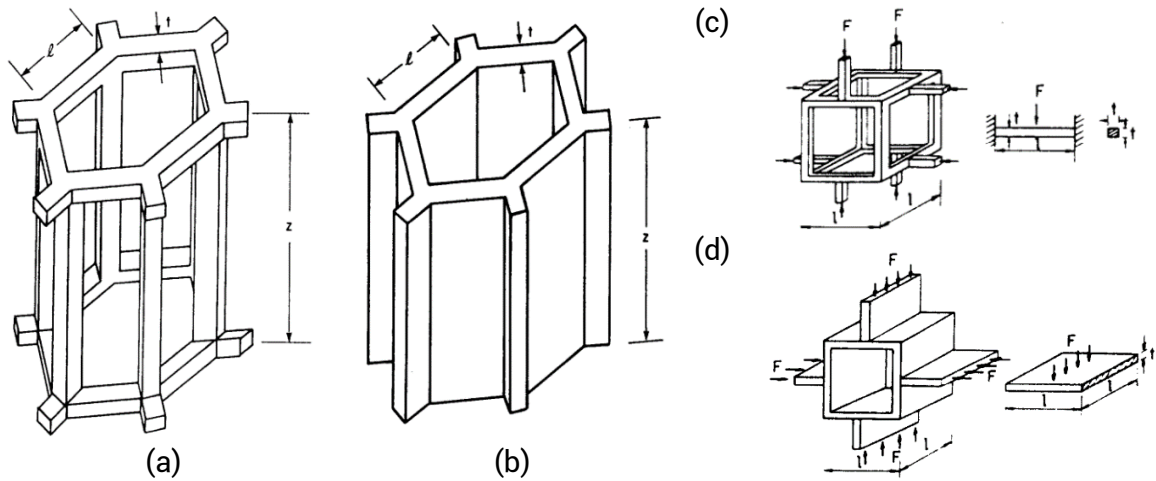


Figure 2.22: Idealised models of trabecular bone structures.

(a) Rod-like columnar, (b) plate-like columnar, (c) rod-like asymmetric, (d) plate-like asymmetric. Applied force is F . Length of unit cell is l , and walls or beams/struts have thickness t .

Images reproduced with permission from the rights holders, Elsevier. [269]

The structures shown in Figure 2.22 have a relative density ρ^*/ρ_s which depends on the structure geometry as well as the density of the constituent solid bone ρ_s which is between 1400 and 2000 kgm^{-3} [270]. Equation 2.4 gives the general relationship between the elastic modulus E or other properties such as compressive strength σ to its relative density ρ/ρ_s .

$$\frac{E}{E_s} = C \left(\frac{\rho}{\rho_s} \right)^n \quad \text{Equation 2.4}$$

The properties can be plotted using curves fitted to data using C and n , when divided by the respective property of the constituent material (E_s or σ_s). Equation 2.4 takes an identical form to Equation 2.3 as discussed in porous structure theory, section 2.1.6. Extensive literature reviews exist which explore the different elasticity-density relationships found empirically for bone from different anatomical locations, giving values for C and n [271,272]. These are important for accurate FE model predictions.

2.3.1 Mechanical behaviour of bone

To maintain the mechanical biocompatibilities of an implant or implant structure, the mechanical properties of the implant should match those at the implant location. The elastic strength and modulus of bone has been tested extensively and shown to be a viscoelastic two-phase porous structure [273]. Table 2.3 details some of the mechanical properties found.

Table 2.3: Selection of tested mechanical properties for trabecular bone

Anatomical location	Young's modulus (MPa)	Strength (MPa)	Authors
Proximal tibia	1.4 - 79	0.2 - 6.7	[274]
Proximal tibia	10 - 500	1.5 - 45	[273]
Proximal tibia	4 - 430	1 - 13	[275]
Proximal femur	1000 - 9800	121 - 310	[276]
Proximal femur	58 - 2248	0.45 - 15.6	[277]

Values shown for bone from proximal femur and tibiae. Adapted from Goldstein [267]

As can be seen from Table 2.3, the properties vary widely. An extensive review was written by Goldstein in 1987 [267]. The compressive strength of bone has also been shown to decrease by 8.5% for each decade a patient has been alive [278]. Trabecular bone is anisotropic, and its load bearing properties vary with direction. For example, bone in the femoral head contains a primary compressive trabeculae group which bears bodyweight loads when standing. This trabecular structure is aligned at a certain angle within the femoral head, stretching from the bottom of the femoral neck to the top of the proximal end of the femoral head. Bone core specimens cut out of the femoral head that are aligned with the primary compressive trabeculae group are 40% stiffer than those offset by 20° [279]. Other locations within the skeleton are similarly anisotropic, and various studies have quantified the difference in stiffness and strength depending on the orientation of bone specimens to the loading direction. Some results are shown in Table 2.4, with greater stiffness values in a superior-inferior (SI) direction, and lower values in an anterior-posterior (AP) or medial-lateral (ML) direction.

Table 2.4: Maximum anisotropic ratio found for Young's modulus in trabecular bone

Anatomical location	Ratio of maximum to minimum modulus	Maximum orientation	Minimum orientation	Authors
Proximal tibia	3.2	SI	AP	[280]
Proximal tibia	6.1	SI	AP/ML	[281]
Proximal femur	1.5	SI	AP	[276]
Proximal femur	2.0	SI	ML	[277]
Mixed locations	2.3	-	-	[282]

Anatomical locations include proximal tibia, proximal femur and other. All tested bone is stiffest in superior-inferior (SI) axis, as opposed to the anterior-posterior (AP) or medial-lateral (ML) axes.

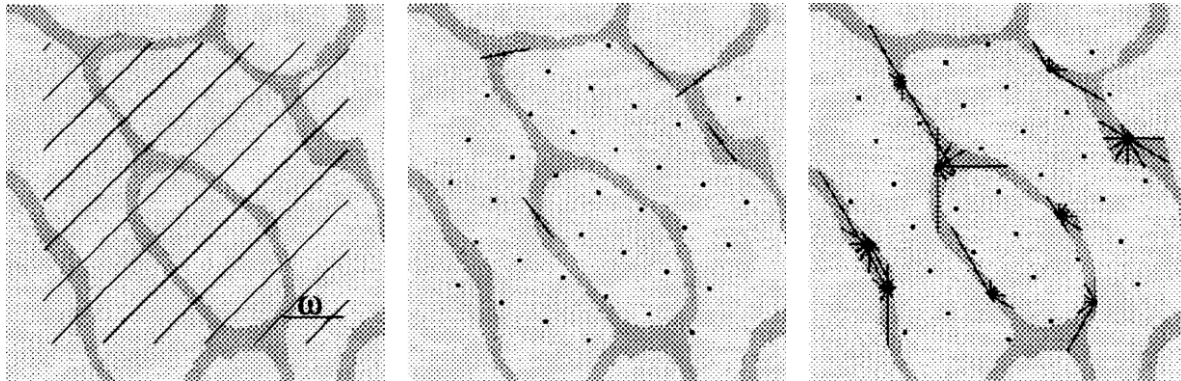
Testing is conducted using cylindrical specimens or cubic ones when retesting each specimen in each axis, with adequate cross-sectional area [283]. Constraint of specimens at the bone/platens interface also vary across experiments, with impact on measured values, due to varying opinions on minimising end effects and frictional effects [284]. Machine compliance is also an important consideration, much like when testing AM porous

structures. For a continuum material assumption to be correct, the specimens must span at least three to five trabeculae at a minimum [285].

2.3.2 Bone architecture

Trabecular bone has anisotropic properties due to the varying architecture throughout, blending between rod-like, plate-like, columnar and asymmetric architecture as required [286]. Various methods exist to quantify this architectural anisotropy. They rely on interrogating the 2D or 3D geometry of trabecular bone from histologies or micro-CT scans. From these, simple measures such as the volume fraction of trabecular bone, trabecular thickness, intertrabecular spacing and trabecular number can be found [287]. More advanced measures, such as mean intercept length (MIL), volume orientation (VO), star length distribution (SLD) and star volume distribution (SVD) show the orientation of the trabecular bone in 3D space, as shown in Figure 2.23 and Figure 2.24.

When used on 3D trabecular bone geometry, these statistical measures (often MIL) can then be used to create a symmetric second order 'fabric' tensor, which can be displayed as a surface which describes the orientation of material within the specimen. An example fabric tensor can be seen in Figure 2.25 in blue. This information about the fabric or geometry of the bone can be combined with FE simulations of the imaged bone to approximate the elastic properties of the sample in all directions. This method was described by Cowin, detailing the algebraic relationship between the fabric tensor and the fourth rank elasticity tensor [288]. It has since been used principally by Odgaard, Zysset and others to explore the anisotropic mechanical properties of bone, via the bone architecture [289–293].



(a) Mean intercept length (MIL) method.

For each orientation angle ω , a grid of lines intersects the bone. The number of intersections is determined.

(b) Volume orientation (VO) method.

For each point within the bone boundary, the orientation of the longest intercept is determined. The resulting orientation is considered the orientation for that point.

(c) Star volume distribution (SVD) and star length distribution (SLD) method.

For each point within the bone, the length of lines at multiple orientations is found. These lengths are used directly for SLD and cubed for SVD.

Figure 2.23: Visual representations of bone architecture quantification methods.

Images reproduced with permission from the rights holders, Elsevier. [294]

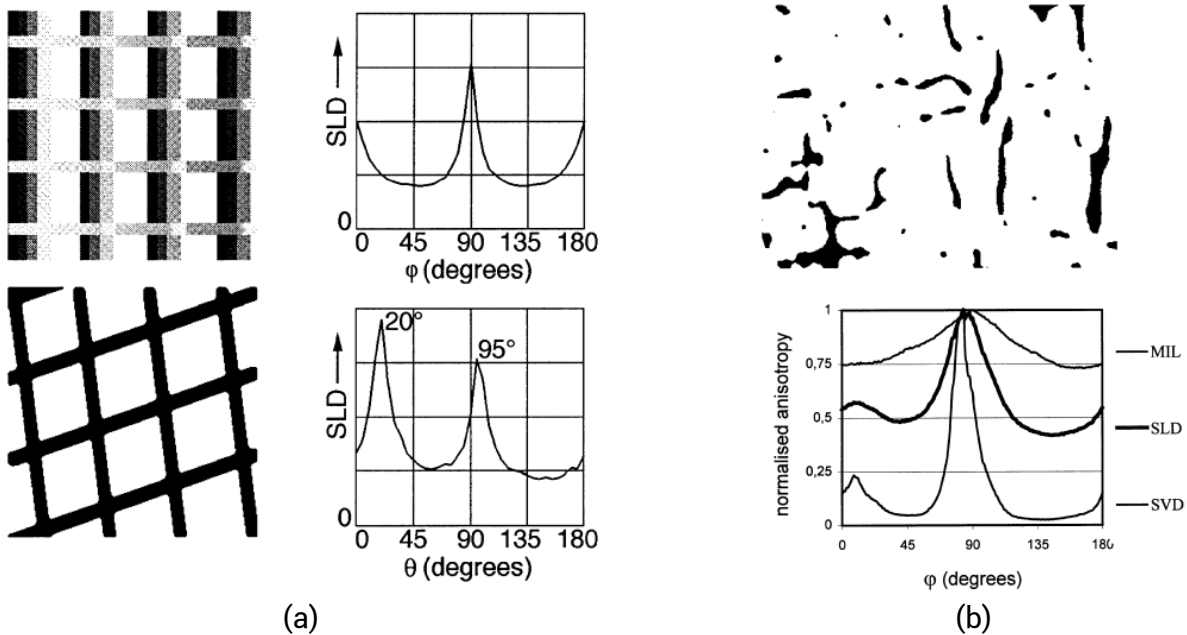


Figure 2.24: Further illustration of the star length distribution method.

(a) Star length distribution (SLD) peaks align with orientation of beams within structure. Oblique view top and bird's eye view on bottom.

(b) Comparison between mean intercept length (MIL), SLD and star volume distribution (SVD) measures, showing sensitivity of those measures to trabecular orientation.

Images reproduced with permission from the rights holders, John Wiley & Sons. [295]

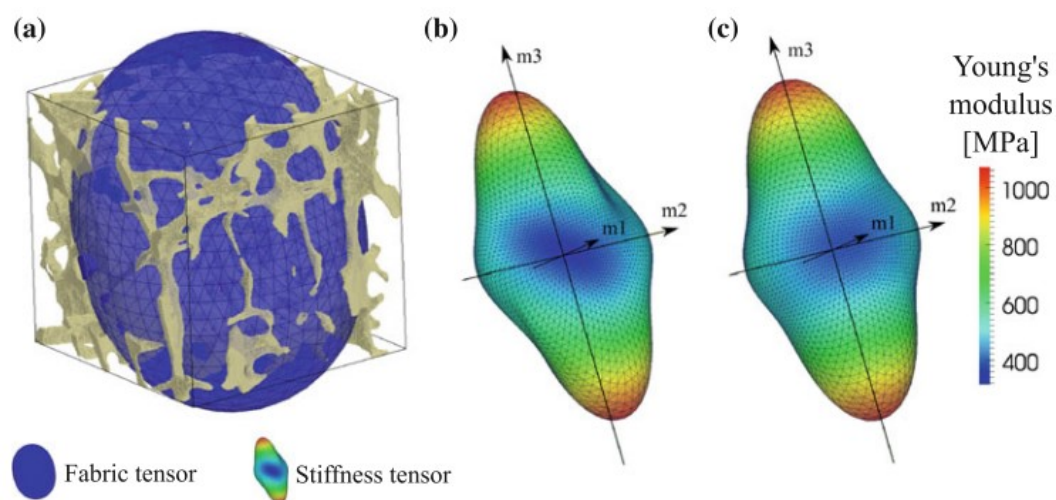


Figure 2.25: Comparison between stiffness tensor and resulting stiffness tensor using measurements from FE model.

- (a) Voxel model of trabecular bone cube with fabric tensor representation;
- (b) full anisotropic stiffness tensor in the fabric coordinate system;
- (c) orthotropic stiffness tensor in the fabric coordinate system

Images reproduced with permission from the rights holders, Springer Nature. [290]

These statistical measures of architectural anisotropy, resulting in predicted elastic anisotropies, compare well with the principal elastic directions found using full FEA models [286]. Simpler measures of the architecture, bone volume fraction and trabecular plate number can also be used to predict up to 90% of properties found using mechanical testing [282]. Other fabric measures such as the Gradient Structure Tensor (GST) and Sobel Structure Tensor (SST) have also been used to quantify anisotropy, using clinical-level CT images and MRI [296–299]. Newer work on the topology of bone shows the node connectivity of trabeculae [300].

2.3.3 Bone remodelling

Bone tissue can repair and reform itself to match its load bearing requirements. This has been mentioned as part of Wolff's Law [267,268], which describes how the arrangement and pattern of trabeculae align with lines of principle compressive and tensile stresses [301]. However, Wolff's law is part of a broader range of concepts which describe the reliance of the bone on strain signals to induce formation. Perren's strain theory [302] and Frost's concept of a bone 'mechanostat' [303] are also included in a theory of bone healing and nonunion (BHN) by Elliot [304]. From an engineering perspective, the strain-related mechanisms by which bone remodels are particularly important due to their response to design decisions in potential implants.

The biological processes by which bone remodelling occurs are complex and will not be covered in full here. In summary, bone remodelling is mediated primarily by interactions

between various cell types including osteoblasts, osteoclasts and osteocytes [305]. Osteoclasts cause the resorption of existing bone and are created by precursors in bone marrow and blood. Osteoblasts cause formation of new bone and are derived from stem cells within the bone marrow. Osteocytes act as mechanosensors and regulate the bone remodelling process [306], by detecting mechanical pressures and loads through the interstitial fluid within their interconnected system of lacunae and caniculi [306–308]. This results in the secretion of growth factors and other molecules prompting bone formation, the full process referred to as mechano-reception and mechano-transduction.

BHN theory states that in the case of a bone fracture, the tissue that forms there can be referred to as a 'bone healing unit' (BHU), that varies in composition so as to mediate the strain throughout, keeping it below the maximum strain that the tissue can tolerate [304]. Perren stated this maximum strain as 2% [302]. However, as the tissue lowers the strain such that bone can form and the bone is unified, then normal physiological conditions can apply as in homeostasis, where bone is turned over and remodelled with balanced osteoblast and osteoclast function. This is seen as point B in Figure 2.26a where net formation remains near zero, which is expanded in Figure 2.26b. Point A in Figure 2.26a represents extreme low strain environments, such as microgravity, and the area to the right of point C include fractures and nonunion prior to the formation of the BHU.

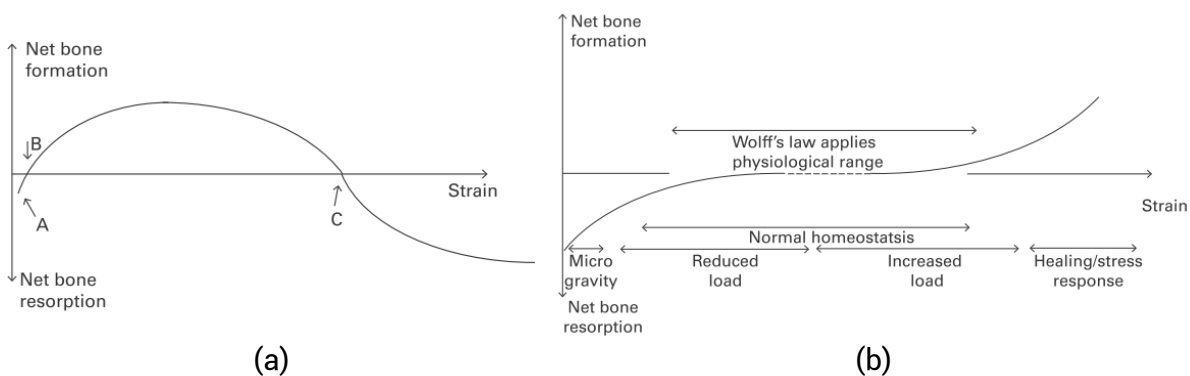


Figure 2.26: Diagram of bone formation as described by Elliot in BHN theory.

(a) A wide range of strains throughout which tissue in a fracture or nonunion operates.

(b) Shows the processes within the physiological range, where Wolff's law applies, and bone resorbs or heals in response to stress change.

Images reproduced with permission from the rights holder, the British Editorial Society of Bone & Joint Surgery. [304]

Clinical evidence for the increase in bone formation at greater strains than point B are shown in the adaptation of bones in athletes operating at greater loads [309] and in various in vivo and finite element analyses [304]. Earlier structural mechanics work on functional bone remodelling shows that bone growth is driven by dynamic loading [310,311], which has

resulted in structural models which attempt to predict bone distribution by iterating FE elements to a target stress/strain stimulus [312,313]. A study used micro-CT imaging to quantify bone formation and resorption in the distal tibia of healthy post-menopausal women at 1-month intervals [314]. FEA of the imaged tibias was used to calculate the strain energy density (SED) throughout the tibias. Bone resorption peaked at low SED, and formation peaked at high SED (Figure 2.27a) and net bone formation frequency correlated strongly with tissue loading (Figure 2.27b). As such, the potential for implant design that triggers bone formation, by lowering the implant stiffness and inducing greater levels of periprosthetic strain is presented by BHN theory.

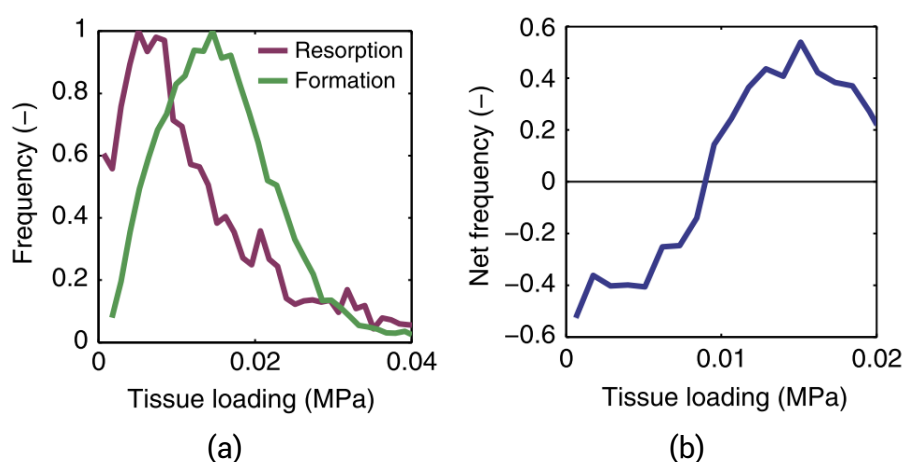


Figure 2.27:
Bone formation
frequency as a function
of tissue loading.

(a) Frequency of bone
resorption and formation
as a function of tissue
loading.
(b) Net frequency of bone
formation as a function
of tissue loading
(subtraction of graphs in
(a)).

Images reproduced with
permission from the
rights holder, Springer
Nature. [314]

The literature is varied in how it treats bone ingrowth into implants, especially in bone tissue engineering, where there is a large focus on pore size and its effect on bone ingrowth, with some debate as to the ideal size [315–317]. Some studies favour smaller pore sizes, either a range of 100 - 400 μm as ideal with no lower limit [318], whilst others show bone ingrowth with pores as small as 10 μm [319]. Some favour larger pores, with studies showing greater ingrowth with pore sizes of 300 μm - 500 μm [320,321]. Another study found a contradictory result of 600 μm - 900 μm pore diameter preferred, when compared to 300 μm [196,322]. The focus on pore size may be due to interest in other biological processes, such as vascularisation, which has been shown to plateau above pore sizes of 400 μm [323]. The size of pores directly affects properties such as hydraulic conductance and diffusivity [317], which would affect the flow of bone growth factors. However, an increase in pore size normally entails a lower relative density, thereby reducing the stiffness of the lattice or scaffold, with all else held constant. This focus on pore size rather than stiffness as the independent variable may be preventing a full account of how bone implants affect the formation of bone through increased strain considering BHN theory.

2.4 Musculoskeletal applications for metal AM

In this literature review, the use of metallic alloys as reliable structural biomaterials has been established. Previous attempts at using different materials such as polymers and composites in hip stems to alleviate stress shielding resulted in poor clinical outcomes, due to poor fixation, and no clear influence on bone remodelling. Since then, a better understanding has been developed of the use of bioactive materials, such as HA to improve fixation, and of the strain-dependent mechanisms that influence bone remodelling. Metal AM changes the paradigm for the creation of porous lattice structures for musculoskeletal applications, with the potential to take full control of the bone remodelling response (to reach peak bone formation in periprosthetic bone in Figure 2.26a), whilst avoiding the problems of poor fixation. As well as using bioactive coatings, AM itself can be used for better mechanical fixation of AM implants [324].

As the current literature has a large focus on pore size of lattices for musculoskeletal applications, there is more work to be done that focuses on the stiffness of implants as the property to optimise. This requires further investigation into lattice architecture and features which affect the stiffness of real printed parts, to prove that they are suitable for implant applications. The true mechanical behaviour of porous lattices is also not fully understood, especially in multiple directions, so it is unclear that strain would be distributed in trabecular bone in a predictable way.

2.4.1 Optimising mechanical behaviour

Some recent works have attempted to optimise porous lattices for stiffness, when implanted into trabecular bone. Lattices of varying stiffnesses were created for an ovine study. Commercially pure titanium (CPTi) and polyamide lattices were implanted into the medial femoral condyle of 6 ewes, and the resulting bone ingrowth generally increased as the stiffness of the lattices decreased [18]. Most but not all ewes responded well to the very low stiffness polyamide lattices, so it is not clear whether the peak bone remodelling response as in Figure 2.26a was reached adequately. In the same experiment, one CPTi lattice was designed with the aim to maintain the mechanical homeostasis of bone i.e. that match the local stiffness of the trabecular bone. The local mechanical properties of the ovine bone were also characterised [315]. The average bone ingrowth into the CPTi lattice was $10.73 \pm 2.97\%$ after 6 weeks.

A similar in vivo study did not focus on the designed stiffness of the Ti6Al4V implant [325]. However, a bone mechanoregulation algorithm was used to model bone ingrowth, and it was shown that a lower stiffness implant would improve bone ingrowth into the scaffold. Both

studies using animal models get closer to demonstrating that the lattice stiffness is a fundamental driver of bone ingrowth in vivo. More research is still needed to map the full range of in vivo results of implants with different designed stiffnesses. In contrast, the porous femoral stems that have been discussed previously often do not fully characterise the stiffness of the printed structures, and do not validate the predicted bone formation in vivo [199,226,237].

2.4.2 Aims and objectives of the thesis

As stated in the Introduction, section 1.2, the overall aim of the thesis is to investigate the mechanical properties of AM lattice structures for musculoskeletal applications. Specific shortcomings have been identified in this literature review, which form objectives for each chapter of the thesis.

Chapter 3 will address the different kinds of unit cell topologies seen in the AM literature. The objectives for this Chapter link to the first focus of the thesis: the design of lattices, and the impact that the choice of internal architecture has on the macro-scale behaviour of the structure.

- i. Many kinds of unit cells exist, with varying mechanical anisotropy. Some unit cell based lattices have exhibited inconsistent performance when tested in different directions. A method of testing a lattice in compression, in multiple directions, is needed to fill gaps in the literature, which invariably tests lattices in one direction only.
- ii. There is relatively little research about stochastic lattices. As they resemble metallic foams, it is intuitive to think that stochastic lattices would have more uniform mechanical behaviour than some unit cell based lattices that are anisotropic. A comparison between stochastic lattices and unit cell based lattices is needed.

Chapter 4 will involve tensile testing of individual laser PBF lattice struts. The following objectives link to the second focus of the thesis: the fundamental mechanical and morphological properties of AM metal as fabricated.

- i. The elastic modulus and strength of individual struts is reduced, compared to the bulk material, in many studies. There are differences between studies for the methodology that has been used, from strain measurement to the method for measuring the strut diameter. This leads to ambiguity about the true mechanical properties. Individual struts need to be tested using a robust method, to have a better understanding of how they are affecting lattice behaviour.

- ii. The properties of individual struts also vary depending on their angle to the build platform. Most studies only test struts that have been built perpendicularly to the build platform. The effect of build angle on these properties should be found.

Chapter 5 will incorporate the learnings from both previous chapters, to arrive at designs for lattice structures for musculoskeletal applications.

- i. Current lattices are constrained by AM limitations, such as poor manufacturing of struts at a low build angle. Designs that are 'self-supporting' and that overcome these manufacturing limitations may improve the performance of lattices in multiple directions.
- ii. AM lattices have been designed with a large range of mechanical properties. For an AM lattice to be used as a structural biomaterial, it must have an elastic modulus that is within the range of trabecular bone, in multiple directions.

3 Lattice architecture and anisotropy

Porous lattices made using additive manufacturing (AM) can have varied internal architecture, which impacts the macro mechanical behaviour, much like for trabecular bone. Many types of lattice exist, though most literature focuses on periodic or repeating unit cell architecture. These have anisotropic properties that can be quantified non-destructively using architectural measures of the CAD geometry, or by mechanical testing of the physical structure in multiple directions. The work in this chapter compares the architecture of two AM lattices, a periodic BCC lattice, and a culled stochastic lattice using the star length distribution (SLD). A micro-CT of trabecular bone is also analysed using the SLD for qualitative comparison. The mechanical properties of the two AM structures are compared using uniaxial compression tests ($n = 5$) in 10 load orientations relative to the structure, including the three orthogonal axes. The SLD measure varied widely, with the BCC structure showing high anisotropy, and the stochastic culled structure displaying less anisotropy with similarities to trabecular bone. Mechanical testing results reflected the internal structure of the lattices, however the BCC structure had a ratio of maximum to minimum elastic modulus of 3.9, whereas this value was 4.3 for the stochastic culled structure. Whilst the SLD results are linked to the underlying architecture of the structure, they cannot be relied upon to predict the response of the structures in loading scenarios. Mechanical testing, whilst destructive, is a robust measure that is more appropriate for characterising AM lattices for musculoskeletal applications. Further investigation into strut behaviour and lattice design that overcomes AM limitations is needed, to create lattices that better match trabecular bone architecture and mechanical anisotropy.

Parts of this chapter have been published in *Additive Manufacturing* 32 (2020) [19] and were presented at the International Society for Technology in Arthroplasty (ISTA) 2018 Congress, in the 3D Printed Implants and PSI seminar. All material within the chapter is my own work.

M. Munford, U. Hossain, S. Ghose, J.R.T. Jeffers, Prediction of anisotropic mechanical properties for lattice structures, Additive Manufacturing 32 (2020) 101041.

3.1 Introduction

Additive manufacturing (AM) methods allow fine control over the internal architecture of porous lattice structures [216–219]. By varying the arrangement of material within the structure, it is also possible to control the elastic modulus in multiple directions [172,182]. Human bone is a complex material, the interior of which resembles a porous lattice structure and which can also vary in architecture and stiffness [268,326]. As such, AM methods are of particular interest in musculoskeletal applications such as orthopaedic implants or bone scaffolds [15,327,328]. The mass and architecture of bone are intrinsically linked to its mechanical environment, due to Wolff's Law [267] and the role of mechanotransduction in bone formation [329]. However, current implants manufactured through casting or machining may have elastic moduli orders of magnitude higher than that of the bone they replace [55]. Consequently, the physiological loads through the bone are disrupted and there is a risk of the stress-shielding phenomenon, causing bone resorption where load is removed from the bone [65,72].

Following porous material theory, components containing a porous lattice have a lower stiffness than the bulk material [330]. AM methods such as powder bed fusion (PBF) can be used to manufacture porous lattices with elastic moduli in the range of bone [195,215,331,332]. This capability can be used to create scaffolds or implants that influence bone remodelling in musculoskeletal applications [15,308]. Architectural features of lattices such as pore size have been shown to affect surrounding bone ingrowth, with the ideal pore size varying in the literature from 100–900 μm [196,318,320]. However, pore size is linked to the stiffness of a lattice due to both being controlled by the relative density of the structure. Studies looking directly at the effect of implanting a lower modulus lattice on bone ingrowth have also been conducted [208,315].

Trabecular bone has an elastic modulus that can vary from 0.02–2 GPa, the least stiff including bone from the proximal tibia [273–275,280]. Trabecular bone is also anisotropic and its load bearing properties vary with direction depending on the anatomical location [276,280,286]. Trabecular architecture is also shown to vary, changing between a rod-like, plate-like and columnar structure depending on functional requirement [269]. Statistical methods exist which quantify the architecture of bone, commonly referred to in this context as the 'fabric' of the structure. The methods rely on interrogation of a 3D reconstruction of the bone from a micro-CT scan or magnetic resonance imaging. These different measures are detailed in Chapter 2, section 2.3.2. The star length distribution (SLD) measure shows an adequate sensitivity to trabecular orientation. These statistical measures of anisotropy can

be closely related to the principal elastic directions [286]. Through FEA, these measures of the fabric anisotropy combined with the bone's relative density have been shown to predict up to 98% of the elastic properties [289]. These methods have also been used to predict anisotropic yield properties of vertebral trabecular bone [291].

A second order fabric tensor as described by Zysset [293] has been found for some AM lattices, and was used to predict mechanical properties of the lattice in multiple directions [19]. A good agreement was found with mechanical testing results. However, a direct comparison has not been made between the architecture or fabric of AM lattices and the architecture of bone. This chapter aims to make this comparison using the architectural measures described previously and conduct mechanical compression testing of two lattice structures with potential for musculoskeletal applications. The results should clarify the requirements for porous lattice structures which replace trabecular bone in an implant or scaffold.

3.2 Materials and methods

3.2.1 3D models for architecture investigation

Two lattice structures were considered and are detailed in the first two columns of Table 3.1. The first was a body centred cubic (BCC) structure with a regular unit cell, comprising of beams or struts which meet in the centre from all 8 outer vertices.

The second was a stochastic culled structure, which does not have a regular unit cell. It was created by populating a volume with pseudo-random points using a Poisson-disc algorithm, forming an even distribution of points that is not biased in a particular direction. The points were then joined by lines (struts), using a nearest-neighbour algorithm, subject to three parameters:

1. The number of connections to make at a node
2. The minimum length of a connection
3. The maximum length of a connection

These struts are arranged in an equally random distribution of directions. Lastly, a modification is made to the structure that improves manufacturability using AM methods. Struts that are horizontal and close to the x-y plane are prone to defects due to the nature of layer-wise manufacturing inherent in PBF, as discussed in section 2.2.5 [191,200,205,209,245,248,249,260]. Therefore, struts at an angle lower than 30° to the x-y plane were removed, or 'culled'. The resulting stochastic culled structure was described by Ghouse et al. [162]. The initial three parameters were varied such that a certain density and

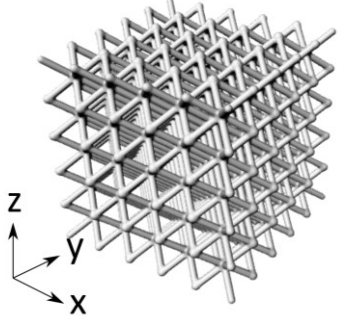
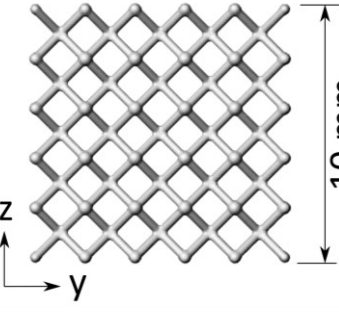
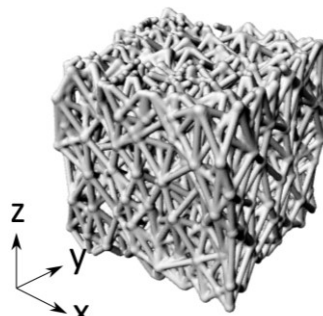
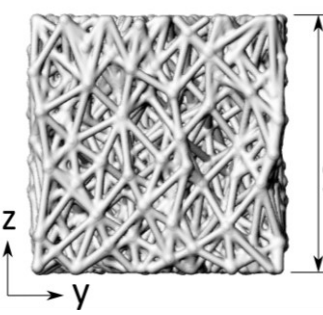
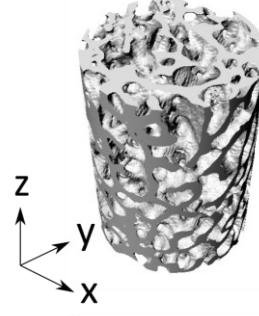
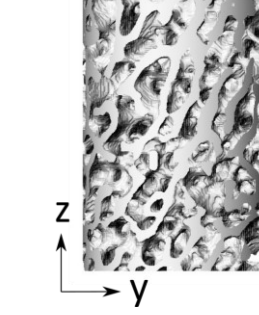
'connectivity' was achieved, defined as the number of struts terminating at a given node. This is to ensure that the structure is dense enough to 'self-support', i.e. the structure is not so sparse that there are areas of 'floating lattice', and each region is supported by struts below. The density required for this kind of lattice has been found to be 4 struts per mm³, as well as an average connectivity of 5.5. This method, which uses Rhinoceros 5.0 and Grasshopper (Robert McNeel & Associates) was described by Ghouse et al. [162].

These two lattice structures were chosen with the properties detailed in Table 3.1, as they represent two kinds of lattice topology, using a periodic (repeating) unit cell versus a stochastic (randomised) arrangement of struts. The vast majority of unit cell topologies in the literature for biomechanical applications feature a periodic unit cell (seen in the literature review, section 2.2.2, Porous lattices and musculoskeletal research). Using the methods detailed in the following sections, these are likely to have contrasting performance in different directions, and so a comparison can be made between periodic and stochastic topologies.

For qualitative comparison to these two CAD structures, a trabecular bone structure was obtained using a micro-CT scan of a bone core (10mm height, 7mm diameter) from the primary/principal compressive trabeculae group in a human proximal femur. This is also detailed in Table 3.1. This individual CAD model of trabecular bone was used as a point of comparison for evaluating the architectural measure described in the following section.

The bone core used in this chapter was procured by A. Jin, in his work investigating trabecular bone microarchitecture [333]. Bone cores were taken from healthy femurs, and from patients who have suffered from osteoporosis and had been treated with bone metabolic medication (bisphosphonates). The trabecular bone used in this chapter came from a 75-year-old female hip fracture patient with no history of hip disease or bone metabolic medication. The bone from the proximal femur was used in this chapter as it is often replaced with a metallic femoral stem as detailed in section 2.1.2 of the literature review. To obtain the micro-CT, a Nikon X-Tek HMXST-225 scanning system was used and an appropriate 3D model was found by reconstructing the scan using CTPro 2.0 (Nikon Metrology UK, Tring, United Kingdom) [333]. The scan was then thresholded into a binary image using the ImageJ optimise threshold plugin, and the voxel data was converted into a surface using Monolith, a Grasshopper™ plugin. An STL triangular surface mesh was generated for all three structures, with the dimensions detailed below.

Table 3.1: Lattice structures and trabecular structure to compare

BCC	Stochastic culled	Trabecular bone
  10mm x 10mm x 10mm 330 μm strut diameter 2mm BCC unit cell	  10mm x 10mm x 10mm 330 μm strut diameter 4.0 struts/mm ³ , 5.5 average connectivity	  10mm H x 6.3mm D - -

3.2.2 Star length distribution

A 3-dimensional version of the star length distribution (SLD) architectural measure, as described in Figure 2.23 and Figure 2.24 (Chapter 2, literature review, section 2.3.2), was implemented in Grasshopper™, a plugin for Rhinoceros 3D. The SLD was chosen over other measures as volume-based measures such as SLD and star volume distribution (SVD) can pick up anisotropies in geometry that interface-based measures such as mean-intercept length (MIL) cannot [294]. Smit et al. also found that in analytical cases, SLD is a better measure than SVD for inferring mechanical properties [295].

The specific equation used for the SLD algorithm in this chapter is shown below, Equation 3.1. The algorithm resembles a root mean square of the 'available length' within the structure in a given direction, where L_i is the total length for a given position in polar space, (θ, φ) . This follows the method used in the SLD, although this uses geometry in 3D space, as opposed to a voxel-based CT volume, as would be common for bone, or a 2D slice of bone from a histology. The Grasshopper implementation is described in Figure 3.1 below.

$$SLD(\theta, \varphi) = \frac{\sum_{i=1}^n (L_i(\theta, \varphi))^2}{\sum_{i=1}^n L_i(\theta, \varphi)} \tag{Equation 3.1}$$

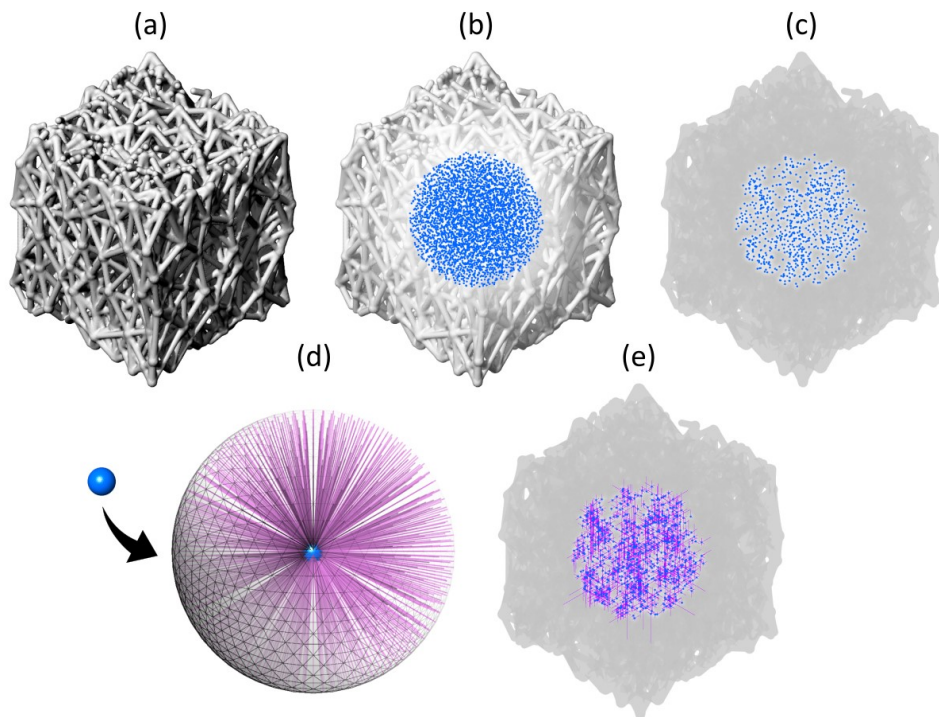


Figure 3.1: Process to calculate star length distribution measure from 3D model of structure.

(a) Original structure, (b) sampling points used, (c) sample points within structure, (d) directions that lines are projected in from each point, (e) resulting lines terminating at the boundary of the structure.

The resulting line lengths are summed using a root mean square algorithm, giving an average value in each direction.

Figure 3.1a shows the stochastic culled structure that was analysed, (also in Table 3.1). In Figure 3.1b the total sampling points are shown. 8000 sampling points were used for each structure and were introduced in a spherical volume in the centre, with a diameter given as 0.5 times the smallest specimen dimension. This was to prevent edge effects of lines terminating at the sides of the structure prematurely. Figure 3.1d shows the final projection directions. An equal spherical distribution of points was needed to prevent biasing of the method in any one direction. Therefore, the directions were found by calculating the vector from a centre point to the vertices of a subdivided tetrahedron, resulting in 1026 directions. A similar method was also used by Ketcham et al. [334]. Finally, Figure 3.1e shows the projected lines from each sampling point. To find the final SLD value for a given direction, the total line lengths were summed and averaged with those for the opposite direction. This shows an overall average of the length available, forwards and backwards along that vector. This calculation is made according to Equation 3.1 over all sampling points. This SLD architectural measure was implemented on all three of the CAD models in Table 3.1 above. Only the individual trabecular bone core pictured in Table 3.1 was included as a point of qualitative comparison.

3.2.3 Printed specimens for mechanical testing

Mechanical testing of AM printed structures was also conducted for the BCC and stochastic culled structures. Compression test specimens were generated such that the outer cuboid geometry was aligned in 10 different directions, as shown in Figure 3.2b. The inner structure always remained at the same orientation with respect to the build direction. Five specimens were tested per direction. Specimen dimensions were 10 x 10 x 12 mm and conformed to ISO 13314:2011 [238]. The mechanical testing did not include any trabecular bone, as it is impractical to carry out destructive testing of bone in multiple directions for a given anatomical location and is outside of the remit of this chapter.

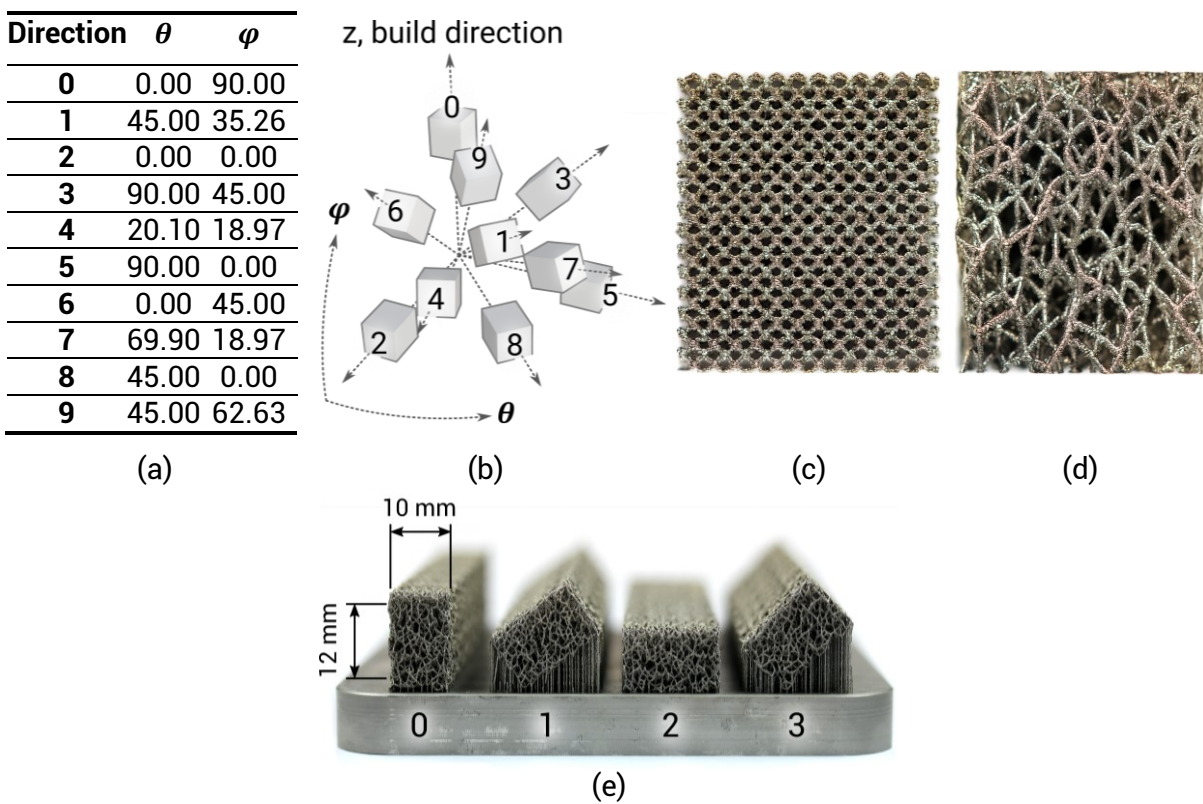


Figure 3.2: Test directions for structures

(a) Spherical coordinates of each direction, (b) specimen orientations, (c) Body centre cubic specimen in direction 0, (d) stochastic culled specimen in direction 0 (e) Built specimens.

3.2.4 Materials and manufacturing

To build the BCC and stochastic culled structures using laser PBF, the laser employed a single-exposure or points strategy, which has been used previously to build porous lattice structures [162,186,201,335]. For solid geometry, the laser usually traces outer contours and ‘fills in’ with hatching [162]. However, due to the small strut dimensions used in these specimens, the laser was focused on a single point and the exposure time was varied to increase the diameter of the melt pool. This method works well for structures comprising

solely of struts and individual lines. The geometry was sliced at a 50 μm layer thickness to create build files using Material Engine 1.0 (Betatype Ltd, www.betatype.pe, London, UK). Laser power was kept constant at 50 W, and the exposure time varied from 600 μs to 3300 μs . All specimens were printed using a Renishaw AM250 PBF additive manufacturing system. Titanium alloy (Ti6Al4V ELI, Grade 23) spherical powder of particle size range 10–45 μm was used to create specimens, supplied by Renishaw plc. The build chamber was vacuumed to -960 mbar and then back filled with 99.995% pure Argon to 10 mbar with an O content of $\sim 0.1\%$. Specimens were removed from the buildplate using wire erosion, ensuring that the wire path preserved the intended part geometry, then cleaned using ultrasonic bath and air jet. Each specimen was individually measured thrice in each dimension using Vernier callipers, and dry weighed thrice at normal atmospheric conditions. The relative density was then calculated by dividing the specimen weight by the bulk weight of the metal that corresponds to the specimen macro volume. A density of 4.42 g/cm^3 was used for Ti6Al4V ELI.

3.2.5 Mechanical testing

A materials testing machine (Instron 8872) with a 10 kN load cell was used to perform quasi-static compression testing at an extension rate of 2 mm/min, which corresponds to a strain rate within standard limits [238]. Displacement was measured using two LVDTs (RDP D6/05000A) either side of the specimen to remove compliance effects. A sampling rate of 30 Hz was used. The platens of the machine were lubricated to remove any frictional effects. Stress-strain curves were obtained using the individual macro dimensions of each specimen (engineering stress). The loading regime included a single cycle of loading/unloading (loading loop) to account for localised yielding within the porous structure. This was carried out from 70% of the yield stress (σ_{70}), to 20% of the yield stress (σ_{20}) and then the specimen was fully compressed to a high strain [238]. A preliminary specimen was compressed to 50% strain at 2 mm/min to find the required reference stresses. The elastic modulus was then calculated using an average of the linear regression of the loading loop from both LVDTs.

3.3 Results

3.3.1 Star length distribution rose diagrams

The SLD was plotted in two different ways in Figure 3.3. Firstly, as a rose diagram, a 3-dimensional representation of the SLD values. Secondly, the SLD values in each of the 10 directions investigated for mechanical testing were found and plotted as a bar chart (see Figure 3.2b). The 10 directions were rotated into each octant, and the values for directions 0 through 9 were then averaged from the resulting 8 per direction.

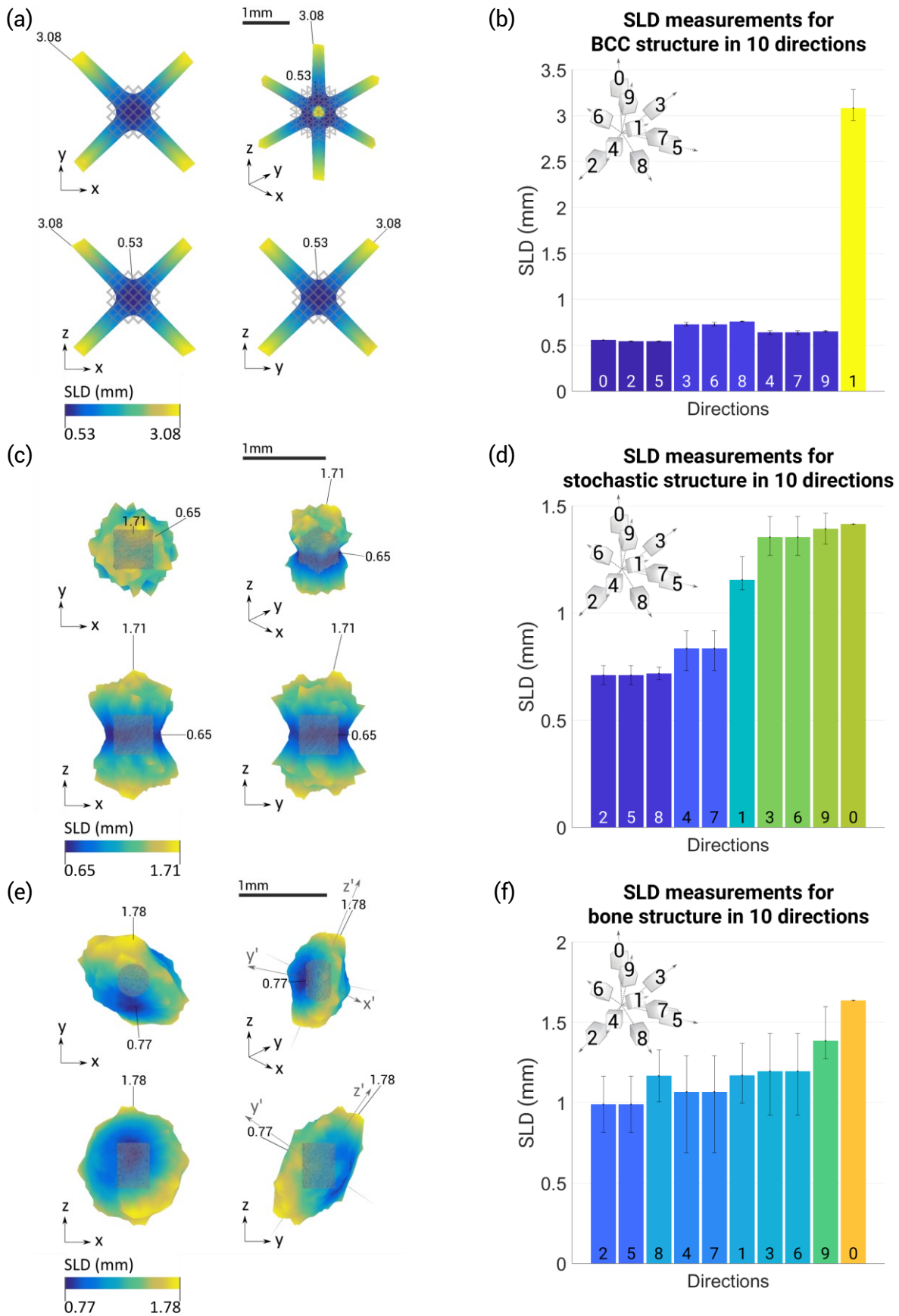


Figure 3.3: Rose diagram and interpolated results in 10 directions for all three structures

Error bars indicate the full range of results ($n = 5$). BCC structure described in (a) and (b). Stochastic culled structure in (c) and (d), and the trabecular bone structure in (e) and (f). Structures are superimposed in grey.

The SLD measure calculated for the BCC structure appeared as 'spikey' in the rose diagram in Figure 3.3a, with high peaks in the corners. The ordering of the bars in this bar chart is different from the other charts, to reflect the rotational symmetry of this structure. The ratio between the maximum and minimum of the SLD measure was 5.8, showing a high anisotropy. The peak in direction 1 (Figure 3.3b) reflects the arrangement of the unit cell, and a concentration of material in a very specific direction compared to all other directions.

The SLD measure for the stochastic culled structure in Figure 3.3c exhibited a lower anisotropy, with a maximum to minimum SLD ratio of 2.6. The rose diagram (Figure 3.3d) also showed a less severe change in material orientation. However, there are lower values in the x-y plane and for directions 2, 5 and 8 compared to in the z-direction, and direction 1.

The SLD measure for the trabecular bone structure shown in Figure 3.3e was less anisotropic still, with a maximum to minimum SLD ratio of 2.3. The rose diagram resembled a disc shape with a minor axis almost aligned with the y-axis, implying fewer trabeculae oriented in that direction. Conversely, there was not one direction that necessarily dominates, with a roughly equal distribution of material in the x-z plane. The averaged values in 10 directions in Figure 3.3f varied the least of the 3 structures. To capture more of the variance in the SLD values in Figure 3.3f, a transformation was applied to the rose diagram to re-align the y and z axes to the minimum and maximum. This shifted the 10 directions to better reflect the data in the rose diagram. The resulting new axes are shown in Figure 3.3e as x', y' and z'.

3.3.2 Mechanical testing

Table 3.2 details the average outer dimensions and standard deviations of the final specimens. The manufactured BCC specimens had an average relative density of 23.7%, and the stochastic culled specimens had a relative density of 15.8%.

Table 3.2: Manufactured specimen dimensions compared to intended dimensions

Specimens	Average width \pm SD (mm)	Average depth \pm SD (mm)	Average height \pm SD (mm)
Intended	10 \pm 0	10 \pm 0	12 \pm 0
BCC	10.19 \pm 0.37	10.16 \pm 0.37	11.95 \pm 0.22
Stochastic culled	9.95 \pm 0.25	9.98 \pm 0.23	13.15 \pm 0.76

The results for the compression testing are shown below in Figure 3.4, as a rose diagram and bar chart. Engineering stress is used throughout. To create a rose diagram, the results have been mirrored to appear in each octant. This is possible due to the mechanical symmetry of both structures. The bar charts are displayed with the directions ordered to match the rotational symmetry for the BCC structure and ordered in ascending angle to the horizontal plane for the stochastic culled structure.

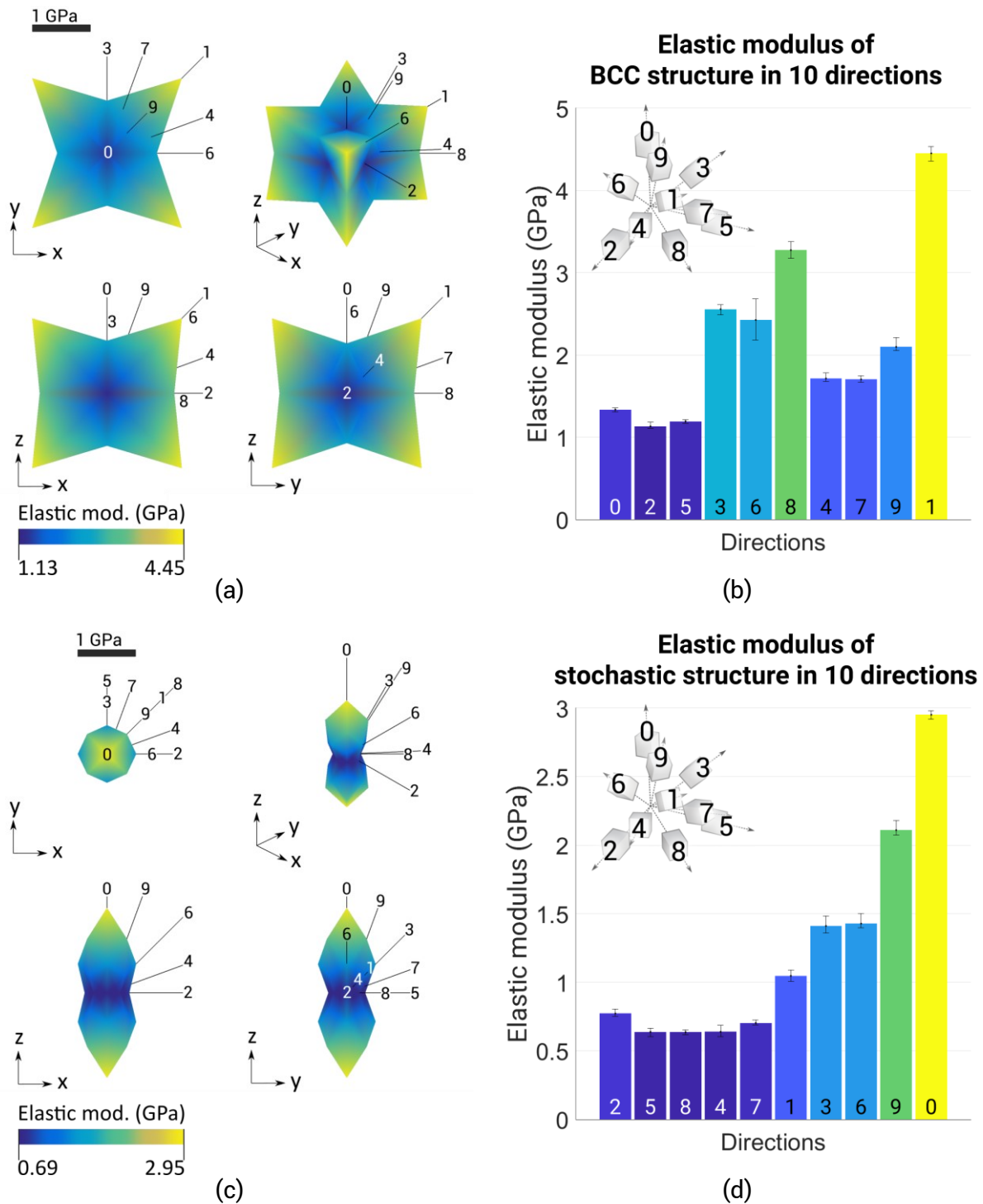


Figure 3.4: Results for mechanical testing shown as a rose diagram and bar chart.

BCC structure in (a) and (b). Bars are ordered to group directions that are rotationally symmetric, i.e. 0, 2, 5 as the orthogonal axes, etc. Stochastic culled structure in (c) and (d). Bars are ordered with increasing angle of the direction to the ground plane, i.e. upwards from 2, 5 and 8. Error bars indicate the full range of results (n = 5). Engineering stress is used throughout. Testing directions are inset into both bar charts.

The BCC structure had a peak in elastic modulus at 4.45 GPa, in direction 1, corresponding with the orientation of the unit cell and the peak SLD measure. Similarly, the lowest modulus was found in the orthogonal x, y and z directions, or directions 0, 2 and 5. The ratio between maximum and minimum modulus was 3.9.

The stochastic culled structure also bore a superficial resemblance to the SLD measure, with a peak in stiffness in direction 0. The elastic modulus was reduced as the directions approach the horizontal plane, due to the vertical orientation of the structure. Rather than being symmetric in the x-z and y-z planes, the elastic response of the structure was rotationally symmetric around the z-axis. This is due to the stochastic nature of the structure, which has no unit cell. Conversely to the SLD measure however, the elastic response was more anisotropic than the BCC structure, with a maximum to minimum ratio of 4.3.

3.4 Discussion

Lattice architecture can vary widely based on the choice of structure, with the BCC structure showing large amounts of anisotropy in the SLD measure. The stochastic culled structure displayed an architecture that was less anisotropic, and more closely resembled that of trabecular bone. This is due to the orientation of material within the structures. The BCC structure is highly symmetric, so, the architecture is essentially defined by the direction of one strut going from the vertex to the centre of the unit cell. The stochastic culled structure has a random internal architecture by nature, allowing an even distribution of material in all directions. There is, however, one axis of symmetry resulting from the removal of struts at a low angle to the horizontal plane. Thus, the rotational symmetry in one axis is shared by the architecture of the trabecular bone. However, this relationship is superficial, as for the stochastic structure this is caused by potential manufacturing limitations, and for the trabecular bone it is due to functional requirements in the proximal femur.

Mechanical compression testing of the BCC and stochastic culled structures showed intuitive results that reflect the architecture of the lattices. The elastic modulus of the BCC structure had peaks in the same direction 1 as the SLD architecture measure. The stochastic culled lattice also had a stiffness peak that corresponded with the SLD measure in direction 0. However, the stochastic culled structure had a higher anisotropy in elastic modulus than the BCC structure, whereas the opposite is true for the SLD architecture measure for both structures. This shows that the elastic modulus of a structure is linked to the underlying architecture, however, the SLD measure of the structure alone cannot be relied upon to predict the response of the structure in loading scenarios. Not all features of the lattice that contribute to its stiffness are accounted for in this measure, such as its connectivity or density.

The BCC structure had a ratio of maximum to minimum elastic modulus of 3.9, whereas this value was 4.3 for the stochastic culled structure. Lattices with similarly anisotropic

mechanical properties include the cubic lattice. Using FEA, the maximum elastic modulus of the lattice has been shown to be over 5 times the minimum in different orientations [166,172]. Another unit cell resembling a 'face-centred cubic' structure varied by over 6 times [207]. Overall, the average elastic modulus for both structures was 2.18 GPa and 1.23 GPa for the BCC and stochastic culled structures respectively. This is within the range of stiffness for trabecular bone, closer to values in the proximal femur [273–275,280].

The amount of mechanical anisotropy in trabecular bone depends on anatomical location. Cubic specimens have mainly been tested in three orthogonal directions (anterior-posterior, medial-lateral, and superior-inferior) due to the constraints of repeated compression tests on a single specimen. Trabecular bone from the proximal tibia shows a maximum mechanical anisotropy of around 3.2 [280], and from the proximal femur around 1.5 [276]. The average anisotropy from several metaphyseal locations was shown to be 2.3 [282]. However, similarly to a BCC structure, the principal direction of stiffness in trabecular bone may not exactly align with the three axes and may be due to functional requirements [336]. This can be seen with the result for the SLD measure of trabecular bone calculated in Figure 3.3e. It has also been shown that the elastic modulus of specimens aligned with the primary compressive trabeculae group in the proximal femur is reduced by 40% when the alignment of the specimens are offset by 20° [279].

Limitations in this work include the analysis of only one trabecular bone mesh to find the SLD measure. Bone architecture will vary with specimens from different femurs due to different physiological loading, and from changes in anatomical location when removing bone cores. In the absence of mechanical testing of the bone, the analysis of one trabecular bone core still provides useful qualitative comparison to the lattice structures. The SLD rose diagram in Figure 3.3e also matches results from the literature for bone from the same location and using the same technique [334].

The geometry of the STL meshes used for the SLD analysis did not necessarily match the final manufactured specimens, which makes it harder to draw quantitative comparisons between the architecture and mechanical testing results. The relative densities between the BCC and stochastic culled specimens also differed by 7.9%, so the volumes of material within the structures also differed. However, only qualitative comparisons were made between the results to illustrate the difference in performance between unit-cell based lattices and stochastic lattices using the same AM methods. Further testing could involve stricter controls on lattice geometry so that comparisons between structures are applicable.

These limitations informed the methods used in the subsequent chapters in this thesis. Advanced imaging techniques, such as micro-CT, were used on as-built structures in Chapter 4 to make sure that any analysis of geometry or morphology of specimens accurately reflected the specimens. Chapter 5 uses the same mechanical testing methodology as in this chapter, ensuring that the structures were directly comparable.

Neither of the structures investigated showed an architecture or mechanical anisotropy that matched trabecular bone well, with the BCC structure showing a peak in the SLD measure that is unlikely to exist in bone. Whilst the stochastic culled structure would intuitively seem to be a better candidate structure for matching bone, it also has a high mechanical anisotropy of 4.3 due to the culling of struts at a low angle to the build direction, resulting in a peak in stiffness in the z-direction. Further investigation into low-angle struts and what properties they have compared to vertically oriented struts will help inform the creation of a stochastic lattice that has a better mechanical performance. Advanced imaging techniques will also be used to get a clearer understanding of the morphology of as-built structures.

4 Tensile testing of struts

Additive manufacturing methods such as laser powder bed fusion (PBF) can produce micro-lattice structures which consist of 'micro-struts', which have properties that differ from the bulk metal and that can vary depending on the orientation of the strut to the build direction (the strut build angle). Characterising these mechanical and morphological changes would help explain macro-scale lattice behaviour. Individual stainless steel (SS316L) and titanium alloy (Ti6Al4V) laser based PBF struts were built at 20°, 40°, 70° and 90° to the build platform, with 3 designed diameters and tested in uniaxial tension (n = 5). Micro-CT was used to quantify changes in surface roughness, eccentricity and cross-section. There was no clear relationship between elastic modulus and build angle, and the average value across all build angles was 61.5 GPa and 37.5 GPa for SS316L and Ti6Al4V respectively, showing a decrease in performance compared to the bulk material. Yield strength was uniform over build angle for SS316L, but for Ti6Al4V it varied from 40% to 98% of the bulk value from 20° to 90°. All lower angle struts had worse morphology, with higher roughness and less circular cross-sections. These data should help inform micro-lattice design, especially in safety critical applications, such as in the orthopaedic field, where lower mechanical performance must be compensated.

The work in this chapter has been submitted to Additive Manufacturing.

4.1 Introduction

Additive manufacturing (AM) methods, such as laser-based powder bed fusion (PBF), can be used to create lattice structures made of individual beams or struts, each with a diameter between 100-500 μm , also known as micro-lattice structures [186,201,215,331,337]. AM methods can also create solid components with comparable properties to cast or extruded metal, but the properties of struts or 'micro-struts' can be significantly different to the bulk material, and harder to characterise. This can impede the creation of robust FEA models of lattices and may cause unpredictable behaviour in manufactured lattices. Micro-struts have been manufactured in materials such as stainless steel (SS316L) and Ti6Al4V, a titanium alloy [201,203,241]. Further details can be found in Table 4.2. The latter is particularly useful for its biocompatibility, and several studies have explored its use in additively manufactured bone implants [188,235,338]. This chapter will characterise the mechanical properties of individual micro-struts using tensile tests. This will help improve the understanding of fundamental mechanical properties and may explain their influence on macro scale AM lattice behaviour.

Tensile specimens for standard material testing normally use dog-bone specimens and follow ISO 6892-1:2016 [243], or the equivalent ASTM standard [244]. However, to investigate the specific influence AM methods have on the mechanical properties of micro-struts, it is necessary to use a modified test method due to the much smaller specimen dimensions. Established methods opt for one single strut 'as-built' which is gripped or fixed at each end so as to avoid slipping at the grip/strut interface [201,203,204,240]. However a 'group' of struts in lieu of the gauge section can also be used [245] and sometimes gripping 'tabs' are printed on the end [191,254].

Strain has been measured in various ways. A clip gauge extensometer [201,240] overcomes any underestimation of elastic modulus due to machine compliance, especially given the low stiffness of the small specimens. However, these can also be cumbersome also due to the fragility of the specimens. They may also need to be counterbalanced to avoid adding stress concentrations on the strut where they attach. Where the crosshead extension has been used, compliance correction has to be introduced for improved accuracy [201,241]. Optical methods have also been used, which also measure strain along the gauge length of the specimen [203,242]. This has also been achieved using LVDTs that are fixed between the grips, parallel to the tensile direction [204]. This relies on the grip on the specimen to be reliable, ensuring that the force is applied to strut deformation rather than shearing at the grip/strut interface. This has been achieved before using grit paper or adhesive [240,241].

The gauge length varies between existing studies, and there is no fixed ratio between specimen diameter and gauge length. However, changing the gauge length does not influence the calculated mechanical properties, assuming the specimen is long enough to not encounter end-effects near the grips [204].

The mechanical properties found from tensile testing of laser PBF micro-struts, such as elastic modulus and ultimate tensile strength, are below that of the bulk material. For stainless steel (SS316L), the modulus has been found to be between 37% and 74% of a bulk value of 190 GPa [201,203,204,240]. A reduction is also seen for the yield strength, varying between 29% and 57% of a bulk value of 494 MPa [257]. For titanium alloy Ti6Al4V, the elastic modulus has been reported as 107 GPa, 85% of the bulk value 129 GPa [241]. Renishaw provide datasheets for the mechanical properties of their fully dense laser PBF bulk metals, to which the following results are compared in Table 4.1 [257,258]. E , σ_y , and σ_{UTS} refer to the elastic modulus, yield strength and ultimate tensile strength (UTS) respectively. The subscript s refers to the bulk material property.

Table 4.1: Comparison of mechanical properties found for micro-struts built using laser PBF in SS316L and Ti6Al4V

Material	E (GPa)	$\frac{E}{E_s}$	σ_y (MPa)	$\frac{\sigma_y}{(\sigma_y)_s}$	σ_{UTS} (MPa)	$\frac{\sigma_{UTS}}{(\sigma_{UTS})_s}$	Strain measurement	Author
SS316L	140	0.74	144	0.29	-	-	Clip-gauge	[201]
SS316L	97	0.51	250	0.51	450	0.72	Clip-gauge	[240]
SS316L	71	0.37	280	0.57	-	-	Optical method	[203]
SS316L	81.3	0.43	263.3	0.53	575.3	0.92	LVDTs	[204]
SS316L	-	-	~340	0.69	~480	0.77	Crosshead disp.	[261]
SS316L	-	-	339	0.69	459	0.61	Crosshead disp.	[339]
Ti6Al4V	102	0.81	-	-	-	-	Compliance corr.	[241]
Ti6Al4V	107	0.85	997	1.01	-	-	Optical method	[242]

Table 4.2: Comparison of methodologies for tensile tests of laser PBF micro-struts built in SS316L and Ti6Al4V

Material	Strut diameter (μm)	Diameter measurement	Strut orientation	Laser power (W)	Laser exposure (μs)	Author
SS316L	200 \pm 17	SEM micrograph	Vertical	140	500	[201]
SS316L	207 \pm 10	Archimedes	Vertical	90	1000	[240]
SS316L	~220	Caliper + correction	Vertical	-	-	[203]
SS316L	170 - 410	SEM micrograph	45°	125	70 - 800	[204]
SS316L	300 - 740	Digital microscope	Vertical	195	-	[261]
SS316L	250	Digital microscope	Vertical	-	-	[339]
Ti6Al4V	370	Micrometer	35°	200	1000	[241]
Ti6Al4V	300-1200	SEM + correction	Vertical	200	-	[242]

The measurement of the strut diameter is a key step in calculating the mechanical properties and may be difficult to measure non-destructively. An accurate measure prior to tensile testing has been attempted by finding the ratio of the value found using a Vernier caliper to that using sectioned struts at various locations, dividing the sectioned diameter by the caliper diameter. This ratio, roughly 0.86, was then used as a correction factor for all caliper measurements [203]. A similar method uses the correlation between the Feret diameter (synonymous with the caliper diameter) and the true equivalent diameter [242], or uses the volume fraction of a lattice using a similar strut to calculate the diameter analytically [240]. Advanced imaging techniques such as SEM and micro-CT have been used to provide precise measurement of strut geometry and highlight defects such as strut 'waviness' and internal porosity [193,209,246–249,254]. Due to the variation seen in strut geometry it is unclear what the best value is for the effective diameter, which affects stiffness calculation. In this chapter, this shortcoming is addressed by comparing different ways of defining the cross section of additively manufactured struts and investigating how they affect mechanical properties.

Many studies show the impact of these morphology variations on finite element analysis models [200,205,245,250–255]. Properties of the strut morphology that have been highlighted include diameter, porosity and eccentricity, and introducing these defects on a statistical basis throughout the model can help improve predictions [252]. However, a key requirement for such statistical models is the input data used to define the statistical variance.

The layer-wise fabrication of PBF components has an impact on the stiffness of micro-lattice structures overall [259], but there is also a difference in mechanical properties and morphology of single micro-struts when built vertically versus at a low angle to the build platform [191,200,262,263,340,341,205,209,245,248,249,254,260,261]. Struts have been imaged using micro-CT or microscope, and the impact of the angle of struts to the build direction on strut morphology has been investigated. This includes its effect on the cross section [191,245,248], 'waviness' or eccentricity [200,209] and roughness [260,340,341]. Tensile tests of struts built using laser PBF at varying angles to the build direction have been conducted [201,261,262], but there is little data in the literature on the relationship between build angle and elastic modulus and strength. Some research has also shown a better fatigue life for micro-struts built using electron beam melting at 45° versus 90° to the build platform [340]. These orientation-dependent parameters are essential to model the behaviour of complex lattices reliably.

Detailed investigation of both the mechanical properties of micro-struts and their morphology is conducted in this chapter. This aims to give clear insight into how the morphology and build angle are related, and how these two variables affect the elastic modulus and strength of the micro-struts. A secondary aim is to investigate the circularity of struts, their surface finish, and how different ways of defining diameter affect the calculated mechanical properties. This fundamental knowledge will improve our understanding of the mechanical properties of micro-lattices.

4.2 Materials and methods

4.2.1 Specimen manufacture

All strut specimens were built in two materials using a Renishaw AM250 powder bed fusion (PBF) additive manufacturing system (spot size of $70\ \mu\text{m}$ and wavelength of $1.07\ \mu\text{m}$). Stainless steel (SS316L) and titanium alloy (Ti6Al4V ELI, Grade 23) spherical powders were used, with a particle size range of $10\text{--}45\ \mu\text{m}$. These were supplied by Carpenter Additive Ltd. Specimens were $25.8\ \text{mm}$ long, for an eventual $5\ \text{mm}$ gauge length (see Methods section 4.2.4) and built at a range of angles, measured as the inclination vertically from the build platform. 20° , 40° , 70° , and 90° were chosen as these cover a large range of overhang at which micro-struts of this length can be built using PBF (Figure 4.1). Three designed specimen diameters were applied to the specimens, 250 , 300 and $350\ \mu\text{m}$. These diameters are chosen as they are used regularly in micro-lattice structures [186,201,215,331,337].

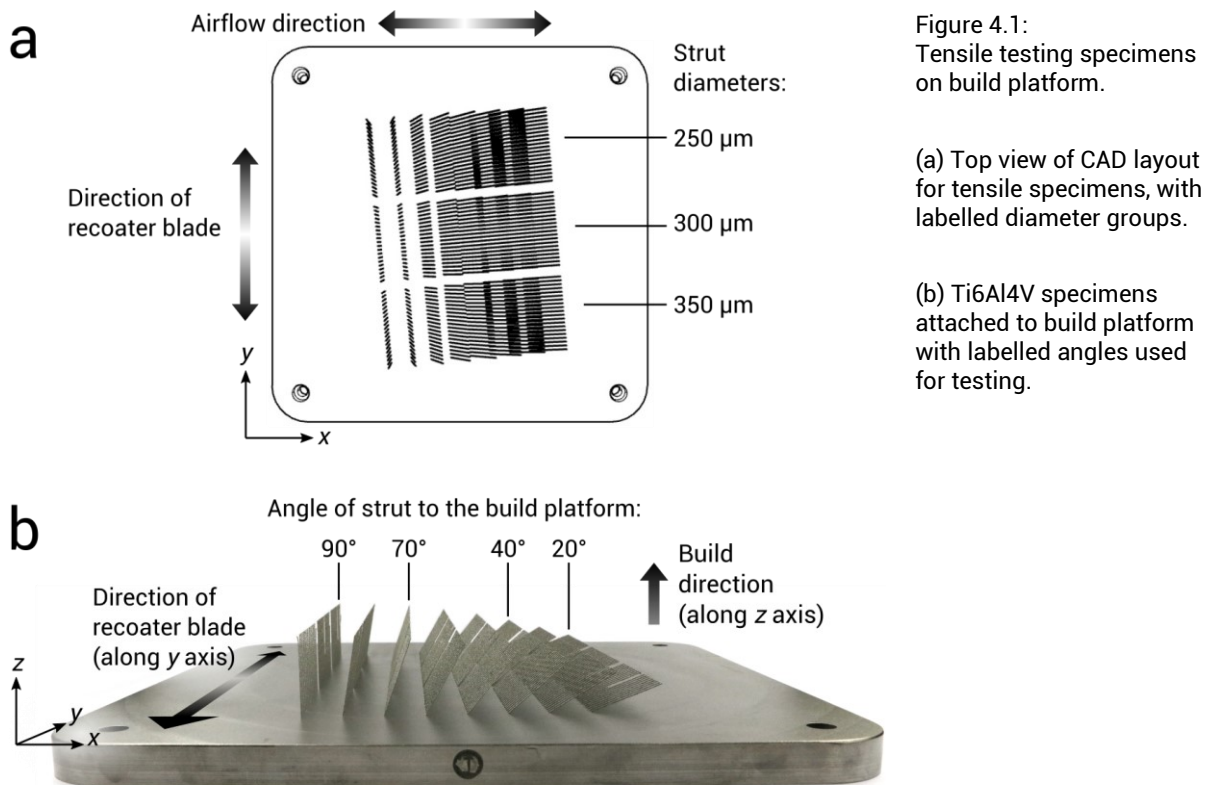


Figure 4.1: Tensile testing specimens on build platform.

(a) Top view of CAD layout for tensile specimens, with labelled diameter groups.

(b) Ti6Al4V specimens attached to build platform with labelled angles used for testing.

Figure 4.1 shows the resulting build platform, where 20 specimens per variable were built to include redundancies, 240 specimens in total. 5 replicates per variable ($n = 5$) were required, 120 successful specimens in total, avoiding the inclusion of unsatisfactory specimen data that may occur. The strut overhang was angled in the x direction, to avoid damage by the recoater blade, which moves along the y-axis. A 5° anti-clockwise rotation was also applied to the struts to avoid repeated scraping of the recoater blade by the struts. Airflow was perpendicular in the x-axis.

Material Engine 1.0 was used (Betatype Ltd, www.betaty.pe, London, UK) to generate final build files for the machine. For each strut, the software calculates the intersection between the strut and the slice layer. At each intersection, an ellipse was calculated which reflects the angle of the strut to the build platform. Traditionally, the ellipse contour is traced by the laser and 'hatch' scans are used to fill in the strut cross-section, However, in this chapter the contour diameter was set as equal to the laser spot size (70 μm), ensuring that the centre of the strut is melted, and the strut thickness is then controlled by laser exposure time to increase the size of the melt pool, as shown in previous work [162,342]. The laser exposure times were chosen on a strut-by-strut basis, to achieve the desired diameters. For SS316L, the laser power was 200 W and exposure time varied from 40 to 100 μs . For Ti6Al4V, the laser power was 50 W and exposure time varied from 50 to 600 μs . The elliptical contour was traced out in points, with a spacing between points around the contours of 45 μm for all specimens. A 50 μm slice thickness was used. The method described herein is used in previous work [204]. The specimens were carefully removed from the plate using pliers, ensuring no deformation of the specimen, and were then stored individually before scanning.

4.2.2 Micro-CT scanning

To obtain high resolution information about the morphology of the struts and its variation over build angle, micro-CT scans of the struts were conducted. Compared to other measuring techniques, this revealed detailed information about the surface of the struts as well as any internal porosity. Radiolucent strut holders were designed to keep struts in place whilst scanning to ensure no 'ghosting' in the images due to movement, and to minimise distance of the struts to the X-ray source (Figure 4.2). These were manufactured using a fused deposition manufacturing (FDM) process on a Markforged Mark Two printer (www.markforged.com, Massachusetts, US). The Onyx filament was used, a fibre-reinforced nylon thermoplastic [343].



Figure 4.2:
3D-printed
radioluscent strut
holder.

Shown assembled
and disassembled
with closeup on
individual struts.

Micro CT volumes of each batch of struts were acquired using a Bruker SkyScan 1272 (www.bruker.com, Kontich, Belgium). A series of optimisation scans were conducted to find the ideal balance of angular spacing between rotational X-ray images, voxel size and frame averaging which captured the fine detail of pores and semi-sintered particles on the strut surface. A comparison is shown in Table 4.3.

Table 4.3: Comparison of strut cross-section using different scanning parameters, with final selection in red

Resolution:	Low-res	Low-res	Low-res	Low-res	High-res	High-res	High-res	High-res
Voxel size (µm):	6	6	3	3	3	3	3	3
Frame averaging:	2	0	2	0	2	2	2	3
Angular spacing (°):	1	0.5	2	1	4	1	1	0.5

With images acquired at 1° spacing, and no frame averaging, a voxel size of 3.5 µm was achieved for all scans. The voxel size had to increase slightly from 3 µm to ensure the full gauge length was captured. The source voltage and current were 100 kV and 100 µA respectively. A 0.11 mm Cu beam hardening filter was used to improve the image contrast and remove streak artifacts [344]. The volume reconstruction from X-ray images was calculated using NRecon 1.7.1.0 (www.bruker.com, Kontich, Belgium). These volumes were then split up into one for each beam. An example micro-CT 'slice' is shown in Figure 4.3.

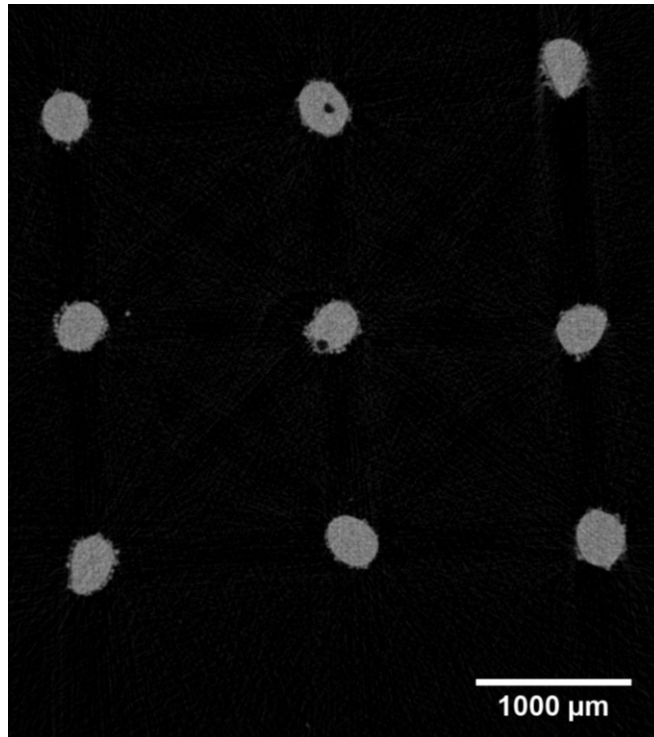


Figure 4.3:
Example slice of
reconstructed micro
computed tomography
(microCT) volume.

Slice contains SS316L
struts built at 20° to
horizontal.

4.2.3 Segmentation and analysis

Treatment of the micro-CT voxel volume

The central 5 mm of each scan of the beam was analysed as this would be the critical gauge length section of the strut undergoing the tensile test. A threshold operation was applied to all volumes automatically, creating a binary image using Otsu's method (step 2 of Figure 4.4), as the grayscale images were assumed to contain two classes (air or metal) and that the histogram of the images was therefore bimodal [345]. This ensured consistency across all struts. Pores below the minimum pore size threshold were removed to allow for successful meshing of the beam (step 3 of Figure 4.4). The threshold was 150 voxels in volume, corresponding to an equivalent pore diameter of 2.17 μm , which is roughly an order of magnitude below the diameter of the powder particles themselves. Extraneous particles which were unconnected to the strut volume were removed so they did not influence any results.

Meshing of micro-CT voxel volume

A triangular surface mesh was generated for the outer surface of the strut and inner pore surfaces using the iso2mesh meshing algorithm [346], which is a MATLAB implementation of the CGAL 3D Surface Mesh Generation library [347] (step 5 of Figure 4.4). The mesh was generated at the boundaries within the binary volume. The maximum radius of the Delaunay sphere used to mesh the surfaces was 17.5 μm , lower than the average radius of the powder

particles, ensuring that surface detail caused by powder particles would be captured. A tetrahedral mesh of the volume of the strut was also generated using the triangular surface mesh as an input. The maximum target volume for the tetrahedral elements was 25 voxels, equivalent to a spherical of diameter of $6.35 \mu\text{m}$ (step 6 of Figure 4.4).

To find the axis of the strut, the centroids of each mesh volume element were plotted in 3D space. A line was then fit to those points in 3 dimensions using a least squares method. The mesh was then realigned so that the strut axis followed the global Z-direction, allowing control of the mesh in global coordinates. The strut was translated so the axis midpoint was at the global origin. In the final step of the mesh manipulation, the mesh was scaled from voxel units to metres (step 9 of Figure 4.4). For subsequent analysis, the triangular surface mesh of the strut and internal pores was intersected to find the cross-section, giving the perimeter geometry and the cross section of any pores in the plane of the cross section. 400 measurements were taken along the 5 mm gauge length of the beam, once every $12.5 \mu\text{m}$ (step 10 of Figure 4.4).

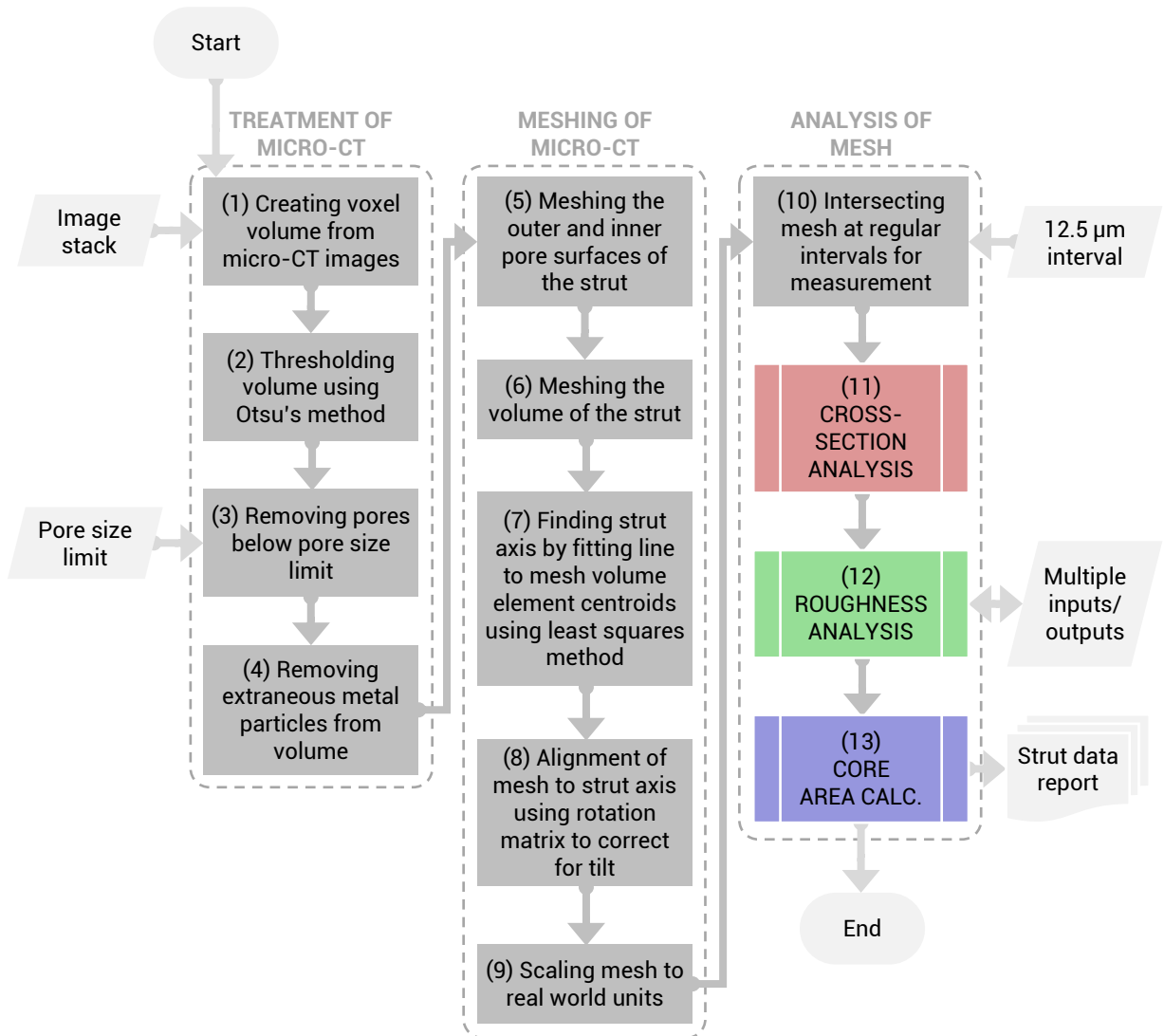


Figure 4.4: Flowchart of segmentation and analysis of micro-CT data, showing overview of full process

Analysis of the mesh

The three subroutines shown as steps 11, 12 and 13 of Figure 4.4 are expanded on in the second flowchart Figure 4.5. The internal steps for each part of the analysis are explained further.

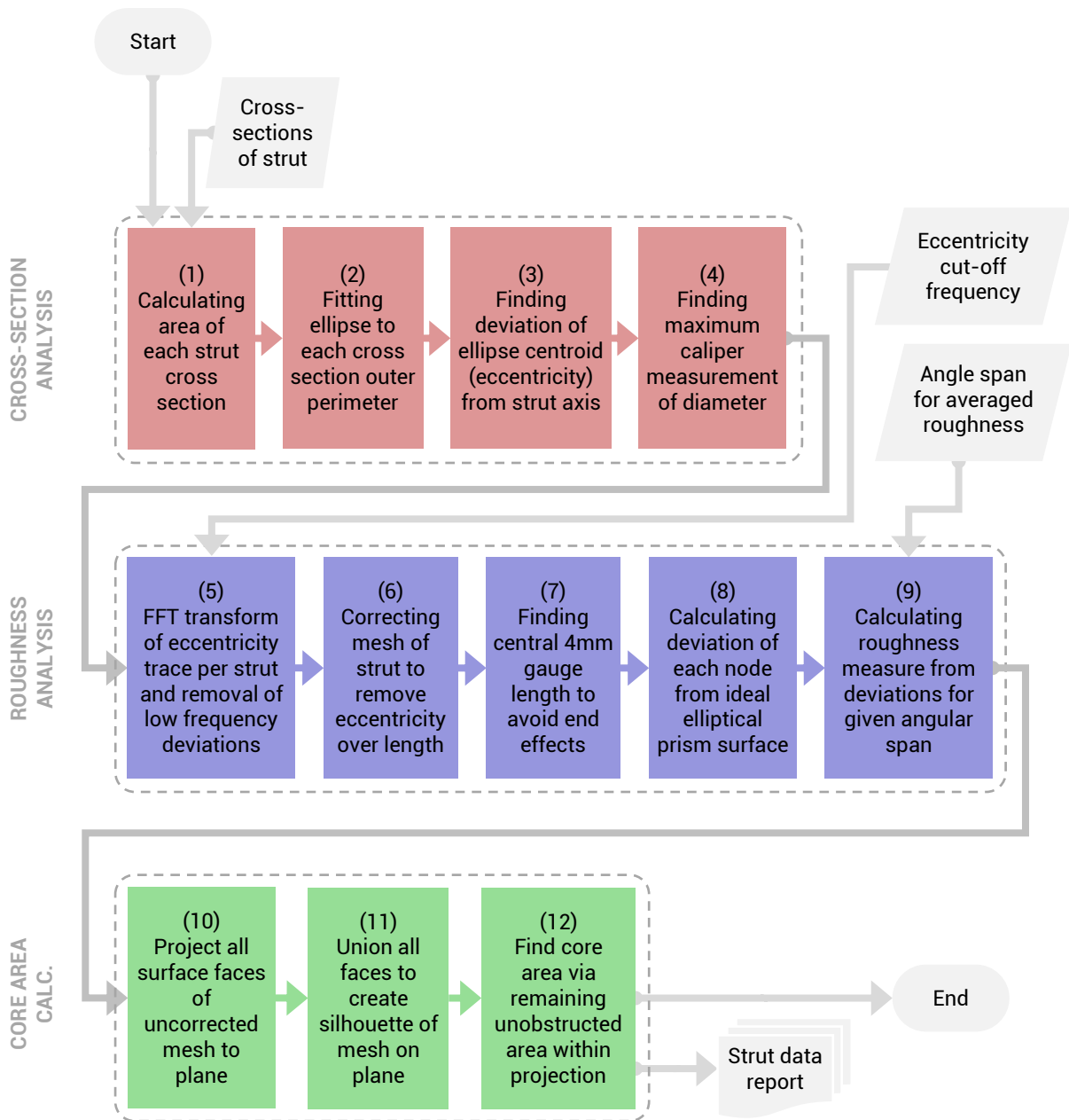


Figure 4.5: In depth flowchart of last three stages of analysis, for cross sections, roughness and minimum effective area

Cross-section analysis

Overall measurements of the strut geometry were taken in the cross-section analysis stage. The cross-sectional area of each intersection was found and an ellipse was fitted to the outer perimeter (not including any points from pore intersections). This was used to calculate an effective diameter per cross section, the results of which were averaged at the end for an average diameter (D_{avg}). The minimum of these effective diameters was also recorded as the minimum diameter (D_{min}). By dividing the major axis length by the minor axis length of the resulting ellipse, the elliptical ratio was found at each measurement point along the strut.

This is 1 if perfectly circular and increases as the cross-section deviates from the intended geometry (Figure 4.6b).

The centroid of the ellipse was also found at each point along the strut. The distance from the centroid to the strut axis at (0,0) was found, quantifying the eccentricity of the strut along its length (Figure 4.6c).

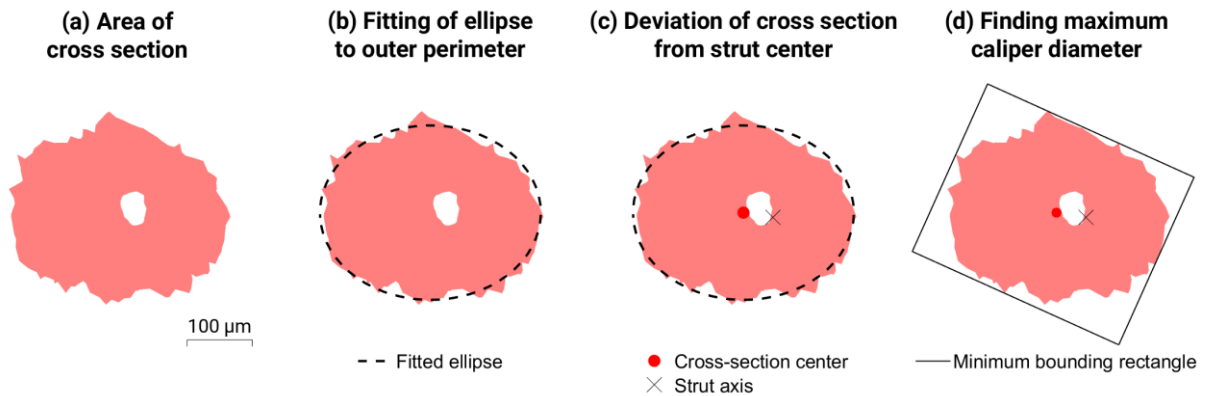


Figure 4.6: Operations on strut cross sections showing the results of the ellipse fit and minimum bounding rectangle algorithm

To compare to the average and minimum diameter measurements, a value was found per cross section which simulates the maximum diameter measurement achieved by caliper (Figure 4.6d). This was found by generating the minimum bounding box that contains the cross-section perimeter and using the larger of the two side measurements as the maximum caliper diameter (D_{cal}). This is synonymous with the maximum Feret diameter [242].

Roughness analysis

To find an accurate measure of roughness for the surface of the strut, any variation of the surface due to overall deviation of the strut from the strut axis had to be accounted for. Therefore, the strut mesh was corrected for eccentricity.

The eccentricity of an example strut in Figure 4.7a is plotted over its length as a single trace, with a dotted red line in Figure 4.7b. This is the variation of the centroid of cross-sections along the strut length (Figure 4.6c). Both the x and y components vary over z (the length), but in Figure 4.7b only the magnitude of the x component is shown. $x = 0$ at the strut axis shown in a grey dashed line in Figure 4.7a. High frequency variation can be seen in the trace, linked to surface roughness, as well as gradual variation due to waves in the building of the strut. To separate the high frequency variation from low frequency variation, an FFT transform of this trace was conducted for both the x coordinate and y coordinate of the eccentricity. The

sampling frequency used was 81.4 samples/mm, which equals the rate of original measurements of the cross section.

As the trace is measured over the length of the strut instead of over time, this resulted in the components of the trace in the frequency domain measured in 'per mm' instead of 'per second' (Hz). Any variation in the strut mesh that occurred on a small frequency was filtered out, leaving only the changes in frequency that occur over a longer distance (low pass filter). The cut-off frequency corresponded to any changes occurring every 0.5 mm, which is 10 times the layer thickness of 50 μm , ensuring that the filtered trace would only reflect longer scale variation and not surface roughness. The trace was transformed back into the space domain, resulting in the black trace in Figure 4.7b.

Triangular surface mesh elements were described by 3 vertices with x, y and z coordinates. This 'smoothed' trace was subtracted from the vertex coordinates for both the x and y coordinates, resulting in the corrected mesh in Figure 4.7c, which still included high frequency variation of the beam due to surface roughness. Using this mesh, any eccentricity in the beam did not contribute to roughness measurements.

However, after filtering the eccentricity trace, there were end effects due to a lack of high frequency variation in the trace (visible at the start and end of the filtered eccentricity trace in Figure 4.7b). Therefore, only the middle 4 mm of the 5 mm gauge length was used for the roughness measurements. An ellipse was fitted to all vertices of the corrected mesh after projection into the X-Y plane (Figure 4.8b) so that the mean surface could be found. The strut surface was compared to this ideal elliptical prism to find the roughness at different angular locations around the surface of the strut.

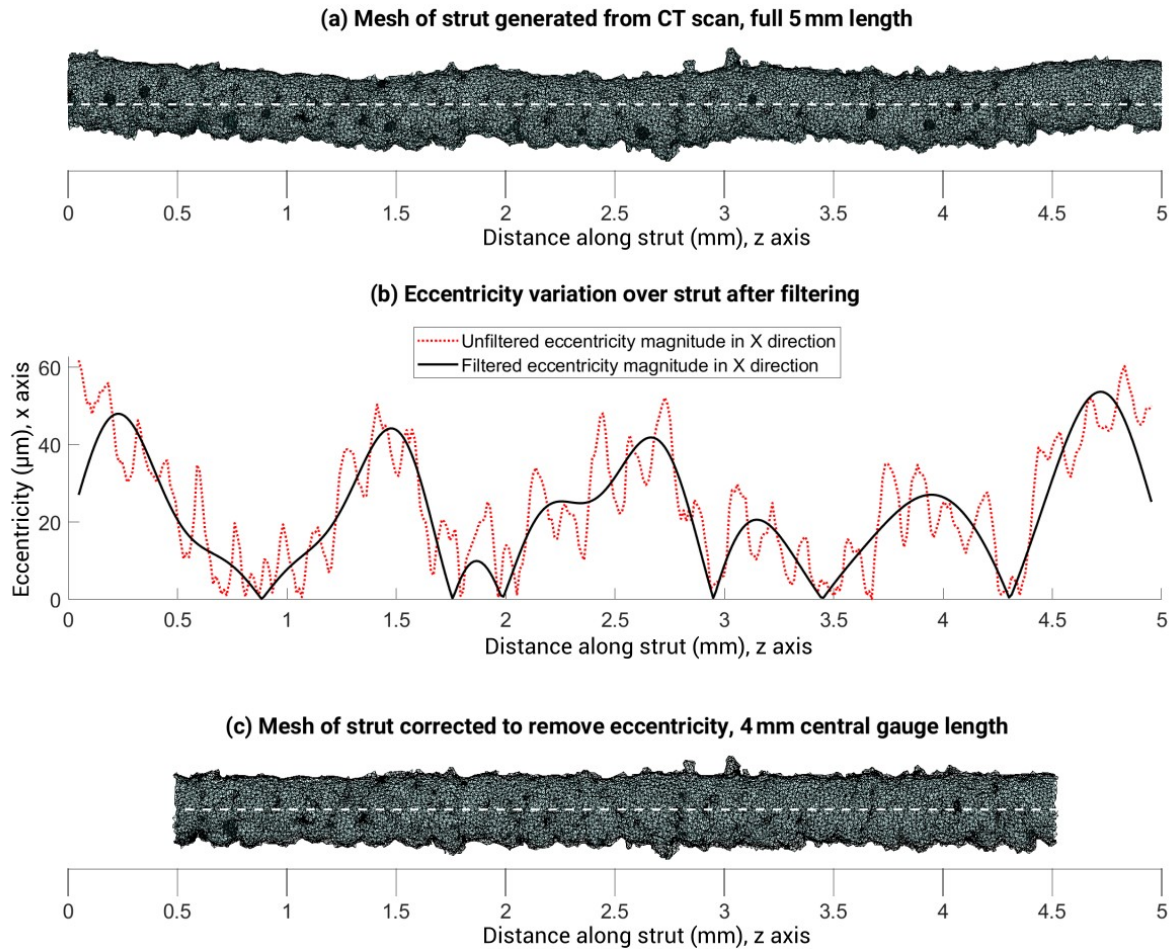


Figure 4.7: Removal of eccentricity from strut mesh before roughness analysis.

(a) An example strut surface mesh, showing overall eccentricity (waviness) and high detail surface roughness. Average strut axis shown in grey dashed line.

(b) Dotted red trace showing magnitude of eccentricity of the strut. This is the variation of the centroid of cross-sections along the strut length. Black solid trace is the result of a low pass filter of the eccentricity using an FFT transform, removing changes that occurred every 0.5 mm and below.

(c) Strut surface mesh after having the low pass filtered eccentricity (black trace) subtracted from all mesh vertices, correcting the mesh for gradual eccentricity.

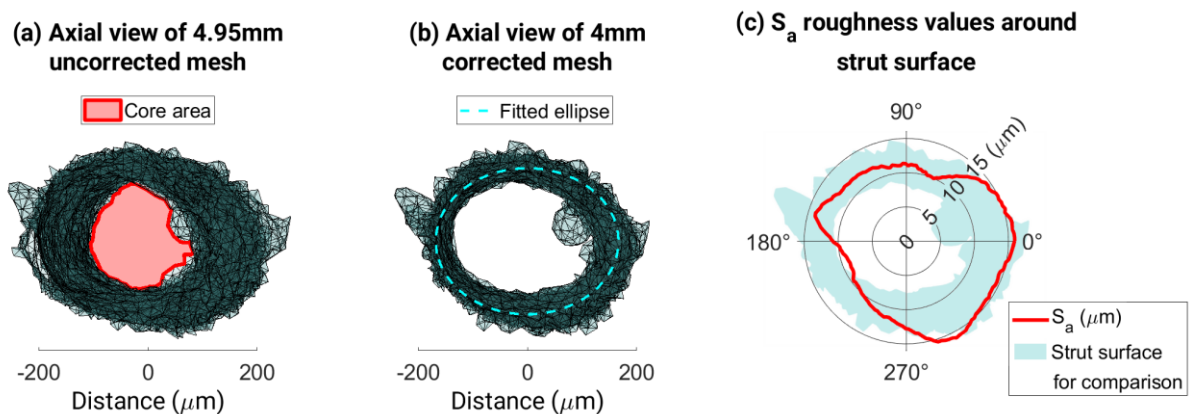


Figure 4.8: Process of calculating the core area, and the ideal elliptical prism representing the mean surface of the strut.

Dark green mesh shows the calculated surface of the strut, the inside is not a cavity, and is dense metal.

The absolute value of the deviation of each node in the mesh from this elliptical mean surface y_i was found. This was defined by the difference between the radial height of the node from the origin and the radial distance of the elliptical surface in the same direction to the origin. Then, the deviations of the nodes within a given angular span of 10° were summed and averaged over the number of nodes n queried. This calculation (shown in Equation 4.1) was made every 2° in an angular direction around the strut. The surface roughness S_a could then be provided for a particular angle, as shown in Figure 4.8c.

$$S_a = \frac{1}{n} \sum_{i=1}^n |y_i| \quad \text{Equation 4.1}$$

The mean and deviation of the surface roughness were also found to give average results for the whole strut surface.

Finding core area diameter

Another measure of the diameter was calculated for comparison to others. The core area diameter would be the diameter corresponding to the unobstructed area down the axis of the strut, which is consistent throughout the gauge length despite any eccentricity. To find this area, all faces of the outer surface mesh were projected to the X-Y plane and added together in a Boolean union operation. This resulted in one connected flat mesh geometry with an outer 'maximum' surface perimeter and 'minimum' unobstructed core perimeter, shown in Figure 4.8a. Only the start and end 0.025 mm were omitted, leaving 4.95 mm gauge length which the minimum area related to. This was to maximise the length of the strut that was used. The area of the inner core was found and a corresponding cylindrical diameter, D_{core} , was calculated for comparison to other diameter measurements, D_{avg} , D_{min} and D_{cal} . A summary of diameter measurements is shown in Table 4.4 below.

Table 4.4: Summary of diameter measurements for each strut

Diameter measurement	D_{core}	D_{min}	D_{avg}	D_{cal}
Description	Equivalent diameter of consistent inner core	Minimum equivalent diameter from strut mesh	Average equivalent diameter along strut	Maximum simulated Vernier caliper diameter

4.2.4 Tensile testing

209 of the 240 strut specimens were successfully scanned, meshed, and analysed using the methods discussed. 194 of these specimens were subject to uniaxial tensile tests to find their mechanical properties. Five replicates ($n = 5$) were required for each combination of material (SS316L or Ti6AL4V), build angle (20° , 40° , 70° and 90°) and designed diameter

(250 μm , 300 μm and 350 μm), a total of 120 specimens. The testing rig shown in Figure 4.9 was used in a uniaxial Instron 5570 testing machine with a 100 N load cell. The strain across the gauge length was measured on opposite sides using LVDTs (RDP D6/05000A) at 30 Hz, removing any systematic error due to machine compliance. Clip-on extensometers were deemed too impractical due to the small gauge length and diameter of the specimens, whereas using LVDTs allowed the specimen to remain undisturbed during testing. The average of these LVDT strain measurements were used in any properties that include strain in their calculation.

Specimens were gripped between two additively manufactured surfaces, a plate with a small ($\sim 100 \mu\text{m}$) 90° groove to align the specimen and a flat surface. The AM surface was unfinished to allow the rougher texture to aid in gripping. Plates with deeper grooves ($\sim 200 \mu\text{m}$) were used for larger specimens. The plate clamped down close to the strut in four locations, on approximately 10.4 mm of length on each end.

The alignment was checked visually using a camera before the test began (photo shown in close up in Figure 4.9). The camera field of view was aligned to the grips visually using the plate grooves, and the gauge length of the specimen was also visually checked to align with the camera field of view. A Canon 750D DSLR camera was used with a 24.2-megapixel CMOS sensor, and a 42 mm extension tube with 35 mm f/2.8 macro lens, resulting in an approximate horizontal FOV of 12 mm and an approximate vertical field of view of 7 mm. 1080p video allowed a pixel size of $\sim 6 \mu\text{m}$. Tests where failure had occurred inside of the grips or too close to the grips were discarded, to avoid inclusion of data where failure was influenced by stress concentrations at the grips. This occurred for 46 of the 194 tests. Video footage of each test was reviewed and slipping of the specimen was visually identified were discarded. 4 of the tests were rejected due to slipping.

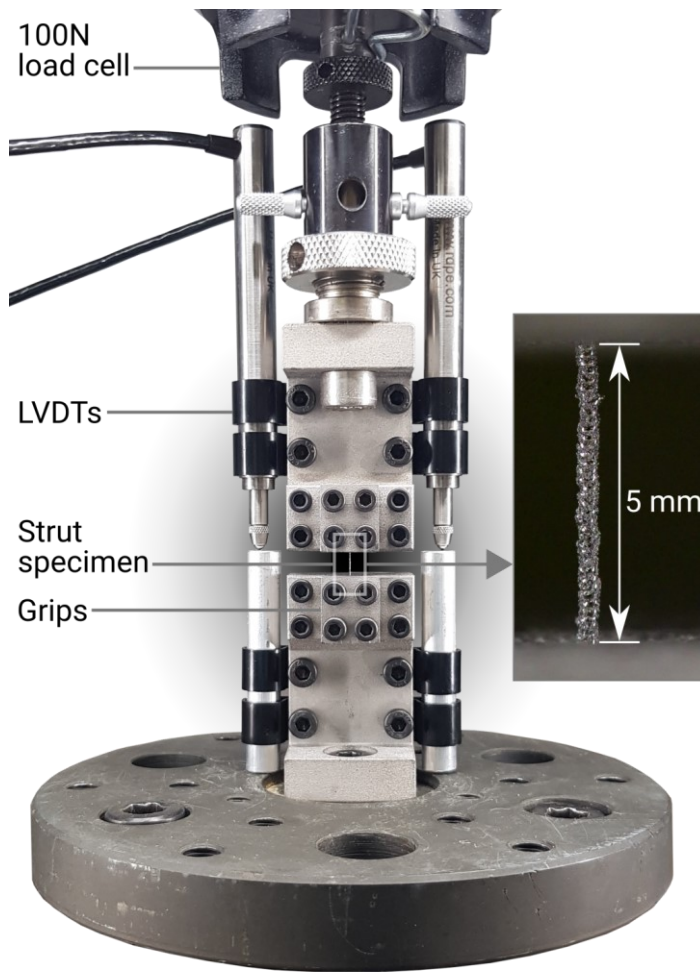


Figure 4.9:
Tensile testing rig using
linear variable differential
transformers (LVDTs).

Custom grips are shown with
5 mm specimen gauge
length, and connection to
load cell.

Quasi-static strain rates were used in testing, $1.67 \times 10^{-3} \text{ s}^{-1}$ for SS316L and $3.33 \times 10^{-4} \text{ s}^{-1}$ for Ti6Al4V specimens. These rates fall within range 2 and 3 of ISO 6892-1 A [243]. Due to the brittle nature of Ti6Al4V titanium alloy, a slower strain rate was used to capture more data within the elastic range of the test.

Specimens were loaded continuously until failure, and stress-strain curves were used to calculate the elastic modulus (E) of each specimen, using a linear regression on points in the elastic region. This region was defined as between 5 and 30% of the ultimate tensile strength (σ_{UTS}) for SS316L and between 10 and 50% for Ti6Al4V specimens. The yield strength (σ_y) was also reported for SS316L specimens, defined as the stress at a 0.2% strain offset from the elastic region of the curve. An example stress-strain curve for a SS316L specimen can be seen in Figure 4.10.

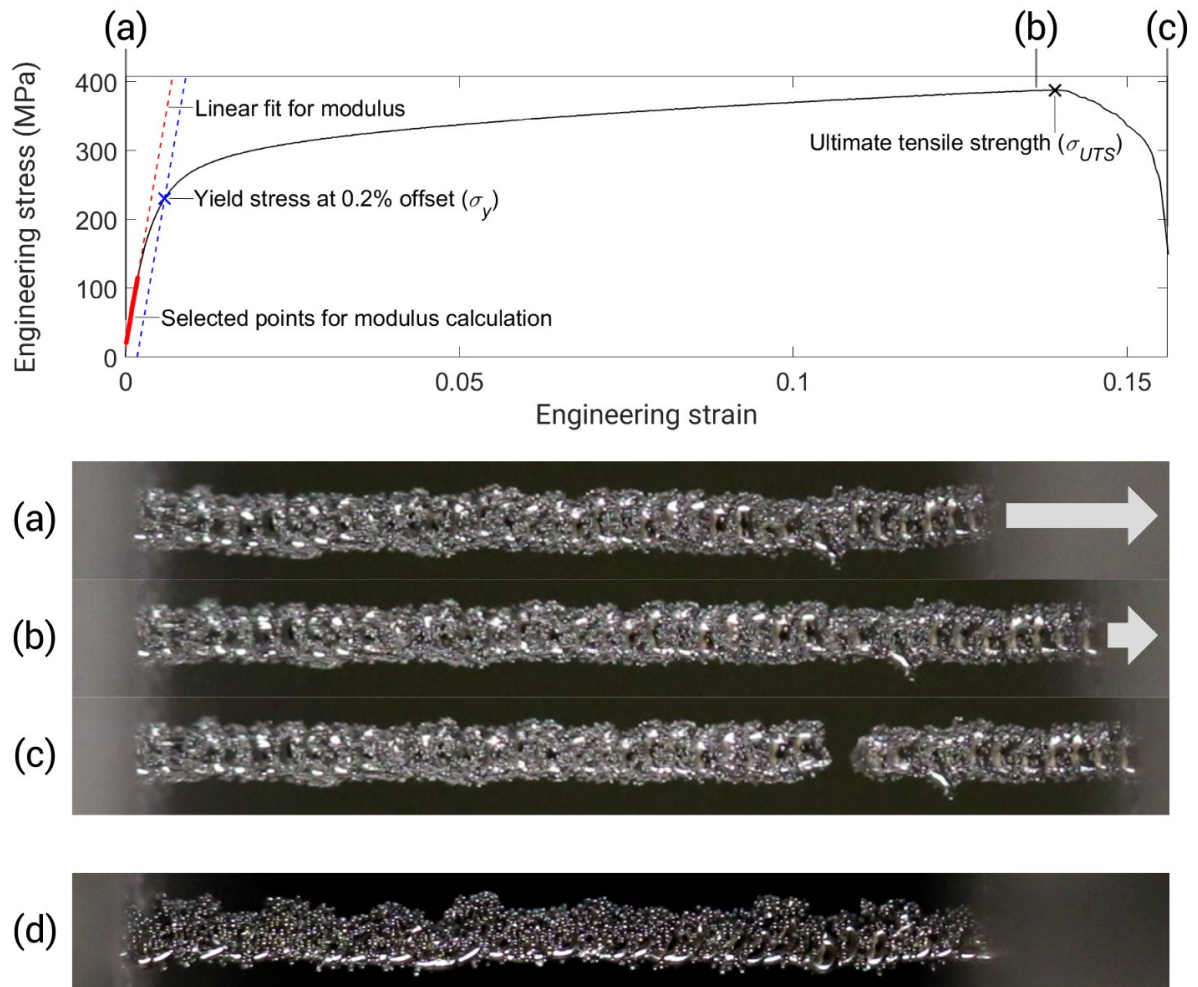


Figure 4.10: Example stress-strain curve for a stainless steel specimen.

SS316L specimen built at 20° to the build platform with designed diameter of 250 μm, (a) shows specimen in the beginning of the test, (b) just before necking, and (c) after fracture. (d) A Ti6Al4V specimen also built at 20° and with designed diameter of 250 μm.

The average diameter (D_{avg}) was used in calculations of the elastic modulus (E) of all specimens, and the minimum diameter (D_{min}) was used in calculations of the ultimate tensile strength (σ_{UTS}) and yield strength (σ_y). As the specimen could have a varying cross section unlike a standard tensile specimen, using the minimum area for properties involving yielding improved the accuracy of the measurement, as plastic deformation was more likely to occur at weaker points along the strut.

4.3 Results

All shading in the following figures (Figure 4.11 to Figure 4.18) represent the maximum and minimum results for the five replicates tested per variable combination.

4.3.1 Diameter measurements

A comparison between the different methods for measuring diameter are presented in Figure 4.11, where each are shown normalised by the calculated average diameter D_{avg} and displayed for each designed diameter. For both materials, D_{core} was consistently the lowest of the diameter measurements, whereas D_{cal} was the largest. D_{avg} and D_{min} fall between the two. The variance of the data tended to decrease as the designed diameter increases, suggesting less variation in the strut overall. The resulting diameters as manufactured were not always constant as a function of build angle, despite varying the laser exposure times to compensate for potential changes. The average difference across all struts between the manufactured average diameter D_{avg} and the designed diameter was an increase of 11.9% (s.d. 8.3%).

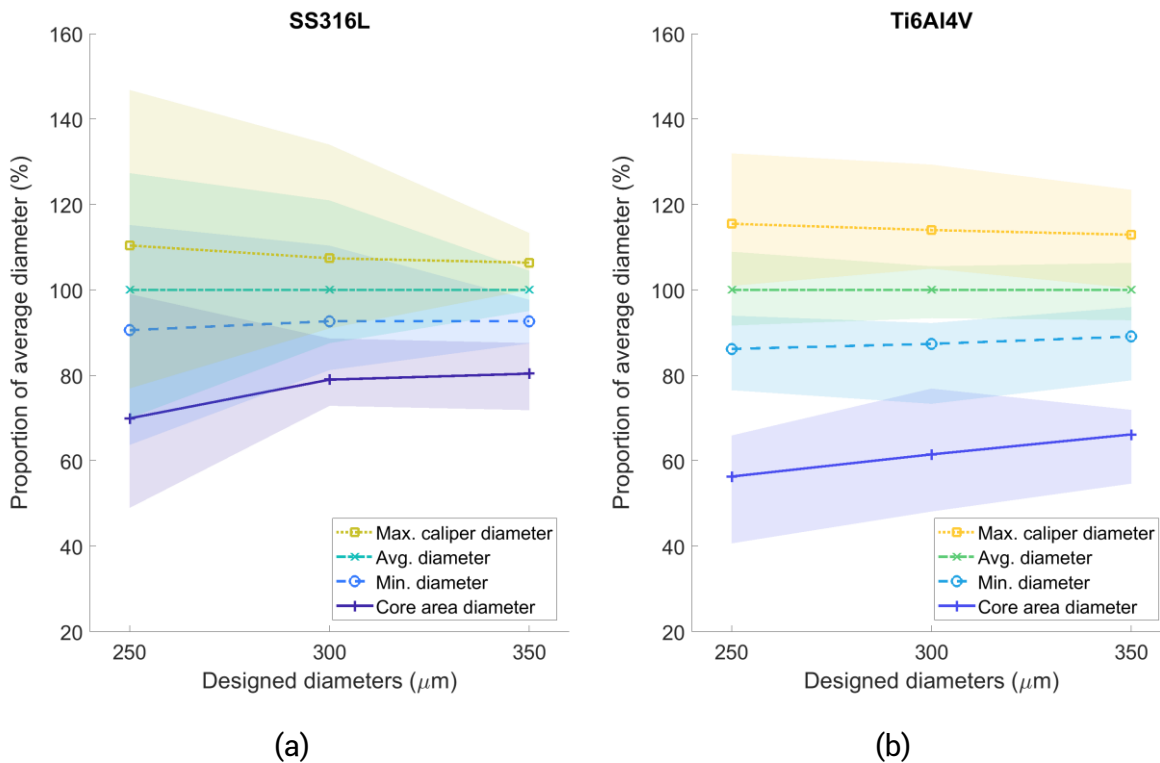


Figure 4.11: Comparison of diameter measurement methods per designed diameters of tensile specimens.

(a) SS316L and (b) Ti6Al4V struts, normalised by the average diameter. Shaded areas represent full range of results.

4.3.2 Strut morphology

Elliptical ratio

The average elliptical ratio ranged from 1.06 to 1.34 overall and was closer to unity at higher build angles, for all parameters. The results are shown in Figure 4.12 as a function of build angle with reference cross-sections on the y-axis. For both materials, the struts were less circular at lower build angles, possibly due to the increased overhang of successive layers when the struts were being built. However, Ti6Al4V struts showed slightly worse morphology than SS316L overall. The average value for the elliptical ratio across all struts was 1.17.

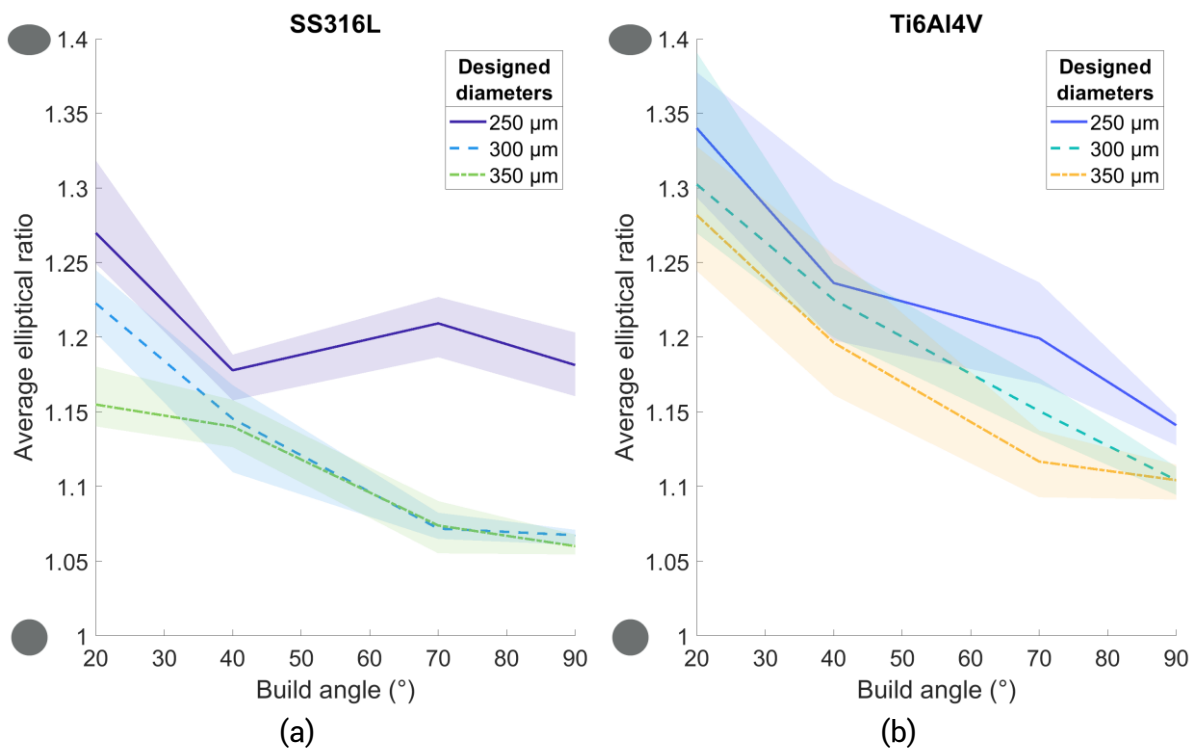


Figure 4.12: Changing elliptical ratio over build angle for strut cross-sections.

(a) SS316L and (b) Ti6Al4V struts. 1 is circular, and values above are progressively more elliptical. Shaded areas represent full range of results.

Roughness

Average S_a generally decreased at higher build angles for all parameters and materials, with a slight deviation for SS316L 250 μm struts built at 90° (Figure 4.13). Compared to Ti6Al4V struts, the variance of the SS316L data is lower. The average S_a roughness for Ti6Al4V struts was 18.6 μm , 1.89 times as rough as stainless-steel specimens. There was little difference in roughness between the different thickness struts for both Ti6Al4V and SS316L.

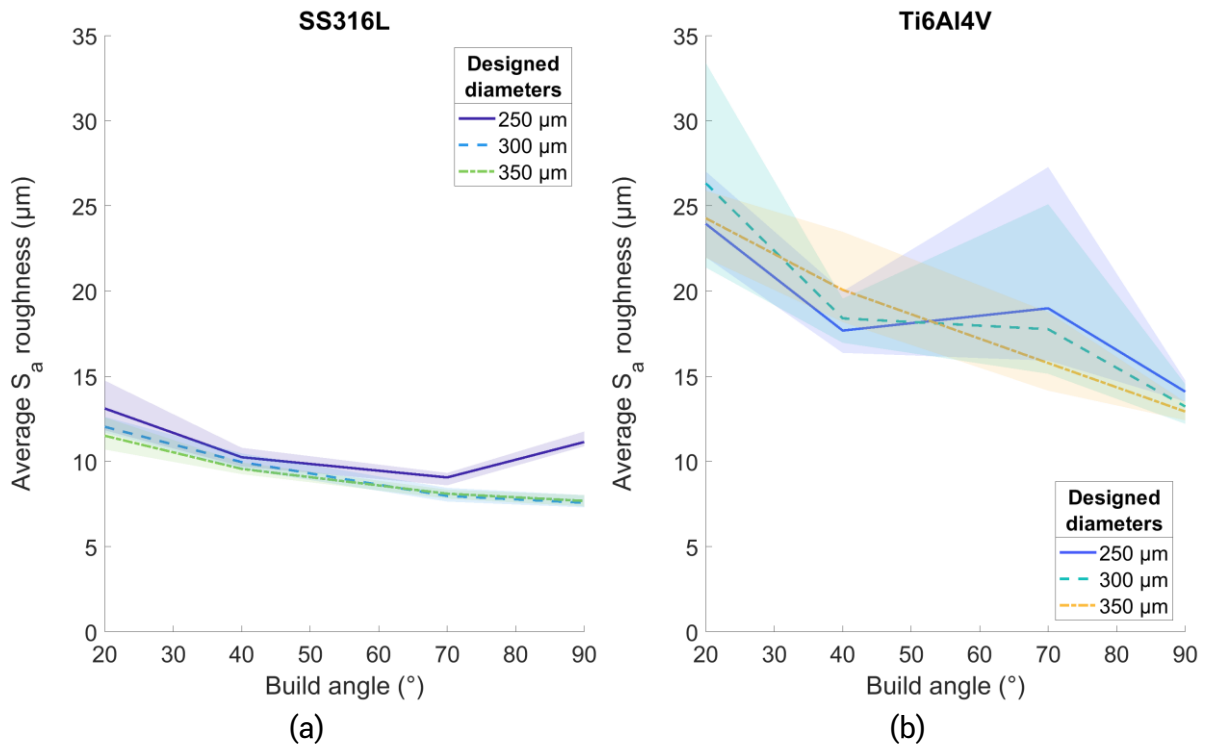


Figure 4.13: Average S_a roughness values (over entire strut surface) versus build angle.

(a) SS316L struts and (b) Ti6Al4V struts. Shaded areas represent full range of results.

Data for the eccentricity of struts can be found in the Appendix, section A1.1.

4.3.3 Tensile testing results

SS316L struts exhibited a ductile failure during testing (as in Figure 4.10), whereas Ti6Al4V struts failed in a brittle manner shortly after leaving the elastic regime. The mechanical properties have been compared to bulk values from Renishaw datasheets, where specimens made from additively manufactured material were tested in the 'Z' direction, parallel to the build direction [257,258].

Elastic modulus

The average value of E for SS316L was 61.5 GPa, 32% of the bulk value of 190 GPa [257] (Figure 4.14a). There was no clear trend for E changing with strut thickness or build angle. Calculating E using any of the diameter methods still gave a value below that of the bulk material, as shown in Figure 4.14b. For Ti6Al4V struts, average E was 37.5 GPa, 30% of the bulk value of 126 GPa [258] (Figure 4.15a). There was no clear trend for E changing with strut thickness or build angle. Calculating E using the core area diameter gave a value comparable to the bulk material, but the other diameter methods gave an E value below that of the bulk material (Figure 4.15b).

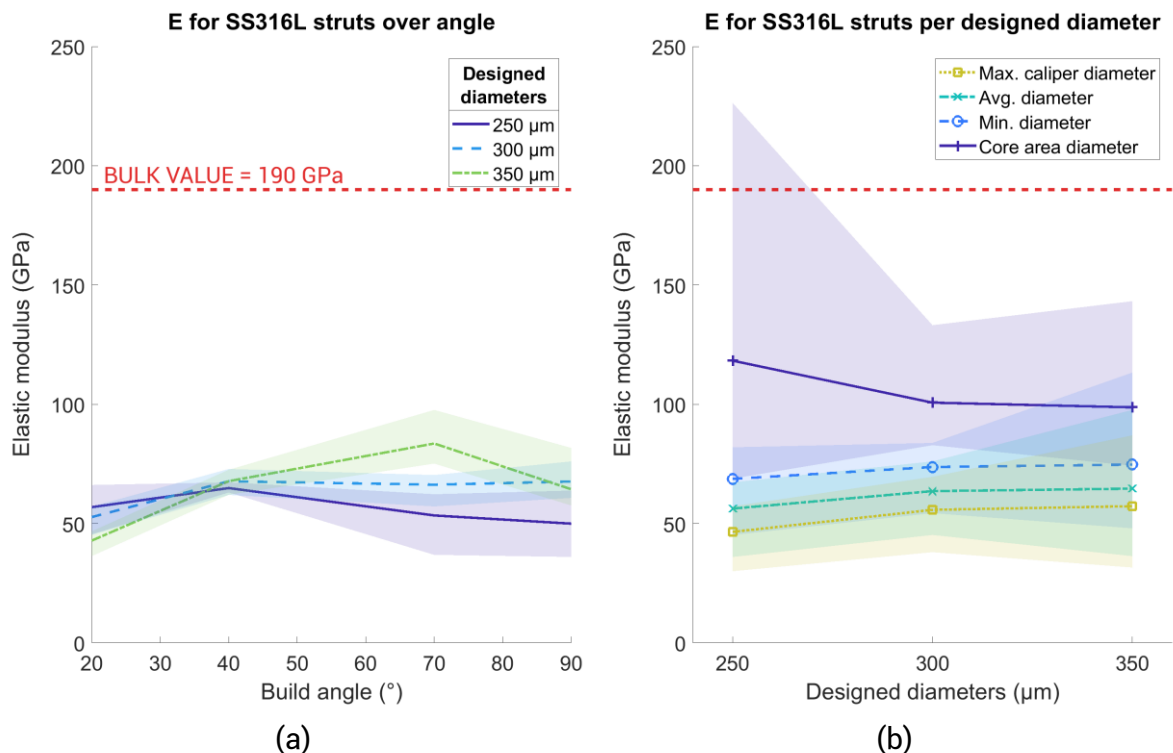


Figure 4.14: Elastic modulus (E) for SS316L struts.

(a) Variation over build angle, using average diameter and (b) change in E using different diameter values, over designed diameter. Bulk value shown with red dashed line. Shaded areas represent full range of results.

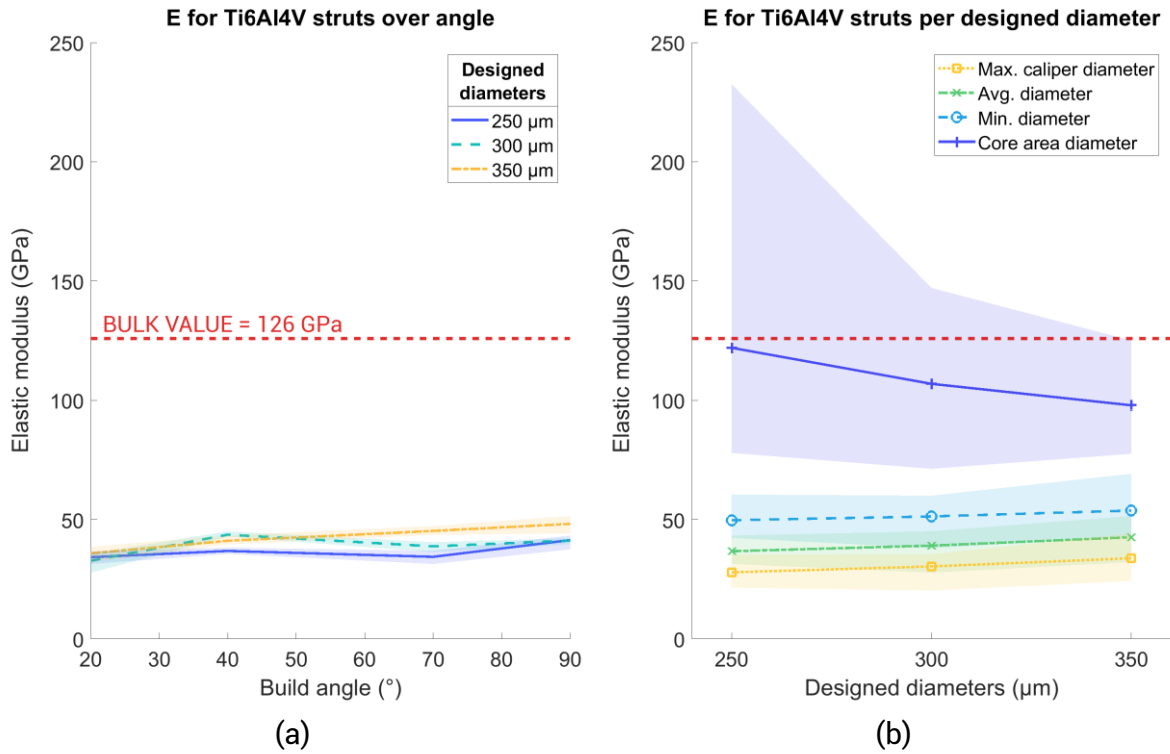


Figure 4.15: Elastic modulus (E) for Ti6Al4V struts.

(a) Variation over build angle, using average diameter and (b) change in E using different diameter values, over designed diameter. Bulk value shown with red dashed line. Shaded areas represent full range of results.

Ultimate tensile strength

For SS316L, the average σ_{UTS} across all struts, calculated using the minimum diameter, was 531 MPa, around 85% of the bulk value of 624 MPa [257], as seen in Figure 4.16a. There was no clear change in σ_{UTS} with either build angle or strut thickness. Using the core area diameter gave a σ_{UTS} value greater than σ_{UTS} of the bulk material, using the other diameter methods gave a σ_{UTS} less than the σ_{UTS} of the bulk material (Figure 4.16b).

For Ti6Al4V the average value of σ_{UTS} across all struts was 794 MPa, around 73% of the bulk value of 1085 MPa [258] as shown in Figure 4.17a. There is a trend for increased σ_{UTS} as a function of build angle, with the strongest specimens ($\sigma_{UTS} = 750$ MPa) built at 90° to the build plate and the weakest specimens ($\sigma_{UTS} = 290$ MPa) built at 20° to the build plate. There was no clear influence of strut diameter on σ_{UTS} . Using the core area diameter gave a σ_{UTS} value greater than the σ_{UTS} of the bulk material. Using the other diameters gave a σ_{UTS} less than the σ_{UTS} of the bulk material (Figure 4.17b).

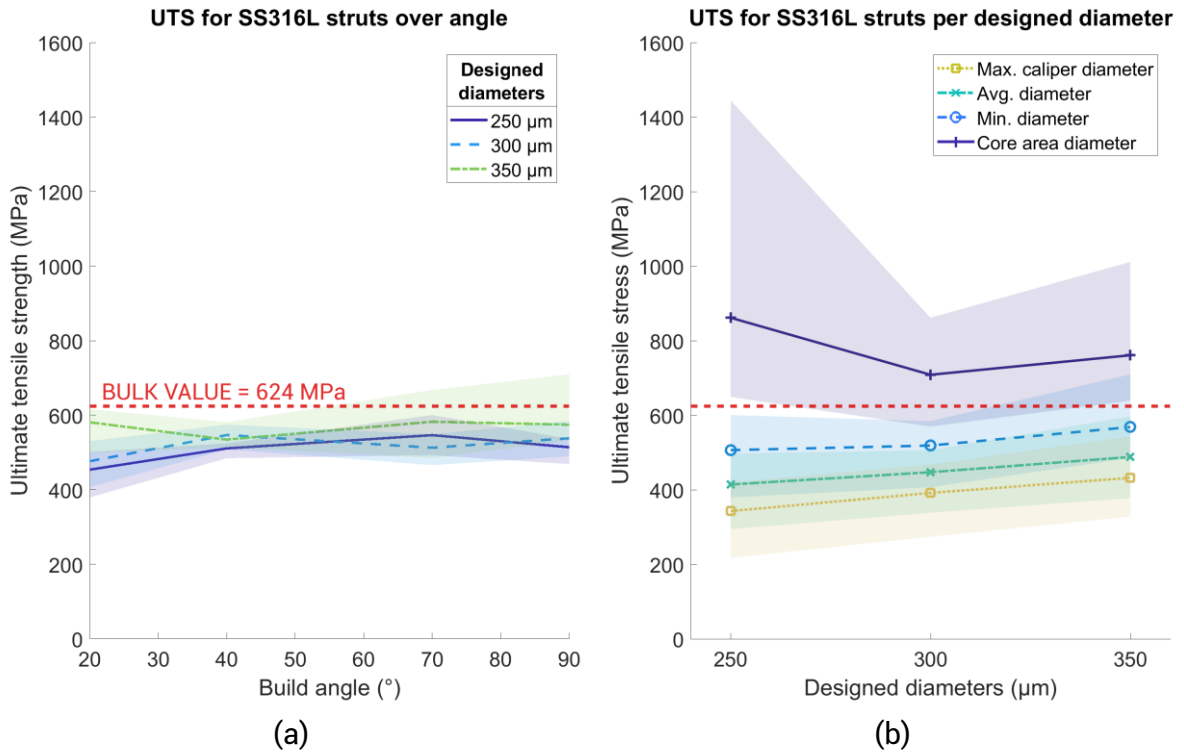


Figure 4.16: Ultimate tensile strength (σ_{UTS}) for SS316L struts.

(a) Variation over build angle, using minimum diameter and (b) change in E using different diameter values, over designed diameter. Bulk value shown with red dashed line. Shaded areas represent full range of results.

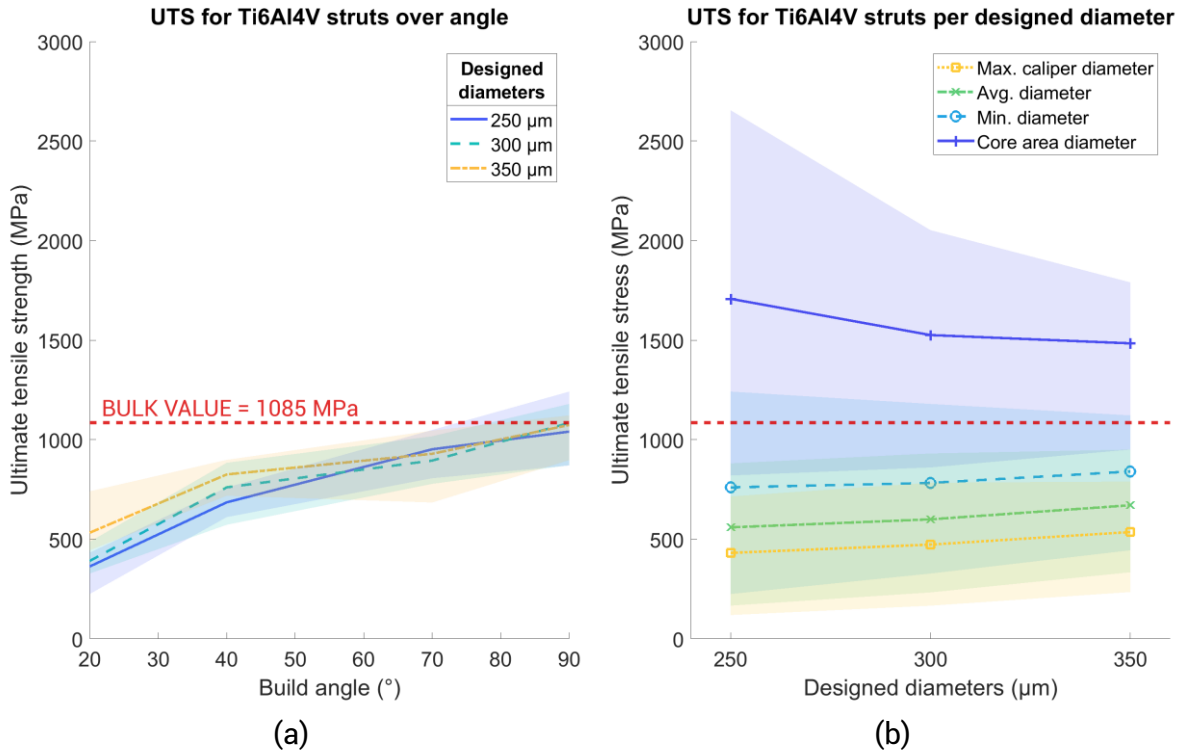


Figure 4.17: Ultimate tensile strength (σ_{UTS}) for Ti6Al4V struts.

(a) Variation over build angle, using minimum diameter and (b) change in E using different diameter values, over designed diameter. Bulk value shown with red dashed line. Shaded areas represent full range of results.

Yield strength

The yield strength σ_y , calculated using the minimum diameter, is shown as a function of build angle in Figure 4.18a for SS316L struts. The average σ_y found across all struts was 318 MPa, proportionally 64% of the bulk value of 494 MPa [257]. There was no clear relationship between σ_y and strut diameter or build angle. Calculation of σ_y using the core diameter gave values higher than exists for the bulk material, for 250 μm struts, while the other diameter methods underestimated σ_y compared to the bulk material (Figure 4.18b).

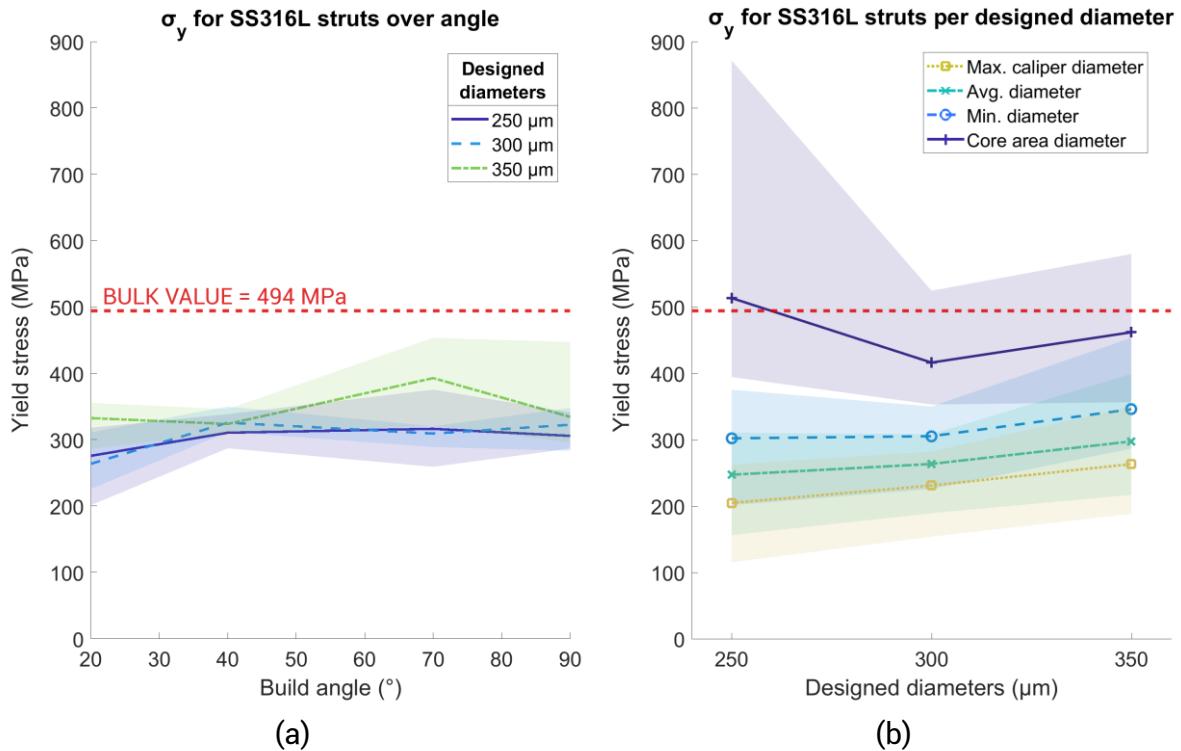


Figure 4.18: Yield stress (σ_y) for SS316L struts.

(a) Variation over build angle, using minimum diameter and (b) change in E using different diameter values, over designed diameter. Bulk value shown with red dashed line. Shaded areas represent full range of results.

4.4 Discussion

The most important findings of this work are that the elastic modulus of both the AM SS316L and Ti6Al4V material, and the strength of the SS316L material, did not change as a function of build angle or strut diameter. The strength of the Ti6Al4V material was not affected by diameter but was affected by build angle, more than doubling for a strut built at 90° compared to one built at 20° as shown in Figure 4.16. For both materials, as the build angle increased, the surface roughness decreased, and the circularity increased. This relationship was more pronounced for the Ti6Al4V material. The Ti6Al4V struts were less ductile than the SS316L struts and the increased surface roughness and associated stress concentration points may

explain the increased sensitivity of strength to build angle. This work also demonstrated how the definition of strut diameter affects all the properties and may partly explain the reduced stiffness of the struts compared to the parent material.

The mechanical properties calculated for SS316L and Ti6Al4V struts are comparable to those found in the literature (Table 4.1 and Table 4.2). For SS316L struts, the elastic modulus was calculated as 61.5 GPa, 32% of the bulk value, lower than the previously reported results 71 GPa, 84 GPa and 140 GPa (37%, 44% and 74% of the bulk value respectively) [201,203,204,240]. The elastic modulus is highly sensitive to how the cross section of the strut is measured, and this may explain some of the variation. Previous work has investigated the impact of diameter on the microstructure and mechanical properties of vertically built SS316L struts, testing diameters from 0.25 mm to 5 mm [339]. Struts with a sub-millimetre diameter had a reduced microhardness, and the yield strength also decreased with diameter. The elastic modulus was not reported, however the effects of changing microstructure in SS316L micro-struts may also explain the variation in reported stiffness.

The yield stress σ_y found for SS316L struts of 318 MPa is in the range of values previously reported, between 144 and 380 MPa [201,339]. The ultimate tensile strength has been reported for SS316L struts as 450 MPa and 575.3 MPa [204,240], which bounds my value of 531 MPa. The higher values for E and lower values for σ_y may be due to the average diameter D_{avg} for calculating E and a lower value of the diameter used for yield related mechanical properties, D_{min} . The true effective diameter of these varying struts probably falls somewhere between these two values. For E , variation in the strut makes it less stiff than a completely straight and consistent beam with the same average diameter. so D_{avg} may be an overestimate. For σ_y , yielding may occur at a few different sites along the beam that are thicker than D_{min} , the minimum diameter along the beam.

Less data exists for Ti6Al4V struts, although the elastic modulus E has been calculated before as 102 GPa and 107 GPa, 81-85% of the value [241,242], which is higher than our value, calculated as 37.5 GPa, 30% of the bulk value. The methods used in this chapter for strain measurement (LVDTs) did not require machine compliance correction though the modulus is still lower than that found using optical methods [242]. These differences may be related to how the cross section is measured. Previous work has used a correlation between maximum caliper diameter or Feret diameter and the average diameter as observed in sectioned struts by SEM. It is possible that the diameter is underestimated with this method as compared to using micro-CT. It is also possible that there is a difference in Ti6Al4V microstructure, as the struts in work by Wang et al. were built using a laser power of 120 W,

whereas the struts in this work were built at 50 W (Table 4.3). Ti6Al4V lattices have been shown to be slightly stiffer in compression when built at 200 W versus 50 W [162]. Microhardness of laser PBF Ti6Al4V has also shown to increase with increased energy input [348,349]. The average value of 1066 MPa for the ultimate tensile stress (σ_{UTS}) of Ti6Al4V struts built at 90° compares well with the value of yield stress found by Wang. et al. of 997 MPa, as the struts in this work failed immediately after yielding.

Methods for quantifying differences in diameter measurement have been conducted by Suard et al. [249], who described two kinds of measurement of their struts. A 'geometrically equivalent cylinder', (notionally similar to the core diameter D_{core} in this work) was calculated, and a 'numerical equivalent cylinder' was found by conducting FEA on voxelized models of their strut specimens, and a 'numerically equivalent diameter' was found from this FEA effective stiffness. These were both smaller than the nominal designed diameter, consistent with the results in Figure 4.11. Their differences in diameter measurement also varied over build angle. The comparison between a Vernier caliper or Feret diameter and the true diameter has also been explored before, showing an overestimation [242].

The elliptical ratio and how it changes over build angle has also been explored [191,245,248,249]. It has been shown to vary from 1 to 2 when building Ti6Al4V struts using EBM manufacturing [249], and as averaging at ~ 1.15 for Ti6Al4V struts built using powder bed fusion at 45° [248]. The trend towards circular cross sections as the strut is built closer to 90° is well confirmed in this work, and an average elliptical ratio 1.17 is within the established range. Similar variations in the cross section have been reported for AM struts built using aluminium alloy AlSi10Mg [191,245].

The roughness of Ti6Al4V laser PBF struts have also been shown to vary over build angle [248,260,340]. Weißman et al. showed that struts built at 90° and 45° had significantly different R_a values ($p < 0.001$), with higher roughness values at 45° [248]. Alghamdi et al. showed a similar trend [260]. The Ti6Al4V struts in this work also decreased in roughness at a higher build angle as shown in Figure 4.13b. Further results showing the variation of eccentricity with build angle bear some similarity to the trends for roughness. These data can be found in the Appendix, A.1.1.

This chapter investigated the effect of build angle and strut diameter on material properties, but other variables such as wiper blade direction, support of the strut in the print (how likely it is to move in the printing process) and availability of heat dissipation all may play a part in changing the morphological properties of the strut. Another limitation is that specimens were printed as one long 25.8 mm strut. Struts as part of a lattice normally have nodal connections

that support the strut in the build process and may have different morphological properties as a result. However, for accurate measurement of mechanical properties enough length was needed to grip the specimen. Another limitation was the use of varying laser exposure times to compensate for the changing build angle and maintain a consistent diameter did not work as expected, and the diameter of manufactured specimens did vary. However, the mechanical and morphological properties reported are on a per strut basis and account for any variation. Other mechanical properties such as fatigue strength are also important to find, for the purpose of building useful lattices with satisfactory performance *in vivo*. However, these were not covered within this chapter. As fatigue strength would be flaw dominated, there may be a greater impact on performance due to build angle.

LVDTs were used in this work instead of optical methods to measure elongation of the specimen. These are equivalent, assuming that the grip of the specimen is adequate to avoid slippage. Only specimens with no visible slippage were included in the study after reviewing footage of the test and assessing the stress strain curves for any evidence of slipping.

Digital image correlation (DIC) methods were also investigated in the preparation of this work as a method to capture strain along a strut as it was being tested. Figure 4.19 shows that the axial strain varies along the gauge length and plastic strain accumulates at various points prior to failure. However, LVDTs were still chosen as the final method of measurement, as accurate DIC requires maintaining good parallax and consistent lighting for all 120 specimens, as well as time consuming data analysis. This was ultimately prohibitive.

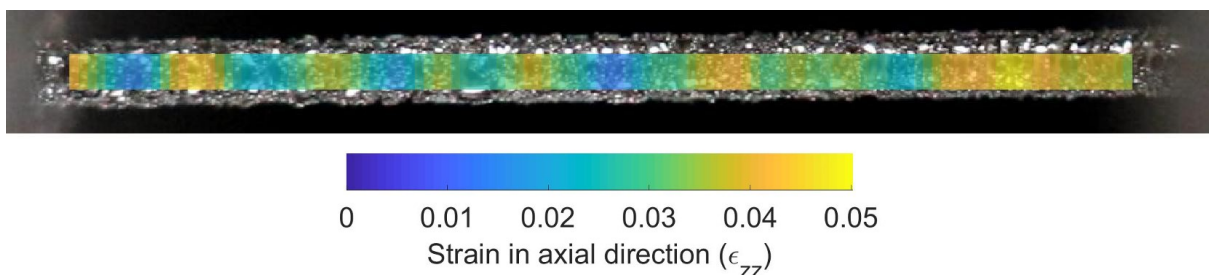


Figure 4.19: Digital image correlation (DIC) strain map for a SS316L tensile specimen.

Specimen was a parameter C strut built at 70°. The varying axial strain across the gauge length of the strut is shown. The gross/nominal strain of the specimen was 0.0319.

A final limitation is that the calculation method for the roughness value S_a is closer to an area roughness value and is not directly comparable to an R_a value that is captured using more sophisticated and dedicated hardware. This value can still be used however to compare between struts within this work. As the value comes from interrogating the mesh of each strut, the measure is still subject to any deviation of the mesh from the true metal surface,

although the element size was picked to capture sub-particle details. Similar micro-CT and mesh based roughness measurements have been used in the literature [340,350].

The outcome of this work has presented a detailed study on the effects of build angle and strut morphology on the mechanical properties of individual struts. For steel struts, the material strength is uniform across build angles and diameters, but for titanium the strength is highly dependent on build angle, being stronger at more vertical build directions. The lower angle struts have worse morphology, being rougher and less circular in cross-section, which may explain weaker titanium at lower build angle where imperfections in surface may contribute to a lower tensile strength. These data should help inform the design and manufacture of AM lattices by allowing struts at different angles to be assigned stiffness and strength properties based on these experimental measurements. For lattices that may be used in safety critical applications like implantable medical devices, extra care must be taken to compensate for mechanical properties that may be below the bulk value, and change depending on orientation of the lattice to the build direction.

5 Compression testing of structures

Additive manufacturing (AM) enables fine control over the architecture of porous lattice structures, and the resulting mechanical performance. Orthopaedic implants may benefit from the tailored stiffness/elastic modulus of these AM biomaterials, as the stiffness can be made to closer match the properties of the replaced trabecular bone. This chapter used laser powder bed fusion (PBF) to create stochastic porous lattice structures in stainless steel (SS316L) and titanium alloy (Ti6Al4V), with modifications that aimed to overcome PBF manufacturing limitations of build angles. The structures were tested in uniaxial compression ($n = 5$) in 10 load orientations relative to the structure, including the three orthogonal axes. The testing verified that no hidden peaks in elastic modulus existed in the stochastic structure that occur in unit cell based lattices, causing unwanted mechanical performance. The stiffness of the lattices in directions close to horizontal were improved when made in SS316L. The range of stiffness results in the different directions decreased for both materials, indicating the structures were more isotropic. These modified stochastic lattices have similar stiffness to cancellous bone and have controllable anisotropy, giving them the potential to be used within implants which match the stiffness of trabecular bone.

The work in this chapter has resulted in a patent application, filed on the 6th April 2020. The application details are as follows.

UK Patent Application No 2005050.6

Stochastic lattice structure with isotropy in axial loading

Imperial College Innovations Ltd.

Further details can be found in Appendix A2.2.

The work in this chapter has been accepted for publication in Additive Manufacturing.

5.1 Introduction

Additive manufacturing (AM) methods enable fine control of porous lattice structures [172,201,337,351,352]. This control allows the internal architecture of an additively manufactured component to be determined and optimised for specific mechanical performance, such as tailored stiffness properties [228,353]. Orthopaedic implants stand to benefit from this AM design opportunity [15,327]. Normally made through casting or CNC of biocompatible alloys such as titanium or cobalt-chrome, implants have a bulk elastic moduli much higher than that of bone [15,55]. Stress shielding can occur due to this mismatch in implant and bone properties, causing bone resorption in the stress shielded zone [72]. These alloys could be printed instead using AM methods such as powder bed fusion (PBF) to achieve porous lattices with elastic moduli more comparable to bone [195,215,331,332].

Commercially, there are many examples of implants using AM methods for reconstructive surgery in the orthopaedic field [170,354,355]. For example, patient-specific implants are successfully manufactured by Stanmore Implants [169] using AM. There is also growing popularity of mass produced AM implants, for example Stryker's Triathlon Titanium Knee system [16]. However, although the AM method is now common, it has not been used to manufacture implants with a similar stiffness to bone. This would be highly beneficial as it could prevent the undesirable stress shielding phenomenon, but such a design would require a comprehensive understanding and control of lattice structure and elastic isotropy.

Examples of this control include optimising the lattice porosity for minimum bone resorption and interface failure [222–224]. Graded lattices for bone scaffold applications have also been created using various initial unit cells, with elastic moduli comparable to bone when tested in one direction [195,236]. However, the repeating unit cell design of these lattices means they have an inherent anisotropy that may not be desired for bone stiffness matching [172]. The stiffness of a cubic lattice structure can vary by over 5 times depending on the orientation [166,172], whilst the stiffness of other unit cells can vary by over 6 times at different orientations [207]. This is a cause for concern as porous lattices are often used as 'space-filling' geometry within a component.

Lattices that aim to control stiffness anisotropy have been developed in the fields of lightweighting and structural mechanics. One study achieves stiffness isotropy, by mixing plate-based unit cells [173]. However, the final structures are closed-cell, preventing bone ingrowth, and manufactured using an AM method not applicable to biomaterials. Other theoretical unit cells have addressed this issue [172,216] but in the absence of multi-direction mechanical confirmatory testing to rule out AM printing limitations. An alternative

repeating structure similar to a Schwarz-P minimal surface unit cell has demonstrated isotropic behaviour in both theoretical models and mechanical testing, but the surface structure may not be suitable for a bone ingrowth orthopaedic application [182].

Anisotropy also occurs due to differences in print quality at low build angles. This is apparent when the build orientation is varied with respect to the unit cell orientation in compression tests [214,259,356]. The stiffness properties of individual struts in a lattice can vary more widely than fully solid printed metal. Tensile tests have shown a difference in mechanical properties [201] and strut morphology [249] for struts printed at different angles (a full exploration of which was conducted in the previous chapter). However, all examples of anisotropy in lattices focus on repeating unit cell structures. There is an increasing interest in stochastic structures with controlled anisotropy [217], but little data exists on the anisotropy of such structures when printed using PBF.

An isotropic stochastic lattice has the potential to avoid the pitfalls of anisotropic unit cell geometry. By varying the density of the stochastic lattice, a better match could be achieved with the changing modulus of bone at different anatomical locations [315]. However, the testing of such structures needs to be conducted in multiple directions to demonstrate that stiffness isotropy is improved relative to periodic unit cell based structures. Thus, the aim of this chapter is to investigate the anisotropy of a stochastic lattice structure and potential methods to prevent the anisotropy that occurs due to AM limitations.

5.2 Materials and methods

5.2.1 Specimen design and manufacture

A stochastic structure was created by populating a volume with pseudo-random points using a Poisson-disc algorithm. The points were then joined by lines (struts) subject to three parameters:

1. The number of connections to make at a node
2. The minimum length of a connection
3. The maximum length of a connection

These were varied such that a certain 'connectivity' was achieved, defined as the number of struts terminating at a given node. This method, which uses Rhinoceros 5.0 and Grasshopper (Robert McNeel & Associates) was described by Ghouse et al. [162].

With both bone ingrowth and vascularisation in mind (see section 2.3.3 of the Literature review), the minimum distance that was allowed as a strut connection was 0.4 mm, allowing space between nodes and creating a pore size of around 400 μm .

The density of the structure was 4.06 struts/mm^3 and with an average connectivity at each node of 5.80, after varying the three parameters listed above. This was found through trial and error testing to be an adequate density to be printed correctly, i.e. without parts of the structure lacking support due to lack of connection between struts.

Stochastic structure variations

Three variants of the stochastic structure were generated. The first variant, variant A, was as described above with no further action, including horizontal or low angle struts relative to the build direction (see Figure 5.1a). A second variant, variant B, was created where all struts with an angle less than 25° to the horizontal plane were identified as 'close to horizontal' and potentially prone to building poorly (shown in pink in Figure 5.1). These struts are split into two parts and redrawn in a 'kinked' configuration, such that the strut subtends the same points but now kinks upwards to increase the angle of the strut to the horizontal, to at least 25° (Figure 5.1b). A third variant, variant C, was created where in addition to the kinked horizontal struts, all remaining struts with an angle more than 25° to the horizontal direction (identified as 'vertical' and highlighted in blue in Figure 5.1) were kinked to an angle matching the average resulting angle of the horizontal kinking in the second variant (Figure 5.1c).

The critical angle of 25° was chosen after conducting pilot testing using SS316L. Full details of this pilot testing is included in the Appendix, section A2.1. Other angles that were investigated included 20° and 30° .

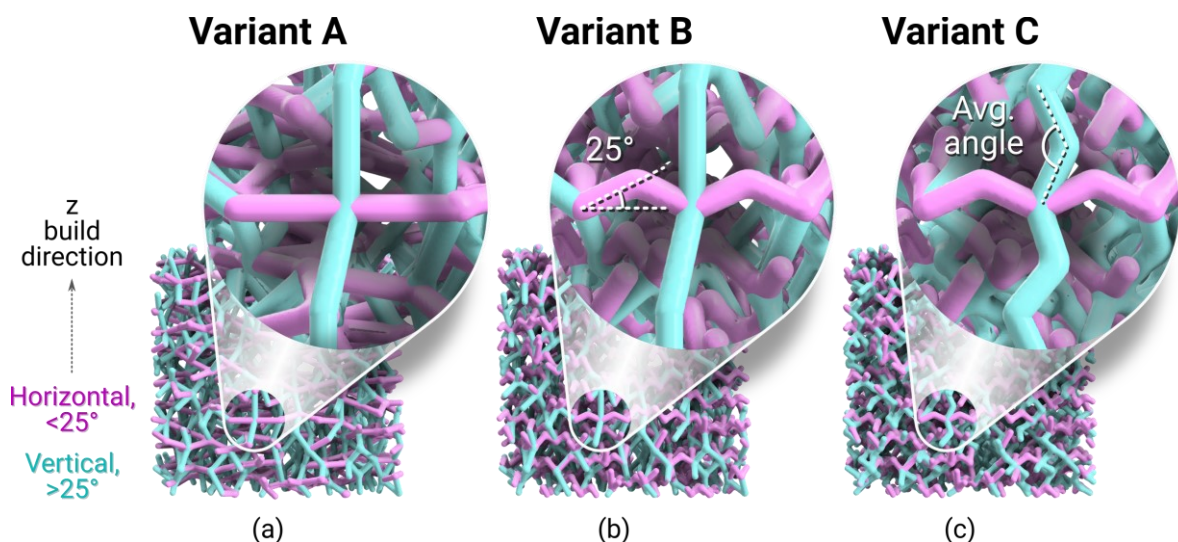
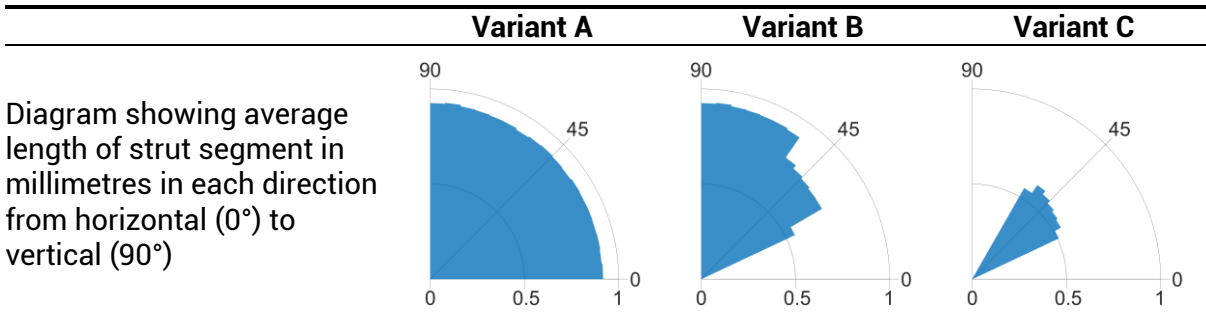


Figure 5.1: Stochastic structure variations.

(a) Variant A, no change, (b) variant B, horizontal struts kinked, and (c) variant C, vertical struts also kinked. Struts in pink are classed as 'horizontal', with an angle to build platform of less than 25° . All other struts in blue are classed as 'vertical'.

The resulting change in the distribution of strut 'directions' in each variant of the lattice structure is shown in Table 5.1 below. It is important to note that the node locations, strut density and average connectivity remained the same between variants.

Table 5.1: Comparison of each variant and the distribution of struts in each direction



The precise logic for the initial kinking of the structure, and the subsequent kinking of all the structure to an 'average angle' is detailed further in Figure 5.2.

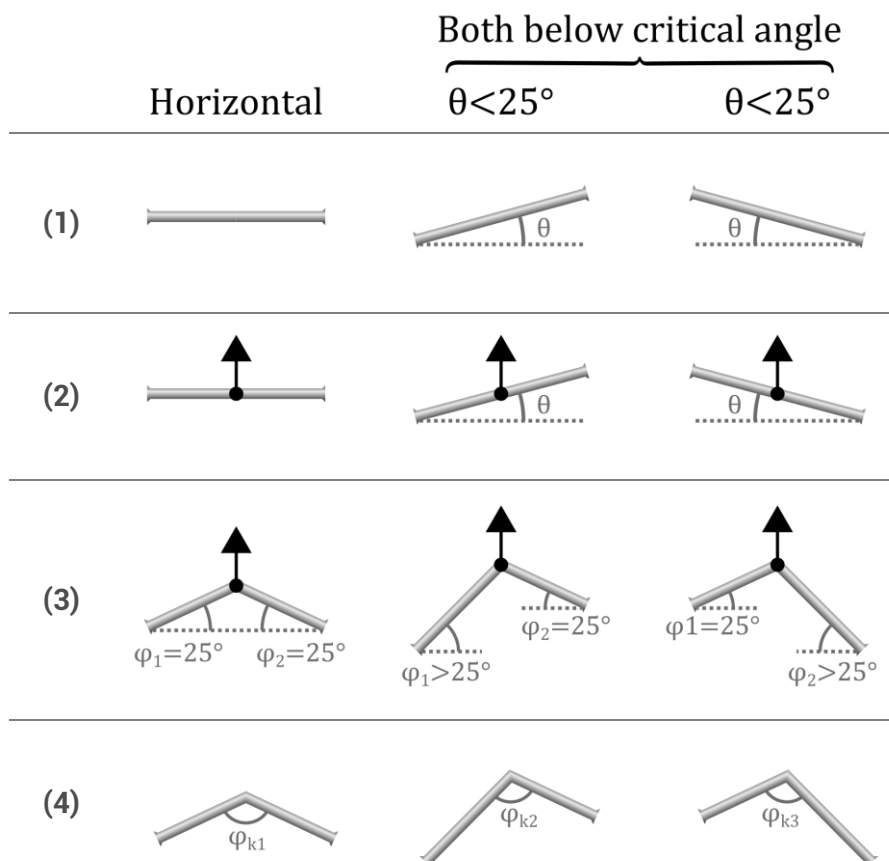


Figure 5.2: Detailed process description for creating structure variant A, B and C

The steps in Figure 5.2 are clarified as follows:

- 1) Shown are 3 struts that are close to the horizontal plane. These are struts that have an angle to the horizontal θ of less than 25° , the critical angle.
- 2) A point in the middle of the strut is selected for the split into two parts to occur. This point is moved directly upwards.
- 3) The point is moved upwards until the following condition is satisfied: both φ_1 and φ_2 are larger than the critical angle 25° . Notice that the angle to the horizontal of the 'lower' half of the strut will reach 25° first, and the movement is stopped when the higher half reaches 25° . For a truly horizontal strut, both angles will be the same.
- 4) The average angle of the kinking φ_k is found from the resulting distribution in the population of struts close to the horizontal, for use in the third structure variant. In the diagram you can see a range of kinking angles φ_{k1} , φ_{k2} and φ_{k3} due to range of struts included in the original population.

Printed specimens

Cuboid compression specimens were generated containing the structure variants aligned in 10 different directions to the testing axis (Figure 5.3). Five specimens were tested per direction. Specimen dimensions were 10 x 10 x 12mm and conformed to ISO 13314:2011 [238].

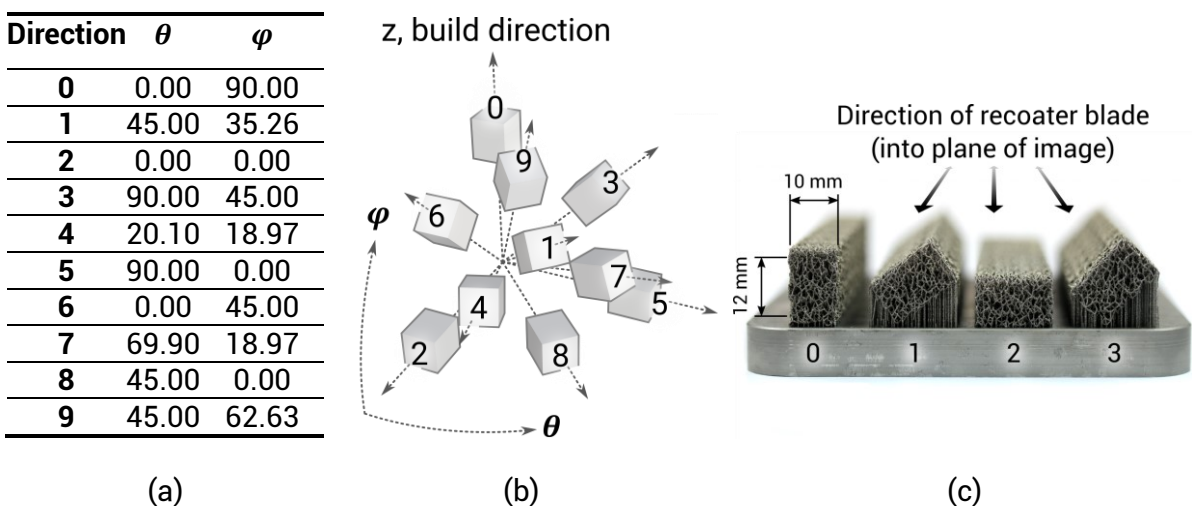


Figure 5.3: Test directions for uniaxial compression of structures.

(a) Spherical coordinates, (b) specimen orientations and (c) printed specimens. Airflow direction is from left to right, perpendicular to recoater blade direction.

5.2.2 Materials and manufacturing

Solid STL geometry is usually printed using a contour-hatch printing strategy [162]. For this small-scale line geometry, the contour-only method was used to melt the required cross section of each strut as described by Ghouse et al. [162]. Contours are traced with individual points, holding the laser at a point for a specified exposure time and then moving to the next point in the sequence. Slice data (build files) were generated at 50 μm layer thickness using Material Engine 1.0 (Betatype Ltd).

All specimens were printed using a Renishaw AM250 PBF additive manufacturing system. Both stainless steel (SS316L) and titanium alloy (Ti6Al4V ELI, Grade 23) spherical powder of particle size range 10–45 μm were used to create specimens, supplied by Carpenter Additive Ltd and Renishaw plc respectively. The build chamber was vacuumed to -960 mbar and then back filled with 99.995% pure Argon to 10 mbar with an O content of $\sim 0.1\%$. For SS316L, laser power was constant at 200 W whilst exposure times varied from 30 to 60 μs to maintain a constant strut thickness. For Ti6Al4V, laser power was constant at 50 W whilst exposure times varied from 100 to 150 μs .

Specimens were removed from the buildplate using wire erosion, ensuring that the wire path preserved the intended part geometry, then cleaned using an ultrasonic bath and air jet. Each specimen was individually measured thrice in each dimension using Vernier callipers and averaged, and dry weighed thrice at normal atmospheric conditions and averaged. The relative density was then calculated by dividing the average specimen weight by the bulk weight of the metal that corresponds to the average specimen macro volume. A density of 8.1 g/cm^3 was used for SS316L and for Ti6Al4V ELI, 4.42 g/cm^3 . A selection of Ti6Al4V specimens to be tested in direction '0' were imaged using a Hitachi S-3400N scanning electron microscope to compare the structure variations.

5.2.3 Mechanical testing

A materials testing machine (Instron 5570) with a 10 kN load cell was used to perform quasi-static compression testing at an strain rate of 2 mm/min, which corresponds to a strain rate within standard limits [238]. Displacement was measured using LVDTs to remove any compliance effects from the test apparatus. A sampling rate of 30 Hz was used. The platens of the machine were lubricated to remove any frictional effects. Stress-strain curves were obtained using the individual macro dimensions of each specimen.

The loading regime includes a single cycle of loading/unloading (loading loop) to account for localised yielding within the porous structure. This was carried out from 70% of the yield stress (σ_{70}), to 20% of the yield stress (σ_{20}) and the specimen was then fully compressed to

a high strain [238]. A preliminary specimen was compressed to 50% strain at 2 mm/min to find the required reference stresses for both materials. The elastic modulus was then calculated using a linear regression analysis of the loading loop. For all specimens, the 1% offset yield stress was calculated to define the yield properties, as recommended by ISO standard 13314:2011(E) [238]. The strength to stiffness ratio was also calculated to see if the modifications to the structure affected one property more than the other. To quantify the variation in the results over each direction, the standard deviation for each variant was also calculated for each mechanical property.

5.3 Results

Table 5.2 details the average outer dimensions of the final specimens built SS316L and Ti6Al4V, as well as the relative density of the final specimens. These values are compared to the intended dimensions and average intended relative density, calculated using the volumes of the CAD geometry of all designed specimens.

Table 5.2: Manufactured specimen dimensions compared to intended dimensions

Specimens	Average width \pm SD (mm)	Average depth \pm SD (mm)	Average height \pm SD (mm)	Average relative density \pm SD (%)
Intended	10 \pm 0	10 \pm 0	12 \pm 0	12.57 \pm 0.73
SS316L	10.25 \pm 0.20	9.76 \pm 0.22	11.95 \pm 0.04	13.00 \pm 0.98
Ti6Al4V	10.00 \pm 0.20	10.23 \pm 0.20	11.95 \pm 0.05	12.51 \pm 0.48

5.3.1 Mechanical testing

Example stress strain curves for a variant C specimen in direction '0' is shown in Figure 5.4, for both materials.

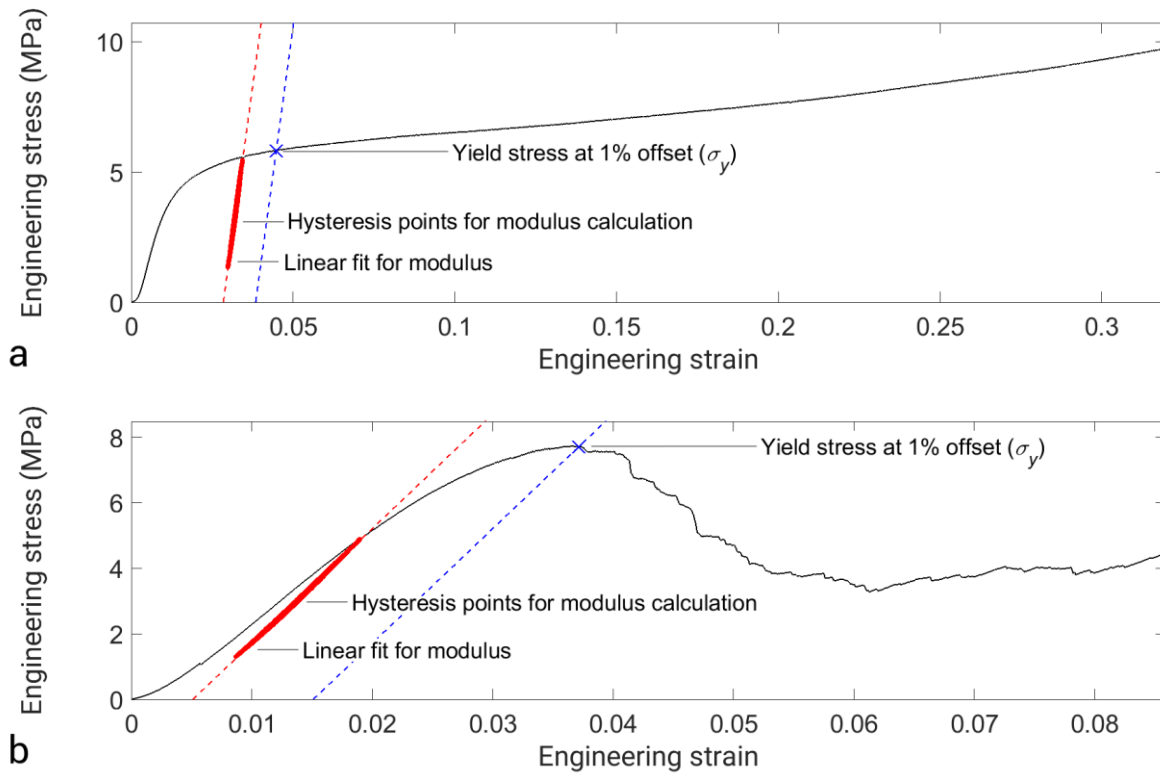


Figure 5.4: Stress strain curve for a specimen of variant C in the '0' direction. (a) SS316L and (b) Ti6Al4V.

SS316L specimens failed in a ductile manner and were gradually compressed until densification. Ti6Al4V specimens failed in a brittle manner and never recovered the same strength after yielding. Figure 5.5 compares the progression of specimen failure SS316L and Ti6Al4V specimens of variant A in the '0' direction.

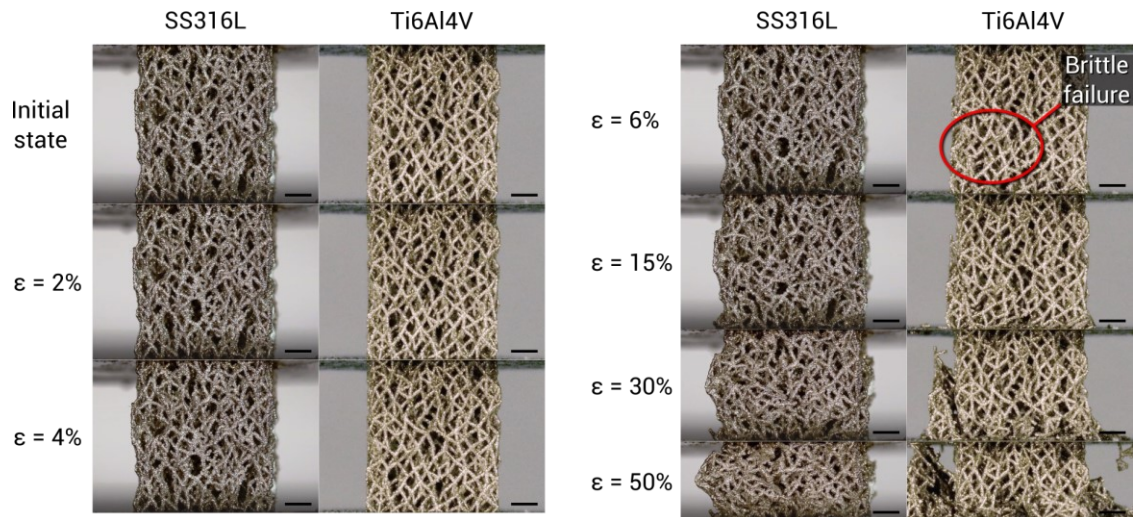


Figure 5.5: Photographs of variant A specimens in the '0' direction for both SS316L and Ti6Al4V undergoing compression.

The start of brittle failure can be seen in Ti6Al4V at $\epsilon = 6\%$ (highlighted in red). Black scale bar on bottom right of images is 2 mm.

The results for the mechanical testing show the values for each direction in order of increasing angle to the buildplate, i.e. from horizontal directions to vertical. The directions are described in Figure 5.3b.

Elastic modulus

Elastic modulus results are shown in Figure 5.6. For SS316L specimens, the moduli of each direction for variant A (no change) ranged from 384 MPa to 1058 MPa. The overall elastic modulus of the structure increased with variant B (kinking low angle struts) to an average of 1191 MPa, whilst reducing range of the results to 449 MPa. Variant C (kinking all struts) had a lower average modulus of 973 MPa, but also a lower range of 363 MPa.

For Ti6Al4V specimens, the average elastic modulus was reduced with each succeeding variant, going from 680 MPa for variant A to 500 MPa for variant B, and then to 350 MPa for variant C, though the results did overlap in values. The range also decreased, going from variant A to C, from 288 MPa to 158 MPa.

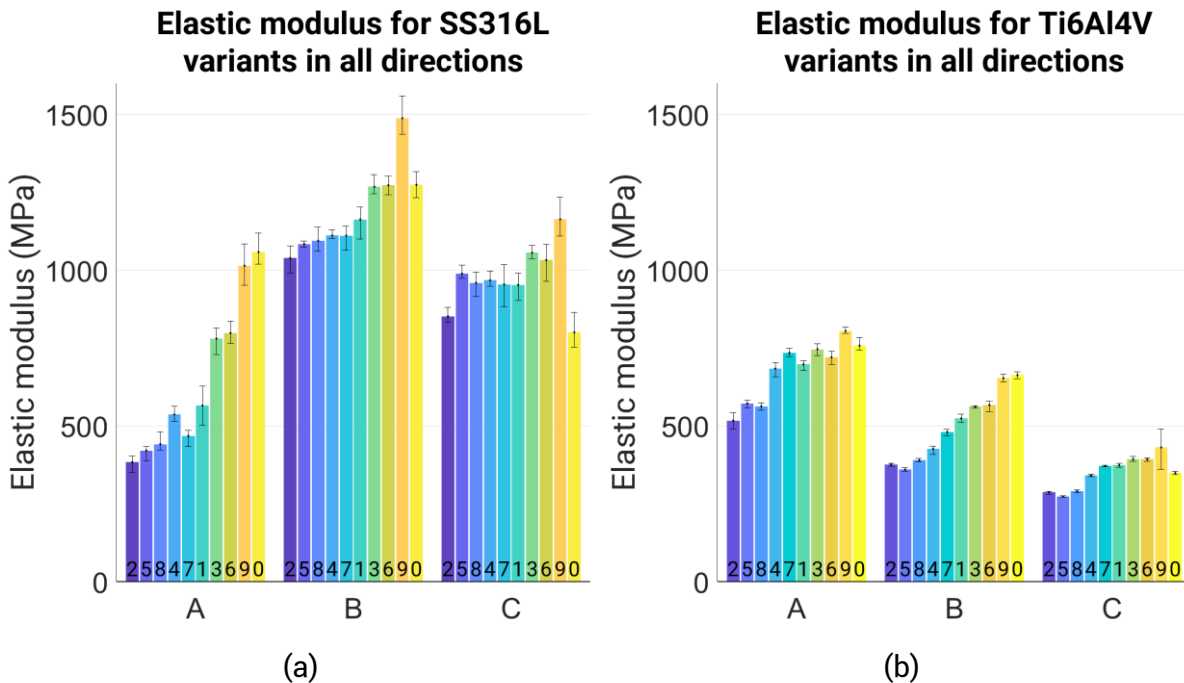


Figure 5.6: Elastic modulus vs test directions.

Directions are grouped by the structure variant A, B and C for (a) SS316L and (b) Ti6Al4V specimens. Engineering stress. Error bars indicate the full range of results.

Yield strength

Figure 5.7 shows similar results for the plastic properties of both materials as for the elastic properties in Figure 5.6. For SS316L specimens, the average 1% offset yield stress increased from variant A at 4.45 MPa to 6.80 MPa for variant B. There was no clear difference in the results going to variant C. The range of the results showed the same trend as before, decreasing from 2.14 MPa to 1.18 MPa.

For Ti6Al4V specimens, the average 1% offset yield stress decreased from 11.76 MPa for variant A, to 9.24 MPa for variant B, and then to 7.72 MPa for variant C, though the results did overlap in values. There was no clear variation in the range of results.

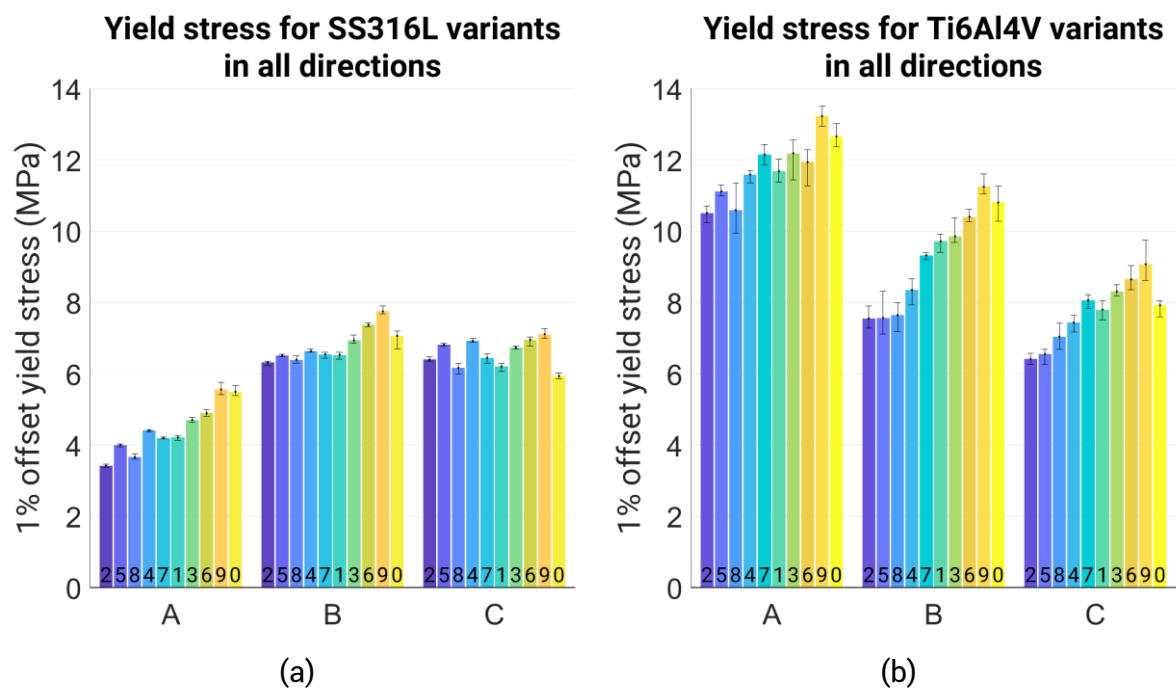


Figure 5.7: Yield stress vs test directions.

Directions are grouped by the structure variant A, B and C for (a) SS316L and (b) Ti6Al4V specimens. Engineering stress. Error bars indicate the full range of results.

Strength over stiffness ratio

Figure 5.8 shows the strength to stiffness ratio for both materials. This ratio compares how the plastic strength properties are affected compared to the elastic stiffness properties, with the changes to the structure made by each variant. For SS316L specimens, the ratio did not change dramatically with each variant. The average ratio decreased by 9%, going from variant A to C, showing that there was some small loss in strength/stiffness by modifying the structure.

For Ti6Al4V, the ratio steadily increased, going from variant A to C, by 27% overall. Whilst both strength and stiffness decreased for Ti6Al4V variants, the stiffness or elastic properties decreased more readily than the plastic strength properties.

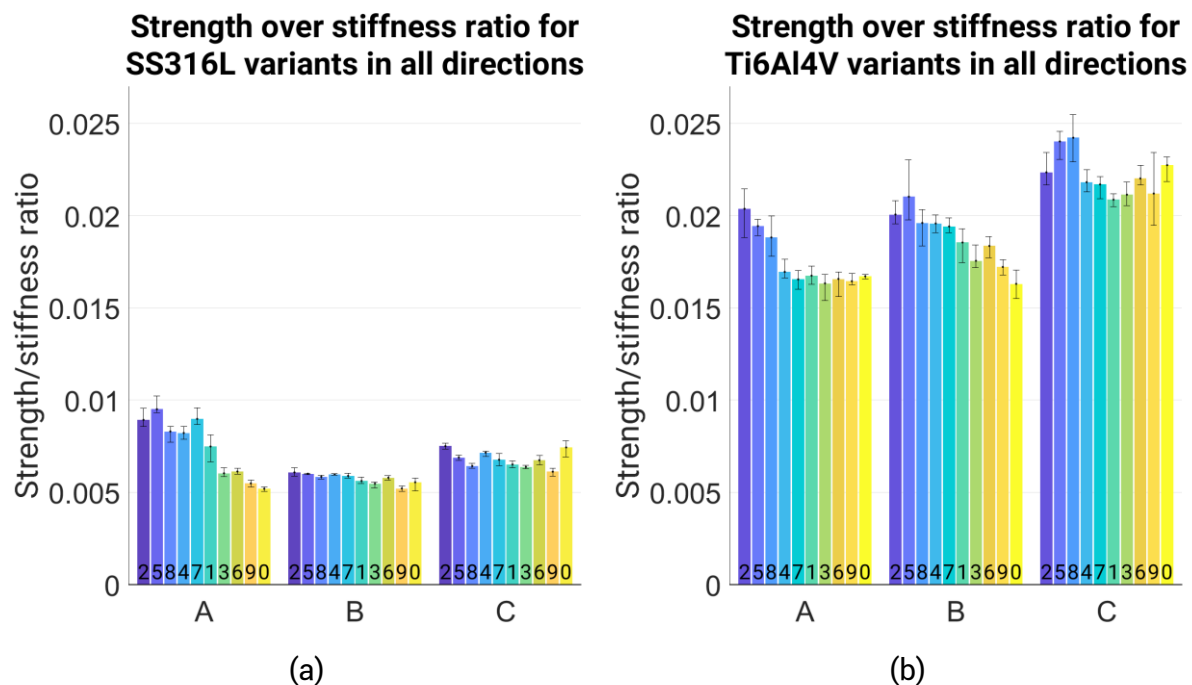


Figure 5.8: Strength over stiffness ratio vs test directions.

Directions are grouped by the structure variant A, B and C for (a) SS316L and (b) Ti6Al4V specimens. Engineering stress. Error bars indicate the full range of results.

5.3.2 SEM imaging

SEM images show the effect of each modification from variant A to C on the print quality and final geometry of the printed structure (Figure 5.9). A failed horizontal strut in variant A can be seen, having been successfully built in variants B and C due to the kinking process.

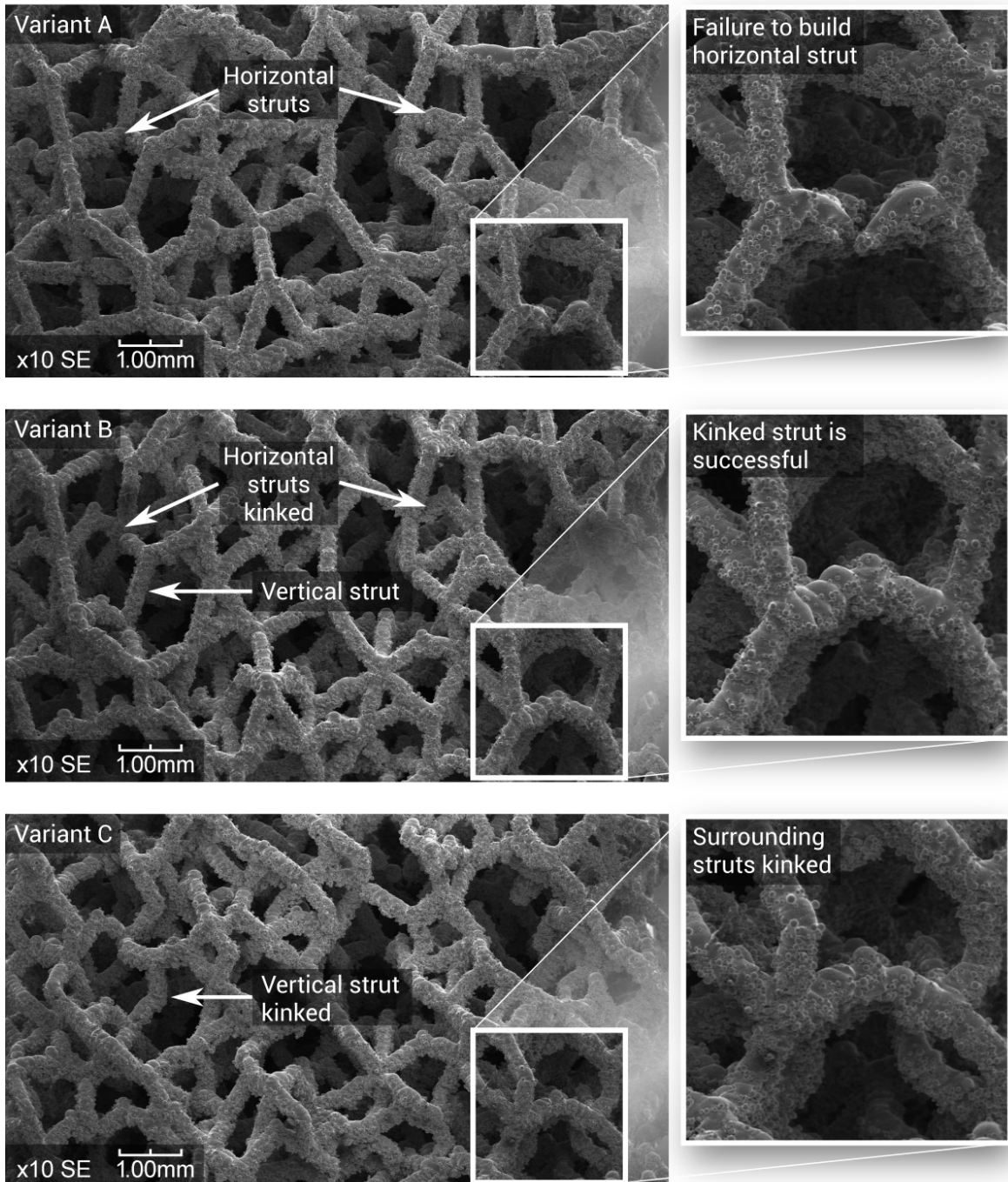


Figure 5.9: SEM images of the same location on a Ti6Al4V specimen '0' structure for each variant A, B and C.

Effect of kinking is shown on horizontal and vertical struts. In the close-up on right hand side, a horizontal strut is shown to build better after the kinking process.

5.4 Discussion

This work shows that a modified stochastic lattice can overcome the mechanical anisotropy inherent in lattice structures, due to unit cell geometry. For both materials, testing these properties in 10 directions verified that there are no hidden peaks in elastic modulus or yield stress. The greatest ratio of maximum to minimum stiffness was 1.58 for Ti6Al4V variant C structures, as opposed to a value over 5 as can occur in cubic structures [166,172]. The gradual change in properties over the spherical coordinates is characteristic of stochastic structures. The effect that each modification variant B and C introduced were intuitive and decreased the variability in the stiffness properties in each direction.

An isotropic stochastic structure can subsequently be modified to have a custom stiffness in each direction by modifying the strut diameters as required [315]. With an average stiffness of 350 MPa, the variant C Ti6Al4V stochastic lattice is within the range of stiffness needed to replace trabecular bone, which is between 0.02-2 GPa [15,55]. This includes the lower density bone found in the proximal tibia [273–275,280]. As 350 MPa is on the lower end of the stiffness needed for trabecular bone, increasing the strut diameter and therefore the stiffness could result in elastic moduli that approach that of the proximal femur [276,277]. In the proximal tibia, the ratio of elastic modulus in the axial direction versus in the transverse plane can be between 3.2 to 6.1 at maximum [280,281]. To achieve this specific anisotropy with the lattice, struts in the vertical direction could be stiffened preferentially to match the anatomical location, tuning the diameters as necessary.

The variation in the yield properties for Ti6Al4V specimens did not improve as modifications were introduced as compared to SS316L (shown in Figure 5.7b). This may be due to the strong relationship between build angle of individual struts and the ultimate tensile strength (a good approximation for the yield strength) for Ti6Al4V struts shown in Chapter 4, Figure 4.17a. The UTS increases by over 2.5 times from a build angle of 20° to 90°, so these properties would translate into the performance of the macro structure. This changing yield strength may also be impacting the performance of the lattice in the elastic regime, as low-angle struts prematurely yield and compromise the stiffness of the lattice. Increasing the thickness of struts in the lattice would increase the overall stiffness but also increase the threshold at which the weakest parts of the lattice yield due to their low build angle. Using post processing techniques such as chemical etching may smooth out stress concentrations and roughness present in the lattice [266,350,357], which also disproportionately affect low angle struts as shown in Chapter 4, Figure 4.13b.

The strength to stiffness ratio is a useful measure for trabecular bone replacement as the required elastic modulus is low, whilst the yield properties should be maximised to extend fatigue life. The strength to stiffness ratio plotted in Figure 5.8 demonstrates that the modifications did not disproportionately affect the elastic over the plastic properties or vice versa, especially for SS316L. The ratio did increase by 27% for Ti6Al4V variant C specimens however, and whilst both the strength and the stiffness do decrease, going from variant A to C, the strength decreased less as the modifications are made. This is a useful improvement for musculoskeletal applications.

Prior work involving isotropic lattices tends to begin with a unit cell design. These are analysed using FEA and then manually rearranged with optimisation of beam diameters [216,358] or the unit cell undergoes topological optimisation to reach elastic isotropy [172,182,359]. Many unit cells produced this way present a challenge to manufacture using PBF due to the presence of horizontal struts [172,216], or of closed cavities that may trap metal powder [173]. The topology-optimised unit cell presented by Takezawa et al. resembles that of a Schwarz P minimal surface and so would be better able to self-support during manufacturing [182]. However, compared to the other unit cells which are strut-based and create an open cell structure, it has been optimised for high stiffness and is less suitable for bone ingrowth applications.

In contrast, the stochastic method used in this chapter precludes the use of FEA in this way due to the lack of a regular unit cell. Elastic isotropy is achieved instead throughout the 'continuum' of the printed structure. The use of a 'critical angle' in the stochastic method presented here avoids any variability in strut morphology that can occur at low print angles [201,249]. Testing in ten directions, including the three axial directions, verifies the mechanical properties of the lattice are consistent throughout. The advantages of open cell structures for bone ingrowth are also retained. A further advantage of the stochastic structure is that the stress-strain curve is similar to that of a continuum material. There are no failure planes that could occur from a repeating unit cell, where the same part of the cell fails at once under a critical load (a shear band-type global failure) [360].

When looking to control the overall stiffness of lattice, increasing or decreasing the relative density would be necessary as per the Gibson-Ashby model for porous materials. Where unit cells have been specifically arranged and balanced for isotropy, they are limited to one volume fraction [216], and would have to be re-optimised for a different volume fraction [172,182,359]. Stochastic lattices may not have this problem and increasing the beam diameter should suffice. Further testing is required to see if the benefits of strut modification

can be replicated at higher volume fractions. A lattice with anisotropy that has been tailored to match an anatomical location will potentially have a different relative density to those investigated in this chapter.

All open cell, strut-based isotropic lattice designs will have their properties dictated in some way by the AM technique used, and thus relying on FEA data alone may not capture manufacturing effects due to build angles and build quality. However the experimental approach taken here and reported by others [182] avoids this outcome. For example, the pilot data for this work indicated that the 25° critical angle was appropriate for our setup, and this may not be the case for different materials, build parameters or manufacturing methods. The critical angle was chosen after conducting pilot testing using SS316L. Full details of this pilot testing is included in the Appendix, section A2.1. Other angles that were investigated included 20° and 30°.

Other limitations of the work presented here relate to the manufacturing process. When creating porous lattices with feature sizes from 100 – 300 µm using PBF manufacturing, factors such the slicing method, and the quality of air filtration/optical train all influence the lattice performance. These may vary from printer to printer, so further tests would be necessary to evaluate the robustness of the structure against manufacturing method.

Some parameters have been fixed for this study, which may have a key role in the mechanical behaviour. The effect of the value chosen for the critical angle of 25° has not been explored. Further work would explore how the mechanical isotropy changes with variation in that angle. The structures have also been tested at one density only. Testing at higher densities would allow a relationship with strength and modulus to be established, and whether this fits the Gibson-Ashby model for porous materials. It is also possible that the kinks act as 'stress raisers', which may impact on the fatigue properties of the lattice. Further testing would be needed to investigate this.

The modified stochastic structure presented here has the potential to be used as a base lattice for stiffness matched implants for areas of trabecular bone. Overcoming PBF manufacturing limitations that cause anisotropy in stochastic lattices reduces the dependence of the lattice performance on build direction, especially compared to some unit cell based lattices. This has the benefit of allowing a greater range of orientations that the lattice could take within an implant component. This increases the options for arranging components on a print bed as different orientations would be possible, reducing the space required and providing flexibility. A patent has been filed to this effect as a result of the work in this chapter, the details of which can be found in the Appendix, A2.2.

Modified stochastic lattices have been designed which produce more isotropic mechanical behaviour. These low stiffness lattices could be used within implants which match the stiffness of trabecular bone.

6 Discussion

6.1 Most important findings

The work in this thesis has shown that the mechanical behaviour of a laser PBF AM lattice structure is affected by the lattice architecture and the underlying mechanical properties of AM metal. Lattice topology impacts the performance of the lattice in multiple directions. Lattice structures that have material arranged in highly aligned directions, such as a BCC structure, will have an anisotropic stiffness that reflects that architecture (Chapter 3). A stochastic structure can have a varying anisotropic stiffness, depending on whether low-angle struts are removed or have been kept in and modified. Modified stochastic structures will have a gradual change in properties over spherical coordinates with no hidden peaks in stiffness (Chapters 3 and 5). Statistical measures of lattice architecture such as the SLD do not necessarily predict the mechanical performance of lattices, as they do not consider connectivity or density (Chapter 3). Mechanical testing is a better method for comparing between lattice topologies.

The underlying elastic modulus for SS316L and Ti6Al4V micro-struts in a lattice has no clear relationship to build angle but is substantially lower than that for the bulk material. In contrast, the ultimate tensile strength of Ti6Al4V struts has a strong relationship with build angle. The average value for the UTS of Ti6Al4V struts more than doubles from struts built at 20° versus those built at 90°, though this relationship does not exist for SS316L. The morphology of low angle struts is also compromised with respect to elliptical ratio, roughness and eccentricity for both materials (Chapter 4). This change in morphology may explain the poor mechanical performance of unmodified stochastic lattices at low build angles.

The modifications to the stochastic lattice introduced in Chapter 5 help overcome the poor print quality at low build angles, and constitute a low-stiffness lattice which could be tuned using a varying density to match the preferred mechanical stiffness and anisotropy for a given anatomical location. The resulting lattice used in a bone implant could help achieve peak bone formation in the periprosthetic bone.

6.2 Implications of the findings for implant design

These findings have implications for the challenge of implant design. Importantly, the methodology developed for compression testing of a lattice in multiple directions in Chapters 3 and 5 has shown that testing in only one direction is insufficient. As loading of implants is often dynamic, in both the magnitude and orientation of the load, consideration of planes of weakness for a lattice design needs to be considered.

AM implants would invariably use Ti6Al4V over SS316L. The elastic modulus of Ti6Al4V struts in a lattice does not have a clear relationship with build angle, whereas the UTS does. However, it is not yet clear exactly what contribution surface defects and stress concentrations had on the relationship between strut build angle and UTS. As yield properties are important in lattice design, further testing would be needed regarding fatigue properties of the Ti6Al4V lattices, and whether the relationship between Ti6Al4V strut build angle and UTS causes anisotropic fatigue properties.

Chapter 5 demonstrates a method for modifying stochastic lattices to have more uniform stiffness properties. This works well for SS316L lattices but could be improved for Ti6Al4V lattices. However, there is a lot of room for experimentation with the different variables, such as strut diameter, the critical angle of 25°, and for including post-processing techniques such as heat treatments as well as acid etching processes. These are not investigated in the thesis but would be important for implants that can be easily sterilised, and do not include semi-fused particles.

6.3 Limitations

Chapter 3 was limited to the investigation of two kinds of lattice, BCC and stochastic. Comparison to further architectures and unit-cell designs would be instructive, especially as the multi-directional methodology employed in this thesis is not often used in the literature to highlight peaks and variability in lattice structures. However, the aim of creating a methodology which tested lattices in multiple directions was accomplished (Aims and objectives of the thesis, section 2.4.2) A full comparison between many unit cells would have benefitted many researchers, though including a stochastic lattice did address a lack of data in the literature.

Chapter 4 included build angle and strut diameter as independent variables when investigating fundamental mechanical properties, fulfilling the broad aims of this chapter. However, other variables such as wiper blade direction and support for the strut (normally available as part of a lattice) would also affect the mechanical and morphological properties.

Fatigue strength was also not investigated. It was also established using a robust method that the mechanical properties are lower than that of the bulk material for both SS316L and Ti6Al4V. Digital image correlation may have been a more accurate method of strain measurement, but the method used LVDTs and took many precautions to avoid machine compliance.

The structures in Chapter 5 had some parameters fixed, such as the critical angle of 25°, and the structures were tested at one density only. Changing the strut diameter to affect the lattice density as suggested may cause changes in the performance of the lattice in multiple directions. Micro-CT imaging was also not used on full lattice structures as built to analyse defects in the same way as for individual struts. Imaging lattices in full would ensure that the morphological properties found for individual struts match those that are found in a built lattice. However, the aims set out for this Chapter were achieved, with a specific method that improved the manufacturability of SS316L stochastic lattices. The resulting Ti6Al4V lattices had an elastic modulus that was within the range of trabecular bone, in multiple directions.

6.4 Comparison to existing work

There is very limited work that explores the kind of stochastic lattice established by Ghouse et al. in the Imperial College London Biomechanics group [162,315,342], and which features in this thesis. Examples exist outside of the metal AM literature [217,230,353], but this lack of work on stochastic structures may be because design tools and software commonly used in engineering favour regular structures rather than those using pseudo-random points. Current work in metal AM that uses lattices designed using a random input, does not explore the full mechanical behaviour, or is not suitable for biomaterial applications [186,187,199]. However, modified stochastic lattices have been shown in this thesis to behave more like a 'continuum' material, without hidden peaks in stiffness as can be found for unit-cell based lattices.

The uniaxial tensile testing and morphology investigation for individual micro-struts at varying build angle is the first comparison between SS316L and Ti6Al4V struts with the same methodology. The results confirm that the mechanical properties of laser PBF metal are lower than that for the bulk material, and that strut morphology is impacted for struts at low build angles. The use of micro-CT imaging to quantify the morphology of tensile test specimens has not been done previously, and the work in Chapter 4 adds substantially to the reported mechanical properties of micro-struts built at different angles.

The method used in this thesis for multi-directional uniaxial compression testing of stiffness for lattices is novel, and similar comprehensive testing for other kinds of lattices is not

always implemented. Where mechanical testing has been performed in multiple directions, it is only carried out in one or two extra directions [182,213,214], or the structure is not tested such that the build direction remains consistently oriented to the lattice structure [207]. Otherwise, FEA is used to test in multiple directions [166,172,173,206,220,358]. However, the inconsistencies in metal AM highlighted in Chapter 4 show that this approach may not be reliable if these are not taken account in the material model. One topology optimised lattice has been tested in 3 directions, but has been designed for biomaterial applications [182]. As such, the work in this thesis has tried to address this area of the literature.

6.5 Future work

When considering implant design, there are benefits to further testing for mechanical properties of Ti6Al4V struts. As the yield-related properties such as ultimate tensile strength do seem to be related to build angle, possibly due to poor surface morphology, the effect of post-processing on individual struts need to be considered. Heat treatments as well as acid etching processes should all be tested to see if improvements are made to the mechanical and morphological properties.

These post processes will also affect the macro behaviour of lattices. They may improve the effect that the modifications have on stochastic lattices made using Ti6Al4V. Compared to SS316L lattices, the Ti6Al4V lattices did not have a dramatic improvement to their performance at low angles. Heat treatments may increase the ductility of the Ti6Al4V lattices. The yield behaviour of the lattices is also important due to the requirements of implants, specifically suitable fatigue properties. The effect that the stochastic lattice modifications have on fatigue behaviour is also important, as they may be a cause of further stress concentrations/stress raisers.

The modified stochastic lattice structures introduced in Chapter 5 could be explored further, as there are multiple variables that impact the lattice architecture and would impact the lattice performance. The 25° critical angle for struts defining them as 'horizontal' to the build platform could be subject to a sensitivity analysis. Tests on individual 'kinked' struts could provide detail as to the magnitude of bending that is induced and the relationship with changing strut morphology. Various densities of modified stochastic could also be evaluated, to see if tuning the stiffness by increasing strut diameter as suggested causes other mechanical effects.

Analysing full lattice structures using micro-CT as well as SEM, and mechanically testing the same specimens, would allow for useful feedback loops. This geometric data could be used to minimise error when manufacturing the lattices, especially with respect to strut diameter.

Equally, using more advanced imaging techniques for measuring strain, such as the DIC method briefly introduced in Chapter 4, would provide higher resolution data about the accumulation of strain in individual AM struts. Further work could correlate the location of defects and stress concentrations with failure locations. Chapter 4 also showed that stiffness of SS316L did vary at certain build angles as a function of tensile specimen diameter. Microstructural effects could be the reason for this variance, so analysis of AM metallurgy may be useful for fine control of lattice performance.

In using micro-CT imaging for the individual struts, full volumetric meshes can be calculated for each strut. These can be converted into a tetrahedral FEA mesh for further analysis *in silico*. Tensile tests could be conducted using FEA, and the results compared to the physical tests. This could help clarify the true effective stiffness of the strut geometry, retaining the geometry imperfections that are not captured using an average diameter for the whole gauge length.

A useful development of the work would be to continue testing porous lattices *in vivo*, either using animal models or a bioreactor with loading capabilities. This would take the work to the next step, demonstrating how modifications of a lattice affect bone remodelling directly, rather than using FEA or testing the lattice alone. The Biomechanics group in Imperial College London has shown some promising initial results with their bioreactor, with bone cells kept alive and exhibiting response to strain input. This bodes well for future experiments that can rapidly iterate between lattice designs, optimising for peak bone formation.

6.6 Further applications of the work

As SS316L has also been tested alongside Ti6Al4V, there are broader applications for the work in this thesis beyond musculoskeletal applications. SS316L has high corrosion resistance and excellent weldability [361]. It is useful where a higher stiffness is needed than Ti6Al4V. It is also more ductile than SS316L. Chapter 5 also showed how the modifications to stochastic lattices improved the performance of SS316L lattices when loaded at a low angle. Therefore, the SS316L modified stochastic lattice from Chapter 5 could be used in a range of light-weighting, energy absorption or heat exchanging applications, where a more uniform stiffness is needed, and manufacturing limitations do not allow an unmodified stochastic lattice to be built.

The results for the tensile testing in Chapter 4 will also be helpful for researchers outside of the orthopaedic field, who use SS316L regularly in their lattice designs. It will be useful to know that the mechanical properties of SS316L do not have a clear relationship with build angle.

6.7 Research impact

Various parts of this thesis have been presented, published or are currently under review. The multi-directional compression testing of a culled stochastic lattice in Chapter 3 was employed in a paper published in Additive Manufacturing (December 2019 issue), and the comparison between BCC and stochastic structures was presented at the International Society for Technology in Arthroplasty (ISTA) 2018 Congress. The tensile testing work in Chapter 4 has been submitted to Additive Manufacturing. The compression testing work of modified stochastic lattices in Chapter 5 has resulted in a patent application (UK Patent Application No 2005050.6). Full details can be found in Appendix A2.2. The work has also been accepted for publication in Additive Manufacturing.

6.8 Conclusion

AM lattices have been designed, manufactured, and tested for musculoskeletal applications. The investigation of fundamental mechanical and morphological properties has revealed manufacturing limitations in laser PBF and provided data that could be used to better predict lattice behaviour. The modified stochastic lattice structures that have been designed overcome these limitations. The resulting lattice shows improved stiffness isotropy and could be tuned to match the stiffness and anisotropy of local trabecular bone.

7 Bibliography

- [1] A.M. Briggs, A.D. Woolf, K. Dreinhöfer, N. Homb, D.G. Hoy, D. Kopansky-Giles, K. Åkesson, L. March, Reducing the global burden of musculoskeletal conditions, *Bull. World Health Organ.* 96 (2018) 366.
- [2] D.J. Schofield, R.N. Shrestha, M. Cunich, R. Tanton, S. Kelly, M.E. Passey, L.J. Veerman, Lost productive life years caused by chronic conditions in australians aged 45-164 years, 2010-2030, *Med. J. Aust.* 203 (2015) 260.e1-260.e6. <https://doi.org/10.5694/mja15.00132>.
- [3] E. Sebbag, R. Felten, F. Sagez, J. Sibilia, H. Devilliers, L. Arnaud, The world-wide burden of musculoskeletal diseases: A systematic analysis of the World Health Organization Burden of Diseases Database, *Ann. Rheum. Dis.* 78 (2019) 844–848. <https://doi.org/10.1136/annrheumdis-2019-215142>.
- [4] Global Burden of Disease Study 2013 Collaborators, Global, regional, and national incidence, prevalence, and years lived with disability for 301 acute and chronic diseases and injuries in 188 countries, 1990-2013: A systematic analysis for the Global Burden of Disease Study 2013, *Lancet.* 386 (2015) 743–800. [https://doi.org/10.1016/S0140-6736\(15\)60692-4](https://doi.org/10.1016/S0140-6736(15)60692-4).
- [5] A.D. Woolf, P. Brooks, K. Åkesson, G.M. Mody, Prevention of musculoskeletal conditions in the developing world, *Best Pract. Res. Clin. Rheumatol.* 22 (2008) 759–772. <https://doi.org/10.1016/j.berh.2008.07.003>.
- [6] National Joint Registry, 16th Annual Report 2019, (2019) 1–248. https://reports.njrcentre.org.uk/Portals/0/PDFdownloads/NJR_16th_Annual_Report_2019.pdf.
- [7] N. Arden, M.C. Nevitt, Osteoarthritis: Epidemiology, *Best Pract. Res. Clin. Rheumatol.* 20 (2006) 3–25. <https://doi.org/10.1016/j.berh.2005.09.007>.
- [8] E.L. Francois, M.J. Yaszemski, Chapter 43 - Preclinical Bone Repair Models in Regenerative Medicine, in: A. Atala, R. Lanza, A.G. Mikos, R. Nerem (Eds.), *Princ. Regen. Med.* (Third Ed., Third Edit, Academic Press, Boston, 2019: pp. 761–767. <https://doi.org/https://doi.org/10.1016/B978-0-12-809880-6.00043-6>.

- [9] A.R. Amini, C.T. Laurencin, S.P. Nukavarapu, Bone tissue engineering: Recent advances and challenges, *Crit. Rev. Biomed. Eng.* 40 (2012) 363–408. <https://doi.org/10.1615/CritRevBiomedEng.v40.i5.10>.
- [10] L. Polo-Corrales, M. Latorre-Esteves, J.E. Ramirez-Vick, Scaffold design for bone regeneration, *J. Nanosci. Nanotechnol.* 14 (2014) 15–56. <https://doi.org/10.1166/jnn.2014.9127>.
- [11] T. Kurien, R.G. Pearson, B.E. Scammell, Bone graft substitutes currently available in orthopaedic practice: The evidence for their use, *Bone Jt. J.* 95 B (2013) 583–597. <https://doi.org/10.1302/0301-620X.95B5.30286>.
- [12] M. Navarro, A. Michiardi, O. Castaño, J.A. Planell, Biomaterials in orthopaedics, *J. R. Soc. Interface.* 5 (2008) 1137–1158. <https://doi.org/10.1098/rsif.2008.0151>.
- [13] O. Ethgen, O. Bruyère, F. Richy, C. Dardennes, J.Y. Reginster, Health-Related Quality of Life in Total Hip and Total Knee Arthroplasty: A Qualitative and Systematic Review of the Literature, *J. Bone Jt. Surg. - Ser. A.* 86 (2004) 963–974. <https://doi.org/10.2106/00004623-200405000-00012>.
- [14] L.L. Hench, J.M. Polak, Third-generation biomedical materials, *Science* (80-.). 295 (2002) 1014–1017.
- [15] X. Wang, S. Xu, S. Zhou, W. Xu, M. Leary, P. Choong, M. Qian, M. Brandt, Y.M. Xie, Topological design and additive manufacturing of porous metals for bone scaffolds and orthopaedic implants: A review, *Biomaterials.* 83 (2016) 127–141. <https://doi.org/10.1016/j.biomaterials.2016.01.012>.
- [16] Stryker, Triathlon Tritanium Knee System, Stryker Orthop. - Prod. Broch. (2015). <https://www.stryker.com/us/en/joint-replacement/products/triathlon-tritanium.html> (accessed November 23, 2017).
- [17] C. Chu, G. Graf, D.W. Rosen, Design for additive manufacturing of cellular structures, *Comput. Aided. Des. Appl.* 5 (2008) 686–696. <https://doi.org/10.3722/cadaps.2008.686-696>.
- [18] N. Reznikov, O.R. Boughton, S. Ghouse, A.E. Weston, L. Collinson, G.W. Blunn, J.R.T. Jeffers, J.P. Cobb, M.M. Stevens, Individual response variations in scaffold-guided bone regeneration are determined by independent strain- and injury-induced

- mechanisms, *Biomaterials*. 194 (2019) 183–194. <https://doi.org/10.1016/j.biomaterials.2018.11.026>.
- [19] M. Munford, U. Hossain, S. Ghouse, J.R.T. Jeffers, Prediction of anisotropic mechanical properties for lattice structures, *Addit. Manuf.* 32 (2020) 101041. <https://doi.org/10.1016/j.addma.2020.101041>.
- [20] M. Niinomi, Recent metallic materials for biomedical applications, *Metall. Mater. Trans. A*. 33 (2002) 477–486. <https://doi.org/10.1007/s11661-002-0109-2>.
- [21] M. Niinomi, Mechanical biocompatibilities of titanium alloys for biomedical applications, *J. Mech. Behav. Biomed. Mater.* 1 (2008) 30–42. <https://doi.org/10.1016/j.jmbbm.2007.07.001>.
- [22] J. Charnley, Surgery of the Hip-Joint, *Br. Med. J.* 1 (1960) 821–826. <https://doi.org/10.1136/bmj.1.5176.821>.
- [23] G.K. McKee, J. Watson-Farrar, Replacement of arthritic hips by the McKee-Farrar prosthesis, *J. Bone Joint Surg. Br.* 48 (1966) 245–259.
- [24] P.S. Walker, B.L. Gold, The tribology (friction, lubrication and wear) of all-metal artificial hip joints, *Wear*. 17 (1971) 285–299. [https://doi.org/10.1016/0043-1648\(71\)90032-9](https://doi.org/10.1016/0043-1648(71)90032-9).
- [25] J. Charnley, Arthroplasty of the hip: a new operation, *Lancet*. 277 (1961) 1129–1132.
- [26] J. Charnley, Total hip replacement by low-friction arthroplasty, *Curr. Orthop. Pract.* 25 (2014) 105–113. <https://doi.org/10.1097/01.bco.0000443748.36521.01>.
- [27] J.O. Galante, W. Rostoker, Wear in Total Hip Prostheses: An Experimental Evaluation of Candidate Materials, *Acta Orthop. Scand.* 43 (1972) 1–46. <https://doi.org/10.3109/ort.1972.43.suppl-145.01>.
- [28] M. Long, H.J. Rack, Titanium alloys in total joint replacement--a materials science perspective., *Biomaterials*. 19 (1998) 1621–1639. [https://doi.org/10.1016/S0142-9612\(97\)00146-4](https://doi.org/10.1016/S0142-9612(97)00146-4).
- [29] R. Vaishya, M. Chauhan, A. Vaish, Bone cement, *J. Clin. Orthop. Trauma*. 4 (2013) 157–163. <https://doi.org/10.1016/j.jcot.2013.11.005>.

- [30] A. Buford, T. Goswami, Review of wear mechanisms in hip implants: Paper I - General, *Mater. Des.* 25 (2004) 385–393. <https://doi.org/10.1016/j.matdes.2003.11.010>.
- [31] H. McKellop, I. Clarke, K. Markolf, H. Amstutz, Friction and wear properties of polymer, metal, and ceramic prosthetic joint materials evaluated on a multichannel screening device, *J. Biomed. Mater. Res.* 15 (1981) 619–653. <https://doi.org/10.1002/jbm.820150503>.
- [32] V. Saikko, Wear and friction properties of prosthetic joint materials evaluated on a reciprocating pin-on-flat apparatus, *Wear.* 166 (1993) 169–178.
- [33] J.H. Dumbleton, M.T. Manley, A.A. Edidin, A literature review of the association between wear rate and osteolysis in total hip arthroplasty, *J. Arthroplasty.* 17 (2002) 649–661. <https://doi.org/10.1054/arth.2002.33664>.
- [34] Y. Abu-Amer, I. Darwech, J.C. Clohisy, Aseptic loosening of total joint replacements: Mechanisms underlying osteolysis and potential therapies, *Arthritis Res. Ther.* 9 (2007) S6. <https://doi.org/10.1186/ar2170>.
- [35] M.E. Müller, The benefits of metal-on-metal total hip replacements, *Clin. Orthop. Relat. Res.* (1995) 54–59.
- [36] I.C. Clarke, V. Good, P. Williams, D. Schroeder, L. Anissian, A. Stark, H. Oonishi, J. Schuldies, G. Gustafson, Ultra-low wear rates for rigid-on-rigid bearings in total hip replacements, *Proc. Inst. Mech. Eng. Part H J. Eng. Med.* 214 (2000) 331–347. <https://doi.org/10.1243/0954411001535381>.
- [37] F.W. Chan, J.D. Bobyn, J.B. Medley, J.J. Krygier, M. Tanzer, Wear and lubrication of metal-on-metal hip implants, *Clin. Orthop. Relat. Res.* (1999) 10–24. <https://doi.org/10.1097/00003086-199912000-00003>.
- [38] Y.S. Park, Y.W. Moon, S.J. Lim, J.M. Yang, G. Ahn, Y. La Choi, Early osteolysis following second-generation metal-on-metal hip replacement, *J. Bone Jt. Surg. - Ser. A.* 87 (2005) 1515–1521. <https://doi.org/10.2106/JBJS.D.02641>.
- [39] H. Wynn-Jones, R. MacNair, J. Wimhurst, N. Chirodian, B. Derbyshire, A. Toms, J. Cahir, Silent soft tissue pathology is common with a modern metal-on-metal hip arthroplasty, *Acta Orthop.* 82 (2011) 301–307. <https://doi.org/10.3109/17453674.2011.579518>.

- [40] M.A. Mont, T.P. Schmalzried, Modern metal-on-metal hip resurfacing: important observations from the first ten years., *J. Bone Joint Surg. Am.* 90 Suppl 3 (2008) 3–11. <https://doi.org/10.2106/JBJS.H.00750>.
- [41] D.J. Langton, S.S. Jameson, T.J. Joyce, J.N. Gandhi, R. Sidaginamale, P. Mereddy, J. Lord, A.V.F. Nargol, Accelerating failure rate of the ASR total hip replacement, *J. Bone Joint Surg. Br.* 93-B (2011) 1011–1016. <https://doi.org/10.1302/0301-620x.93b8.26040>.
- [42] D.J. Langton, S.S. Jameson, T.J. Joyce, N.J. Hallab, S. Natu, A.V.F. Nargol, Early failure of metal-on-metal bearings in hip resurfacing and large-diameter total hip replacement: A consequence of excess wear, *J. Bone Jt. Surg. - Ser. B.* 92 (2010) 38–46. <https://doi.org/10.1302/0301-620X.92B1.22770>.
- [43] R.N. De Steiger, J.R. Hang, L.N. Miller, S.E. Graves, D.C. Davidson, Five-year results of the ASR XL acetabular system and the ASR hip resurfacing system: An analysis from the Australian Orthopaedic Association National Joint Replacement Registry, *J. Bone Jt. Surg. - Ser. A.* 93 (2011) 2287–2293. <https://doi.org/10.2106/JBJS.J.01727>.
- [44] N.M. Bernthal, P.C. Celestre, A.I. Stavrakis, J.C. Ludington, D.A. Oakes, Disappointing Short-Term Results With the DePuy ASR XL Metal-on-Metal Total Hip Arthroplasty, *J. Arthroplasty.* 27 (2012) 539–544. <https://doi.org/10.1016/j.arth.2011.08.022>.
- [45] I. Laaksonen, G.S. Donahue, R. Madanat, K.T. Makela, H. Malchau, Outcomes of the Recalled Articular Surface Replacement Metal-on-Metal Hip Implant System: A Systematic Review, *J. Arthroplasty.* 32 (2017) 341–346. <https://doi.org/10.1016/j.arth.2016.06.060>.
- [46] G. Jin, J. Ran, W. Chen, Y. Xiong, J. Bao, L. Wu, The 10-year outcomes of the ASR XL Acetabular System: A single-center experience from China, *J. Orthop. Surg. Res.* 14 (2019) 1–9. <https://doi.org/10.1186/s13018-019-1173-2>.
- [47] I.C. Clarke, Role of ceramic implants. Design and clinical success with total hip prosthetic ceramic-to-ceramic bearings., *Clin. Orthop. Relat. Res.* (1992) 19–30.
- [48] W.N. Capello, J.A. D'Antonio, J.R. Feinberg, M.T. Manley, M. Naughton, Ceramic-on-Ceramic Total Hip Arthroplasty: Update, *J. Arthroplasty.* 23 (2008) 39–43. <https://doi.org/10.1016/j.arth.2008.06.003>.

- [49] M. Slonaker, T. Goswami, Review of wear mechanisms in hip implants: Paper II - ceramics IG004712, *Mater. Des.* 25 (2004) 395–405. <https://doi.org/10.1016/j.matdes.2003.11.011>.
- [50] L.M. Jazrawi, E. Bogner, C.J. Della Valle, F.S. Chen, K.I. Pak, S.A. Stuchin, V.H. Frankel, P.E. Di Cesare, Wear rates of ceramic-on-ceramic bearing surfaces in total hip implants: A 12-year follow-up study, *J. Arthroplasty.* 14 (1999) 781–787. [https://doi.org/10.1016/S0883-5403\(99\)90025-6](https://doi.org/10.1016/S0883-5403(99)90025-6).
- [51] S. Yin, D. Zhang, H. Du, H. Du, Z. Yin, Y. Qiu, Is there any difference in survivorship of total hip arthroplasty with different bearing surfaces? A systematic review and network meta-analysis, *Int. J. Clin. Exp. Med.* 8 (2015) 21871–21885.
- [52] T.M. Grupp, S. Utzschneider, C. Schröder, J. Schwiesau, B. Fritz, A. Maas, W. Blömer, V. Jansson, Biotribology of alternative bearing materials for unicompartmental knee arthroplasty, *Acta Biomater.* 6 (2010) 3601–3610. <https://doi.org/10.1016/j.actbio.2010.04.003>.
- [53] C.L. Brockett, S. Carbone, J. Fisher, L.M. Jennings, PEEK and CFR-PEEK as alternative bearing materials to UHMWPE in a fixed bearing total knee replacement: An experimental wear study, *Wear.* 374–375 (2017) 86–91. <https://doi.org/10.1016/j.wear.2016.12.010>.
- [54] D. Vogel, H. Dempwolf, A. Baumann, R. Bader, Characterization of thick titanium plasma spray coatings on PEEK materials used for medical implants and the influence on the mechanical properties, *J. Mech. Behav. Biomed. Mater.* 77 (2018) 600–608. <https://doi.org/10.1016/j.jmbbm.2017.09.027>.
- [55] M. Niinomi, Recent research and development in titanium alloys for biomedical applications and healthcare goods, *Sci. Technol. Adv. Mater.* 4 (2003) 445–454. <https://doi.org/10.1016/j.stam.2003.09.002>.
- [56] M. Geetha, A.K. Singh, R. Asokamani, A.K. Gogia, Ti based biomaterials, the ultimate choice for orthopaedic implants - A review, *Prog. Mater. Sci.* 54 (2009) 397–425. <https://doi.org/10.1016/j.pmatsci.2008.06.004>.
- [57] M. Niinomi, M. Nakai, J. Hieda, Development of new metallic alloys for biomedical applications, *Acta Biomater.* 8 (2012) 3888–3903.

<https://doi.org/10.1016/j.actbio.2012.06.037>.

- [58] J. Black, Biologic performance of tantalum, *Clin. Mater.* 16 (1994) 167–173. [https://doi.org/10.1016/0267-6605\(94\)90113-9](https://doi.org/10.1016/0267-6605(94)90113-9).
- [59] M. Niinomi, M. Nakai, Titanium-based biomaterials for preventing stress shielding between implant devices and bone, *Int. J. Biomater.* 2011 (2011). <https://doi.org/10.1155/2011/836587>.
- [60] W.R. Lacefield, Materials Characteristics of Uncoated/Ceramic-Coated Implant Materials, *Adv. Dent. Res.* 13 (1999) 21–26. <https://doi.org/10.1177/08959374990130011001>.
- [61] D.P. Byrne, K.J. Mulhall, J.F. Baker, Anatomy & Biomechanics of the Hip, *Open Sport. Med. J.* 4 (2014) 51–57. <https://doi.org/10.2174/1874387001004010051>.
- [62] D.R. Sumner, Long-term implant fixation and stress-shielding in total hip replacement, *J. Biomech.* 48 (2015) 797–800. <https://doi.org/10.1016/j.jbiomech.2014.12.021>.
- [63] F. HM, Wolff's Law and Bone's Structural Adaptations to Mechanical Usage: An Overview for Clinicians, *Angle Orthod.* 64 (1994). [https://doi.org/10.1043/0003-3219\(1994\)064<0175:WLABSA>2.0.CO;2](https://doi.org/10.1043/0003-3219(1994)064<0175:WLABSA>2.0.CO;2).
- [64] J.D. Bobyn, E.S. Mortimer, A.H. Glassman, C.A. Engh, J.E. Miller, C.E. Brooks, Producing and avoiding stress shielding: Laboratory and clinical observations of noncemented total hip arthroplasty, *Clin. Orthop. Relat. Res.* (1992) 79–96. <https://doi.org/10.1097/00003086-199201000-00010>.
- [65] J.D. Bobyn, a H. Glassman, H. Goto, J.J. Krygier, J.E. Miller, C.E. Brooks, The effect of stem stiffness on femoral bone resorption after canine porous-coated total hip arthroplasty., *Clin. Orthop. Relat. Res.* (1990) 196–213.
- [66] C.K. McCarthy, G.G. Steinberg, M. Agren, D. Leahey, E. Wyman, D.T. Baran, Quantifying bone loss from the proximal femur after total hip arthroplasty, *J. Bone Jt. Surg. - Ser. B.* 73 (1991) 774–778. <https://doi.org/10.1302/0301-620x.73b5.1894664>.
- [67] C.J. Sychterz, L.D. Timmie Topoleski, M. Sacco, C.A. Engh, Effect of femoral stiffness on bone remodeling after uncemented arthroplasty, *Clin. Orthop. Relat. Res.* (2001) 218–227. <http://www.scopus.com/inward/record.url?eid=2-s2.0->

0034903526&partnerID=tZOtx3y1.

- [68] H. Kroger, P. Venesmaa, J. Jurvelin, H. Miettinen, O. Suomalainen, E. Alhava, Bone density at the proximal femur after total hip arthroplasty, *Clin. Orthop. Relat. Res.* (1998) 66–74.
- [69] P. Grant, A. Aamodt, J.A. Falch, L. Nordsletten, Differences in stability and bone remodeling between a customized uncemented hydroxyapatite coated and a standard cemented femoral stem A randomized study with use of radiostereometry and bone densitometry, *J. Orthop. Res.* 23 (2005) 1280–1285. <https://doi.org/10.1016/j.orthres.2005.03.016.1100230607>.
- [70] T. Karachalios, C. Tsatsaronis, G. Efraimis, P. Papadelis, G. Lyritis, G. Diakoumopoulos, The long-term clinical relevance of calcar atrophy caused by stress shielding in total hip arthroplasty: A 10-year, prospective, randomized study, *J. Arthroplasty.* 19 (2004) 469–475. <https://doi.org/10.1016/j.arth.2003.12.081>.
- [71] J. Karrholm, C. Anderberg, F. Snorrason, J. Thanner, N. Langeland, H. Malchau, P. Herberts, Evaluation of a femoral stem with reduced stiffness: A randomized study with use of radiostereometry and bone densitometry, *J. Bone Jt. Surg. - Ser. A.* 84 (2002) 1651–1658. <https://doi.org/10.2106/00004623-200209000-00020>.
- [72] R. Huiskes, H. Weinans, B. van Rietbergen, The relationship between stress shielding and bone resorption around total hip stems and the effects of flexible materials., *Clin. Orthop. Relat. Res.* (1992) 124–134. <https://doi.org/10.1097/00003086-199201000-00014>.
- [73] G.H. van Lenthe, M.C. de Waal Malefijt, R. Huiskes, STRESS SHIELDING AFTER TOTAL KNEE REPLACEMENT MAY CAUSE BONE RESORPTION IN THE DISTAL FEMUR, *J. Bone Joint Surg. Br.* 79-B (1997) 117–122. <https://doi.org/10.1302/0301-620X.79B1.0790117>.
- [74] S. Gross, E.W. Abel, A finite element analysis of hollow stemmed hip prostheses as a means of reducing stress shielding of the femur, *J. Biomech.* 34 (2001) 995–1003. [https://doi.org/10.1016/S0021-9290\(01\)00072-0](https://doi.org/10.1016/S0021-9290(01)00072-0).
- [75] H. Weinans, R. Huiskes, B. Van Rietbergen, D.R. Sumner, T.M. Turner, J.O. Galante, Adaptive bone remodeling around bonded noncemented total hip arthroplasty: A

- comparison between animal experiments and computer simulation, *J. Orthop. Res.* 11 (1993) 500–513. <https://doi.org/10.1002/jor.1100110405>.
- [76] B. Van Rietbergen, R. Huiskes, H. Weinans, D.R. Sumner, T.M. Turner, J.O. Galante, The mechanism of bone remodeling and resorption around press-fitted THA stems, *J. Biomech.* 26 (1993) 369–382. [https://doi.org/10.1016/0021-9290\(93\)90001-U](https://doi.org/10.1016/0021-9290(93)90001-U).
- [77] M.J. Fagan, A.J.C. Lee, Role of the collar on the femoral stem of cemented total hip replacements, *J. Biomed. Eng.* 8 (1986) 295–304. [https://doi.org/10.1016/0141-5425\(86\)90061-0](https://doi.org/10.1016/0141-5425(86)90061-0).
- [78] R.M.A. Al-Dirini, D. Huff, J. Zhang, T. Besier, J.G. Clement, M. Taylor, Influence of collars on the primary stability of cementless femoral stems: A finite element study using a diverse patient cohort, *J. Orthop. Res.* 36 (2017) 1185–1195. <https://doi.org/10.1002/jor.23744>.
- [79] G. Demey, C. Fary, S. Lustig, P. Neyret, T.A. Si Selmi, Does a Collar Improve the Immediate Stability of Uncemented Femoral Hip Stems in Total Hip Arthroplasty? A Bilateral Comparative Cadaver Study, *J. Arthroplasty.* 26 (2011) 1549–1555. <https://doi.org/10.1016/j.arth.2011.03.030>.
- [80] J.N. Lamb, J. Baetz, P. Messer-Hannemann, I. Adekanmbi, B.H. van Duren, A. Redmond, R.M. West, M.M. Morlock, H.G. Pandit, A calcar collar is protective against early periprosthetic femoral fracture around cementless femoral components in primary total hip arthroplasty, *Bone Joint J.* 101-B (2019) 779–786. <https://doi.org/10.1302/0301-620X.101B7.BJJ-2018-1422.R1>.
- [81] T. Nishino, H. Mishima, S. Miyakawa, H. Kawamura, N. Ochiai, Midterm results of the Synergy cementless tapered stem: Stress shielding and bone quality, *J. Orthop. Sci.* 13 (2008) 498–503. <https://doi.org/10.1007/s00776-008-1272-0>.
- [82] W. Brodner, P. Bitzan, F. Lomoschitz, P. Krepler, R. Jankovsky, S. Lehr, F. Kainberger, F. Gottsauner-Wolf, Changes in bone mineral density in the proximal femur after cementless total hip arthroplasty. A five-year longitudinal study, *J. Bone Jt. Surg. - Ser. B.* 86 (2004) 20–26. <https://doi.org/10.1302/0301-620X.86B1.14637>.
- [83] H.U. Cameron, The 3–2–6-year results of a modular noncemented low-bending stiffness hip implant: A preliminary study, *J. Arthroplasty.* 8 (1993) 239–243.

[https://doi.org/10.1016/S0883-5403\(06\)80084-7](https://doi.org/10.1016/S0883-5403(06)80084-7).

- [84] J. Schmidt, M.H. Hackenbroch, The Cenos hollow stem in total hip arthroplasty: first experiences in a prospective study, *Arch. Orthop. Trauma Surg.* 113 (1994) 117–120. <https://doi.org/10.1007/BF00441616>.
- [85] R. Bombelli, R. Mathys, Cementless isoelastic RM total hip prosthesis, *J. R. Soc. Med.* 75 (1982) 588.
- [86] A.H. Glassman, J.D. Bobyn, M. Tanzer, New Femoral Designs: Do They Influence Stress Shielding?, *Clin. Orthop. Relat. Res.* 453 (2006) 64–74. <https://doi.org/10.1097/01.blo.0000246541.41951.20>.
- [87] M. Spector, I. Heyligers, J.R. Roberson, Porous polymers for biological fixation., *Clin. Orthop. Relat. Res.* (1988) 207–219.
- [88] E.W. Morscher, W. Dick, Cementless fixation of “isoelastic” hip endoprotheses manufactured from plastic materials., *Clin. Orthop. Relat. Res.* (1983) 77–87.
- [89] R. Trebse, I. Milosev, S. Kovac, M. Mikek, V. Pisot, Poor results from the isoelastic total hip replacement, *Acta Orthop.* 76 (2005) 169–176. <https://doi.org/10.1080/00016470510030535>.
- [90] P.G.M. Maathuis, J.D. Visser, High failure rate of soft-interface stem coating for fixation of femoral endoprotheses, *J. Arthroplasty.* 11 (1996) 548–552. [https://doi.org/10.1016/S0883-5403\(96\)80108-2](https://doi.org/10.1016/S0883-5403(96)80108-2).
- [91] J.H.M. Goosen, R.M. Castelein, W.C. Runne, D.A. Dartee, C.C.P.M. Verheyen, Long-term results of a soft interface- (Proplast-) coated femoral stem, *Acta Orthop.* 77 (2006) 585–590. <https://doi.org/10.1080/17453670610012647>.
- [92] H.S. Tullos, B.L. McCaskill, R. Dickey, J. Davidson, Total hip arthroplasty with a low-modulus porous-coated femoral component., *J. Bone Jt. Surg.* 66 (1984) 888–898. <https://doi.org/10.2106/00004623-198466060-00009>.
- [93] A.H. Glassman, R.D. Crowninshield, R. Schenck, P. Herberts, A low stiffness composite biologically fixed prosthesis, *Clin. Orthop. Relat. Res.* 393 (2001) 128–136.
- [94] M.A. Ritter, E. Michael Keating, P.M. Faris, A porous polyethylene-coated femoral

- component of a total hip arthroplasty, *J. Arthroplasty*. 5 (1990) 83–88. [https://doi.org/10.1016/S0883-5403\(06\)80014-8](https://doi.org/10.1016/S0883-5403(06)80014-8).
- [95] W.C. Runne, K.J.M. van Sambeek, J.L. Stierum, R.B. van Tongerloo, Femoral Endoprosthesis Fixation With a Soft, Flexible Low Modulus Stem Coating Four to Six Year Clinical Results, *Orthopedics*. 12 (1989) 529–535.
- [96] S. Allcock, M.A. Ali, Early failure of a carbon-fiber composite femoral component, *J. Arthroplasty*. 12 (1997) 356–358. [https://doi.org/10.1016/S0883-5403\(97\)90038-3](https://doi.org/10.1016/S0883-5403(97)90038-3).
- [97] A.S. Wong, A.M.R. New, G. Isaacs, M. Taylor, Effect of Bone Material Properties on the Initial Stability of a Cementless Hip Stem: A Finite Element Study, *Proc. Inst. Mech. Eng. Part H J. Eng. Med.* 219 (2005) 265–275. <https://doi.org/10.1243/095441105X34293>.
- [98] B. Elliott, T. Goswami, Implant material properties and their role in micromotion and failure in total hip arthroplasty, *Int. J. Mech. Mater. Des.* 8 (2012) 1–7. <https://doi.org/10.1007/s10999-011-9172-4>.
- [99] E.J. Harvey, J.D. Bobyn, M. Tanzer, G.J. Stackpool, J.J. Krygier, S.A. Hacking, Effect of flexibility of the femoral stem on bone-remodeling and fixation of the stem in a canine total hip arthroplasty model without cement, *JBJS*. 81 (1999) 93–107.
- [100] J.M. Anderson, Biological Responses to Materials, *Annu. Rev. Mater. Res.* 31 (2001) 81–110. <https://doi.org/10.1146/annurev.matsci.31.1.81>.
- [101] D. Apostu, O. Lucaciu, C. Berce, D. Lucaciu, D. Cosma, Current methods of preventing aseptic loosening and improving osseointegration of titanium implants in cementless total hip arthroplasty: a review, *J. Int. Med. Res.* 46 (2018) 2104–2119. <https://doi.org/10.1177/0300060517732697>.
- [102] A.F. Mavrogenis, R. Dimitriou, J. Parvizi, G.C. Babis, Biology of implant osseointegration, *J. Musculoskelet. Neuronal Interact.* 9 (2009) 61–71. <http://europepmc.org/abstract/MED/19516081>.
- [103] P.A. Revell, Biological causes of prosthetic joint failure, in: *Jt. Replace. Technol.*, Elsevier Inc., 2014: pp. 298–369. <https://doi.org/10.1533/9780857098474.3.298>.
- [104] I. Kutzner, G. Hallan, P.J. Høl, O. Furnes, Ø. Gøthesen, W. Figved, P. Ellison, Early aseptic

- loosening of a mobile-bearing total knee replacement: A case-control study with retrieval analyses, *Acta Orthop.* 89 (2018) 77–83. <https://doi.org/10.1080/17453674.2017.1398012>.
- [105] M. Bohner, Calcium orthophosphates in medicine: From ceramics to calcium phosphate cements, *Injury.* 31 (2000). [https://doi.org/10.1016/S0020-1383\(00\)80022-4](https://doi.org/10.1016/S0020-1383(00)80022-4).
- [106] J.O. Hollinger, J. Brekke, E. Gruskin, D. Lee, Role of bone substitutes, *Clin. Orthop. Relat. Res.* (1996) 55–65. <https://doi.org/10.1097/00003086-199603000-00008>.
- [107] E. Truumees, H.N. Herkowitz, Alternatives to autologous bone harvest in spine surgery, *Univ. Pennsylvania Orthop. J.* 12 (1999) 77–88.
- [108] C.A. van Blitterswijk, J.J. Grote, W. Kuijpers, W.T. Daems, K. de Groot, Macropore tissue ingrowth: a quantitative and qualitative study on hydroxyapatite ceramic, *Biomaterials.* 7 (1986) 137–143. [https://doi.org/10.1016/0142-9612\(86\)90071-2](https://doi.org/10.1016/0142-9612(86)90071-2).
- [109] W.R. Lacefield, Hydroxyapatite coatings, *Ann. N. Y. Acad. Sci.* 523 (1988) 72–80.
- [110] R.J. Furlong, J.F. Osborn, Fixation of hip prostheses by hydroxyapatite ceramic coatings, *J. Bone Joint Surg. Br.* 73 (1991) 741–745.
- [111] L. Sun, C.C. Berndt, K.A. Gross, A. Kucuk, Material fundamentals and clinical performance of plasma-sprayed hydroxyapatite coatings: A review, *J. Biomed. Mater. Res. An Off. J. Soc. Biomater. Japanese Soc. Biomater. Aust. Soc. Biomater. Korean Soc. Biomater.* 58 (2001) 570–592.
- [112] S.D. Cook, K.A. Thomas, J.E. Delton, T.K. Volkman, T.S. Whitecloud, J.F. Key, Hydroxylapatite coating of porous implants improves bone ingrowth and interface attachment strength, *J. Biomed. Mater. Res.* 26 (1992) 989–1001. <https://doi.org/10.1002/jbm.820260803>.
- [113] K. Søballe, E.S. Hansen, H. Brockstedt-Rasmussen, V.E. Hjortdal, G.I. Juhl, C.M. Pedersen, I. Hvid, C. Bünger, Gap healing enhanced by hydroxyapatite coating in dogs., *Clin. Orthop. Relat. Res.* (1991) 300–307.
- [114] K. Søballe, E.S. Hansen, H. B.-Rasmussen, P.H. Jørgensen, C. Bünger, Tissue ingrowth into titanium and hydroxyapatite-coated implants during stable and unstable

- mechanical conditions, *J. Orthop. Res.* 10 (1992) 285–299. <https://doi.org/10.1002/jor.1100100216>.
- [115] K. Søballe, E.S. Hansen, H. Brockstedt-Rasmussen, C. Bungler, Hydroxyapatite coating converts fibrous tissue to bone around loaded implants, *J. Bone Jt. Surg. - Ser. B.* 75 (1993) 270–278. <https://doi.org/10.1302/0301-620x.75b2.8444949>.
- [116] K. Søballe, S. Overgaard, The current status of hydroxyapatite coating of prostheses., *J. Bone Joint Surg. Br.* 78 (1996) 689–691. <https://doi.org/10.1302/0301-620x.78b5.0780689>.
- [117] K. Saptaji, M.A. Gebremariam, M.A.B.M. Azhari, Machining of biocompatible materials: a review, *Int. J. Adv. Manuf. Technol.* 97 (2018) 2255–2292.
- [118] J. V. Abellán-Nebot, H.R. Siller, C. Vila, C.A. Rodríguez, An experimental study of process variables in turning operations of Ti-6Al-4V and Cr-Co spherical prostheses, *Int. J. Adv. Manuf. Technol.* 63 (2012) 887–902. <https://doi.org/10.1007/s00170-012-3955-0>.
- [119] J.S. Hirschhorn, A.A. McBeath, M.R. Dustoor, Porous titanium surgical implant materials, *J. Biomed. Mater. Res.* 5 (1971) 49–67. <https://doi.org/10.1002/jbm.820050608>.
- [120] H. Hahn, W. Palich, Preliminary evaluation of porous metal surfaced titanium for orthopedic implants, *J. Biomed. Mater. Res. Part A.* 4 (1970) 571–577.
- [121] J. Galante, W. Rostoker, R. Lueck, R.D. RAY, Sintered fiber metal composites as a basis for attachment of implants to bone, *JBJS.* 53 (1971) 101–114.
- [122] M.T. Karagianes, Porous Metals as a Hard Tissue Substitute, *Biomater. Med. Devices. Artif. Organs.* 1 (1973) 171–181. <https://doi.org/10.3109/10731197309118871>.
- [123] J.L. Ong, D.L. Carnes, K. Bessho, Evaluation of titanium plasma-sprayed and plasma-sprayed hydroxyapatite implants in vivo, *Biomaterials.* 25 (2004) 4601–4606. <https://doi.org/10.1016/j.biomaterials.2003.11.053>.
- [124] S. Vercaigne, J.G.C. Wolke, I. Naert, J.A. Jansen, Bone healing capacity of titanium plasma-sprayed and hydroxylapatite-coated oral implants, *Clin. Oral Implants Res.* 9 (1998) 261–271. <https://doi.org/10.1034/j.1600-0501.1998.090407.x>.

- [125] J. Banhart, Manufacture, characterisation and application of cellular metals and metal foams, *Prog. Mater. Sci.* 46 (2001) 559–632. [https://doi.org/10.1016/S0079-6425\(00\)00002-5](https://doi.org/10.1016/S0079-6425(00)00002-5).
- [126] G. Ryan, A. Pandit, D.P. Apatsidis, Fabrication methods of porous metals for use in orthopaedic applications, *Biomaterials.* 27 (2006) 2651–2670. <https://doi.org/10.1016/j.biomaterials.2005.12.002>.
- [127] C. Körner, R.F. Singer, Processing of Metal Foams—Challenges and Opportunities, *Adv. Eng. Mater.* 2 (2000) 159–165. [https://doi.org/10.1002/\(SICI\)1527-2648\(200004\)2:4<159::AID-ADEM159>3.0.CO;2-O](https://doi.org/10.1002/(SICI)1527-2648(200004)2:4<159::AID-ADEM159>3.0.CO;2-O).
- [128] I.H. Oh, N. Nomura, N. Masahashi, S. Hanada, Mechanical properties of porous titanium compacts prepared by powder sintering, *Scr. Mater.* 49 (2003) 1197–1202. <https://doi.org/10.1016/j.scriptamat.2003.08.018>.
- [129] J.M. Martell, R.H. Pierson, J.J. Jacobs, A.G. Rosenberg, M. Maley, J.O. Galante, Primary total hip reconstruction with a titanium fiber-coated prosthesis inserted without cement., *J. Bone Jt. Surg.* 75 (1993) 554–571. <https://doi.org/10.2106/00004623-199304000-00010>.
- [130] F. Li, J. Li, G. Xu, G. Liu, H. Kou, L. Zhou, Fabrication, pore structure and compressive behavior of anisotropic porous titanium for human trabecular bone implant applications, *J. Mech. Behav. Biomed. Mater.* 46 (2015) 104–114. <https://doi.org/10.1016/j.jmbbm.2015.02.023>.
- [131] Y. Yamada, K. Shimojima, Y. Sakaguchi, M. Mabuchi, M. Nakamura, T. Asahina, T. Mukai, H. Kanahashi, K. Higashi, Processing of Cellular Magnesium Materials, *Adv. Eng. Mater.* 2 (2000) 184–187. [https://doi.org/10.1002/\(SICI\)1527-2648\(200004\)2:4<184::AID-ADEM184>3.0.CO;2-W](https://doi.org/10.1002/(SICI)1527-2648(200004)2:4<184::AID-ADEM184>3.0.CO;2-W).
- [132] M. Bram, C. Stiller, H.P. Buchkremer, D. Stöver, H. Baur, High-Porosity Titanium, Stainless Steel, and Superalloy Parts, *Adv. Eng. Mater.* 2 (2000) 196–199. [https://doi.org/10.1002/\(SICI\)1527-2648\(200004\)2:4<196::AID-ADEM196>3.0.CO;2-K](https://doi.org/10.1002/(SICI)1527-2648(200004)2:4<196::AID-ADEM196>3.0.CO;2-K).
- [133] R. Cohen, A porous tantalum trabecular metal: basic science., *Am. J. Orthop. (Belle Mead. NJ)*. 31 (2002) 216–217.

- [134] J.D. Bobyn, G.J. Stackpool, S.A. Hacking, M. Tanzer, J.J. Krygier, Characteristics of bone ingrowth and interface mechanics of a new porous tantalum biomaterial., *J. Bone Jt. Surgery.* 81 (1999) 907–914. <https://doi.org/10.1302/0301-620X.81B5.9283>.
- [135] M.J. Dunbar, D.A.J. Wilson, A.W. Hennigar, J.D. Amirault, M. Gross, G.P. Reardon, Prospective Randomized Study Fixation of a Trabecular Metal Knee Arthroplasty Component. A Fixation of a Trabecular Metal Knee Arthroplasty Component A Prospective Randomized Study, *J Bone Jt. Surg Am.* (2009) 1578–1586. <https://doi.org/10.2106/JBJS.H.00282>.
- [136] A.S. Unger, R.J. Lewis, T. Gruen, Evaluation of a porous tantalum uncemented acetabular cup in revision total hip arthroplasty: Clinical and radiological results of 60 hips, *J. Arthroplasty.* 20 (2005) 1002–1009. <https://doi.org/10.1016/j.arth.2005.01.023>.
- [137] T.G. Nieh, J.H. Kinney, J. Wadsworth, A.J.C. Ladd, Morphology and elastic properties of aluminum foams produced by a casting technique, *Scr. Mater.* 38 (1998) 1487–1494. [https://doi.org/10.1016/S1359-6462\(98\)00090-6](https://doi.org/10.1016/S1359-6462(98)00090-6).
- [138] J. Kováčik, F. Simančík, Aluminium foam - modulus of elasticity and electrical conductivity according to percolation theory, *Scr. Mater.* 39 (1998) 239–246. [https://doi.org/10.1016/S1359-6462\(98\)00151-1](https://doi.org/10.1016/S1359-6462(98)00151-1).
- [139] H. Fusheng, Z. Zhengang, The mechanical behavior of foamed aluminum, *J. Mater. Sci.* 34 (1999) 291–299. <https://doi.org/10.1023/A:1004401521842>.
- [140] L.J. Gibson, M.F. Ashby, Cellular solids. Structure and properties, (1997) 502. <https://doi.org/10.1017/CBO9781139878326>.
- [141] M.F. Ashby, T. Evans, N.A. Fleck, J.W. Hutchinson, H.N.G. Wadley, L.J. Gibson, Metal foams: a design guide, in: Elsevier, 2000: pp. 40–53.
- [142] V.S. Deshpande, M.F. Ashby, N.A. Fleck, Foam topology: Bending versus stretching dominated architectures, *Acta Mater.* 49 (2001) 1035–1040. [https://doi.org/10.1016/S1359-6454\(00\)00379-7](https://doi.org/10.1016/S1359-6454(00)00379-7).
- [143] L.J. Gibson, M.F. Ashby, The Mechanics of Three-Dimensional Cellular Materials, *Proc. R. Soc. A.* 382 (1982). <https://doi.org/DOI:10.1098/rspa.1982.0088>.

- [144] S. Pellegrino, C.R. Calladine, Matrix analysis of statically and kinematically indeterminate frameworks, *Int. J. Solids Struct.* 22 (1986) 409–428. [https://doi.org/10.1016/0020-7683\(86\)90014-4](https://doi.org/10.1016/0020-7683(86)90014-4).
- [145] W.E. Frazier, Metal additive manufacturing: A review, *J. Mater. Eng. Perform.* 23 (2014) 1917–1928. <https://doi.org/10.1007/s11665-014-0958-z>.
- [146] I. Gibson, D. Rosen, B. Stucker, I. Gibson, D. Rosen, B. Stucker, Directed Energy Deposition Processes, in: *Addit. Manuf. Technol.*, Springer New York, 2015: pp. 245–268. https://doi.org/10.1007/978-1-4939-2113-3_10.
- [147] S. Kiakidis, M. (mentor) Hermans, Mechanical and corrosion behaviour of 3D printed aluminium bronzes produced by wire+arc additive manufacturing: In collaboration with RAMLAB (master's thesis), Delft University of Technology, 2017. <https://repository.tudelft.nl/islandora/object/uuid:6394e228-595a-4b1b-bbeb-ae0e98b86f97?collection=education>.
- [148] W. Ya, K. Hamilton, On-Demand Spare Parts for the Marine Industry with Directed Energy Deposition: Propeller Use Case, in: M. Meboldt, C. Klahn (Eds.), *Ind. Addit. Manuf. - Proc. Addit. Manuf. Prod. Appl. - AMPA2017*, Springer International Publishing, Cham, 2018: pp. 70–81. https://doi.org/10.1007/978-3-319-66866-6_7.
- [149] S.W. Williams, F. Martina, A.C. Addison, J. Ding, G. Pardal, P. Colegrove, Wire + Arc Additive Manufacturing, *Mater. Sci. Technol.* 32 (2016) 641–647. <https://doi.org/10.1179/1743284715Y.0000000073>.
- [150] B. Wu, Z. Pan, D. Ding, D. Cuiuri, H. Li, J. Xu, J. Norrish, A review of the wire arc additive manufacturing of metals: properties, defects and quality improvement, *J. Manuf. Process.* 35 (2018) 127–139. <https://doi.org/10.1016/j.jmapro.2018.08.001>.
- [151] M.L. Griffith, D.M. Keicher, C.L. Atwood, J. a. Romero, J.E. Smugeresky, L.D. Harwell, D.L. Greene, Free Form Fabrication of Metallic Components Using Laser Engineered Net Shaping (LENS), *Proc. 7th Solid Free. Fabr. Symp.* (1996) 125–132. <https://doi.org/https://doi.org/10.4028/www.scientific.net/AMR.15-17.175>.
- [152] C. Atwood, M. Griffith, L. Harwell, E. Schlienger, M. Ensz, J. Smugeresky, T. Romero, D. Greene, D. Reckaway, Laser engineered net shaping (LENS™): A tool for direct fabrication of metal parts, *Int. Congr. Appl. Lasers Electro-Optics.* 1998 (1998) E1–E7.

<https://doi.org/10.2351/1.5059147>.

- [153] L. Xue, Y. Li, J. Chen, S. Wang, Laser consolidation-a novel additive manufacturing process for making net-shape functional metallic components for gas turbine applications, in: Proc. ASME Turbo Expo, American Society of Mechanical Engineers (ASME), 2015. <https://doi.org/10.1115/GT2015-43971>.
- [154] C. Schneider-Maunoury, L. Weiss, P. Acquier, D. Boisselier, P. Laheurte, Functionally graded Ti6Al4V-Mo alloy manufactured with DED-CLAD® process, *Addit. Manuf.* 17 (2017) 55–66. <https://doi.org/10.1016/j.addma.2017.07.008>.
- [155] M. Fischer, P. Laheurte, P. Acquier, D. Joguet, L. Peltier, T. Petithory, K. Anselme, P. Mille, Synthesis and characterization of Ti-27.5Nb alloy made by CLAD® additive manufacturing process for biomedical applications, *Mater. Sci. Eng. C.* 75 (2017) 341–348. <https://doi.org/10.1016/j.msec.2017.02.060>.
- [156] I. Gibson, D. Rosen, B. Stucker, I. Gibson, D. Rosen, B. Stucker, Powder Bed Fusion Processes, in: *Addit. Manuf. Technol.*, Springer New York, 2015: pp. 107–145. https://doi.org/10.1007/978-1-4939-2113-3_5.
- [157] Y. Bai, C.B. Williams, Binder jetting additive manufacturing with a particle-free metal ink as a binder precursor, *Mater. Des.* 147 (2018) 146–156. <https://doi.org/10.1016/j.matdes.2018.03.027>.
- [158] M. Galati, P. Minetola, Analysis of Density, Roughness, and Accuracy of the Atomic Diffusion Additive Manufacturing (ADAM) Process for Metal Parts, *Materials (Basel)*. 12 (2019) 4122. <https://doi.org/10.3390/ma12244122>.
- [159] I.H. Karampelas, S. Vader, Z. Vader, V. Sukhotskiy, A. Verma, G. Garg, M. Tong, E. Furlani, Drop-on-demand 3D metal printing, *Informatics, Electron. Microsystems*. (2017) 153–155.
- [160] M. Simonelli, N. Aboulkhair, M. Rasa, M. East, C. Tuck, R. Wildman, O. Salomons, R. Hague, Towards digital metal additive manufacturing via high-temperature drop-on-demand jetting, *Addit. Manuf.* 30 (2019) 100930. <https://doi.org/10.1016/j.addma.2019.100930>.
- [161] V. Bhavar, P. Kattire, V. Patil, S. Khot, K. Gujar, R. Singh, A review on powder bed fusion technology of metal additive manufacturing, in: 4th Int. Conf. Exhib. *Addit. Manuf.*

Technol., 2014: pp. 1–2.

- [162] S. Ghouse, S. Babu, R.J. Van Arkel, K. Nai, P.A. Hooper, J.R.T. Jeffers, The influence of laser parameters and scanning strategies on the mechanical properties of a stochastic porous material, *Mater. Des.* 131 (2017) 498–508. <https://doi.org/10.1016/j.matdes.2017.06.041>.
- [163] Renishaw plc, Renishaw resource centre, (2020). <https://resources.renishaw.com/> (accessed June 2, 2020).
- [164] J. Kruth, B. Vandenbroucke, J. Vaerenbergh, P. Mercelis, Benchmarking of different SLS/SLM processes as rapid manufacturing techniques, *Int. Conf. Polym. Mould. Innov. (PMI)*, Gent, Belgium, April 20–23, 2005. (2005) 1–7. <https://doi.org/10.1002/adv.21381>.
- [165] B. Vayre, F. Vignat, F. Villeneuve, Metallic additive manufacturing: state-of-the-art review and prospects, *Mech. Ind.* 13 (2012) 89–96. <https://doi.org/10.1051/meca/2012003>.
- [166] E. Sallica-Leva, A.L. Jardini, J.B. Fogagnolo, Microstructure and mechanical behavior of porous Ti–6Al–4V parts obtained by selective laser melting, *J. Mech. Behav. Biomed. Mater.* 26 (2013) 98–108. <https://doi.org/10.1016/j.jmbbm.2013.05.011>.
- [167] M. Salmi, J. Tuomi, K.S. Paloheimo, R. Björkstrand, M. Paloheimo, J. Salo, R. Kontio, K. Mesimäki, A.A. Mäkitie, Patient-specific reconstruction with 3D modeling and DMLS additive manufacturing, *Rapid Prototyp. J.* 18 (2012) 209–214. <https://doi.org/10.1108/13552541211218126>.
- [168] A. Popovich, V. Sufiiarov, I. Polozov, E. Borisov, D. Masaylo, Producing hip implants of titanium alloys by additive manufacturing, *Int. J. Bioprinting.* 2 (2016) 78–84. <https://doi.org/10.18063/IJB.2016.02.004>.
- [169] P. Unwin, Fabricating specialised orthopaedic implants using additive manufacturing, *SPIE Photonics West 2014-LASE Lasers Sources.* 8970 (2014) 897005. <https://doi.org/10.1117/12.2044272>.
- [170] A.L. Jardini, M.A. Larosa, C.A. de Carvalho Zavaglia, L.F. Bernardes, C.S. Lambert, P. Kharmandayan, D. Calderoni, R. Maciel Filho, Customised titanium implant fabricated in additive manufacturing for craniomaxillofacial surgery: This paper discusses the

- design and fabrication of a metallic implant for the reconstruction of a large cranial defect, *Virtual Phys. Prototyp.* 9 (2014) 115–125. <https://doi.org/10.1080/17452759.2014.900857>.
- [171] A.J. Miller, J.D. Stimac, L.S. Smith, A.W. Feher, M.R. Yakkanti, A.L. Malkani, Results of Cemented vs Cementless Primary Total Knee Arthroplasty Using the Same Implant Design, *J. Arthroplasty.* 33 (2018) 1089–1093. <https://doi.org/10.1016/j.arth.2017.11.048>.
- [172] V.J. Challis, X. Xu, L.C. Zhang, A.P. Roberts, J.F. Grotowski, T.B. Sercombe, High specific strength and stiffness structures produced using selective laser melting, *Mater. Des.* 63 (2014) 783–788. <https://doi.org/10.1016/j.matdes.2014.05.064>.
- [173] T. Tancogne-Dejean, M. Diamantopoulou, M.B. Gorji, C. Bonatti, D. Mohr, 3D Plate-Lattices: An Emerging Class of Low-Density Metamaterial Exhibiting Optimal Isotropic Stiffness, *Adv. Mater.* 30 (2018) 1–6. <https://doi.org/10.1002/adma.201803334>.
- [174] E.R. Neovius, *Bestimmung zweier speciellen periodischen Minimalflächen*, Helsingfors: Akad, (1883).
- [175] A.H. Schoen, *Infinite periodic minimal surfaces without self-intersections*, National Aeronautics and Space Administration, 1970.
- [176] I. Maskery, L. Sturm, A.O. Aremu, A. Panesar, C.B. Williams, C.J. Tuck, R.D. Wildman, I.A. Ashcroft, R.J.M. Hague, Insights into the mechanical properties of several triply periodic minimal surface lattice structures made by polymer additive manufacturing, *Polymer (Guildf)*. 152 (2018) 62–71. <https://doi.org/10.1016/j.polymer.2017.11.049>.
- [177] A.A. Zadpoor, Bone tissue regeneration: The role of scaffold geometry, *Biomater. Sci.* 3 (2015) 231–245. <https://doi.org/10.1039/c4bm00291a>.
- [178] C.M. Bidan, F.M. Wang, J.W.C. Dunlop, A three-dimensional model for tissue deposition on complex surfaces, *Comput. Methods Biomech. Biomed. Engin.* 16 (2013) 1056–1070. <https://doi.org/10.1080/10255842.2013.774384>.
- [179] D.-J. Yoo, Advanced porous scaffold design using multi-void triply periodic minimal surface models with high surface area to volume ratios, *Int. J. Precis. Eng. Manuf.* 15 (2014) 1657–1666. <https://doi.org/10.1007/s12541-014-0516-5>.

- [180] O. Sigmund, K. Maute, Topology optimization approaches: A comparative review, *Struct. Multidiscip. Optim.* 48 (2013) 1031–1055. <https://doi.org/10.1007/s00158-013-0978-6>.
- [181] M.P. Bendsøe, N. Kikuchi, Generating optimal topologies in structural design using a homogenization method, *Comput. Methods Appl. Mech. Eng.* 71 (1988) 197–224. [https://doi.org/10.1016/0045-7825\(88\)90086-2](https://doi.org/10.1016/0045-7825(88)90086-2).
- [182] A. Takezawa, K. Yonekura, Y. Koizumi, X. Zhang, M. Kitamura, Isotropic Ti–6Al–4V lattice via topology optimization and electron-beam melting, *Addit. Manuf.* 22 (2018) 634–642. <https://doi.org/10.1016/j.addma.2018.06.008>.
- [183] X.Y. Yang, X. Huang, J.H. Rong, Y.M. Xie, Design of 3D orthotropic materials with prescribed ratios for effective Young's moduli, *Comput. Mater. Sci.* 67 (2013) 229–237. <https://doi.org/10.1016/j.commatsci.2012.08.043>.
- [184] X. Huang, A. Radman, Y.M. Xie, Topological design of microstructures of cellular materials for maximum bulk or shear modulus, *Comput. Mater. Sci.* 50 (2011) 1861–1870. <https://doi.org/10.1016/j.commatsci.2011.01.030>.
- [185] A. Panesar, M. Abdi, D. Hickman, I. Ashcroft, Strategies for functionally graded lattice structures derived using topology optimisation for Additive Manufacturing, *Addit. Manuf.* 19 (2018) 81–94. <https://doi.org/10.1016/j.addma.2017.11.008>.
- [186] L. Mullen, R.C. Stamp, P. Fox, E. Jones, C. Ngo, C.J. Sutcliffe, Selective laser melting: A unit cell approach for the manufacture of porous, titanium, bone in-growth constructs, suitable for orthopedic applications. II. Randomized structures, *J. Biomed. Mater. Res. - Part B Appl. Biomater.* 92 (2010) 178–188. <https://doi.org/10.1002/jbm.b.31504>.
- [187] N. Contuzzi, S.L. Campanelli, F. Caiazzo, V. Alfieri, Design and Fabrication of Random Metal Foam Structures for Laser Powder Bed Fusion, *Materials (Basel)*. 12 (2019) 1301. <https://doi.org/10.3390/ma12081301>.
- [188] L.E. Murr, S.M. Gaytan, F. Medina, H. Lopez, E. Martinez, B.I. Machado, D.H. Hernandez, L. Martinez, M.I. Lopez, R.B. Wicker, J. Bracke, Next-generation biomedical implants using additive manufacturing of complex, cellular and functional mesh arrays, *Philos. Trans. R. Soc. A Math. Phys. Eng. Sci.* 368 (2010) 1999–2032. <https://doi.org/10.1098/rsta.2010.0010>.

- [189] V.S. Deshpande, N.A. Fleck, M.F. Ashby, Effective properties of the octet-truss lattice material, *J. Mech. Phys. Solids.* 49 (2001) 1747–1769. [https://doi.org/10.1016/S0022-5096\(01\)00010-2](https://doi.org/10.1016/S0022-5096(01)00010-2).
- [190] M. Mazur, M. Leary, S. Sun, M. Vcelka, D. Shidid, M. Brandt, Deformation and failure behaviour of Ti-6Al-4V lattice structures manufactured by selective laser melting (SLM), *Int. J. Adv. Manuf. Technol.* 84 (2016) 1391–1411. <https://doi.org/10.1007/s00170-015-7655-4>.
- [191] Z. Dong, Y. Liu, W. Li, J. Liang, Orientation dependency for microstructure, geometric accuracy and mechanical properties of selective laser melting AlSi10Mg lattices, *J. Alloys Compd.* 791 (2019) 490–500. <https://doi.org/10.1016/j.jallcom.2019.03.344>.
- [192] K. Ushijima, W.J. Cantwell, D.H. Chen, Prediction of the mechanical properties of micro-lattice structures subjected to multi-axial loading, *Int. J. Mech. Sci.* 68 (2013) 47–55. <https://doi.org/10.1016/j.ijmecsci.2012.12.017>.
- [193] S. Van Bael, G. Kerckhofs, M. Moesen, G. Pyka, J. Schrooten, J.P. Kruth, Micro-CT-based improvement of geometrical and mechanical controllability of selective laser melted Ti6Al4V porous structures, *Mater. Sci. Eng. A.* 528 (2011) 7423–7431. <https://doi.org/10.1016/j.msea.2011.06.045>.
- [194] J. Sun, Y. Yang, D. Wang, Mechanical properties of a Ti6Al4V porous structure produced by selective laser melting, *Mater. Des.* 49 (2013) 545–552. <https://doi.org/10.1016/j.matdes.2013.01.038>.
- [195] S. Limmahakhun, A. Oloyede, K. Sitthiseripratip, Y. Xiao, C. Yan, Stiffness and strength tailoring of cobalt chromium graded cellular structures for stress-shielding reduction, *Mater. Des.* 114 (2017) 633–641. <https://doi.org/10.1016/j.matdes.2016.11.090>.
- [196] N. Taniguchi, S. Fujibayashi, M. Takemoto, K. Sasaki, B. Otsuki, T. Nakamura, T. Matsushita, T. Kokubo, S. Matsuda, Effect of pore size on bone ingrowth into porous titanium implants fabricated by additive manufacturing: An in vivo experiment, *Mater. Sci. Eng. C.* 59 (2016) 690–701. <https://doi.org/10.1016/j.msec.2015.10.069>.
- [197] R. Wauthle, J. Van Der Stok, S.A. Yavari, J. Van Humbeeck, J.P. Kruth, A.A. Zadpoor, H. Weinans, M. Mulier, J. Schrooten, Additively manufactured porous tantalum implants, *Acta Biomater.* 14 (2015) 217–225. <https://doi.org/10.1016/j.actbio.2014.12.003>.

- [198] F.S.L. Bobbert, K. Lietaert, A.A. Eftekhari, B. Pouran, S.M. Ahmadi, H. Weinans, A.A. Zadpoor, Additively manufactured metallic porous biomaterials based on minimal surfaces: A unique combination of topological, mechanical, and mass transport properties, *Acta Biomater.* 53 (2016) 572–584. <https://doi.org/10.1016/j.actbio.2017.02.024>.
- [199] C. Simoneau, P. Terriault, B. Jetté, M. Dumas, V. Brailovski, Development of a porous metallic femoral stem: Design, manufacturing, simulation and mechanical testing, *Mater. Des.* 114 (2017) 546–556. <https://doi.org/10.1016/j.matdes.2016.10.064>.
- [200] L. Liu, P. Kamm, F. García-Moreno, J. Banhart, D. Pasini, Elastic and failure response of imperfect three-dimensional metallic lattices: the role of geometric defects induced by Selective Laser Melting, *J. Mech. Phys. Solids.* 107 (2017) 160–184. <https://doi.org/10.1016/j.jmps.2017.07.003>.
- [201] S. Tsopanos, R.A.W. Mines, S. McKown, Y. Shen, W.J. Cantwell, W. Brooks, C.J. Sutcliffe, The Influence of Processing Parameters on the Mechanical Properties of Selectively Laser Melted Stainless Steel Microlattice Structures, *J. Manuf. Sci. Eng.* 132 (2010) 041011. <https://doi.org/10.1115/1.4001743>.
- [202] M. Smith, Z. Guan, W.J. Cantwell, Finite element modelling of the compressive response of lattice structures manufactured using the selective laser melting technique, *Int. J. Mech. Sci.* 67 (2013) 28–41. <https://doi.org/10.1016/j.ijmecsci.2012.12.004>.
- [203] P. Li, Constitutive and failure behaviour in selective laser melted stainless steel for microlattice structures, *Mater. Sci. Eng. A.* 622 (2015) 114–120. <https://doi.org/10.1016/j.msea.2014.11.028>.
- [204] S. Ruiz de Galarreta, J.R.T. Jeffers, S. Ghouse, A validated finite element analysis procedure for porous structures, *Mater. Des.* 189 (2020) 108546. <https://doi.org/10.1016/j.matdes.2020.108546>.
- [205] B. Lozanovski, M. Leary, P. Tran, D. Shidid, M. Qian, P. Choong, M. Brandt, Computational modelling of strut defects in SLM manufactured lattice structures, *Mater. Des.* 171 (2019) 107671. <https://doi.org/10.1016/j.matdes.2019.107671>.
- [206] A. du Plessis, I. Yadroitsava, I. Yadroitsev, S.G. le Roux, D.C. Blaine, Numerical

- comparison of lattice unit cell designs for medical implants by additive manufacturing, *Virtual Phys. Prototyp.* 13 (2018) 266–281. <https://doi.org/10.1080/17452759.2018.1491713>.
- [207] V. Weißmann, R. Bader, H. Hansmann, N. Laufer, Influence of the structural orientation on the mechanical properties of selective laser melted Ti6Al4V open-porous scaffolds, *Mater. Des.* 95 (2016) 188–197. <https://doi.org/10.1016/j.matdes.2016.01.095>.
- [208] J. Van Der Stok, O.P. Van Der Jagt, S. Amin Yavari, M.F.P. De Haas, J.H. Waarsing, H. Jahr, E.M.M. Van Lieshout, P. Patka, J.A.N. Verhaar, A.A. Zadpoor, H. Weinans, Selective laser melting-produced porous titanium scaffolds regenerate bone in critical size cortical bone defects, *J. Orthop. Res.* 31 (2013) 792–799. <https://doi.org/10.1002/jor.22293>.
- [209] D. Melancon, Z.S. Bagheri, R.B. Johnston, L. Liu, M. Tanzer, D. Pasini, Mechanical characterization of structurally porous biomaterials built via additive manufacturing: experiments, predictive models, and design maps for load-bearing bone replacement implants, *Acta Biomater.* 63 (2017) 350–368. <https://doi.org/10.1016/j.actbio.2017.09.013>.
- [210] C. Yan, L. Hao, A. Hussein, P. Young, Ti-6Al-4V triply periodic minimal surface structures for bone implants fabricated via selective laser melting, *J. Mech. Behav. Biomed. Mater.* 51 (2015) 61–73. <https://doi.org/10.1016/j.jmbbm.2015.06.024>.
- [211] R. Wauthle, S.M. Ahmadi, S. Amin Yavari, M. Mulier, A.A. Zadpoor, H. Weinans, J. Van Humbeeck, J.-P. Kruth, J. Schrooten, Revival of pure titanium for dynamically loaded porous implants using additive manufacturing, *Mater. Sci. Eng. C.* 54 (2015) 94–100. <https://doi.org/10.1016/j.msec.2015.05.001>.
- [212] J. Parthasarathy, B. Starly, S. Raman, A. Christensen, Mechanical evaluation of porous titanium (Ti6Al4V) structures with electron beam melting (EBM), *J. Mech. Behav. Biomed. Mater.* 3 (2010) 249–259. <https://doi.org/10.1016/j.jmbbm.2009.10.006>.
- [213] A. Cuadrado, A. Yáñez, O. Martel, S. Deviaene, D. Monopoli, Influence of load orientation and of types of loads on the mechanical properties of porous Ti6Al4V biomaterials, *Mater. Des.* 135 (2017) 309–318. <https://doi.org/10.1016/j.matdes.2017.09.045>.

- [214] A. Ataee, Y. Li, D. Fraser, G. Song, C. Wen, Anisotropic Ti-6Al-4V gyroid scaffolds manufactured by electron beam melting (EBM) for bone implant applications, *Mater. Des.* 137 (2018) 345–354. <https://doi.org/10.1016/j.matdes.2017.10.040>.
- [215] P. Heinl, L. Müller, C. Körner, R.F. Singer, F.A. Müller, Cellular Ti-6Al-4V structures with interconnected macro porosity for bone implants fabricated by selective electron beam melting, *Acta Biomater.* 4 (2008) 1536–1544. <https://doi.org/10.1016/j.actbio.2008.03.013>.
- [216] S. Xu, J. Shen, S. Zhou, X. Huang, Y.M. Xie, Design of lattice structures with controlled anisotropy, *Mater. Des.* 93 (2016) 443–447. <https://doi.org/10.1016/j.matdes.2016.01.007>.
- [217] J. Martínez, H. Song, J. Dumas, S. Lefebvre, Orthotropic k -nearest foams for additive manufacturing, *ACM Trans. Graph.* 36 (2017) 1–12. <https://doi.org/10.1145/3072959.3073638>.
- [218] J. Wu, N. Aage, R. Westermann, O. Sigmund, Infill Optimization for Additive Manufacturing - Approaching Bone-Like Porous Structures, *IEEE Trans. Vis. Comput. Graph.* 24 (2018) 1127–1140. <https://doi.org/10.1109/TVCG.2017.2655523>.
- [219] P.F. Egan, V.C. Gonella, M. Engensperger, S.J. Ferguson, K. Shea, Computationally designed lattices with tuned properties for tissue engineering using 3D printing, *PLoS One.* 12 (2017) 1–20. <https://doi.org/10.1371/journal.pone.0182902>.
- [220] M. Alaña, A. Lopez-Arancibia, A. Pradera-Mallabiarrena, S. Ruiz de Galarreta, Analytical model of the elastic behavior of a modified face-centered cubic lattice structure, *J. Mech. Behav. Biomed. Mater.* 98 (2019) 357–368. <https://doi.org/10.1016/j.jmbbm.2019.05.043>.
- [221] A. Yáñez, A. Herrera, O. Martel, D. Monopoli, H. Afonso, Compressive behaviour of gyroid lattice structures for human cancellous bone implant applications, *Mater. Sci. Eng. C.* 68 (2016) 445–448. <https://doi.org/10.1016/j.msec.2016.06.016>.
- [222] S. Arabnejad Khanoki, D. Pasini, Multiscale Design and Multiobjective Optimization of Orthopaedic Cellular Hip Implants, *ASME 2011 Int. Des. Eng. Tech. Conf. Comput. Inf. Eng. Conf.* (2011). <https://doi.org/10.1115/1.4006115>.
- [223] S.A. Khanoki, D. Pasini, The Fatigue Design of a Bone Preserving Hip Implant With

- Functionally Graded Cellular Material, *J. Med. Device.* 7 (2013) 20907. <https://doi.org/10.1115/1.4024310>.
- [224] S. Arabnejad Khanoki, D. Pasini, Multiscale Design and Multiobjective Optimization of Orthopedic Hip Implants with Functionally Graded Cellular Material, *J. Biomech. Eng.* 134 (2012) 031004. <https://doi.org/10.1115/1.4006115>.
- [225] S. Arabnejad, B. Johnston, M. Tanzer, D. Pasini, Fully porous 3D printed titanium femoral stem to reduce stress-shielding following total hip arthroplasty - SUPPORTING INFO, *J. Orthop. Res.* (2016). <https://doi.org/10.1002/jor.23445>.
- [226] B. Jetté, V. Brailovski, M. Dumas, C. Simoneau, P. Terriault, Femoral stem incorporating a diamond cubic lattice structure: Design, manufacture and testing, *J. Mech. Behav. Biomed. Mater.* 77 (2018) 58–72. <https://doi.org/10.1016/j.jmbbm.2017.08.034>.
- [227] J. Wieding, A. Wolf, R. Bader, Numerical optimization of open-porous bone scaffold structures to match the elastic properties of human cortical bone, *J. Mech. Behav. Biomed. Mater.* 37 (2014) 56–68. <https://doi.org/10.1016/j.jmbbm.2014.05.002>.
- [228] P. Zhang, J. Toman, Y. Yu, E. Biyikli, M. Kirca, M. Chmielus, A.C. To, Efficient Design-Optimization of Variable-Density Hexagonal Cellular Structure by Additive Manufacturing: Theory and Validation, *J. Manuf. Sci. Eng.* 137 (2015) 021004. <https://doi.org/10.1115/1.4028724>.
- [229] A. Rahimizadeh, Z. Nourmohammadi, S. Arabnejad, M. Tanzer, D. Pasini, Porous architected biomaterial for a tibial-knee implant with minimum bone resorption and bone-implant interface micromotion, *J. Mech. Behav. Biomed. Mater.* 78 (2018) 465–479. <https://doi.org/10.1016/j.jmbbm.2017.11.041>.
- [230] S. Gómez, M.D. Vlad, J. López, E. Fernández, Design and properties of 3D scaffolds for bone tissue engineering, *Acta Biomater.* 42 (2016) 341–350. <https://doi.org/10.1016/j.actbio.2016.06.032>.
- [231] A. Boccaccio, A.E. Uva, M. Fiorentino, L. Lamberti, G. Monno, A mechanobiology-based algorithm to optimize the microstructure geometry of bone tissue scaffolds, *Int. J. Biol. Sci.* 12 (2016) 1–17. <https://doi.org/10.7150/ijbs.13158>.
- [232] C. Schumacher, B. Bickel, J. Rys, S. Marschner, C. Daraio, M. Gross, Microstructures to control elasticity in 3D printing, *ACM Trans. Graph.* 34 (2015) 136:1–136:13.

<https://doi.org/10.1145/2766926>.

- [233] N. Yang, Z. Quan, D. Zhang, Y. Tian, Multi-morphology transition hybridization CAD design of minimal surface porous structures for use in tissue engineering, *CAD Comput. Aided Des.* 56 (2014) 11–21. <https://doi.org/10.1016/j.cad.2014.06.006>.
- [234] S.Y. Choy, C.N. Sun, K.F. Leong, J. Wei, Compressive properties of functionally graded lattice structures manufactured by selective laser melting, *Mater. Des.* 131 (2017) 112–120. <https://doi.org/10.1016/j.matdes.2017.06.006>.
- [235] C. Han, Y. Li, Q. Wang, S. Wen, Q. Wei, C. Yan, L. Hao, J. Liu, Y. Shi, Continuous functionally graded porous titanium scaffolds manufactured by selective laser melting for bone implants, *J. Mech. Behav. Biomed. Mater.* 80 (2018) 119–127. <https://doi.org/10.1016/j.jmbbm.2018.01.013>.
- [236] M. Dumas, P. Terriault, V. Brailovski, Modelling and characterization of a porosity graded lattice structure for additively manufactured biomaterials, *Mater. Des.* 121 (2017) 383–392. <https://doi.org/10.1016/j.matdes.2017.02.021>.
- [237] S. Arabnejad, B. Johnston, M. Tanzer, D. Pasini, Fully porous 3D printed titanium femoral stem to reduce stress-shielding following total hip arthroplasty, *J. Orthop. Res.* (2016) 29–31. <https://doi.org/10.1002/jor.23445>.
- [238] British Standard, ISO 13314:2011(E) Mechanical testing of metals – ductility testing – compression test for porous and cellular metals, 2011 (2011) 1–7.
- [239] S.R. Kalidindi, A. Abusafieh, E. El-Danaf, Accurate characterization of machine compliance for simple compression testing, *Exp. Mech.* 37 (1997) 210–215. <https://doi.org/10.1007/BF02317861>.
- [240] R. Gümrük, R.A.W. Mines, Compressive behaviour of stainless steel micro-lattice structures, *Int. J. Mech. Sci.* 68 (2013) 125–139. <https://doi.org/10.1016/j.ijmecsci.2013.01.006>.
- [241] R. Hasan, R.A.W. Mines, S. Tsopanos, Determination of Elastic Modulus Value for Selectively Laser Melted Titanium Alloy, *J. Mech. Eng. Technol.* 2 (2010) 17–26.
- [242] Z. Wang, P. Li, Characterisation and constitutive model of tensile properties of selective laser melted Ti-6Al-4V struts for microlattice structures, *Mater. Sci. Eng. A.*

- 725 (2018) 350–358. <https://doi.org/10.1016/j.msea.2018.04.006>.
- [243] BSI, BSI Standards Publication Metallic materials – Tensile testing Part 1 : Method of test at room temperature, Bsi. (2016). <https://doi.org/10.3403/30268532>.
- [244] ASTM Committee on Mechanical Testing, Standard Test Methods for Tension Testing of Metallic Materials, ASTM Int. ASTM Stds. (2013) 1–28. <https://doi.org/10.1520/E0008>.
- [245] R. Vrána, O. Cervinek, P. Manas, D. Koutný, D. Paloušek, Dynamic loading of lattice structure made by selective laser melting-numerical model with substitution of geometrical imperfections, *Materials (Basel)*. 11 (2018). <https://doi.org/10.3390/ma11112129>.
- [246] H. Gong, K. Rafi, H. Gu, T. Starr, B. Stucker, Analysis of defect generation in Ti–6Al–4V parts made using powder bed fusion additive manufacturing processes, *Addit. Manuf.* 1–4 (2014) 87–98. <https://doi.org/10.1016/j.addma.2014.08.002>.
- [247] S.L. Sing, W.Y. Yeong, F.E. Wiria, B.Y. Tay, Characterization of Titanium Lattice Structures Fabricated by Selective Laser Melting Using an Adapted Compressive Test Method, *Exp. Mech.* 56 (2016) 735–748. <https://doi.org/10.1007/s11340-015-0117-y>.
- [248] V. Weißmann, P. Drescher, R. Bader, H. Seitz, H. Hansmann, N. Laufer, Comparison of Single Ti6Al4V Struts Made Using Selective Laser Melting and Electron Beam Melting Subject to Part Orientation, *Metals (Basel)*. 7 (2017) 91. <https://doi.org/10.3390/met7030091>.
- [249] M. Suard, G. Martin, P. Lhuissier, R. Dendievel, F. Vignat, J.J. Blandin, F. Villeneuve, Mechanical equivalent diameter of single struts for the stiffness prediction of lattice structures produced by Electron Beam Melting, *Addit. Manuf.* 8 (2015) 124–131. <https://doi.org/10.1016/j.addma.2015.10.002>.
- [250] S. Cahill, S. Lohfeld, P.E. McHugh, Finite element predictions compared to experimental results for the effective modulus of bone tissue engineering scaffolds fabricated by selective laser sintering, *J. Mater. Sci. Mater. Med.* 20 (2009) 1255–1262. <https://doi.org/10.1007/s10856-009-3693-5>.
- [251] S.I. Park, D.W. Rosen, S. kyum Choi, C.E. Duty, Effective mechanical properties of lattice

- material fabricated by material extrusion additive manufacturing, *Addit. Manuf.* 1 (2014) 12–23. <https://doi.org/10.1016/j.addma.2014.07.002>.
- [252] G. Campoli, M.S. Borleffs, S. Amin Yavari, R. Wauthle, H. Weinans, A.A. Zadpoor, Mechanical properties of open-cell metallic biomaterials manufactured using additive manufacturing, *Mater. Des.* 49 (2013) 957–965. <https://doi.org/10.1016/j.matdes.2013.01.071>.
- [253] H. Karaca, M. Kadkhodaei, S.N. Esfahani, M. Elahinia, A. Ghaei, M.R.K. Ravari, M.T. Andani, On the effects of geometry, defects, and material asymmetry on the mechanical response of shape memory alloy cellular lattice structures, *Smart Mater. Struct.* 25 (2016) 025008. <https://doi.org/10.1088/0964-1726/25/2/025008>.
- [254] X. Cao, Y. Jiang, T. Zhao, P. Wang, Y. Wang, Z. Chen, Y. Li, D. Xiao, D. Fang, Compression experiment and numerical evaluation on mechanical responses of the lattice structures with stochastic geometric defects originated from additive-manufacturing, *Compos. Part B Eng.* 194 (2020) 108030. <https://doi.org/10.1016/j.compositesb.2020.108030>.
- [255] R.M. Gorguluarslan, S.K. Choi, H.J. Choi, Uncertainty quantification and validation of lattice structures fabricated by selective laser melting, in: *Proc. ASME Des. Eng. Tech. Conf., American Society of Mechanical Engineers (ASME)*, 2017. <https://doi.org/10.1115/DETC2017-67438>.
- [256] M. Saunders, *Design for metal AM - a beginner's guide*, Renishaw Plc., Gloucestershire, UK. (2017).
- [257] Renishaw plc., SS 316L-0407 powder for additive manufacturing, (2018). <https://www.renishaw.com/en/data-sheets-additive-manufacturing--17862> (accessed April 1, 2020).
- [258] Renishaw plc., Ti6Al4V ELI-0406 powder for additive manufacturing, (2017). <https://www.renishaw.com/en/data-sheets-additive-manufacturing--17862> (accessed April 1, 2020).
- [259] R. Wauthle, B. Vrancken, B. Beynaerts, K. Jorissen, J. Schrooten, J.P. Kruth, J. Van Humbeeck, Effects of build orientation and heat treatment on the microstructure and mechanical properties of selective laser melted Ti6Al4V lattice structures, *Addit.*

- Manuf. 5 (2015) 77–84. <https://doi.org/10.1016/j.addma.2014.12.008>.
- [260] A. Alghamdi, D. Downing, M. McMillan, M. Brandt, M. Qian, M. Leary, Experimental and numerical assessment of surface roughness for Ti6Al4V lattice elements in selective laser melting, *Int. J. Adv. Manuf. Technol.* 105 (2019) 1275–1293. <https://doi.org/10.1007/s00170-019-04092-4>.
- [261] J. Bültmann, S. Merkt, C. Hammer, C. Hinke, U. Prahl, Scalability of the mechanical properties of selective laser melting produced micro-struts, *J. Laser Appl.* 27 (2015) S29206.
- [262] Y. Shen, S. Mckown, S. Tsopanos, C.J. Sutcliffe, R.A.W. Mines, W.J. Cantwell, The Mechanical Properties of Sandwich Structures Based on Metal Lattice Architectures, *J. Sandw. Struct. Mater.* 12 (2010) 159–180. <https://doi.org/10.1177/1099636209104536>.
- [263] Z.S. Bagheri, D. Melancon, L. Liu, R.B. Johnston, D. Pasini, Compensation strategy to reduce geometry and mechanics mismatches in porous biomaterials built with Selective Laser Melting, *J. Mech. Behav. Biomed. Mater.* 70 (2017) 17–27. <https://doi.org/10.1016/j.jmbbm.2016.04.041>.
- [264] G. Savio, S. Rosso, A. Curtarello, R. Meneghello, G. Concheri, Implications of modeling approaches on the fatigue behavior of cellular solids, *Addit. Manuf.* 25 (2019) 50–58. <https://doi.org/10.1016/j.addma.2018.10.047>.
- [265] F. Liu, D. Zhang, P. Zhang, M. Zhao, S. Jafar, Mechanical Properties of Optimized Diamond Lattice Structure for Bone Scaffolds Fabricated via Selective Laser Melting, *Materials (Basel)*. 11 (2018) 374. <https://doi.org/10.3390/ma11030374>.
- [266] C. de Formanoir, M. Suard, R. Dendievel, G. Martin, S. Godet, Improving the mechanical efficiency of electron beam melted titanium lattice structures by chemical etching, *Addit. Manuf.* 11 (2016) 71–76. <https://doi.org/10.1016/j.addma.2016.05.001>.
- [267] S.A. Goldstein, The mechanical properties of trabecular bone: Dependence on anatomic location and function, *J. Biomech.* 20 (1987) 1055–1061. [https://doi.org/10.1016/0021-9290\(87\)90023-6](https://doi.org/10.1016/0021-9290(87)90023-6).
- [268] J.Y. Rho, L. Kuhn-Spearing, P. Zioupos, Mechanical properties and the hierarchical structure of bone, *Med. Eng. Phys.* 20 (1998) 92–102. <https://doi.org/10.1016/S1350->

4533(98)00007-1.

- [269] L.J. Gibson, The mechanical behaviour of cancellous bone, *J. Biomech.* 18 (1985) 317–328. [https://doi.org/10.1016/0021-9290\(85\)90287-8](https://doi.org/10.1016/0021-9290(85)90287-8).
- [270] J. Galante, W. Rostoker, R.D. Ray, Physical properties of trabecular bone, *Calcif. Tissue Res.* 5 (1970) 236–246. <https://doi.org/10.1007/BF02017552>.
- [271] B. Helgason, E. Perilli, E. Schileo, F. Taddei, S. Brynjólfsson, M. Viceconti, Mathematical relationships between bone density and mechanical properties: A literature review, *Clin. Biomech.* 23 (2008) 135–146. <https://doi.org/10.1016/j.clinbiomech.2007.08.024>.
- [272] M. Tuncer, U.N. Hansen, A.A. Amis, Prediction of structural failure of tibial bone models under physiological loads: Effect of CT density-modulus relationships, *Med. Eng. Phys.* 36 (2014) 991–997. <https://doi.org/10.1016/j.medengphy.2014.04.006>.
- [273] D.R. Carter, W.C. Hayes, The Compressive Behavior Porous of Bone Structure as a Two-Phase, *J. Bone Jt. Surg.* 59 (1977) 954–962. https://doi.org/10.1007/978-1-4471-5451-8_116.
- [274] O. Lindahl, Mechanical Properties of Dried Defatted Spongy Bone, *Acta Orthop.* 47 (1976) 11–19. <https://doi.org/10.3109/17453677608998966>.
- [275] S.A. Goldstein, D.L. Wilson, D.A. Sonstegard, L.S. Matthews, The mechanical properties of human tibial trabecular bone as a function of metaphyseal location, *J. Biomech.* 16 (1983) 965–969. [https://doi.org/10.1016/0021-9290\(83\)90097-0](https://doi.org/10.1016/0021-9290(83)90097-0).
- [276] T.D. Brown, A.B. Ferguson, Mechanical Property Distributions in the Cancellous Bone of the Human Proximal Femur, *Acta Orthop.* 51 (1980) 429–437. <https://doi.org/10.3109/17453678008990819>.
- [277] M. Martens, R. Vanaudekerckep, P. Delport, the Mechanical Characteristics of Cancellous Bone At the Upper Femoral Region, *J. Biomech.* 16 (1983) 971–983. [https://doi.org/10.1016/0021-9290\(83\)90098-2](https://doi.org/10.1016/0021-9290(83)90098-2).
- [278] R.W. Mccalden, J.A. Mcgeough, C.M. Court-brown, Age-Related Changes in the Compressive Strength of Cancellous Bone . Architecture Age-Related Changes in the Compressive Strength of Cancellous Bone, (2010) 421–427.

- [279] C. Öhman, M. Baleani, E. Perilli, E. Dall'Ara, S. Tassani, F. Baruffaldi, M. Viceconti, Mechanical testing of cancellous bone from the femoral head: Experimental errors due to off-axis measurements, *J. Biomech.* 40 (2007) 2426–2433. <https://doi.org/10.1016/j.jbiomech.2006.11.020>.
- [280] R.B. Ashman, J.Y. Rho, C.H. Turner, Anatomical variation of orthotropic elastic moduli of the proximal human tibia, *J. Biomech.* 22 (1989) 895–900. [https://doi.org/10.1016/0021-9290\(89\)90073-0](https://doi.org/10.1016/0021-9290(89)90073-0).
- [281] J.L. Williams, J.L. Lewis, Properties and an anisotropic model of cancellous bone from the proximal tibial epiphysis, *J. Biomech. Eng.* 104 (1982) 50–56. <https://doi.org/10.1115/1.3138303>.
- [282] R.W. Goulet, S.A. Goldstein, M.J. Ciarelli, J.L. Kuhn, M.B. Brown, L.A. Feldkamp, The relationship between the structural and orthogonal compressive properties of trabecular bone, *J. Biomech.* 27 (1994). [https://doi.org/10.1016/0021-9290\(94\)90014-0](https://doi.org/10.1016/0021-9290(94)90014-0).
- [283] F. Linde, I. Hvid, F. Madsen, The effect of specimen geometry on the mechanical behaviour of trabecular bone specimens, *J. Biomech.* 25 (1992) 359–368. [https://doi.org/10.1016/0021-9290\(92\)90255-Y](https://doi.org/10.1016/0021-9290(92)90255-Y).
- [284] F. Linde, I. Hvid, The effect of constraint on the mechanical behaviour of trabecular bone specimens, *J. Biomech.* 22 (1989) 485–490. [https://doi.org/10.1016/0021-9290\(89\)90209-1](https://doi.org/10.1016/0021-9290(89)90209-1).
- [285] T.P. Harrigan, M. Jasty, R.W. Mann, W.H. Harris, Limitations of the continuum assumption in cancellous bone, *J. Biomech.* 21 (1988) 269–275. [https://doi.org/10.1016/0021-9290\(88\)90257-6](https://doi.org/10.1016/0021-9290(88)90257-6).
- [286] A. Odgaard, J. Kabel, B. Van Rietbergen, M. Dalstra, R. Huiskes, Fabric and elastic principal directions of cancellous bone are closely related, *J. Biomech.* 30 (1997) 487–495. [https://doi.org/10.1016/S0021-9290\(96\)00177-7](https://doi.org/10.1016/S0021-9290(96)00177-7).
- [287] T. Hildebrand, A. Laib, R. Müller, J. Dequeker, P. Rügsegger, Direct three-dimensional morphometric analysis of human cancellous bone: Microstructural data from spine, femur, iliac crest, and calcaneus, *J. Bone Miner. Res.* 14 (1999) 1167–1174. <https://doi.org/10.1359/jbmr.1999.14.7.1167>.

- [288] S.C. Cowin, The relationship between the elasticity tensor and the fabric tensor, *Mech. Mater.* 4 (1985) 137–147. [https://doi.org/10.1016/0167-6636\(85\)90012-2](https://doi.org/10.1016/0167-6636(85)90012-2).
- [289] G. Maquer, S.N. Musy, J. Wandel, T. Gross, P.K. Zysset, Bone volume fraction and fabric anisotropy are better determinants of trabecular bone stiffness than other morphological variables, *J. Bone Miner. Res.* 30 (2015) 1000–1008. <https://doi.org/10.1002/jbmr.2437>.
- [290] T. Gross, D.H. Pahr, P.K. Zysset, Morphology-elasticity relationships using decreasing fabric information of human trabecular bone from three major anatomical locations, *Biomech. Model. Mechanobiol.* 12 (2013) 793–800. <https://doi.org/10.1007/s10237-012-0443-2>.
- [291] U. Wolfram, T. Gross, D.H. Pahr, J. Schwiedrzik, H.J. Wilke, P.K. Zysset, Fabric-based Tsai-Wu yield criteria for vertebral trabecular bone in stress and strain space, *J. Mech. Behav. Biomed. Mater.* 15 (2012) 218–228. <https://doi.org/10.1016/j.jmbbm.2012.07.005>.
- [292] M. Matsuura, F. Eckstein, E.M. Lochmüller, P.K. Zysset, The role of fabric in the quasi-static compressive mechanical properties of human trabecular bone from various anatomical locations, *Biomech. Model. Mechanobiol.* 7 (2008) 27–42. <https://doi.org/10.1007/s10237-006-0073-7>.
- [293] P.K. Zysset, A review of morphology-elasticity relationships in human trabecular bone: Theories and experiments, *J. Biomech.* 36 (2003) 1469–1485. [https://doi.org/10.1016/S0021-9290\(03\)00128-3](https://doi.org/10.1016/S0021-9290(03)00128-3).
- [294] A. Odgaard, Three-dimensional methods for quantification of cancellous bone architecture, *Bone.* 20 (1997) 315–328. [https://doi.org/10.1016/S8756-3282\(97\)00007-0](https://doi.org/10.1016/S8756-3282(97)00007-0).
- [295] T.H. Smit, E. Schneider, A. Odgaard, Star length distribution: A volume-based concept for the characterization of structural anisotropy, *J. Microsc.* 191 (1998) 249–257. <https://doi.org/10.1046/j.1365-2818.1998.00394.x>.
- [296] M.J. Wald, B. Vasilic, P.K. Saha, F.W. Wehrli, Spatial autocorrelation and mean intercept length analysis of trabecular bone anisotropy applied to in vivo magnetic resonance imaging., *Med. Phys.* 34 (2007) 1110–1120. <https://doi.org/10.1118/1.2437281>.

- [297] Z. Tabor, R. Petryniak, Z. Latała, T. Konopka, The potential of multi-slice computed tomography based quantification of the structural anisotropy of vertebral trabecular bone, *Med. Eng. Phys.* 35 (2013) 7–15. <https://doi.org/10.1016/j.medengphy.2012.03.003>.
- [298] M.E. Kersh, P.K. Zysset, D.H. Pahr, U. Wolfram, D. Larsson, M.G. Pandy, Measurement of structural anisotropy in femoral trabecular bone using clinical-resolution CT images, *J. Biomech.* 46 (2013) 2659–2666. <https://doi.org/10.1016/j.jbiomech.2013.07.047>.
- [299] D. Larsson, B. Luisier, M.E. Kersh, E. Dall'Ara, P.K. Zysset, M.G. Pandy, D.H. Pahr, Assessment of Transverse Isotropy in Clinical-Level CT Images of Trabecular Bone Using the Gradient Structure Tensor, *Ann. Biomed. Eng.* 42 (2014) 950–959. <https://doi.org/10.1007/s10439-014-0983-y>.
- [300] N. Reznikov, H. Chase, Y. Ben Zvi, V. Tarle, M. Singer, V. Brumfeld, R. Shahar, S. Weiner, Inter-trabecular angle: A parameter of trabecular bone architecture in the human proximal femur that reveals underlying topological motifs, *Acta Biomater.* 44 (2016) 65–72. <https://doi.org/10.1016/j.actbio.2016.08.040>.
- [301] J. Wolff, Das gesetz der transformation der knochen, *A Hirshwald.* 1 (1892) 1–152.
- [302] S.M. Perren, Physical and biological aspects of fracture healing with special reference to internal fixation, *Clin. Orthop. Relat. Res.* NO. 138 (1979) 175–196.
- [303] H.M. Frost, A 2003 update of bone physiology and Wolff's Law for clinicians, *Angle Orthod.* 74 (2004) 3–15.
- [304] D.S. Elliott, K.J.H. Newman, D.P. Forward, D.M. Hahn, B. Ollivere, K. Kojima, R. Handley, N.D. Rossiter, J.J. Wixted, R.M. Smith, C.G. Moran, A unified theory of bone healing and nonunion, *Bone Joint J.* 98-B (2016) 884–891. <https://doi.org/10.1302/0301-620X.98B7.36061>.
- [305] N. Kohli, S. Ho, S.J. Brown, P. Sawadkar, V. Sharma, M. Snow, E. García-Gareta, Bone remodelling in vitro: Where are we headed?: -A review on the current understanding of physiological bone remodelling and inflammation and the strategies for testing biomaterials in vitro, *Bone.* 110 (2018) 38–46. <https://doi.org/10.1016/j.bone.2018.01.015>.

- [306] R. Florencio-Silva, G.R. da S. Sasso, E. Sasso-Cerri, M.J. Simões, P.S. Cerri, Biology of bone tissue: structure, function, and factors that influence bone cells, *Biomed Res. Int.* 2015 (2015).
- [307] G.Y. Rochefort, S. Pallu, C.L. Benhamou, Osteocyte: The unrecognized side of bone tissue, *Osteoporos. Int.* 21 (2010) 1457–1469. <https://doi.org/10.1007/s00198-010-1194-5>.
- [308] V.I. Sikavitsas, J.S. Temenoff, A.G. Mikos, Biomaterials and bone mechanotransduction, *Biomaterials.* 22 (2001) 2581–2593. [https://doi.org/10.1016/S0142-9612\(01\)00002-3](https://doi.org/10.1016/S0142-9612(01)00002-3).
- [309] C.N. Shaw, J.T. Stock, Habitual throwing and swimming correspond with upper limb diaphyseal strength and shape in modern human athletes, *Am. J. Phys. Anthropol.* 140 (2009) 160–172. <https://doi.org/10.1002/ajpa.21063>.
- [310] C.T. Rubin, L.E. Lanyon, Regulation of bone mass by mechanical strain magnitude, *Calcif. Tissue Int.* 37 (1985) 411–417. <https://doi.org/10.1007/BF02553711>.
- [311] C.H. Turner, Three rules for bone adaptation to mechanical stimuli, *Bone.* 23 (1998) 399–407. [https://doi.org/10.1016/S8756-3282\(98\)00118-5](https://doi.org/10.1016/S8756-3282(98)00118-5).
- [312] Z. Miller, M.B. Fuchs, M. Arcan, Trabecular bone adaptation with an orthotropic material model, *J. Biomech.* 35 (2002) 247–256. [https://doi.org/10.1016/S0021-9290\(01\)00192-0](https://doi.org/10.1016/S0021-9290(01)00192-0).
- [313] A.T.M. Phillips, Structural optimisation: biomechanics of the femur, *Proc. ICE - Eng. Comput. Mech.* 165 (2012) 147–154. <https://doi.org/10.1680/eacm.10.00032>.
- [314] P. Christen, K. Ito, R. Ellouz, S. Boutroy, E. Sornay-Rendu, R.D. Chapurlat, B. Van Rietbergen, Bone remodelling in humans is load-driven but not lazy, *Nat. Commun.* 5 (2014) 1–5. <https://doi.org/10.1038/ncomms5855>.
- [315] S. Ghouse, N. Reznikov, O.R. Boughton, S. Babu, K.C.G. Ng, G. Blunn, J.P. Cobb, M.M. Stevens, J.R.T. Jeffers, The design and in vivo testing of a locally stiffness-matched porous scaffold, *Appl. Mater. Today.* 15 (2019) 377–388. <https://doi.org/10.1016/j.apmt.2019.02.017>.
- [316] V. Karageorgiou, D. Kaplan, Porosity of 3D biomaterial scaffolds and osteogenesis,

- Biomaterials. 26 (2005) 5474–5491.
<https://doi.org/10.1016/j.biomaterials.2005.02.002>.
- [317] A.C. Jones, C.H. Arns, D.W. Hutmacher, B.K. Milthorpe, A.P. Sheppard, M.A. Knackstedt, The correlation of pore morphology, interconnectivity and physical properties of 3D ceramic scaffolds with bone ingrowth, *Biomaterials*. 30 (2009) 1440–1451.
<https://doi.org/10.1016/j.biomaterials.2008.10.056>.
- [318] A.I. Itälä, H.O. Ylänen, C. Ekholm, K.H. Karlsson, H.T. Aro, Pore diameter of more than 100 µm is not requisite for bone ingrowth in rabbits, *J. Biomed. Mater. Res. An Off. J. Soc. Biomater. Japanese Soc. Biomater. Aust. Soc. Biomater. Korean Soc. Biomater.* 58 (2001) 679–683.
- [319] A. Braem, A. Chaudhari, M. Vivan Cardoso, J. Schrooten, J. Duyck, J. Vleugels, Peri- and intra-implant bone response to microporous Ti coatings with surface modification, *Acta Biomater.* 10 (2014) 986–995.
<https://doi.org/10.1016/j.actbio.2013.10.017>.
- [320] Z. Wang, C. Wang, C. Li, Y. Qin, L. Zhong, B. Chen, Z. Li, H. Liu, F. Chang, J. Wang, Analysis of factors influencing bone ingrowth into three-dimensional printed porous metal scaffolds: A review, *J. Alloys Compd.* 717 (2017) 271–285.
<https://doi.org/10.1016/j.jallcom.2017.05.079>.
- [321] G. Li, L. Wang, W. Pan, F. Yang, W. Jiang, X. Wu, X. Kong, K. Dai, Y. Hao, In vitro and in vivo study of additive manufactured porous Ti6Al4V scaffolds for repairing bone defects, *Sci. Rep.* 6 (2016) 1–11. <https://doi.org/10.1038/srep34072>.
- [322] Q. Ran, W. Yang, Y. Hu, X. Shen, Y. Yu, Y. Xiang, K. Cai, Osteogenesis of 3D printed porous Ti6Al4V implants with different pore sizes, *J. Mech. Behav. Biomed. Mater.* 84 (2018) 1–11. <https://doi.org/10.1016/j.jmbbm.2018.04.010>.
- [323] F. Bai, Z. Wang, J. Lu, J. Liu, G. Chen, R. Lv, J. Wang, K. Lin, J. Zhang, X. Huang, The correlation between the internal structure and vascularization of controllable porous bioceramic materials in vivo: A quantitative study, *Tissue Eng. - Part A*. 16 (2010) 3791–3803. <https://doi.org/10.1089/ten.tea.2010.0148>.
- [324] R.J. van Arkel, S. Ghouse, P.E. Milner, J.R.T. Jeffers, Additive manufactured push-fit implant fixation with screw-strength pull out, *J. Orthop. Res.* 36 (2018) 1508–1518.

<https://doi.org/10.1002/jor.23771>.

- [325] V.S. Cheong, A. Mumith, M. Coathup, G. Blunn, P. Fromme, Bone remodeling in additive manufactured porous implants changes the stress distribution, in: P. Fromme, Z. Su (Eds.), *Heal. Monit. Struct. Biol. Syst. IX*, SPIE, 2020: p. 115. <https://doi.org/10.1117/12.2558093>.
- [326] W.J. Whitehouse, E.D. Dyson, Scanning electron microscope studies of trabecular bone in the proximal end of the human femur., *J. Anat.* 118 (1974) 417–44. <http://www.pubmedcentral.nih.gov/articlerender.fcgi?artid=1231543&tool=pmcentre&rendertype=abstract>.
- [327] V. Petrovic, J.V. Haro, J.R. Blasco, L. Portolés, Additive Manufacturing Solutions for Improved Medical Implants, *Biomedicine.* (2012) 147–18'. <https://doi.org/10.5772/2321>.
- [328] X.-Y. Zhang, G. Fang, J. Zhou, Additively Manufactured Scaffolds for Bone Tissue Engineering and the Prediction of their Mechanical Behavior: A Review, *Materials (Basel).* 10 (2017) 50. <https://doi.org/10.3390/ma10010050>.
- [329] R.L. Duncan, C.H. Turner, Mechanotransduction and the functional response of bone to mechanical strain, *Calcif. Tissue Int.* 57 (1995) 344–358. <https://doi.org/10.1007/BF00302070>.
- [330] L.J. Gibson, M.F. Ashby, Cellular solids: Structure and properties, *Mater. Sci. Eng. A.* 123 (1990) 282–283. [https://doi.org/10.1016/0921-5093\(90\)90295-E](https://doi.org/10.1016/0921-5093(90)90295-E).
- [331] L. Mullen, R.C. Stamp, W.K. Brooks, E. Jones, C.J. Sutcliffe, Selective Laser Melting: A regular unit cell approach for the manufacture of porous, titanium, bone in-growth constructs, suitable for orthopedic applications, *J. Biomed. Mater. Res. Part B Appl. Biomater.* 89B (2009) 325–334. <https://doi.org/10.1002/jbm.b.31219>.
- [332] E. Liverani, A.H.A. Lutey, A. Fortunato, A. Ascari, Characterization of Lattice Structures for Additive Manufacturing of Lightweight Mechanical Components, (2017) V002T01A012. <http://dx.doi.org/10.1115/MSEC2017-2835>.
- [333] A. Jin, J. Cobb, U. Hansen, R. Bhattacharya, C. Reinhard, N. Vo, R. Atwood, J. Li, A. Karunaratne, C. Wiles, R. Abel, The effect of long-term bisphosphonate therapy on trabecular bone strength and microcrack density, *Bone Jt. Res.* 6 (2017) 602–609.

<https://doi.org/10.1302/2046-3758.610.BJR-2016-0321.R1>.

- [334] R.A. Ketcham, T.M. Ryan, Quantification and visualization of anisotropy in trabecular bone, *J. Microsc.* 213 (2004) 158–171. <https://doi.org/10.1111/j.1365-2818.2004.01277.x>.
- [335] O. Rehme, Cellular design for laser freeform fabrication, Hamburg University of Technology, Cuvillier Verlag, Göttingen., 2010.
- [336] H. Sugita, M. Oka, J. Toguchida, T. Nakamura, T. Ueo, T. Hayami, Anisotropy of osteoporotic cancellous bone, *Bone.* 24 (1999) 513–516. [https://doi.org/10.1016/S8756-3282\(99\)00021-6](https://doi.org/10.1016/S8756-3282(99)00021-6).
- [337] P. Li, Z. Wang, N. Petrinic, C.R. Siviour, Deformation behaviour of stainless steel microlattice structures by selective laser melting, *Mater. Sci. Eng. A.* 614 (2014) 116–121. <https://doi.org/10.1016/j.msea.2014.07.015>.
- [338] J. Yang, H. Cai, J. Lv, K. Zhang, H. Leng, C. Sun, Z. Wang, Z. Liu, In vivo study of a self-stabilizing artificial vertebral body fabricated by electron beam melting, *Spine (Phila. Pa. 1976)*. 39 (2014) E486–E492. <https://doi.org/10.1097/BRS.0000000000000211>.
- [339] X. Wang, J.A. Muñoz-Lerma, O. Sánchez-Mata, M. Attarian Shandiz, M. Brochu, Microstructure and mechanical properties of stainless steel 316L vertical struts manufactured by laser powder bed fusion process, *Mater. Sci. Eng. A.* 736 (2018) 27–40. <https://doi.org/10.1016/j.msea.2018.08.069>.
- [340] A. Pérez-Sánchez, A. Yáñez, A. Cuadrado, O. Martel, N. Nuño, Fatigue behaviour and equivalent diameter of single Ti-6Al-4V struts fabricated by Electron Beam Melting orientated to porous lattice structures, *Mater. Des.* 155 (2018) 106–115. <https://doi.org/10.1016/j.matdes.2018.05.066>.
- [341] X.Z. Zhang, H.P. Tang, M. Leary, T. Song, L. Jia, M. Qian, Toward Manufacturing Quality Ti-6Al-4V Lattice Struts by Selective Electron Beam Melting (SEBM) for Lattice Design, *J. Miner. Met. Mater. Soc.* 70 (2018) 1870–1876. <https://doi.org/10.1007/s11837-018-3030-x>.
- [342] S. Ghose, S. Babu, K. Nai, P.A. Hooper, J.R.T. Jeffers, The influence of laser parameters, scanning strategies and material on the fatigue strength of a stochastic porous structure, *Addit. Manuf.* 22 (2018) 290–301.

<https://doi.org/10.1016/j.addma.2018.05.024>.

- [343] Markforged, Material Datasheet Composites REV 3.2 - 9/9/2019, (2019) 1.
- [344] N. Rana, D. Rawat, M. Parmar, D. Dhawan, A. Bhati, B. Mittal, Evaluation of external beam hardening filters on image quality of computed tomography and single photon emission computed tomography/computed tomography, *J. Med. Phys.* 40 (2015) 198–206. <https://doi.org/10.4103/0971-6203.170790>.
- [345] N. Otsu, A threshold selection method from gray-level histograms, *IEEE Trans. Syst. Man. Cybern.* 9 (1979) 62–66.
- [346] Q. Fang, D.A. Boas, Tetrahedral mesh generation from volumetric binary and grayscale images, *Proc. - 2009 IEEE Int. Symp. Biomed. Imaging From Nano to Macro, ISBI 2009.* (2009) 1142–1145. <https://doi.org/10.1109/ISBI.2009.5193259>.
- [347] L. Rineau, M. Yvinec, {3D} Surface Mesh Generation, in: {CGAL} User Ref. Man., 5.0.1, CGAL Editorial Board, 2020. <https://doc.cgal.org/5.0.1/Manual/packages.html#PkgSurfaceMesher3>.
- [348] D.K. Do, P. Li, The effect of laser energy input on the microstructure, physical and mechanical properties of Ti-6Al-4V alloys by selective laser melting, *Virtual Phys. Prototyp.* 11 (2016) 41–47. <https://doi.org/10.1080/17452759.2016.1142215>.
- [349] J. Han, J. Yang, H. Yu, J. Yin, M. Gao, Z. Wang, X. Zeng, Microstructure and mechanical property of selective laser melted Ti6Al4V dependence on laser energy density, *Rapid Prototyp. J.* 23 (2017) 217–226. <https://doi.org/10.1108/RPJ-12-2015-0193>.
- [350] T. Persenot, A. Burr, R. Dendievel, J.Y. Buffière, E. Maire, J. Lachambre, G. Martin, Fatigue performances of chemically etched thin struts built by selective electron beam melting: Experiments and predictions, *Materialia.* 9 (2020) 100589. <https://doi.org/10.1016/j.mtla.2020.100589>.
- [351] C. Yan, L. Hao, A. Hussein, D. Raymont, Evaluations of cellular lattice structures manufactured using selective laser melting, *Int. J. Mach. Tools Manuf.* 62 (2012) 32–38. <https://doi.org/10.1016/j.ijmachtools.2012.06.002>.
- [352] C. Yan, L. Hao, A. Hussein, P. Young, D. Raymont, Advanced lightweight 316L stainless steel cellular lattice structures fabricated via selective laser melting, *Mater. Des.* 55

- (2014) 533–541. <https://doi.org/10.1016/j.matdes.2013.10.027>.
- [353] J. Martinez, J. Dumas, S. Lefebvre, Procedural voronoi foams for additive manufacturing, *ACM Trans. Graph.* 35 (2016) 44.
- [354] K.C. Wong, S.M. Kumta, K.H. Chiu, K.W. Cheung, K.S. Leung, P. Unwin, M.C.M. Wong, Computer assisted pelvic tumor resection and reconstruction with a custom-made prosthesis using an innovative adaptation and its validation, *Comput. Aided Surg.* 12 (2007) 225–232. <https://doi.org/10.1080/10929080701536046>.
- [355] C. Mertens, H. Löwenheim, J. Hoffmann, Image data based reconstruction of the midface using a patient-specific implant in combination with a vascularized osteomyocutaneous scapular flap, *J. Cranio-Maxillofacial Surg.* 41 (2013) 219–225. <https://doi.org/10.1016/j.jcms.2012.09.003>.
- [356] S.Y. Choy, C.N. Sun, K.F. Leong, J. Wei, Compressive properties of Ti-6Al-4V lattice structures fabricated by selective laser melting: Design, orientation and density, *Addit. Manuf.* 16 (2017) 213–224. <https://doi.org/10.1016/j.addma.2017.06.012>.
- [357] B. Van Hooreweder, Y. Apers, K. Lietaert, J.P. Kruth, Improving the fatigue performance of porous metallic biomaterials produced by Selective Laser Melting, *Acta Biomater.* 47 (2017) 193–202. <https://doi.org/10.1016/j.actbio.2016.10.005>.
- [358] T. Tancogne-Dejean, D. Mohr, Elastically-isotropic truss lattice materials of reduced plastic anisotropy, *Int. J. Solids Struct.* 138 (2018) 24–39. <https://doi.org/10.1016/j.ijsolstr.2017.12.025>.
- [359] V.J. Challis, A.P. Roberts, J.F. Grotowski, L.C. Zhang, T.B. Sercombe, Prototypes for bone implant scaffolds designed via topology optimization and manufactured by solid freeform fabrication, *Adv. Eng. Mater.* 12 (2010) 1106–1110. <https://doi.org/10.1002/adem.201000154>.
- [360] G.N. Labeas, M.M. Sunaric, Investigation on the static response and failure process of metallic open lattice cellular structures, *Strain.* 46 (2010) 195–204. <https://doi.org/10.1111/j.1475-1305.2008.00498.x>.
- [361] P. Köhnen, C. Haase, J. Bültmann, S. Ziegler, J.H. Schleifenbaum, W. Bleck, Mechanical properties and deformation behavior of additively manufactured lattice structures of stainless steel, *Mater. Des.* 145 (2018) 205–217.

<https://doi.org/10.1016/j.matdes.2018.02.062>.

8 Appendices

A1 Tensile testing of struts

A1.1 Further strut morphology

Eccentricity

Eccentricity is shown as a function of build angle in Figure 8.1. The average eccentricity across all struts was 22.4 μm . There is a general trend to smaller amounts of eccentricity at high build angles for both materials. For SS316L struts the average eccentricity decreased from 26.1 μm at 20° to 12.0 μm at 90°, more than halving the value. A similar trend is seen for Ti6Al4V specimens, with the average eccentricity almost halving from 36.1 μm to 18.7 μm over the range of measurement. The amount of variation for Ti6Al4V specimens is larger than for SS316L and there is not a clear difference between struts with different designed diameters.

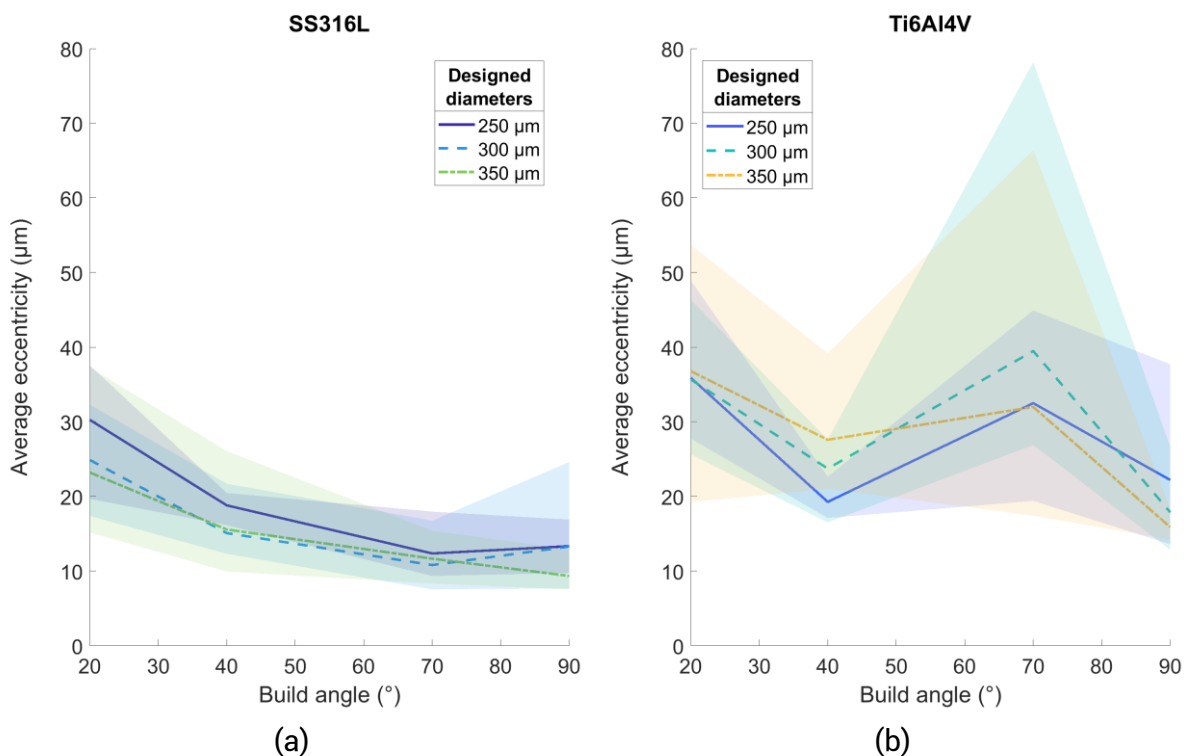


Figure 8.1: Average eccentricity of the strut over build angle.

(a) SS316L struts and (b) Ti6Al4V struts.

A2 Compression testing of structures

A2.1 Pilot data

Pilot testing was conducted for the kinking process detailed in Chapter 5, to find what might be an appropriate critical angle to use for the full set of test specimens. The pilot data was conducted by testing only 4 of the 10 directions, namely direction 0, 1, 2 and 3. Direction 0 was pointed in the z direction, direction 1 at the centre-point between all three axes, direction 2 in the x direction, and direction 3 in between the z and y directions (see Figure 5.3). This covered a range of horizontal to vertical directions. One other constraint was that the tests were only conducted in SS316L, and not Ti6Al4V. Variant A (no modifications) was tested in these directions. A critical angle of 20° was tested with variant B and C. A critical angle of 25° was also tested with variant B and C. Lastly, a critical angle of 30° was tested with variant C.

The elastic modulus was calculated using the method described in section 5.2. The 1% offset yield stress was also calculated as described previously. Lastly, the plateau stress was calculated, which is the average stress from 20% to 30% strain, as recommended by the ISO standard [238].

Elastic modulus

Figure 8.2 shows the elastic modulus results for the pilot data. The variant B structures were shown to improve the low angle stiffness of the structures versus variant A. The elastic modulus increases overall with the other variants. The stiffness of variant C structures was decreased from variant B overall, with variant C-25 showing the smallest range in results.

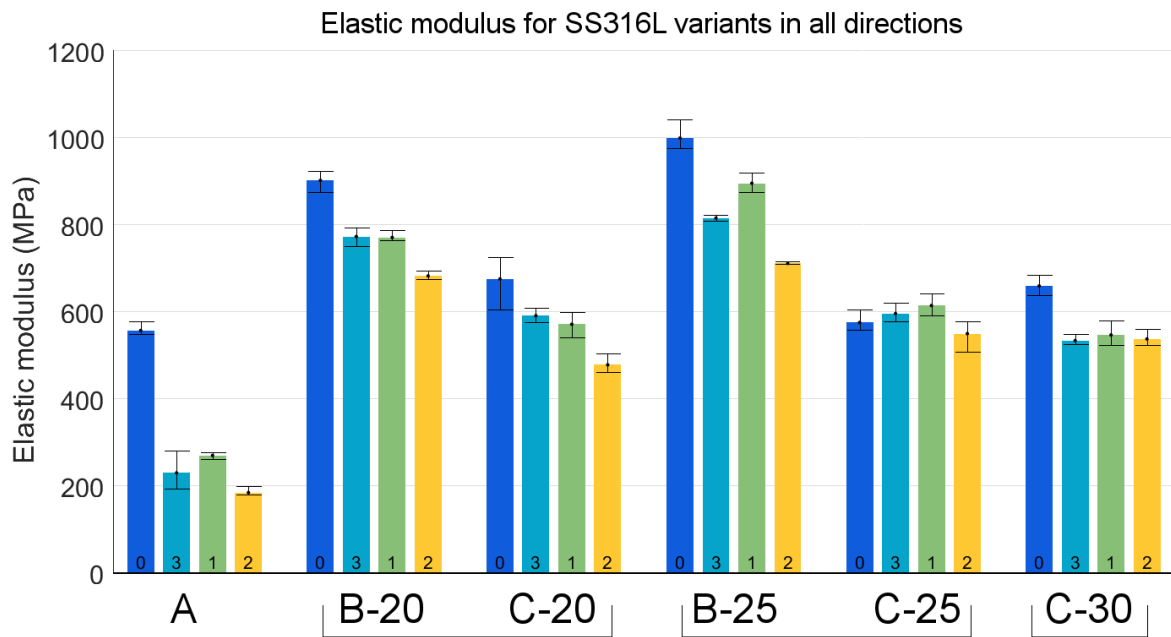


Figure 8.2: Elastic modulus vs test directions 0, 3, 1 and 2, ordered by increasing vertical orientation.

Directions are grouped by the structure variant A, B and C and the critical angle that was chosen.

Yield stress

Figure 8.3 shows the yield stress results for the pilot data. The variant B structures were again shown to improve the low angle yield strength of the structures versus variant A. The yield strength increases overall with the B and C variants. The range in yield strength for variant C-25 was again the smallest.

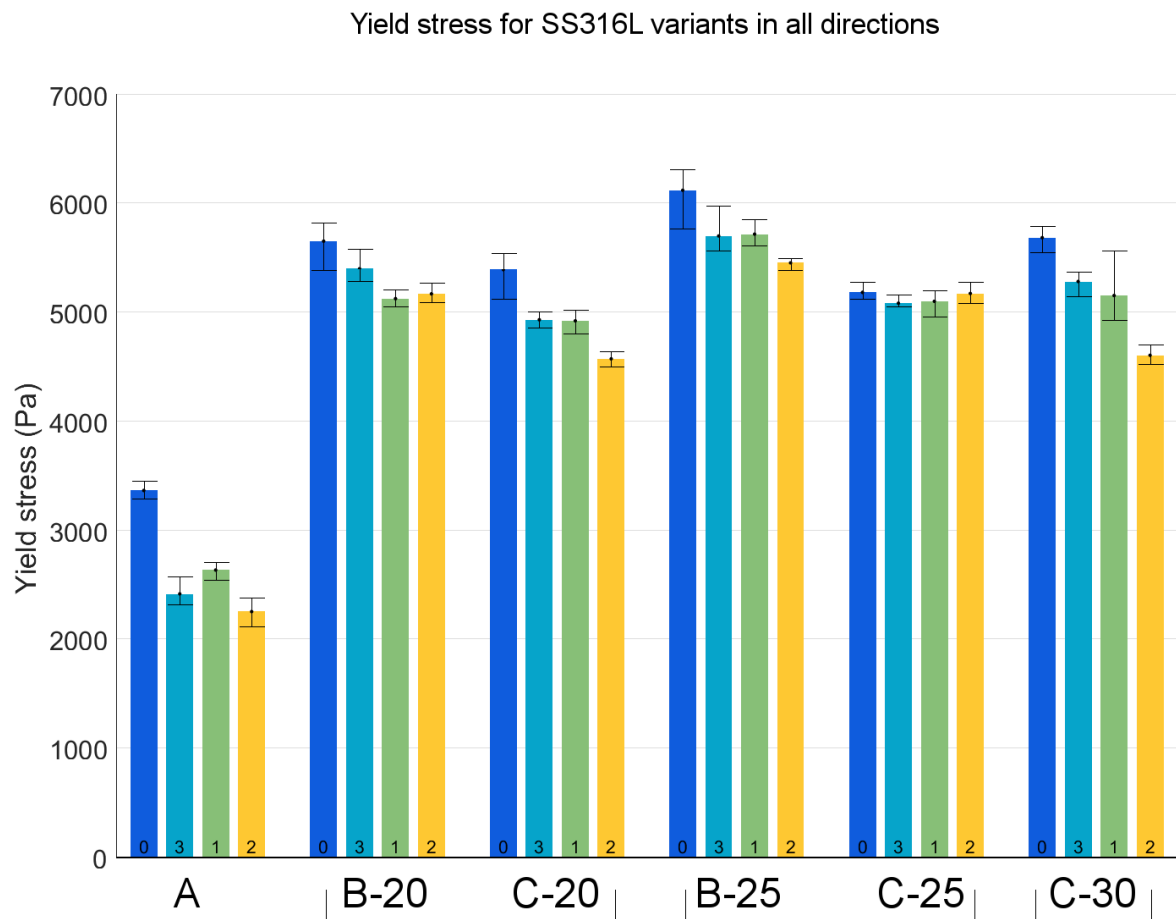


Figure 8.3: Yield stress vs test directions 0, 3, 1 and 2, ordered by increasing vertical orientation.

Directions are grouped by the structure variant A, B and C and the critical angle that was chosen.

Plateau stress

Figure 8.4 shows the plateau stress results for the pilot data. The results are very similar in pattern to the yield stress results, with improved performance by the variant B and C structures. Again, the range of plateau stress for variant C-25 was again the smallest.

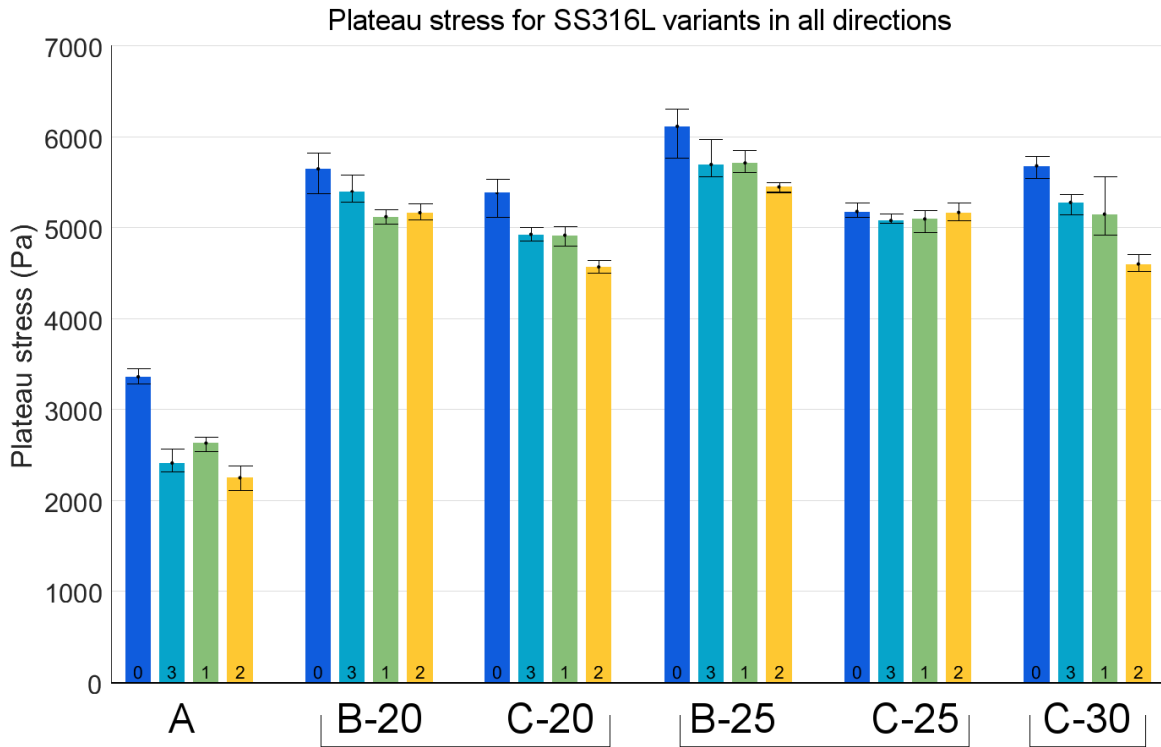


Figure 8.4: Plateau stress vs test directions 0, 3, 1 and 2, ordered by increasing vertical orientation.

Directions are grouped by the structure variant A, B and C and the critical angle that was chosen.

Due to the results found using this pilot data, a critical angle of 25° was chosen for the full set of experiments. However, further testing of different critical angles is still warranted, especially for Ti6Al4V specimens and for different heat treatments thereof.

A2.2 Patent filing receipt



Intellectual
Property
Office

Concept House
Cardiff Road, Newport
South Wales
NP10 8QQ
United Kingdom

Telephone +44 (0)1633 814000

Website <https://www.gov.uk/ipo>

Electronic Filing Receipt

HGF LIMITED
Docketing Handling (London)
1 City Walk
Leeds
Yorkshire
United Kingdom
LS11 9DX

Your Ref: P297573GB/JCU

06 April 2020

PATENT APPLICATION NUMBER 2005050.6

We have received your request for grant of a patent and recorded its details as follows:

Filing date(*)	06 April 2020	
Earliest priority date (if any)		
Applicant(s) / contact point	IMPERIAL COLLEGE INNOVATIONS LTD	
Application fee paid	Yes	
Description (number of pages or reference)	12	
Certified copy of referenced application	Not applicable	
If description not filed	Not applicable	
Claims (number of pages)	3	
Drawings (number of pages)	6	
Abstract (number of pages)	1	
Statement of inventorship (Form 7)	Yes	
Request for search (Form 9A)	Yes	
Request for examination (Form 10)	Yes	
Priority Documents	None	
Other Attachments Received	Pre-conversion archive	P297573GB - precon- version.zip
	PDAS Registration Form	PDASRegistration.pdf

Intellectual Property Office is an operating name of the Patent Office

<https://www.gov.uk/ipo>

	Fee Sheet	FeeSheet.pdf
	Validation Log	ValidLog.pdf
<hr/>		
Signed by	CN=Jack Cundy 46467	
Submitted by	CN=Jack Cundy 46467	
Timestamp of Receipt	06 April 2020, 15:02:27 (BST)	
Digest of Submission	13:B6:F0:D2:F8:BF:34:05:86:94:46:98:F8:8F:5B :1B:3D:87:5D:4F	
<hr/>		
Received	/Intellectual Property Office, Newport/	

Please quote the application number in the heading whenever you contact us about this application.

As requested your application as filed will be lodged in the Priority Document Access Service (PDAS) at WIPO. For further information relating to PDAS please see our website <https://www.gov.uk/government/publications/how-to-file-documents-with-the-intellectual-property-office/how-to-file-documents-with-the-intellectual-property-office#file-on-line> or contact our e-filing section on 01633 814870.

If you have any queries about the accuracy of this receipt, please phone the Document Reception Manager on +44 (0) 1633 814570. For all other queries, please phone our Information Centre on 0300 300 2000 if you are calling from the UK, or +44 (0) 1633 814000 if you are calling from outside the UK. Or e-mail information@ipo.gov.uk

* This date is provisional. We may have to change it if we find during preliminary examination that the application does not satisfy section 15(1) of the Patents Act 1977 or if we re-date the application to the date when we get any later filed documents.

APPENDICES

A3 Permission documents**A3.1 Permissions granted**

The following permissions for reuse were granted, either under a Creative Commons License, using Copyright Clearance Center's RightsLink® service, or by written consent.

Figure location	Extract used	Source of work	Copyright holder	Permission requested on	Permission granted?	Permission note
Figure 2.3a, page 11	Figure 4	T. Nishino, H. Mishima, S. Miyakawa, H. Kawamura, N. Ochiai, Midterm results of the Synergy cementless tapered stem: Stress shielding and bone quality, <i>J. Orthop. Sci.</i> 13 (2008) 498–503. https://doi.org/10.1007/s00776-008-1272-0 .	Elsevier	20/7/20	Yes	RightsLink®
Figure 2.3b, page 11	Figure 1	D.R. Sumner, Long-term implant fixation and stress-shielding in total hip replacement, <i>J. Biomech.</i> 48 (2015) 797–800. https://doi.org/10.1016/j.jbiomech.2014.12.021 .	Elsevier	17/7/20	Yes	RightsLink®
Figure 2.4a, page 13	Figure 1	D. Apostu, O. Lucaciu, C. Berce, D. Lucaciu, D. Cosma, Current methods of preventing aseptic loosening and improving osseointegration of titanium implants in cementless total hip arthroplasty: a review, <i>J. Int. Med. Res.</i> 46 (2018) 2104–2119. https://doi.org/10.1177/0300060517732697 .	SAGE Publications	17/7/20	Yes	CC BY-NC 4.0
Figure 2.4b, page 13	Figure 2	I. Kutzner, G. Hallan, P.J. Høl, O. Furnes, Ø. Gøthesen, W. Figved, P. Ellison, Early aseptic loosening of a mobile-bearing total knee replacement: A case-control study with retrieval analyses, <i>Acta Orthop.</i> 89 (2018) 77–83. https://doi.org/10.1080/17453674.2017.1398012 .	Taylor & Francis	17/7/20	Yes	CC BY-NC 3.0
Figure 2.5, page 15	Figure 1	J. V. Abellán-Nebot, H.R. Siller, C. Vila, C.A. Rodríguez, An experimental study of process variables in turning operations of Ti-6Al-4V and Cr-Co spherical prostheses, <i>Int. J. Adv. Manuf. Technol.</i> 63 (2012) 887–902. https://doi.org/10.1007/s00170-012-3955-0 .	Springer Nature	17/7/20	Yes	RightsLink®

APPENDICES

Figure location	Extract used	Source of work	Copyright holder	Permission requested on	Permission granted?	Permission note
Figure 2.6, page 16	Figure 1	J.D. Bobyn, G.J. Stackpool, S.A. Hacking, M. Tanzer, J.J. Krygier, Characteristics of bone ingrowth and interface mechanics of a new porous tantalum biomaterial., J. Bone Jt. Surgery. 81 (1999) 907–914. https://doi.org/10.1302/0301-620X.81B5.9283	British Editorial Society of Bone & Joint Surgery	17/7/20	Yes	RightsLink®
Figure 2.10, page 20	Figure 1	V.S. Deshpande, M.F. Ashby, N.A. Fleck, Foam topology: Bending versus stretching dominated architectures, Acta Mater. 49 (2001) 1035–1040. https://doi.org/10.1016/S1359-6454(00)00379-7 .	Elsevier	20/7/20	Yes	RightsLink®
Figure 2.13, page 26	-	AM250 machine (jpg) https://resources.renishaw.com/gen/details/am250-machine--38488	© 2001-2020 Renishaw plc	17/7/20	Yes	Written consent
Figure 2.13, page 26	-	AM250 Dental build plate (jpg) https://resources.renishaw.com/gen/details/am250-dental-build-plate--59498	© 2001-2020 Renishaw plc	17/7/20	Yes	Written consent
Figure 2.14a, page 27	Figure 5	A.L. Jardini, M.A. Larosa, C.A. de Carvalho Zavaglia, L.F. Bernardes, C.S. Lambert, P. Kharmandayan, D. Calderoni, R. Maciel Filho, Customised titanium implant fabricated in additive manufacturing for craniomaxillofacial surgery: This paper discusses the design and fabrication of a metallic implant for the reconstruction of a large cranial defect, Virtual Phys. Prototyp. 9 (2014) 115–125. https://doi.org/10.1080/17452759.2014.900857	Taylor & Francis	17/7/20	Yes	RightsLink®
Figure 2.14b, page 27	Figure 1	A.J. Miller, J.D. Stimac, L.S. Smith, A.W. Feher, M.R. Yakkanti, A.L. Malkani, Results of Cemented vs Cementless Primary Total Knee Arthroplasty Using the Same Implant Design, J. Arthroplasty. 33 (2018) 1089–1093. https://doi.org/10.1016/j.arth.2017.11.048	Elsevier	20/7/20	Yes	RightsLink®
Figure 2.15 (1), page 30	Figure 2	E. Sallica-Leva, A.L. Jardini, J.B. Fogagnolo, Microstructure and mechanical behavior of porous Ti–6Al–4V parts obtained by selective laser melting, J. Mech. Behav. Biomed. Mater. 26 (2013) 98–108. https://doi.org/10.1016/j.jmbbm.2013.05.011 .	Elsevier	20/7/20	Yes	RightsLink®

APPENDICES

Figure location	Extract used	Source of work	Copyright holder	Permission requested on	Permission granted?	Permission note
Figure 2.15 (2,6-8), page 30	Figure 2	M. Mazur, M. Leary, S. Sun, M. Vcelka, D. Shidid, M. Brandt, Deformation and failure behaviour of Ti-6Al-4V lattice structures manufactured by selective laser melting (SLM), <i>Int J Adv Manuf Technol.</i> 84 (2016) 1391–1411. https://doi.org/10.1007/s00170-015-7655-4 .	Springer Nature	20/7/20	Yes	RightsLink®
Figure 2.15 (3), page 30	Figure 2	Z. Dong, Y. Liu, W. Li, J. Liang, Orientation dependency for microstructure, geometric accuracy and mechanical properties of selective laser melting AlSi10Mg lattices, <i>J. Alloys Compd.</i> 791 (2019) 490–500. https://doi.org/10.1016/j.jallcom.2019.03.344 .	Elsevier	20/7/20	Yes	RightsLink®
Figure 2.15 (4,5), page 30	Figure 11	K. Ushijima, W.J. Cantwell, D.H. Chen, Prediction of the mechanical properties of micro-lattice structures subjected to multi-axial loading, <i>Int. J. Mech. Sci.</i> 68 (2013) 47–55. https://doi.org/10.1016/j.ijmecsci.2012.12.017	Elsevier	20/7/20	Yes	RightsLink®
Figure 2.15 (9), page 30	Figure 2	S. Van Bael, G. Kerckhofs, M. Moesen, G. Pyka, J. Schrooten, J.P. Kruth, Micro-CT-based improvement of geometrical and mechanical controllability of selective laser melted Ti6Al4V porous structures, <i>Mater. Sci. Eng. A.</i> 528 (2011) 7423–7431. https://doi.org/10.1016/j.msea.2011.06.045	Elsevier	20/7/20	Yes	RightsLink®
Figure 2.15 (10), page 30	Figure 2	J. Sun, Y. Yang, D. Wang, Mechanical properties of a Ti6Al4V porous structure produced by selective laser melting, <i>Mater. Des.</i> 49 (2013) 545–552. https://doi.org/10.1016/j.matdes.2013.01.038	Elsevier	20/7/20	Yes	RightsLink®
Figure 2.15 (11, 22, 23), page 30	Figure 7	L.E. Murr, S.M. Gaytan, F. Medina, H. Lopez, E. Martinez, B.I. Machado, D. H. Hernandez, L. Martinez, M.I. Lopez, R.B. Wicker, J. Bracke, Next-generation biomedical implants using additive manufacturing of complex, cellular and functional mesh arrays, <i>Philos. Trans. R. Soc. A Math. Phys. Eng. Sci.</i> 368 (2010) 1999–2032. https://doi.org/10.1098/rsta.2010.0010	Royal Society	20/7/20	Yes	RightsLink®

APPENDICES

Figure location	Extract used	Source of work	Copyright holder	Permission requested on	Permission granted?	Permission note
Figure 2.15 (12), page 30	Figure 1	S. Limmahakhun, A. Oloyede, K. Sitthiseripratip, Y. Xiao, C. Yan, Stiffness and strength tailoring of cobalt chromium graded cellular structures for stress-shielding reduction, <i>Mater. Des.</i> 114 (2017) 633–641. https://doi.org/10.1016/j.matdes.2016.11.090	Elsevier	20/7/20	Yes	RightsLink®
Figure 2.15 (13), page 30	Figure 1	N. Taniguchi, S. Fujibayashi, M. Takemoto, K. Sasaki, B. Otsuki, T. Nakamura, T. Matsushita, T. Kokubo, S. Matsuda, Effect of pore size on bone ingrowth into porous titanium implants fabricated by additive manufacturing: An in vivo experiment, <i>Mater. Sci. Eng. C.</i> 59 (2016) 690–701. https://doi.org/10.1016/j.msec.2015.10.069	Elsevier	20/7/20	Yes	RightsLink®
Figure 2.15 (14), page 30	Figure 1	R. Wauthle, J. Van Der Stok, S.A. Yavari, J. Van Humbeeck, J.P. Kruth, A.A. Zadpoor, H. Weinans, M. Mulier, J. Schrooten, Additively manufactured porous tantalum implants, <i>Acta Biomater.</i> 14 (2015) 217–225. https://doi.org/10.1016/j.actbio.2014.12.003	Elsevier	20/7/20	Yes	RightsLink®
Figure 2.15 (15, 20), page 30	Figure 1	V.J. Challis, X. Xu, L.C. Zhang, A.P. Roberts, J.F. Grotowski, T.B. Sercombe, High specific strength and stiffness structures produced using selective laser melting, <i>Mater. Des.</i> 63 (2014) 783–788. https://doi.org/10.1016/j.matdes.2014.05.064	Elsevier	20/7/20	Yes	RightsLink®
Figure 2.15 (16-19), page 30	Figure 1	F.S.L. Bobbert, K. Lietaert, A.A. Eftekhari, B. Pouran, S.M. Ahmadi, H. Weinans, A.A. Zadpoor, Additively manufactured metallic porous biomaterials based on minimal surfaces: A unique combination of topological, mechanical, and mass transport properties, <i>Acta Biomater.</i> 53 (2016) 572–584. https://doi.org/10.1016/j.actbio.2017.02.024	Elsevier	20/7/20	Yes	RightsLink®
Figure 2.15 (21), page 30	Figure 8	A. Takezawa, K. Yonekura, Y. Koizumi, X. Zhang, M. Kitamura, Isotropic Ti–6Al–4V lattice via topology optimization and electron-beam melting, <i>Addit. Manuf.</i> 22 (2018) 634–642. https://doi.org/10.1016/j.addma.2018.06.008	Elsevier	20/7/20	Yes	RightsLink®

APPENDICES

Figure location	Extract used	Source of work	Copyright holder	Permission requested on	Permission granted?	Permission note
Figure 2.15 (24), page 30	Figure 5	L. Mullen, R.C. Stamp, P. Fox, E. Jones, C. Ngo, C.J. Sutcliffe, Selective laser melting: A unit cell approach for the manufacture of porous, titanium, bone in-growth constructs, suitable for orthopedic applications. II. Randomized structures, <i>J. Biomed. Mater. Res. - Part B Appl. Biomater.</i> 92 (2010) 178–188. https://doi.org/10.1002/jbm.b.31504	John Wiley & Sons	20/7/20	Yes	RightsLink®
Figure 2.15 (25), page 30	Figure 3	S. Ghouse, S. Babu, R.J. Van Arkel, K. Nai, P.A. Hooper, J.R.T. Jeffers, The influence of laser parameters and scanning strategies on the mechanical properties of a stochastic porous material, <i>Mater. Des.</i> 131 (2017) 498–508. https://doi.org/10.1016/j.matdes.2017.06.041	Elsevier	20/7/20	Yes	CC BY 4.0
Figure 2.15 (26), page 30	Figure 8	N. Contuzzi, S.L. Campanelli, F. Caiazzo, V. Alfieri, Design and Fabrication of Random Metal Foam Structures for Laser Powder Bed Fusion, <i>Materials (Basel)</i> . 12 (2019) 1301. https://doi.org/10.3390/ma12081301	MDPI (Basel, Switzerland)	20/7/20	Yes	CC BY 2.0
Figure 2.15 (27), page 30	Figure 10	C. Simoneau, P. Terriault, B. Jetté, M. Dumas, V. Brailovski, Development of a porous metallic femoral stem: Design, manufacturing, simulation and mechanical testing, <i>Mater. Des.</i> 114 (2017) 546–556. https://doi.org/10.1016/j.matdes.2016.10.064	Elsevier	20/7/20	Yes	RightsLink®
Figure 2.17 (1,2), page 34	Figure 1	S.Y. Choy, C.N. Sun, K.F. Leong, J. Wei, Compressive properties of functionally graded lattice structures manufactured by selective laser melting, <i>Mater. Des.</i> 131 (2017) 112–120. https://doi.org/10.1016/j.matdes.2017.06.006	Elsevier	20/7/20	Yes	RightsLink®
Figure 2.17 (3), page 34	Figure 2	C. Han, Y. Li, Q. Wang, S. Wen, Q. Wei, C. Yan, L. Hao, J. Liu, Y. Shi, Continuous functionally graded porous titanium scaffolds manufactured by selective laser melting for bone implants, <i>J. Mech. Behav. Biomed. Mater.</i> 80 (2018) 119–127. https://doi.org/10.1016/j.jmbbm.2018.01.013	Elsevier	20/7/20	Yes	RightsLink®

APPENDICES

Figure location	Extract used	Source of work	Copyright holder	Permission requested on	Permission granted?	Permission note
Figure 2.17 (4), page 34	Figure 2	S. Limmahakhun, A. Oloyede, K. Sitthiseripratip, Y. Xiao, C. Yan, Stiffness and strength tailoring of cobalt chromium graded cellular structures for stress-shielding reduction, <i>Mater. Des.</i> 114 (2017) 633–641. https://doi.org/10.1016/j.matdes.2016.11.090	Elsevier	20/7/20	Yes	RightsLink®
Figure 2.17 (5), page 34	Figure 1	S. Arabnejad, B. Johnston, M. Tanzer, D. Pasini, Fully porous 3D printed titanium femoral stem to reduce stress-shielding following total hip arthroplasty, <i>J. Orthop. Res.</i> (2016) 29–31. https://doi.org/10.1002/jor.23445	John Wiley & Sons	20/7/20	Yes	RightsLink®
Figure 2.17 (6), page 34	Figure 4	C. Simoneau, P. Terriault, B. Jetté, M. Dumas, V. Brailovski, Development of a porous metallic femoral stem: Design, manufacturing, simulation and mechanical testing, <i>Mater. Des.</i> 114 (2017) 546–556. https://doi.org/10.1016/j.matdes.2016.10.064	Elsevier	20/7/20	Yes	RightsLink®
Figure 2.17 (7), page 34	Figure 25	L.E. Murr, S.M. Gaytan, F. Medina, H. Lopez, E. Martinez, B.I. Machado, D.H. Hernandez, L. Martinez, M.I. Lopez, R.B. Wicker, J. Bracke, Next-generation biomedical implants using additive manufacturing of complex, cellular and functional mesh arrays, <i>Philos. Trans. R. Soc. A Math. Phys. Eng. Sci.</i> 368 (2010) 1999–2032. https://doi.org/10.1098/rsta.2010.0010	Royal Society	20/7/20	Yes	RightsLink®
Figure 2.20, page 39	Figure 4	M. Suard, G. Martin, P. Lhuissier, R. Dendievel, F. Vignat, J.J. Blandin, F. Villeneuve, Mechanical equivalent diameter of single struts for the stiffness prediction of lattice structures produced by Electron Beam Melting, <i>Addit. Manuf.</i> 8 (2015) 124–131. https://doi.org/10.1016/j.addma.2015.10.002	Elsevier	20/7/20	Yes	RightsLink®
Figure 2.21, page 40	Figures 1-3	L.J. Gibson, The mechanical behaviour of cancellous bone, <i>J. Biomech.</i> 18 (1985) 317–328. https://doi.org/10.1016/0021-9290(85)90287-8	Elsevier	20/7/20	Yes	RightsLink®
Figure 2.22, page 41	Figures 5-8	L.J. Gibson, The mechanical behaviour of cancellous bone, <i>J. Biomech.</i> 18 (1985) 317–328. https://doi.org/10.1016/0021-9290(85)90287-8	Elsevier	20/7/20	Yes	RightsLink®

APPENDICES

Figure location	Extract used	Source of work	Copyright holder	Permission requested on	Permission granted?	Permission note
Figure 2.23, page 44	Figure 2	A. Odgaard, Three-dimensional methods for quantification of cancellous bone architecture, <i>Bone</i> . 20 (1997) 315–328. https://doi.org/10.1016/S8756-3282(97)00007-0	Elsevier	20/7/20	Yes	RightsLink®
Figure 2.24, page 44	Figure 4	T.H. Smit, E. Schneider, A. Odgaard, Star length distribution: A volume-based concept for the characterization of structural anisotropy, <i>J. Microsc.</i> 191 (1998) 249–257. https://doi.org/10.1046/j.1365-2818.1998.00394.x	John Wiley & Sons	20/7/20	Yes	RightsLink®
Figure 2.25, page 45	Figure 1	T. Gross, D.H. Pahr, P.K. Zysset, Morphology-elasticity relationships using decreasing fabric information of human trabecular bone from three major anatomical locations, <i>Biomech. Model. Mechanobiol.</i> 12 (2013) 793–800. https://doi.org/10.1007/s10237-012-0443-2	Springer Nature	20/7/20	Yes	RightsLink®
Figure 2.26, page 46	Figures 2 and 3	D.S. Elliott, K.J.H. Newman, D.P. Forward, D.M. Hahn, B. Ollivere, K. Kojima, R. Handley, N.D. Rossiter, J.J. Wixted, R.M. Smith, C.G. Moran, A unified theory of bone healing and nonunion, <i>Bone Joint J.</i> 98-B (2016) 884–891. https://doi.org/10.1302/0301-620X.98B7.36061	British Editorial Society of Bone & Joint Surgery	20/7/20	Yes	RightsLink®
Figure 2.27, page 47	Figure 2	P. Christen, K. Ito, R. Ellouz, S. Boutroy, E. Sornay-Rendu, R.D. Chapurlat, B. Van Rietbergen, Bone remodelling in humans is load-driven but not lazy, <i>Nat. Commun.</i> 5 (2014) 1–5. https://doi.org/10.1038/ncomms5855	Springer Nature	20/7/20	Yes	RightsLink®
Figure 2.27, page 47	Figure 2	P. Christen, K. Ito, R. Ellouz, S. Boutroy, E. Sornay-Rendu, R.D. Chapurlat, B. Van Rietbergen, Bone remodelling in humans is load-driven but not lazy, <i>Nat. Commun.</i> 5 (2014) 1–5. https://doi.org/10.1038/ncomms5855	Springer Nature	20/7/20	Yes	RightsLink®

A3.2 Permission communications

The following communications were used as consent for the use of images from Renishaw plc in Figure 2.13, page 26.

From: Renishaw Web Site <email@renishaw.net>

Sent: 17 July 2020 22:41

To: Communications <Communications@Renishaw.com>

Subject: Renishaw - All other enquiries - Additive manufacturing [GB] - Imperial College London



Contact us - All other enquiries - Additive manufacturing

Any further questions or requests for assistance please contact communications@renishaw.com or call your local Renishaw office - visit www.renishaw.com/worldwidecontacts to find the number.

Your details

Name Umar Hossain

Email address umar.hossain12@imperial.ac.uk

Telephone 07402675947

Company name Imperial College London

Address line 1 32 Ridgeview Road, Whetstone

Address line 2 Whetstone

City / town London

County / state London

Country United Kingdom

Post / zip code N20 0HJ

Enquiry details

Area of interest Additive manufacturing

Purpose of enquiry All other enquiries

Contact method Email

DPA No

Dear Renishaw plc, I am completing my PhD thesis at Imperial College London entitled 'Design and testing of additively manufactured lattice structures for musculoskeletal applications'. I seek your permission to reprint, in my thesis an image from the online Renishaw Resource Centre: <https://resources.renishaw.com/gen/details/am250-machine--38488>. This image is available to download from the URL. I would like to include the image in

Enquiry my thesis which will be added to Spiral, Imperial's institutional repository <http://spiral.imperial.ac.uk/> and made available to the public under a Creative Commons Attribution-Non Commercial-No Derivatives 4.0 International Licence (CC BY-NC-ND). If you are happy to grant me all the permissions requested, please contact me, whereupon I can provide a letter to be signed allowing me to use the image as set out. Yours faithfully, Umar Hossain

Contact details

Your enquiry has been passed to the following contact

Renishaw plc Renishaw plc
New Mills
Wotton-under-Edge
Gloucestershire
United Kingdom
GL12 8JR
www.renishaw.com

Telephone +44 1453 524524

Fax +44 1453 524901

Email communications@renishaw.com

Website www.renishaw.com

[Contact us](#) | [Legal notice](#)

Copyright © 2020 [Renishaw plc](#). All rights reserved.

From: Communications <Communications@Renishaw.com>

Sent: 20 July 2020 08:06

To: Chris Dimery <Chris.Dimery@Renishaw.com>

Cc: Stuart Offer <Stuart.Offer@Renishaw.com>

Subject: FW: Renishaw - All other enquiries - Additive manufacturing [GB] - Imperial College London

From: Chris Dimery <Chris.Dimery@Renishaw.com>

Sent: 20 July 2020 09:25

To: Hossain, Umar <umar.hossain12@imperial.ac.uk>

Subject: RE: Renishaw - All other enquiries - Additive manufacturing [GB] - Imperial College London

Hi Umar,

Its fine to reprint images on the resource centre.

Best regards

Chris